Department of Chemical & Process Engineering

High Energy Density Electrochemical Double Layer Capacitors: The effect of pore size distribution on the performance of room temperature ionic liquids

Fiona B. Sillars

Degree of Doctor of Philosophy

2010

Declaration of Authors Rights

Preface of Publications

Manuscripts Accepted for Publication

F. B. Sillars, M. Mirzaeian, and P. J. Hall "Resorcinol – Formaldehyde Gels as Electrodes for Electrochemical Double Layer Capacitors" *Proceedings of the 234th American Chemical Society International Conference, Boston, August 2007*

F. B. Sillars, S. I. Fletcher, M. Mirzaeian, and P. J. Hall "Evaluation of Activated Carbons with Room Temperature Ionic Liquid Electrolytes for Electrochemical Capacitors" *Proceedings of the 1st International Conference on Sustainable Power Generation and Supply, Nanjing, April 2009*

F. B. Sillars, S. I. Fletcher, M. Mirzaeian, and P. J. Hall, "Ionic Liquid Electrolytes to Enhance Supercapacitor Performance" *Proceedings of the 215th Electrochemical Society International Conference, San Francisco, May 2009*

S. Isobel Fletcher, Fiona B. Sillars, Nicholas E. Hudson & Peter J. Hall. **"**Physical Properties of Selected Ionic Liquids for Use as Electrolytes and other Industrial Applications" *Journal of Chemical and Engineering Data, 2010, 55, 778 – 782*

Submitted for Publication

F. B. Sillars, S. I. Fletcher, M. Mirzaeian, and P. J. Hall "The Effect of Pore Size Distribution on Capacitance Performance of Ionic Liquid based Electrochemical Capacitors" *Energy and Environmental Science*

Planned for Publication

F. B. Sillars, S. I. Fletcher, M. Mirzaeian, and P. J. Hall "Room Temperature Ionic Liquid Electrolytes for High Energy Density Supercapacitors" *Energy and Environmental Science*

R. Carter, F. B. Sillars, A. Cruden and P. J. Hall, "Short Communication - Standardised System for Reporting of Supercapacitor Data" *Journal of Power Sources*

Acknowledgements

I would like to thank my supervisor, Prof. Peter J. Hall for his guidance and support throughout the duration of this project. Thanks also to Dr Mojtaba Mirzaeian and Dr Isobel Fletcher for there help and contributions to my work throughout the project.

Thanks are given to the departmental lecturers, secretarial staff; Mrs K. Morrison, Mrs. C. Rashid, Miss T. Knight, and Miss M. O'Donnell, IT support; Mr M. Kidd, and importantly the laboratory technicians; from the Department of Chemical and Process Engineering Mr J. Murphy, Mr S. Adams, Mr I. Airdrie, Mr J. Wilkes and Mr L. Allan and from the Department of Pure and Applied Chemistry Mr. J. Morrow.

I would like to thank my fellow PhD students and the Postdoctoral researchers I shared time with for making the last 3 years enjoyable.

My biggest thanks go to my partner Mark Symington and my parents Sue and Robert Sillars for their continued support and patience over the years.

Contents

List of Figures

List of Tables

Abstract

Electrochemical capacitors (ECs) are devices that are used to provide short pulses of energy at high power, for example, in regenerative braking and acceleration for transport applications. Additionally, ECs can extend battery lifetimes, improve the range of electric vehicles (EVs) and make driving cycles more efficient. However, commercially available devices based on aqueous or organic electrolytes are only able to operate at 1.2V and 2.7V respectively. This results in large stacks of devices being necessary to meet the requirements of EVs.

The use of room temperature ionic liquid (RTIL) electrolytes promises to improve the energy density of ECs by allowing for operation at higher voltages of 3.7V, this reducing the size of the stacks necessary to meet the demands of EVs . Electrolytes studied were RTILs 1-ethyl-3-methylimidazolium tetrafluoroborate ($EMImBF_4$), 1-ethyl-3-methylimidazolium dicyanamide ($EMImN(CN)_2$), 1,2-dimethyl-3-propylimidazolium bis(trifluoromethylsulfonyl)imide (DMPImTFSI), and 1-butyl-3-methylpyrrolidinium tris(pentafluoroethyl)trifluorophosphate ($BMPyT(f_5Et)PF_3$). Commercially utilised 1M-tetraethylammonium tetrafluoroborate solution in anhydrous propylene carbonate (Et_4NBF_4-PC 1M) was studied for comparison purposes.

Several research groups have shown that the pore size distribution of materials used to produce electrodes is also an important factor in determining EC performance, with micropores (< 1 nm) being identified as essential for high capacitance. However, these studies operated at low charge-discharge rates of 0.1 – 6 A g^{-1}. This indicated that the results could not be used to assess the performance of ECs at the high rates of charge-discharge that would be required for application in EVs. Also none of the research focussed on utilising RTILs at ambient temperature, where the viscosity of the RTILs may hinder mass transport in micropores. From this it was hypothesised that the pore size distributions required for high capacitance, energy and power performance would be greater than those obtained in the literature.

To assess the effect of pore size distribution on RTIL performance, controlled porosity carbons were produced from phenolic resins activated in CO_2. The carbon samples were characterised by nitrogen adsorption-desorption at 77K and the

relevant electrochemical behaviour was characterised by galvanostatic charge – discharge, cyclic voltammetry and electrochemical impedance spectroscopy.

This study has identified that the pore size is an important factor for optimising capacitance performance of carbon-based / RTIL ECs. The best capacitance performance was obtained for the activated carbon xerogel with average pore size 3.5 nm, whereas the optimum rate performance was obtained for average pore size 6 nm. The activated carbon sample with average pore size 6 nm allowed for maximum capacitance retention of approximately 70% at high current density of 64 mA cm^{-2} (32 A g^{-1}). It was found that the performance of the RTIL electrolytes was of the order $EMImBF_4$ > DMPImTFSI > $BMPyT(f_5Et)PF_3$ > $EMImN(CN)_2$. The maximum capacitance values obtained for $EMImBF_4$, DMPImTFSI, $BMPyT(f_5Et)PF_3$, $EMImN(CN)_2$, and Et_4NBF_4-PC 1M under Galvanostatic charge-discharge at 2 mA cm^{-2}, were 140, 105, 41, 27, and 109 F g^{-1}, respectively. A maximum energy density of 175 Wh kg^{-1} and power density of 665.5 kW kg^{-1} were obtained for the activated carbon sample with average pore size 3.5 nm and RTIL electrolyte $EMImBF_4$ at an operating voltage of 3 V. This was an improvement over the commercially utilised organic electrolyte Et_4NBF_4-PC 1M which obtained a maximum energy and power density of 84 Wh kg^{-1} and 528.1 kW kg^{-1} respectively.

This study contradicts the literature by showing that mesopores of 3.5 – 6 nm provide the best performance at high charge-discharge rate, when combined with RTILs. This has implications in the manufacture of ECs for high power and energy applications, where mesoporous materials combined with RTILs may provide superior performance to microporous materials.

The technological impact of this work, an effective doubling of energy density while maintaining power density, will make Electrochemical Capacitors more attractive for transport applications and hence aid the development of a carbonless transport system. RTIL based devices could become the basis for a new capacitor industry.

1.0 Introduction

1.1 Renewable and Sustainable Energy

1.1.1 Renewable and Sustainable Energy Storage Requirements

With the growing emphasis on renewable and sustainable energy to replace the world's heavy dependency on fossil fuels and reduce CO_2 emissions, energy storage has never been more important.

Renewable energy sources, e.g. wind, wave or solar energy, are inherently intermittent and therefore cannot be controlled like that of gas or coal fired power stations where the output can be increased or decreased to match current demand, i.e. power stations are load following. An example of the non-load following nature of renewables is that wind power is generally highest at night, when the energy consumption is lowest. Energy from renewables also fluctuates on a momentary basis, e.g. fluctuation in wind power as the turbines rotate.

Renewables require load-levelling from some external source. To fully utilise the energy from renewable sources it is therefore necessary; (1) to store to the energy for use when required; and (2) that the energy be ready for use quickly during peak times. Current battery technology cannot meet the storage demands of renewables alone, as they are unable to charge and discharge at the high rates required for absorption and consumption of energy. [1]

Another important advance for the reduction of CO_2 emissions is the development of hybrid electric vehicles (HEVs) and fully electric vehicles (EVs). *Figure 1.1* shows the speed and power required by a small passenger car during a standard urban journey. A dashed line indicates the average power. Note that the peak power required by the vehicle is 17 kW, but the average power is just 2.5 kW. [2] This large disparity between the average power requirement and peak power requirement suggests that the way in which energy is stored can be split to increase the efficiency of the system. This has led to the development of energy storage devices that can provide the high power required during periods of fast acceleration that batteries and fuel cells are unable to match.

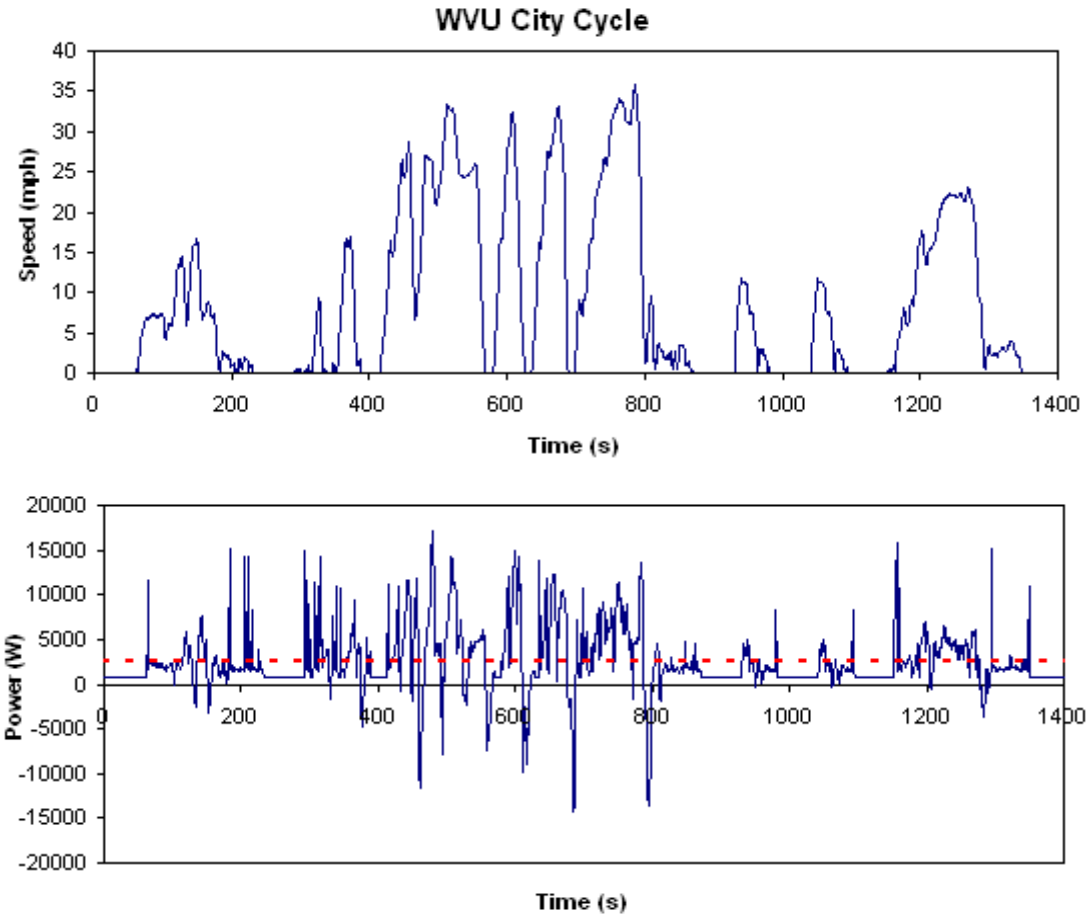

Figure 1.1 – Power Use and Speed throughout a Typical Urban Drive Cycle. [2]
Courtesy of Dr A. Cruden University of Strathclyde EEE Department

1.1.2 Electrochemical Capacitors for Renewable and Sustainable Energy

For the demands of a fossil fuel "free" society to be matched with renewable and sustainable energy, another type of energy storage device is required. Electrochemical Capacitors (ECs) are able to meet these demands. They are able to charge / discharge at high rate, enabling both the load-levelling of renewable energies and the acceleration of EVs. The high rate of charge / discharge is possible as ECs store their energy via electrostatic attraction between the electrode and ions in a liquid electrolyte and therefore do not undergo any rate-limiting Faradaic reactions such as in a battery. [3]

The main advantages of ECs are that they can provide high power capability (specific power of 15 kW kg^{-1} for Maxwell Boostcap 650F Ultracapacitor), excellent reversibility (90 – 95%) and long cycle life (>10^5 cycles). As shown in *Figure 1.2* they are able to bridge the gap between traditional high power, low energy density capacitors and high energy, low power density, batteries and fuel cells. [4] They are also of great interest for use in digital communication devices, digital cameras, mobile phones, electric tools, pulse lasers and uninterruptable power supplies (UPS). [5]

One of the most recent developments in the use of ECs, is their use to recover energy dissipated from braking, by using it to charge the ECs. This recovered energy can then be used to provide peak power for when the batteries cannot match the vehicle demands. *Figure 1.3* shows an Indian urban drive (typical of most city drive cycles) for a vehicle operated on battery power alone. [6] The solid blue line represents the power output provided from the battery pack. The dashed red line shows the power required by the vehicle during this drive cycle. It can be seen from the top half of the graph that at times of peak power demand the battery pack cannot provide the power required and the performance of the vehicle was reduced. The lower portion of the graph shows the energy recovered by the battery pack does not meet that given out by the vehicle, leading to wasted energy. ECs would allow for peak power output and input to the system. Another way ECs would be an advantage to the system would be to use them for load-levelling, where the battery power output is set well below the upper operating limit and the ECs provide for the high power outputs as indicated in *Figure 1.3*. They can also be used for recovering

energy otherwise lost from braking. This allows for the battery to operate at lower power ratings thus prolonging the life of the battery

The solution to powering Electric Vehicles (EVs) may come in the form of a hybrid system of fuel cells, batteries and electrochemical capacitors, where the ECs can be used for periods of high power demand (e.g. fast acceleration) and also for the recovery of energy during braking. This recovered energy can then be stored in the battery packs to allow for smaller fuel cells (the most expensive component) to be used. This may lead to a fully electric vehicle (EV) that does not require plug-in to the grid for recharging, other than on a maintenance basis.

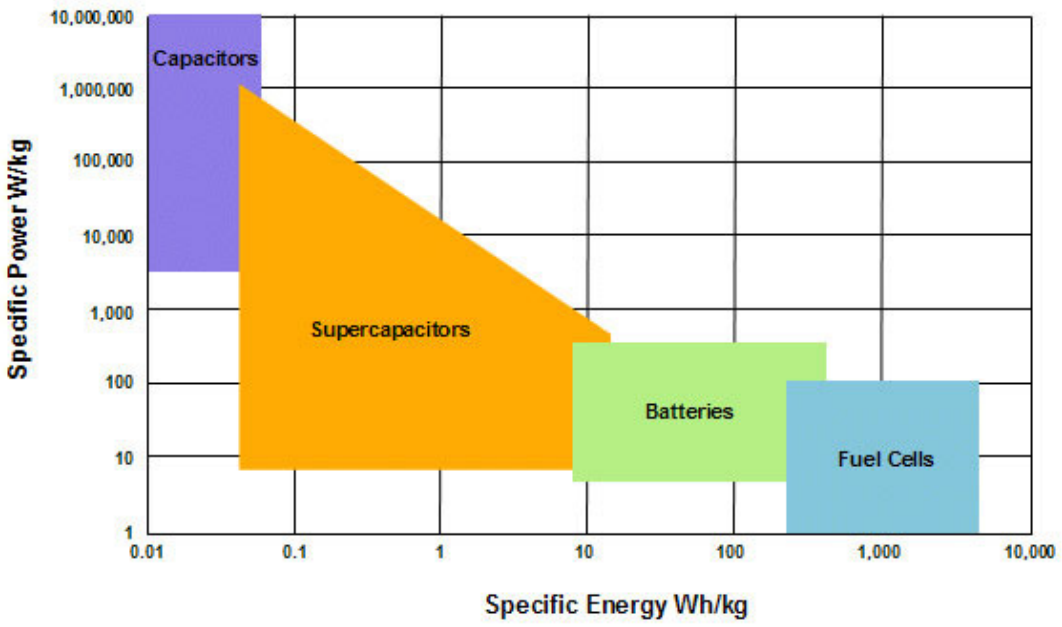

Figure 1.2 – Ragone Plot of Specific Power versus Specific Energy for Various Energy Storage Devices

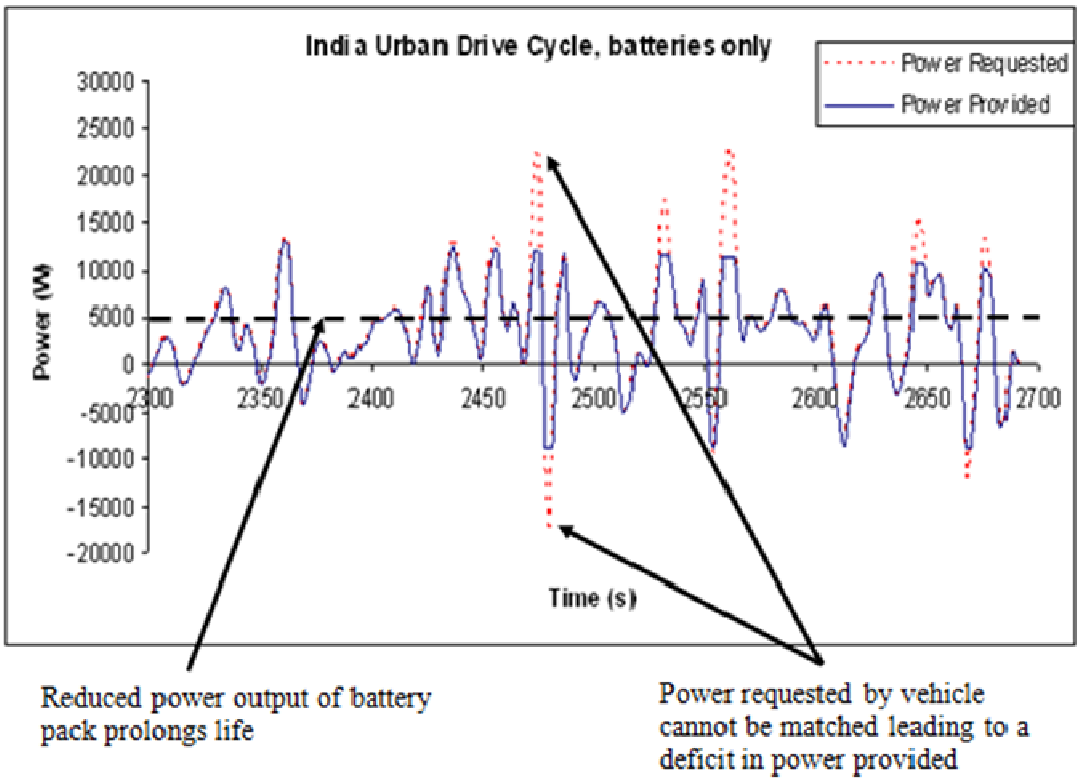

Figure 1.3 – Power Requirements for Battery Powered Electric Vehicle Urban Drive Cycle. Courtesy of Dr A. Cruden University of Strathclyde EEE Department.

1.1.3 Summary of Uses for Electrochemical Capacitors

ECs can be used for a variety of applications, most of which come under one or more of three categories:

1) Energy capture and/or provision of peak power
2) Power quality applications
3) Backup / safety and low maintenance applications

ECs are particularly appropriate in certain applications due to their high power capability, high efficiency and long life span.

1.2 Batteries, Capacitors and Electrochemical Capacitors Background

A modern technological society demands the use and storage of energy on a major scale. Energy consumption or production that relies on the combustion of fossil fuels is forecast to have a severe future impact on world ecology. Electrochemical energy systems are under serious consideration as an alternative energy / power source. The energy in these systems is stored in two fundamentally different ways: [1]

1. Indirectly, as in batteries as potentially available chemical energy requiring Faradaic oxidation and reduction of the electrochemically active reagents to release charges that can perform electrical work when they flow between two different electrodes having differing electrode potentials; and
2. Directly, in an electrostatic way, as negative and positive electric charges on the plates of a capacitor, a process known as non-Faradaic electrical energy storage.

The efficiency of these two modes of storing electrical energy is usually substantially larger than that of fuel combustion systems, which are limited thermodynamically to ~25 – 50%, while electrochemical systems usually involve more reversible processes, with direct conversion of potentially available chemical energy to Gibbs free energy, increasing efficiency to 95 %.

An important difference arises between the reversibility of Faradaic and non-Faradaic systems. For the energy stored by capacitors, only an excess and deficiency of electron charges on the capacitor plates have to be established on charge and the reverse on discharge, i.e., no chemical changes are involved (as shown in the traditional capacitor schematic in *Figure 1.4 (a)*). Whereas for batteries the energy is stored through Faradaic reactions, and chemical conversions of the anode and cathode materials must take place. The conversion of the chemical reagents involved in a battery during the charge and discharge process is not fully reversible and therefore the cycle life of batteries is usually restricted to a maximum of several thousand cycles. Since no chemical changes are involved in the charging and discharging of a traditional capacitor, it has an almost unlimited cycle life. [7]

Over the years batteries have been the technology of choice for most applications, because they can store large amounts of energy in a relatively small volume and weight and provide suitable levels of power for many applications. However as mentioned above, shelf and cycle life have been a problem with most types of batteries. In recent times the power requirements in a number of applications have increased markedly and have exceeded the capability of batteries of standard design. It has therefore become necessary to separate the energy and power requirements by providing for the peak power using a pulse power device (capacitor) that is charged periodically from a primary energy source (battery) to meet these needs. For these applications traditional capacitors cannot store enough energy in the volume and weight available. This is where the ECs represents a new energy storage device that is able to bridge the gap that exists between batteries and capacitors as represented in the Ragone plot[4] in *Figure 1.2*.

Electrochemical capacitors encapsulate two main types of capacitor: electrochemical double layer capacitors (EDLCs) *Figure 1.4 (b) and (c)* and pseudocapacitors *Figure 1.4(d).*

EDLCs contain in comparison to conventional capacitors a significantly enlarged electrode surface and a liquid electrolyte shown in *Figure 1.4(c)*. Carbon is often used as the electrode material, due to its ability to provide a very large specific surface. At the interface between electrode and electrolyte the electrochemical double layer is characterised by a concentration of ions and has a thickness of only a few molecular diameters, by comparison to millimetres for traditional capacitors (*Figure 1.4 (a)*). The storage of charge mechanism occurs via a separation of charge and alignment of dipoles in the electrical double layer as shown in *Figures 1.4 (b) and (c)*. The extremely low thickness of this area coupled with the large electrode area, causes the relative large capacity of the EDLCs compared to conventional capacitors. In normal operation no chemical reactions occur and therefore display in comparison to electrochemical storage systems a high cycle life and a high power density. The devices show a high efficiency and they are insensitive with respect to deep discharge (red dashed line in *Figure 1.3*).

Pseudocapacitors also consist of a porous electrode and a liquid electrolyte. However, potential-dependent reactions result in Faradaic charge transfer across the

double-layer (as shown *in Figure 1.4 (c)*); reactions that become thermodynamically favourable in certain ranges of potential produce capacitive charge / discharge characteristics. This results in a prospective four-fold increase in the capacitance of pseudocapacitors over EDLCs. The electrode materials for pseudocapacitors are generally metal oxides; with the highest volume of research concerning the use of ruthenium oxide. Carbon materials can also exhibit a pseudocapacitance, if there is surface functionality present that is electrochemically active with the electrolyte being used. The presence of the Faradaic reactions reduces the cycle life to below 10,000 cycles. [8]

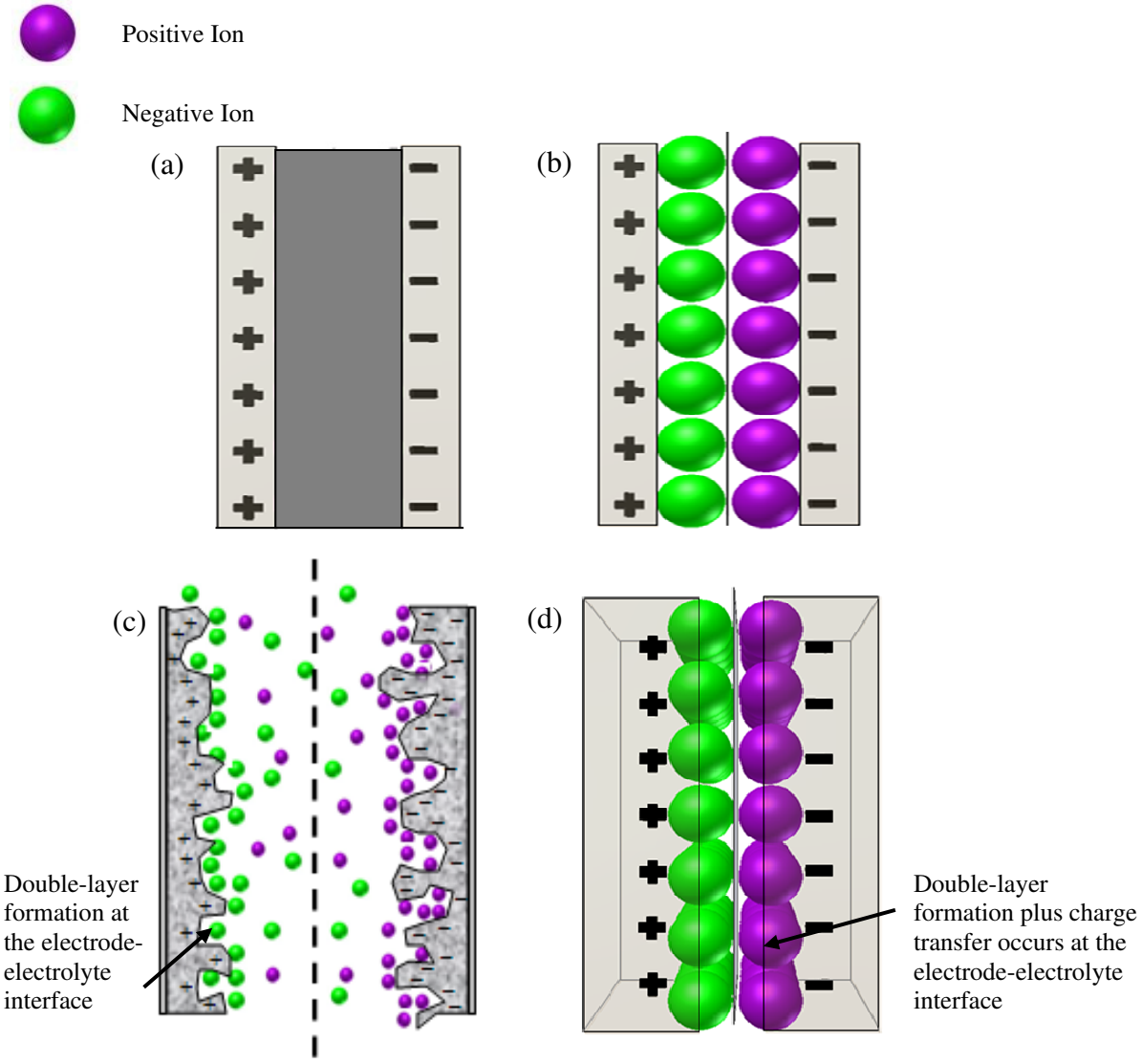

Figure 1.4 – Representation of (a) Traditional Capacitor, (b) an EDLC, (c) High Surface Area Porous Electrode EDLC and (d) Pseudocapacitor

1.3 Historical Development of Capacitors

The nature of electricity took a long time to be understood, from the early experiments on electrostatic electricity in the mid-18th century, e.g. by Galvani, through the time of the invention of the first electric battery by Alessandro Volta in 1800, on to Faraday's and Davy's monumental discoveries on the chemical origin of electricity generated by Volta's pile. At first, two types of electricity were proposed: "animal electricity", as in the works of Galvani on stimulation of the frog's leg nerve by contact between two dissimilar metals and later, "Voltaic electricity" generated chemically from a Volta pile of zinc and silver or copper plates separated by paper wetted with an acid or salt solution. [1]

At the same time extensive work was being carried out on electrostatic electricity generated, for example, by rubbing of naturally occurring amber or by the so-called Wimshurst machine (a rotating circular plate, containing insets of amber-like material, rubbing against charge-collector plates connected overall to a Leyden jar or a spark gap). It was from this direction of research on electricity that the invention of the electric condenser arose, referred to as the "Leyden Jar", shown in *Figures 1.5(a-b)*, [9] capable of storing electric charge generated by a Wimshurst machine. Such a jar had the "capacity", depending on its dimensions and materials of construction, of storing electric charge by bringing it together in a condensed way (hence the term "condenser") on the surfaces of a Leyden Jar at a certain two-dimensional charge density.

Figure 1.5 – (a) Leyden Jar Schematic and (b) Photograph

Although the experimental detail of electrical charging of surfaces, including those of the Leyden Jar condenser, was well understood in the mid- and later part of the eighteenth century, the full physical significance of charging or discharging processes at the plates of the capacitors was not fully understood at the atomic physical level until 140 years after the development of the Leyden Jar capacitor, with the development of EDLCs.

The first EDLC was developed in 1957 by Becker for General Electric using a porous carbon electrode. [10] The patent described electrical energy stored by means of the charge held in the interfacial double-layer at a porous carbon material and an aqueous electrolyte. After Becker, the Standard Oil Company in Cleveland, Ohio, patented a device in 1966 that utilised the high surface area carbon materials, but in a non-aqueous electrolyte.

1.4 Structure of the Double-Layer

Electrochemical double-layer capacitors store energy at the electrolyte / electrode interface through reversible ion adsorption from the bulk electrolyte onto the electrode surface. This interface is known as the "double-layer" and energy stored can be referred to as double-layer capacitance. No Faradaic (redox) reaction is involved in the charge storage mechanism. The main electrode materials to exhibit a double-layer capacitance with no Faradaic reaction are porous carbons. The types of porous carbons studied will be discussed in **Section 2.1**.

The theory of the double-layer was initially introduced by Helmholtz and Gouy and later refined by Stern and Geary, as shown in *Figures 1.6 (a – b.)* [1]

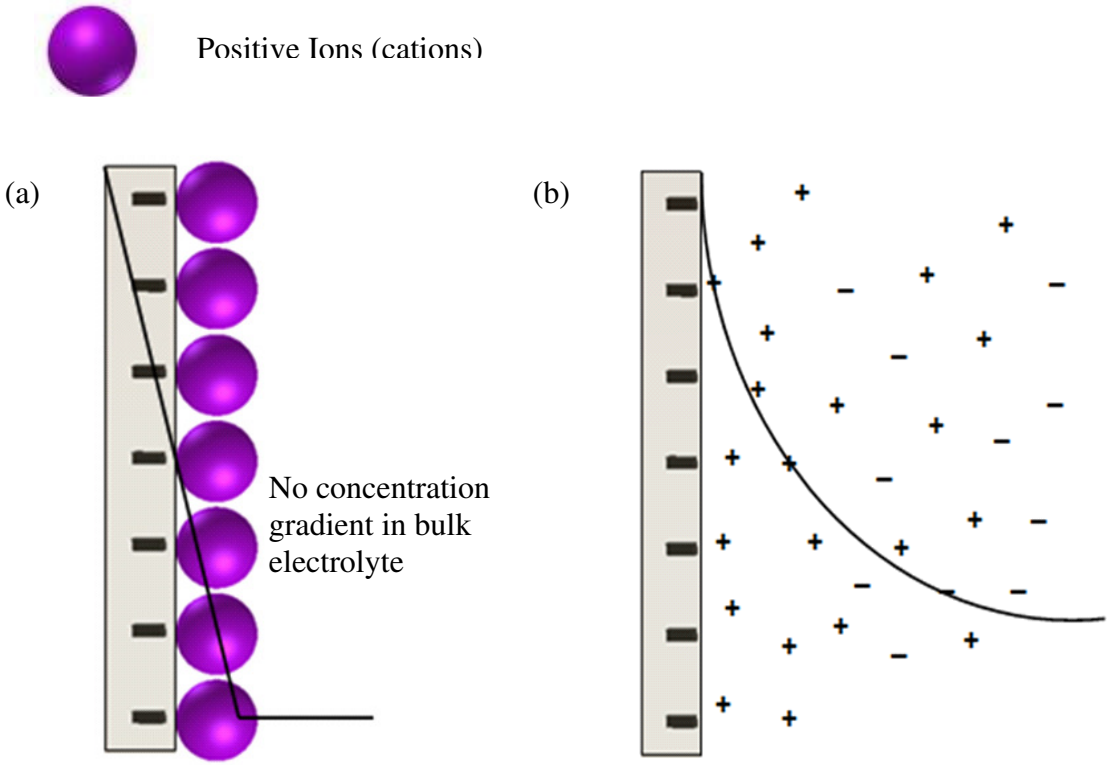

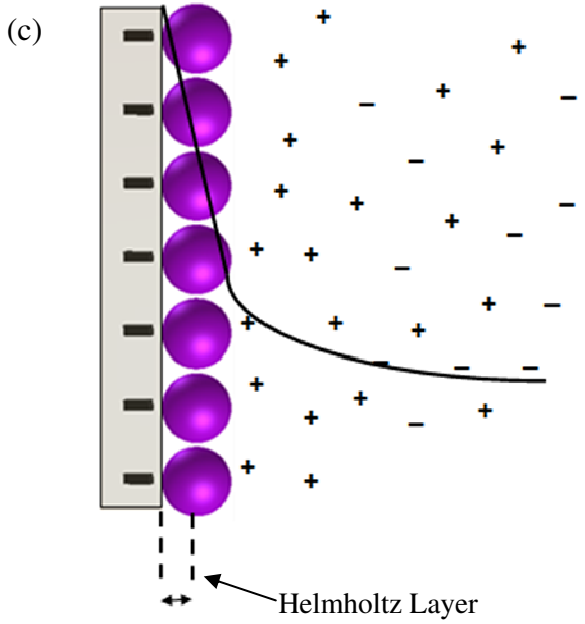

Figure 1.6 – (a) Helmholtz parallel-plate model, (b) Gouy diffuse double-layer model, (c) Stern model combining (a) and (b).

The Helmholtz model (*Figure 1.6 (a)*) was the first to describe the capacitance that occurs as a result of the electrolyte / electrode interface. The model assumed that the excess of positive or negative charge on the electrode had to be countered by a single layer of anions or cations which were adsorbed at the surface with no concentration gradient between the adsorbed ions and the bulk electrolyte. [11]

Gouy modified the previous double-layer model and considered the counterions adsorbed on the electrode surface as part of a 3-dimensional diffusely distributed population of anions and cations from the electrolyte, that would have an equal and opposite net charge density to the 2-dimensional electron excess or deficit charge on the metal surface. In this model the ions were assumed to be point charges, shown in *Figure 1.6(b).* The Gouy model also introduced thermal fluctuations that would occur due to the concentration gradient at the double-layer. [12]

Although the Gouy model was an improvement over the Helmholtz model, it still failed to predict experimental results. The Stern model combined the Helmholtz and Gouy models, shown in *Figure 1.6(c).* The Stern model assumed that the bulk

electrolyte was electroneutral, with an excess charge on the solution side partly contained in a compact Helmholtz layer. [13]

This leads to the development of an equation for the double-layer capacitance, *Equation 1.3*.

$$C = \varepsilon_0 \varepsilon_r \left(\frac{A}{d} \right) \qquad \textbf{Equation 1.1}$$

Where ε_0 is the relative permittivity of a vacuum, ε_r is the dielectric constant of the electrolyte, A is the surface area of the electrode that is accessible to the electrolyte, and d is the thickness of the double-layer. To increase the charge stored, the surface area of the electrode can be increased. This can be done by developing the porosity through the use of different carbon precursors, as well as different synthesis techniques. However, there is no simple linear relationship between specific surface area and specific capacitance. [14] In fact, the capacitance is more related to the pore structure, i.e. the control of the pore size and pore size distribution. This will be discussed further in **Section 2.2**.

1.5 New Developments to Enhance EC Performance

Although, as has been mentioned, ECs possess much higher power densities than batteries one major technological challenge is to increase their energy densities. This is particularly important in, for example, transport applications where space and volume are at a premium. Currently most EC systems operate using aqueous or organic electrolytes, [1] which limits the ECs to 1.2 V and 2.7 V respectively. Since specific energy (E) and power (P) increase quadratically with operating voltage (*Equations 1.2 and 1.3* [1]) one obvious way to increase energy and power density would be to increase their operating voltages. To maximise the operating voltage, new electrolytes must be considered in the form of Room Temperature Ionic Liquids (RTILs).

$$E = \frac{1}{2} C V^2 \qquad \textbf{Equation 1.2}$$

$$P = \frac{1}{4} \frac{V^2}{R} \qquad \textbf{Equation 1.3}$$

where, C is the specific capacitance (F g^{-1}), V is the maximum operating voltage of the electrolyte, and R is the equivalent series resistance for the cell.

Room-temperature ionic liquids (RTILs) have been studied as novel electrolytes since the 1950s, when the chloroaluminate systems were discovered. The use of the chloroaluminates was superseded by the use of fluoroanions BF_4^- and PF_6^- based RTILs, both due to improved properties and that the chloroaluminate systems were found to be unstable in the presence of water and oxygen, with potential to form explosive mixtures on contact with the atmosphere. Although the fluoroanions degrade in contact with air (oxygen) and water, the degradation compounds are stable and can be reversed to the original cation / anion via vacuum drying and storage in an air and water free atmosphere (usually nitrogen or argon). [15,16]

RTILs are composed of asymmetric organic cations and anions that cause them to be molten salts at or below room temperature. RTILs have several benefits over currently utilised electrolytes. Since RTILs are composed of organic ions, the structural variations are unlimited due to the easy preparation of the components.

This means that RTILs have the potential to be tailored to a specific application. As they are molten at low temperature, no voltage limiting solvent is required to form a solution with mobile ions. [15] RTILs are also stable over a large range of temperatures, with decomposition temperatures over 400°C possible. [16] This thermal stability results in very low vapour pressures at low temperatures (below 100°C). These factors combine to make them an interesting choice of electrolyte.

The low-volatility is important as safety has become, in some cases, more of an issue than performance. The high vapour pressures of acetonitrile (AN) based electrolytes results in a narrow operating temperature range, which requires expensive thermal control to keep within safe limits. There is also the potential for explosions to occur with AN under extreme thermal conditions, e.g. during vehicle accidents. [17] These safety issues have resulted in ANs use as an electrolyte solvent being banned in Japan.

RTILs also have advantages over aqueous electrolytes because of their non-corrosive nature. This allows for cheaper materials of construction to be used and cycle life of the full device is prolonged as aggressive corrosive materials have been removed.

1.6 Carbon Based Electrode Materials

Although all materials exhibit double layer capacitance, there are four major requirements for electrodes used in such applications: (1) high surface area, (2) low electrical resistance, (3) good polarisability, and (4) no participation in Faradaic reactions at the applied voltage. [1]

A substantial fraction of the research carried out on electrochemical capacitors has depended, and continues to do so, on an understanding of the properties of carbon. Carbon is an element almost uniquely suited to electrochemical double layer capacitor production due to several allotropic forms (diamond, fullerenes, graphite and nanotubes), various microtextures (more or less ordered) owing to the degree of graphitisation, a rich variety of dimensionality from 0 to 3D and its ability to existence as different forms (from powders to fibres, foams and composites). They are also easy to process, relatively low cost, chemically stable in different solutions (from strongly acidic to basic), able to exhibit very high surface area and are able to perform under a wide range of temperatures. [7]

2.0 Literature Review

2.1 Carbon Electrode Materials

Electrode materials for ECs can be divided in to three main categories [21]:

1. Carbon-based
2. Transition Metal Oxides
3. Conductive Polymers

Section 1.7 identified that porous carbon materials were good candidates for EC electrodes, due to their large specific surface area, high pore accessibility, excellent thermal and chemical stability, as well as being relatively low cost.[7] For this reason, this literature review will concentrate on the types of porous carbon materials suitable for use as EC electrodes. An overview of transition metal oxides and conductive polymers for ECs will be given in **Sections 2.2.1 and 2.2.2,** respectively.

2.1.1 Activated Carbons

Activated carbons are generally produced from the pyrolysis of biomass precursors such as wood, peat, coconut and other agricultural waste products. The specific surface area and porosity of carbons can be significantly increased by an activation process. The manufacture of activated carbons involves two main steps: the production of the carbonaceous raw material at high temperatures (depending on precursor) and the activation of the carbonised product. Therefore, most carbonaceous materials can be converted into activated carbon, although the properties of the final product and the ease with which it can be produced will be dependent on; the nature of the raw material used, the nature of the activating agent, and the conditions of the activation process. There are two methods for activation; physical and chemical. In the chemical activation process, carbonisation and activation are carried out by thermal decomposition of the precursor impregnated with a chemical activating agent, such as KOH, HNO_3 or

H_3PO_4. Physical activation involves gasification of the carbon produced from carbonisation with steam or carbon dioxide at high temperatures [22].

As capacitance is related to the surface area of the electrode, activated carbons are commonly used for EDLC production with surface areas over 2000 $m^2\ g^{-1}$ achieved. Amongst others, Shi [23], Qu and Shi [24] and Frackowiak and Beguin [7] have carried out comprehensive studies on activated carbons to determine the correlation between porous structure and the performance in EDLCs. The specific capacitance varied from 94 – 413 F g^{-1}. It was found that the specific capacitance did not follow a systematic trend with total surface area as would be expected from Equation 1. This was attributed to two flawed assumptions: (1) all surface area accessed by nitrogen at 77K (used to determine surface area) is accessible by electrolyte and (2) the micropore surface area has the same electroadsorption properties as the external surface area.[1] Shi [23] proposed that instead of using one value of C in Equation 1 that this parameter should vary for surfaces that are associated with microporosity and for surfaces associated with external surface area. This new model provided a better fit for the experimental data and suggested that micropores play an important part in double-layer capacitance. Qu and Shi [24] discussed the effect of pore size on the high power capability of the microporous ACs. They found that the ACs that performed best at higher current densities had mean pore sizes of d_{av} = 1.5 nm for aqueous electrolytes.

[1] The IUPAC definitions of a micropore, mesopore and macropore are pores having a diameters < 2 nm, 2 – 50 nm and > 50 nm, respectively.

2.1.2 Carbon Nanotubes

Since the late 1990s there has been a large volume of research carried out on the applicability of carbon nanotubes (CNTs) as EDLC electrodes. CNTs have a highly accessible surface area, low resistivity, and high stability. [25,26]

The basic structure of a CNT is a single seamless cylinder of crystalline graphite, with a well-defined central core, whose end can be capped by a fullerene-type structure. This type of CNT is known as a Single Walled Carbon Nanotube (SWCNT). The more common form of CNTs is as Multi-Wall Carbon Nanotubes (MWCNT), which consist of several graphene cylinders, arranged concentrically around a common axis. CNTs exhibit a narrow pore size distribution, mainly composed of accessible mesopores and surface areas ~10^2 m^2 g^{-1} (surface areas up to 475 m^2 g^{-1} have been reported for activated MWCNTs). [7,26] Their accessible pore network combined with low resistivity and high stability has led to CNTs being extensively researched as materials for EC electrodes. Specific capacitances of between 15 – 300 F g^{-1} have been reported using different configurations of CNTs. [27]

Due to high cost, it is not considered viable to use CNTs as the bulk active material in electrodes. Therefore the most recent developments for the use of CNTs in the manufacture of EDLCs are as conductivity enhancers in place of carbon blacks. They have several advantages over carbon or acetylene blacks as they have an electrical conductivity exceeding 5 x 10^5 S m^{-1} at room temperature for purified materials.[28] The high aspect ratio of CNTs compared to other carbon additives allows for lower weight doping levels to obtain comparable conductivity enhancement. One investigation by Chen *et al.* [29] noted that changing from electrodes based on acetylene black to CNT resulted in a 90% reduction in electrode series resistance. To reduce inter-particle resistance in carbon aerogel electrodes, CNTs were grown directly onto microfibrous carbon paper (MFCP), and then dipped into polyacrylonitrile (PAN) and dimethylformamide (DMF) aquagel. Subsequent carbonisation and activation produced binderless composite electrodes (CNAG) that exhibited a specific capacitance of 524 F g^{-1} (four times that of the pristine carbon aerogel electrode). [30]

2.1.3 Carbon Nanofibres

Carbon nanofibres (CNFs) were first synthesised in the 1990s [32] and differ from the better-known carbon fibres in that their diameters are much smaller and are more difficult to produce in a well-aligned manner. [33] CNFs in many ways represent an ideal material for application in EDLCs; they generally exhibit an open, mesoporous structure, and good conductivity (only along the fibre axis). If they are produced from electrospun polymers, compared to CNTs, they are relatively cheap and easy to manufacture and are therefore an attractive alternative to CNTs. Binderless web structures can also be produced via electrospinning. CNFs can also be produced by chemical vapour deposition.

CNFs have been shown to have diameters between 50 – 500 nm with d_{av} of 3 – 20 nm, and activation can lead to the opening of microporosity. Due to the morphology of activated CNFs most of the porosity is situated on the surface of the fibres leading to more easily accessible active sites. [34-36] Activated CNFs have been noted to possess BET surface areas of up to 1200 $m^2 g^{-1}$ with specific capacitance of 60–175 F g^{-1}.[32-33] Newer multi-branched CNFs exhibited specific capacitance of 300 F g^{-1}. [34]

However, the cost of CNFs is still higher than that of particulate carbons and high inter-fibre resistance can hinder the performance as electrodes. This along with alignment issues which reduce the conductivity, CNFs are not considered the best material for EC development.

2.1.4 Carbide-derived Carbons

The unique nanoporous structure of carbide-derived carbon (CDC) together with the narrow pore size distribution and the possibility to fine-tune the pore size has lead to a large volume of research being carried out to study these materials as electrodes for electrochemical capacitors.

Carbide derived carbons are manufactured by the chlorination of metallic carbides (e.g. TiC, B_4C, ZrC, Ti_3SiC_2, Ti_2AlC, SiC) at elevated temperatures (high enough to facilitate the reaction but lower than that required for graphitisation). The resulting carbons exhibit a high specific surface area with a pore size that can be controlled by choice of starting material and chlorination temperature. [35]

Unlike other materials research for ECs, the research into the use of CDCs has concentrated on the development of microporous carbon materials for improving performance. All results below are for microporous carbon materials with average pore widths below 2 nm.

So far, the best CDC materials for ECs are derived from TiC. Specific capacitances of between 130 – 190 F g^{-1} for TiC derived CDC at 800°C with BET surface area of over 1600 m^2 g^{-1} and average micropore width of 0.7 nm. [36-37]

Recently a new method was developed, which improves the pore size distribution in CDCs, using the chlorination of carbide/oxide mixture, due to which the carbothermal reduction of TiO_2 in chlorine atmosphere gives the possibility to oxidise in situ the desired part of carbon during its formation from the carbide. [38] This method produced microporous carbons with surface areas of up to 1600 m^2 g^{-1} and specific capacitance of 120F g^{-1}.

2.1.5 Template-derived Carbons

Template-derived carbons are produced by filling the porous structure of an inorganic matrix with a carbon precursor (e.g. sucrose, propylene, pitch, or polymer solutions) followed by carbonisation. The inorganic template is then completely removed by hydrofluoric acid. The use of a template allows for the production of porous carbons with well-defined structural characteristics (surface area, pore volume, pore size distribution, particle size, etc.).

Activated carbons can exhibit very wide pore size distributions from micropores up to macropores with pores randomly connected, leading to poor conductivity and ionic transport for use as electrodes. Template-derived carbons can be used to produce high-surface area carbons with regularly interconnected pores that allows for improved ionic transport and therefore higher rate capability. The pore size of the template can be chosen to match the optimum pore width for the given electrolyte. Template-derived carbons showed little reduction in capacitance (10%) with increasing discharge rate compared with Maxsorb activated carbon's 80% reduction. [39] Specific capacitances of up to 220 F g^{-1} have been reported for template-derived carbons with surface areas of 1500 – 1600 m^2 g^{-1}. [40]

As with carbide carbons, high production costs have limited their use for potential commercial development, although they are useful materials for fundamental research.

2.1.6 Graphene

Graphene was first discovered by Geim *et al*. in 2004. [41] It is a 2D material consisting of a monolayer of carbon atoms. As a new carbonaceous material, graphene exhibits characteristics that would be advantageous to ECs. It has a large theoretic surface area of ~2600 m^2 g^{-1} and, unlike porous carbon materials, does not rely on a distribution of pores but layers for high capacitance. The conductivity has also been shown to approach that of pristine graphite (~ 2 x 10^2 S m^{-1}). [42] This high conductivity eliminates the need for conductive additives that are required to enhance the conductivity of activated carbon electrodes.

Graphene has been synthesised via a number of production methods. The first method utilised chemical vapour deposition (CVD) as for CNTs.[42] The micromechanical exfoliation of graphite, epitaxial growth on electrically insulating surfaces such as SiC, aerosol pyrolysis, and solvothermal synthesis have also been investigated.[41, 44-46] However, all of these methods produce small quantities of materials only useful for fundamental studies. For graphene to compete with activated carbons in EC manufacture, large scale production at a reasonable cost must be possible.

One of the most promising methods for the production of graphene is through the formation of colloidal suspensions of graphene oxide sheets from graphite, derivatives of graphite (e.g. graphite oxide) and graphite intercalation compounds. This approach is scalable, allowing for the possibility of high production volumes. It is also well suited to the introduction of surface functionality which enhances the capacitance performance, producing chemically modified graphene (CMG).[47]

Studies carried out by Ruoff *et al.* reported capacitance results for CMG of 137 F g^{-1} in aqueous electrolyte H_2SO_4 and 99 F g^{-1} for organic electrolyte Et_4NBF_4-PC.[47] Chen *et al*. obtained specific capacitances of 164 F g^{-1} with 6M KOH, however the cycle life was found to be poor with only 60% capacitance retention after 700 cycles.[48] Wang *et al.* recently obtained an improved performance of 205 F g^{-1} and capacitance retention of 85% after 1200 cycles. [49]

2.1.7 Phenolic Resin derived Carbons

Phenolic resins for porous carbon production can be synthesised from resorcinol-formaldehyde, cresol-formaldehyde, phenolic-furfural, melamine-formaldehyde, polyurethanes and polyureas. [50-55]

The main phenolic resins that have been studied for the production of carbon and activated carbon for use as electrode materials for ECs, are resorcinol-formaldehyde (RF) aerogels, cryogels and xerogels.[2] RF aero-, cryo and xerogels are formed from the polycondensation of resorcinol and formaldehyde in the presence of a basic catalyst (most commonly sodium carbonate, Na_2CO_3) at elevated temperatures. These organic gels can be carbonised in an inert atmosphere to give carbon aero-, cryo or xerogels in the form of monoliths, powders, microspheres, or in thin film composites.

The difference between the aerogels, cryogels and xerogels occurs during the drying process of the hydrogels. Aerogels are produced when the hydrogels are dried via supercritical carbon dioxide (CO_2), this leads to high surface area, low density gels. This was the method first introduced by Pekala 1989 [50]. Drying with supercritical CO_2 is expensive and not practical on a large scale. Cryogels are dried by submersing the hydrogel into liquid nitrogen followed by sublimation under vacuum. This results in gels with a lower surface area than for the aerogels. Although slightly cheaper than using supercritical CO_2, large ice crystals can form in the gel structure during freezing which results in the formation of large pores, referred to as megalopores. These large pores lead to undesirable wide pore size distributions. Xerogels are produced when the hydrogels undergo evaporative drying, either at ambient pressure or under vacuum. Evaporative drying is the most cost effective method, however due to the capillary forces exerted on the pores during drying, it was always thought that severe pore collapse would occur during evaporative drying. Recent studies proved that this was not always the case, with the surface area of the xerogels equivalent to that of the aerogels. [56] Xerogels still exhibit higher densities

[2] Aerogels are produced when the hydrogels are dried via supercritical CO_2, cryogels are freezedried and xerogels are produced when the hydrogels undergo evaporative drying, either at ambient pressure or under vacuum.

than their counterpart aerogel, but the reduction in processing costs and ease of scale-up make xerogels an interesting alternative to aerogels and cryogels.

The pore structure of the aero-, cryo- and xerogels can be controlled by varying the initial reactant ratios. The reactant ratio that exhibits the largest impact on the structure the initial resorcinol to catalyst ratio (R/C).[50] The effect of catalyst ratio on the resultant gel structure can be attributed to the reaction mechanism followed during the polymerisation reaction. The polymerisation process involves two reaction steps; the addition of formaldehyde to resorcinol which is catalysed by bases; and the condensation of the hydroxyl-methyl derivatives (shown in *Figure 2.1*). As the first step is controlled by the catalyst and involves the formation of the backbone of the polymer gel, any change in the catalyst concentration affects the porosity of the resultant gel.

The most commonly utilised catalyst is sodium carbonate (Na_2CO_3). This was used in the original synthesis procedure by Pekala. [50] However, since the main purpose of the catalyst is to increase the pH and cause the resorcinol molecules to ionise, any basic catalyst could potentially be used. Horikawa *et al.* [57] studied the effect of catalyst type on the resultant aerogel structure. Potassium carbonate (K_2CO_3), sodium carbonate (Na_2CO_3), potassium hydrogencarbonate ($KHCO_3$) and sodium hydrogencarbonate ($NaHCO_3$) were studied as catalysts. It was found that catalyst type did not have a significant effect on the surface area of the carbon aerogels. However, the pore size distribution was affected. K_2CO_3 and Na_2CO_3 produced similar pore size distributions with average pore diameter of 2.2 nm, whilst $NaHCO_3$ and $KHCO_3$ produced wider pore size distributions with average pore diameters of 2.8 nm and 3.8 nm respectively. The increase in pore size distribution was attributed to the variation in particle size formation that occurs in the first catalysed step, when the catalyst is changed. This study also investigated the variation of resorcinol to catalyst ratios R/C 50, 200 and 1000 for K_2CO_3. The surface area and pore volume peaked at R/C 200 for K_2CO_3. It was found that the primary particles formed at R/C ratios 50 and 200 were spherical, however those formed at R/C 1000 were disc shaped.

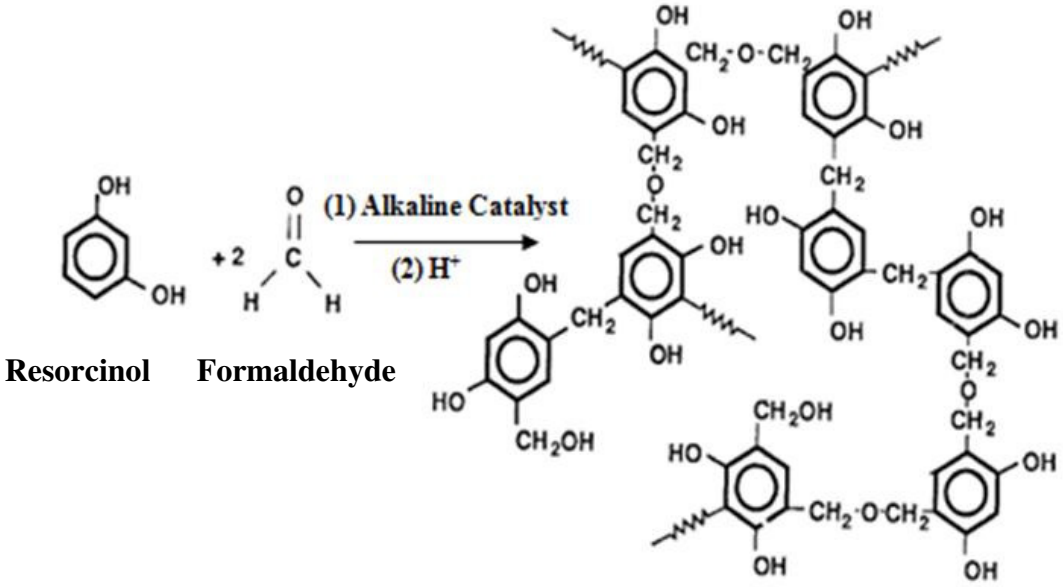

Figure 2.1 – Reaction Mechanism for Resorcinol-Formaldehyde Polymerisation

The monolithic structure, high surface area, and electrical conductivity of carbon aerogels and xerogels make them attractive as electrodes for ECs.

Pekala *et al.* studied carbon aerogels for use in ECs. [58] The study looked at the effect of carbonisation temperature and activation time on the capacitance performance. The optimum carbonisation temperature range was 800 – 900°C, where the graph plateaued before reducing. An activation time of 3 hours at 800°C provided the optimum capacitance results.

Li *et al.* [59] studied the effect of carbon aerogel catalyst ratio on EC performance. The performance of carbon aerogels in KOH, Na_2CO_3, and $(NH_4)_2SO_4$ aqueous electrolytes was also studied. Carbon aerogels were prepared with varying resorcinol to catalyst ratios of R/C = 500, 1000 and 1500. The surface areas obtained were in the range 600 – 1000 m^2 g^{-1}, with the highest for R/C 500. Although the highest surface area occurred for R/C 500, the highest capacitance occurred for R/C 1500 with a specific capacitance of 184 F g^{-1}. (NOTE: no information was given on pore size distribution). Li *et al.*[59] followed a different gelation temperature profile to that utilised in the other carbon aerogel EC studies. The RF gels were held at 25°C for 24 hrs, 60°C for 48 hrs and 80°C for 72 hrs, as opposed to constant temperature of 85 -

90°C. This variation in gelation procedure may have resulted in the increase in specific capacitance. [58,60]

Kim *et al*. [60] studied the performance of carbon xerogels in 4M $KOH_{(aq)}$ and 3M $H_2SO_{4(aq)}$. The carbon xerogel carbonised at 800°C, which exhibited a surface area of 500 m^2 g^{-1}, produced specific capacitances of 35 F g^{-1} in KOH and 40 F g^{-1} $H_2SO_{4(aq)}$. Zhu *et al*. [61] produced activated carbon xerogels, with maximum surface area, pore size and pore volume of 2800 m^2 g^{-1}, 2.5 nm, and 1.35 cm^3 g^{-1}, respectively. This produced specific capacitances of 295 F g^{-1} in 6M $KOH_{(aq)}$ electrolyte. Although synthesis and measurement procedures were not identical, these two studies show that activation greatly improves the performance of carbon xerogels.

Arbizzani *et al.* [62] and Lazzari *et al*. [63] investigated the use of RTIL electrolytes with a commercially available activated carbon material (from Pica) and carbon xerogels, aerogels and cryogels. On normalising capacitance to mesopore surface area the carbon xerogels and cryogels outperform the activated carbon, proving that most of the surface area of the carbon xerogels and cryogels is accessible to the RTIL electrolyte. (A more in depth discussion on the effect of pore size, as found in these studies, is given in **Section 2.5 – Porosity in EDLC electrodes**.)

2.1.8 Theoretical Modelling of carbon/RTIL ECs

On carrying out a review of the literature, a lack of studies into the molecular simulation of carbon/ RTIL EC systems was found. This is despite the growing interest in these systems in the laboratory.

Federov *et al.* [64] carried out molecular dynamics (MD) simulations for the capacitance response of a simple dense RTIL made up of positively and negatively charged Lennard-Jones spheres on two parallel square lattices. This study provided an oversimplified model for the capacitance behaviour of RTILs, as real RTILs would be affected by the non-spherical shape of the ions and pair potentials. However, it provides the necessary basis for rationalising the behaviour of these systems.

Shim *et al.* [65] recently highlighted the need for more systematic analysis of ECs in RTILs at the molecular level with computational methods. Shim *et al.* proposed

that current models available for other EC systems were not valid for RTILs, as both the counterions and co-ions make contributions to capacitance. The proposed model examined the structure of, and charge distributions resulting from, $EMIm^+$ and BF_4^- ions, which interact with a model micropore consisting of a uniformly charged, SWCNT.

Shim *et al.* [65] proposed a relationship between pore size and specific capacitance, with a maximum in specific capacitance occurring at a pore size of 0.7 nm. This agrees qualitatively with that observed experimentally by Chmiola *et al.* [35]. However, the overall magnitude of specific capacitance exhibited a significant departure from the experimental data. While this gives some confidence as to the basic modelling approach, clearly some refinement needs to be made to the Shim model. Shim *et al.* concluded that the reasons for this discrepancy include the neglect of the dielectric constant, absence of diffuse character of electron density and related spill over density in the simulations. There was also uncertainty in the determination of pore area and pore geometry between MD and the experiments. An important issue not accounted for in this particular model was the effect of RTIL transport inside the pore on the performance. Since this publication there have been no further developments.

Although the current MD models are not yet appropriate for the simulation of experimental data, the results obtained in the above study provide promise of this with further modelling research and development.

2.1.7 Carbon Overview

Section 2.1 has shown that EC's are likely to have globally widespread applications and as such, the costs and ease of production are likely to be key, apart from a few niche applications. This will exclude some of the more specialised carbons such as carbide-derived and template-derived because they involve long complex and frequently unsafe production methods. This is not to lessen their immense utility in fundamental studies or the fact that they can frequently out perform cheaper and commercially available materials. Although time will tell, it is unlikely that carbon nanotubes or nanofibres will be economically competitive with biomass or polymer derived carbons. Therefore, the mass commercial development of ECs must be based around the latter forms.

Of these, biomass derived carbons have the advantage of being significantly cheaper but have the disadvantage of possessing wider pore size distributions. Polymer derived carbons have the advantage that is it possible to engineer pore size distributions much more precisely but, of course, are more costly. The fundamental importance of pore size distribution will be considered shortly. However, carbon nanotubes and nanofibres may be important components, at small concentrations, to reduce electrode resistance.

2.2 Electrode Materials

2.2.1 Transition Metal Oxides

Transition metal oxides are considered the best electrode materials for the production of pseudocapacitors. Transition metal oxides can exhibit very high values of specific capacitance, compared with carbon-based EDLCs, with values over 1200 F g^{-1} for composite electrodes amorphous $Ru_{1-y}Cr_yO_2/TiO_2$ in 1M $KOH_{(aq)}$. [66] They may also give rise to very low values of equivalent series resistance (ESR), resulting in high specific power. This makes them appealing in most commercial applications.

Ruthenium dioxide (RuO_2), is the most common transition metal oxide used as a pseudocapacitor electrode material due to its high specific capacitance up to 650 F g^{-1}, [67] long cycle life (10^4 cycles), high metallic conductivity, and good electrochemical stability, as well as good rate capability. [21,68] Also several voltage-dependent redox processes overlap in the operating range of potential, resulting in a fairly constant capacitance. However, due to the limited supply and very high cost of the precious metal ruthenium, other transition metal oxides have been sought after. Alternative metal oxides considered include $Ru_{1-y}Cr_yO_2/TiO_2$, WC, NiO_2, MnO_2, $MnFe_2O_4$, Fe_3O_4, V_2O_5 and porous silicon [66,69–75]. Jayalakshmi and Balasubramanian [76] carried out a comprehensive review of metal oxide materials for use as pseudocapacitor electrodes. This study identified manganese oxide and vanadium oxide as two promising materials for development, with some of main points summarised below.

Most of the research has focussed on hydrous manganese oxide as a candidate for an alternative pseuodcapacitor electrode material. This is due to the low cost and the more environmentally friendly nature of manganese, over the other transition metals. Manganese can be present in three different valence states and its oxides are highly complex. The theoretical capacitance of manganese oxides reaches up to 1100 F g^{-1} (from Mn (IV) to Mn (III)), however, the electrochemical reversibility of manganese dioxides are usually low leading to poor cycle performance. They also exhibit very high values of ESR. These issues need to be addressed before progress on this material is considered significant. Prasad and Miura reported a capacitance value

between 400 and 621 F g^{-1} for amorphous electrolytic manganese dioxide and MnO_2-based mixed oxides. [77, 78]

Vanadium pentaoxide (V_2O_5), in particular, has been widely examined as an electrode material for ECs that use organic electrolytes. [79-81] Since V_2O_5 has a modest electronic conductivity, composites with metal fibres or carbonaceous materials have been prepared in an attempt to improve electrode performance. [82-87] Amorphous, nanoporous and mesoporous forms of V_2O_5 have been synthesized in order to enhance the specific capacitance of the oxide and the performance was evaluated in KCl electrolytes [88-90]. Composite electrodes of V_2O_5 thin layer on conductive materials, such as metal fibres or carbonaceous materials have recently attracted much attention as high rate intercalation electrodes for pseudocapacitor applications. [80,84,91-93] Analysis of recent reports on the transition metal oxides for pseudocapacitor applications indicates that high specific capacitance and rate capability could be obtained, especially when a small amount of metal oxide is uniformly dispersed on conductive and porous carbonaceous materials with a very high surface area, due to the increased electrochemical utilization of the metal oxide and low concentration polarization of the electrolyte. [94-99]

2.2.2 Conductive Polymers

Conductive polymers have been investigated as alternative pseudocapacitor electrode materials to the metal oxides discussed in **Section 2.2.1.** They have shown their ability to exhibit high capacitances and can be electrochemically deposited at low cost. [21]

The pseudocapacitance of electronically conducting polmers arises due to the fast and reversible oxidation and reduction processes related to the π-conjugated polymer chains. [1,21] The polymer chains result in good electronic conductivity and give these types of compounds the ability to be oxidised or reduced at an electrode interface. [1] Polymers that have been considered as electrode materials for ECs include polymethyl methacrylate (PMMA) [100] p-phenylenevinylene (PPV) [101] polypyrrole (PPy) [102] polythiophenes (PTP) [103] and polyaniline (PANI) [104]. Of these polymers polyaniline has produced the most promising

results, due to its easy polymerisation process, good capacitance performance, low cost, and it is considered environmentally friendly. [105] The drawback of this material is the high ESR associated with the random deposition method utilised in manufacturing. To overcome this high resistivity, the conductive polymers are used in composite electrodes with conductive fillers that exhibit high conductivity, high surface area and good capacitance. The properties exhibited by porous carbons, in particular CNTs have been used due their high conductivity. [106-108]

The long-term stability during cycling has proved to be a problem, with swelling and shrinking of electroactive polymers lead to degradation of the electrode. [8]

2.3 Surface functionality

Porous carbons used in ECs are rarely pure carbon, exhibiting impurities or surface functionality, retained through incomplete carbonisation of the precursor, or they are added during the production process (inadvertently or intentionally). These impurities or surface functionality can be grouped under the heading of heteroatoms.

Typically, inadvertent heteroatoms present in appreciable quantities (up to 10 wt%) [109] include oxygen, hydrogen and nitrogen. To a lesser extent, residual catalyst particles, such as iron or sodium, are also found. Other functionality can be added deliberately to enhance the capacitative behaviour of the ECs, through increasing capacitance by producing Faradaic reactions or reducing the ESR by improving the electrode wettability in the electrolyte.

2.3.1 Oxygen

The presence of oxygen-containing functional groups on carbons is almost unavoidable, as empty valencies remaining from high-temperature treatment are highly reactive. Atmospheric oxygen is reversibly physisorbed, as well as being irreversibly chemisorbed, by carbons on exposure to air yielding reactive surface moieties such as phenol, carbonyl, carboxyl, quinone and lactone groups. [109, 110]

The activation process, thermal treatment in a reactive atmosphere (such as CO_2), usually results in the addition of acidic oxygen functionalities to the carbon surface. [109] On the other hand, basic oxygen groups form when a carbon subjected to high-temperature treatment in an inert environment, is cooled and exposed to atmospheric oxygen.

Self-discharge characteristics are known to be influenced by the oxygen content of the carbon. Specifically, carbons with acidic surface character exhibit high rates of self-discharge due to redox reactions. [111] This is usually accompanied by an increase in the electrode series resistance and decrease in electrode stability. Furthermore the presence of oxide groups can cause gas to be evolved on charge/discharge.

2.3.2 Hydrophobic Surface Functionality

To improve the hydrophobic nature of carbon surfaces for use with organic electrolytes, physical or chemical methods have been utilised [110]. Physical methods involve the use of gases (H_2 or inert) to remove hydrophilic functional groups, however, removal is rarely complete. Chemical modification can be carried out by coating in an organosilicon or gas phase fluorination or through the use of liquid organosilicon compounds. The most effective surface modification technique for hydrophobisation has been found to be treatment with a surfactant. Fang *et al.* [112, 113] produced activated carbon aerogels (ACAs) modified with sodium oleate and vinyltrimethoxysilane (vtmos). Both surfactants added hydrophobic functional groups to the carbon surface with very little effect on the surface area. The addition of vtmos functional groups increased capacitance by 10 F g^{-1} with no pseudocapacitance present and reduced the mass transport resistance from 5 to 1.8 Ω cm^{-2}. Capacitance decay over 20,000 cycles was only 3.5% showing vtmos surface groups do not significantly affect the cycling ability of the EDLC. [114]

2.4 Electrolytes

The type of electrolyte employed in ECs has a significant effect on the amount of energy stored in the cell, and how quickly this energy can be released. Due to the relationship governing the amount of energy stored in EDLCs (*Equation 1.2*, **Section 1.7**) it is evident that the operating voltage is of importance in determining their energy densities. In EDLCs, the decomposition voltage of the electrolyte determines the operating voltage of the cell.

2.4.1 Aqueous based Electrolytes.

For aqueous electrolytes, the maximum operating voltage is theoretically limited by the electrolysis of water to 1.2V (at 25°C). Larger amounts of energy can be stored in ECs when using an organic electrolyte, where the operating voltage is limited to roughly 2.7V (for propylene carbonate solvent), and wider operating ranges are attainable when using ionic liquid electrolytes (ca. 3.5V). Electrolyte conductivity has a significant effect on the equivalent series resistance of the cell, which in turn determines power output. Aqueous electrolytes tend to produce faster rates of charge/discharge due to the relatively high conductivity of concentrated solutions. The conductivity of 6M KOH at 25°C is 625 mS cm^{-1} and this compares to 20 mS cm^{-1} for tetraethlyammonium tetrafluoroborate in propylene carbonate (Et_4NBF_4 – PC 1M) and ~10 mS cm^{-1} for typical RTILs. [1] Further advantages associated with aqueous electrolytes are that they are cheap and easily processed in comparison to organic based and RTIL electrolytes, where, due to their sensitivity to oxygen and water, means they have to be processed in inert atmosphere glove boxes (see **Sections 2.4.2, 2.4.3, and 1.5** for further details). The most commonly employed aqueous electrolytes are 1M H_2SO_4 and 6M KOH although neutral electrolytes, such as NaCl [115] and KCl [116] have been investigated.

Relatively concentrated electrolytes are required to minimise the ESR and maximise power output, however, strong acids and bases dictate materials selection for cell manufacture. The use of concentrated electrolytes also increases the rate of self-discharge displayed by the capacitor.

2.4.2 Organic based Electrolytes

Organic electrolytes were developed to allow for increased operating voltages of up to 2.7V and thus an increased energy density (according to *Equation 1.2*, **Section 1.5**). Typically, the operating voltage is set to 2.5V to prevent oxidation of the electrolyte through over-charging. However, to ensure that the electrolytes can operate at the higher voltages the electrolytes must be synthesised and utilised in an atmosphere free of water and oxygen. This ensures that the evolution of H_2 and O_2 gases at potential differences above 1.23V does not occur. [5]

Salts are added to organic solvents to provide mobile ions for transport to the double-layer, this provides a wider variety of electrolyte-solvent systems compared with aqueous electrolytes. [1] The two most common organic solvents used are propylene carbonate (PC) and acetonitrile (AC). Acetonitrile was often preferred, as its ESR is a factor of three lower than that of propylene carbonate. However, there is continuing controversy over the safety of acetonitrile, in particular in vehicles, due to its high toxicity and flammability. Research aimed at developing a non-toxic electrolyte with low resistivity has proved unsuccessful. [6] Most organic electrolyte based ECs available commercially utilise propylene carbonate as the solvent. However, tetraalkylammonium salts of anions PF_6^- and BF_4^- are preferred for organic electrolytes due to their high solubility, higher dielectric constant, and good conductivity (relative to other organic salts-solvent systems).

The disadvantage of organic electrolytes is that they exhibit a significantly higher equivalent series resistance (typical increase by a factor of 50 – 100), due to a lower conductivity and higher viscosity. The increased viscosity also results in reduced wettability, further increasing the ESR and lowering the capacitance due to under utilised electrode surface area. Studies comparing the performance of the same electrode materials in varying electrolytes have shown a reduction in capacitance by up to 50% going from an aqueous (2M H_2SO_4) to an organic electrolyte (1M $TEABF_4$-AN). [116] However, it was also shown in other studies that through the use of the organic electrolyte Et_4NBF_4 – PC 1M, the energy density increased by 300% and, despite an increase in the ESR the increased voltage still gave rise to an increase in power density of 35% due to the increased

operating voltage.

2.4.3 Room Temperature Ionic Liquid Electrolytes

RTILs are essentially molten salts with melting temperatures at or below room temperature. Some typical examples of cations are:

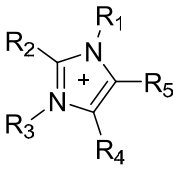

immidazolium

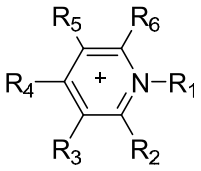

pyridinium

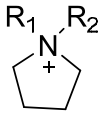

pyrrolidinium

R_1 to R_6 represent locations of alkyl groups or hydrogen atoms. Other examples of cations include ammonium and phosphonium based ion. [117-123]

Typical examples of anions include simple halides e.g. Cl^-, I^-, Br^-; larger more complex ions e.g. BF_4 and PF_6 and larger and even more complex ions, examples of which are shown below:

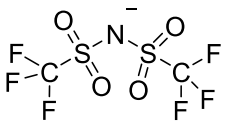

bis(trifluoromethylsulfonyl)imide

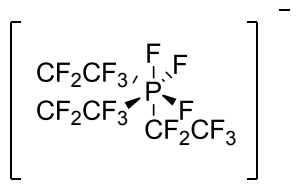

tris(pentafluoroethyl)trifluorophosphate

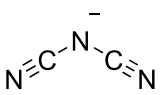

dicyanamide

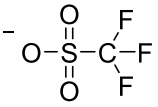

trifluoromethylmethanesulfonate

As this is by no means an exhaustive list, allowing for different anion-cation combinations and for different types, numbers and chain lengths of attached groups; there are a vast number of possible ionic liquids although not all will be liquid at room temperature. Currently one of the most popular RTIL for electrolyte use is the

patented 1-ethyl-3-methylimidazolium bis(trifluoromethylsulfonyl)imide although new RTILs are appearing on the market on a regular basis.

The main advantage of using a RTIL electrolyte is a large electrochemical window. Anodic voltages of up to 4.2V have been reported. [124,125] This allows up to a sixteen fold increase in energy storage compared to an EDLC with an aqueous electrolyte. Other advantages include non-volatility and some (but not all) RTILs are non-flammable. There are however, also some disadvantages. RTILs have relatively high viscosities [126,21,127-130] and much lower ionic conductivities than aqueous electrolytes. Not all RTILs have particularly large anodic windows; some no larger than an aqueous electrolyte. [131-137] Operation at low temperatures may be difficult as many RTILs have melting temperatures just above 273 K. Some RTILs, notably tetrafluoroborates and hexafluorophosphates, are known to produce HF posing a potential safety and disposal hazard and also the destruction of the capacitor materials. RTILs absorb water readily reducing the voltage window and have to be kept in a moisture free environment. A major disadvantage of using RTILs is the high cost, although larger scale production may reduce the price in future.

The capacity for these electrolytes in an activated carbon EDLC was between 45 – 180F g^{-1} of carbon with an electrochemical stability window of 4.5V. Up to 6V has been achieved with glassy carbon electrodes. [21]

Their high viscosity at ambient temperature has limited the practical application of RTILs. This high viscosity results in an increase in the internal resistance that hinders the power output capability.

A new RTIL of interest is 1-ethyl-3-methylimidazolium thiocyanate, which has a high conductivity and a lower viscosity at room temperature compared with the RTILs mentioned above leading to improved capacity of 233F g^{-1}, however the electrochemical stability window of this RTIL is low at 2.6 V. [138]

2.5 Porosity in EDLC electrodes

To improve supercapacitor performance, worldwide research efforts have been concentrating on optimising the pore size distribution of nanoporous carbon materials. By optimising the pore size distribution of carbon materials the accessible surface area for double layer formation can be maximised.

A number of research groups have attempted to determine the importance of mesoporosity in carbon electrode materials. There are two broad schools of thought concerning the role of meso- and microporosity. Many investigations suggest that micropores are not accessible to electrolyte solution [62-63], because electrolytes with solvation shells are too large, and ionic liquids too viscous, to enter the microporosity. However, other studies [35, 139-142] have stressed the importance of microporosity in maximising capacitance.

One study carried out on biomass-derived activated carbons concluded that mean pore size (d_{av}) was more important than surface area for enhancing specific capacitance. [125] In this study, the optimum pore sizes for aqueous and organic electrolytes were 0.7 and 0.8 nm respectively. [139] Further studies determined the mechanism by which micropores become accessible to ions. [35, 139-141] Chmiola *et al.* [140,141] used carbide derived carbons (CDCs) with a unimodal pore size distribution (d_{av} = ~1 nm) and reported a capacitance increase in an organic electrolyte, when compared with other carbon materials with d_{av}> 2 nm. This was attributed to the desolvation of ions upon entering the micropores. To confirm this theory a solvent free ionic liquid electrolyte at 333 K, combined with microporous CDCs were studied in an attempt to match pore size to ion size. [143] A maximum specific capacitance of 160 F g^{-1} (40 F g^{-1} higher than for an equivalent mesoporous material) was obtained for the CDC, with d_{av} equivalent to ion size, indicating that ion adsorption is achieved in the most efficient way, thus minimising free space. It was established that as d_{av} of the carbon increased above the optimum, the capacitance continued to decrease and below this pore width ion sieving occurred. As the larger pore widths could still only accommodate one ion, the decrease in capacitance was attributed to an increase in double-layer thickness.

Ania *et al.* [144] used solvent free ionic liquids as *in situ* probes to determine

the effect of ion size on electrochemical capacitor performance. Activated carbon from Norit with micropores accounting for 80% of the total pore volume was studied for use with four ionic liquid electrolytes with varying cation size from 0.8 – 2 nm. An almost proportional dependence of capacitance on accessible volume was found, confirming the relationship between pore size and ion size for enhancing capacitor performance. As ion size determines the "accessible volume", this study shows that the optimum pore size of the carbon electrode is dependent on the ion size(s) of the electrolyte used.

Other studies have looked at the effect of mesoporosity on specific capacitance and continue to challenge the original belief that mesopores are necessary to provide wider transport paths for ion diffusion into smaller pores, thus increasing accessible surface area and reducing resistance. [145] Twelve phenolic resin based activated carbons were studied with five being exclusively microporous with average widths of between 0.6 and 1.2 nm and the remaining samples exhibiting a bimodal pore structure of micro- and mesopores. The samples were compared by selecting a microporous and mesoporous carbon with the same average micropore length so the only difference was the presence of mesoporosity. The study proved that mesopores in the structure had a detrimental effect on the volumetric capacitance of the ECs reducing the volumetric capacitance from 60 F cm^{-3} to 47 F cm^{-3} in aqueous electrolytes and 46 F cm^{-3} to 26 F cm^{-3} in organic electrolyte. To confirm that mesoporosity is not necessary for fast diffusion of ions at high current rates, the reduction in capacitance with increasing current density was studied. The ratio of the fastest rate capacitance to the slowest rate capacitance was compared to average micropore size. For aqueous electrolytes the ratio was found to be independent of pore size as the small ions of the aqueous electrolyte are able to access even the smallest micropores in the carbon materials studied. For the organic electrolyte the diffusion of the ions becomes increasingly hindered by the decrease in average micropore width, with a pore width of 1.2 nm optimising rate capability of the organic electrolyte, which is in contrast to the optimum claimed in [35, 139-141].

The traditional EDLC model is based on the interactions between planar electrodes and an electrolyte solution. This model is insufficient where three-dimensional networks of interconnected pores are involved in the charge storage

mechanism. A heuristic theoretical model was proposed by Huang *et al*. [146] using data from the above sources to account for the deviation from the traditional model in *Equation 1.1,* **Section 1.4**. Huang *et al*. recognised the effect of pore curvature on capacitance and found that *Equation 1.1* only holds for macroporous (pores > 50 nm) materials where the effect of pore curvature is negligible. Separate models are proposed for mesopores and micropores. *Equations 2.1a and 2.1b* are representative of mesopores (pores 2 – 50 nm), where the mesopores are assumed to be cylindrical and solvated counterions enter the pores and approach the pore walls to form electrochemical double-cylinder capacitors (EDCCs). *Equation 2.2* is representative of micropores (< 2nm), where the pores are still assumed to be cylindrical, however, the small pores do not allow for formation of a double-cylinder. Micropores instead give rise to the formation of electrochemical wire-in-cylinder capacitors, where the solvated (or desolvated) counterions line up singularly inside the pore. These models only hold for unimodal pore distributions.

$$\frac{C}{A} = \frac{2\pi\varepsilon_r\varepsilon_0 L}{\ln(b/a)} \qquad \textbf{Equation 2.1a}$$

$$\frac{C}{A} = \frac{\varepsilon_r\varepsilon_0}{b\ln[b/(b-d)]} \qquad \textbf{Equation 2.1b}$$

$$\frac{C}{A} = \frac{\varepsilon_r\varepsilon_0}{b\ln(b/a_0)} \qquad \textbf{Equation 2.2}$$

Where, C is the specific capacitance, ε_0 is the electric constant, ε_r is the dielectric constant of the electrolyte, d is the double-layer thickness, A is the surface area of the electrode that is accessible to the electrolyte, a and b are the radii of the inner and outer cylinders, respectively and a_0 is the effective size of the counterions inside a micropore.

Other groups still maintain that mesopores are essential for the full surface area of the porous carbons to be utilised for double-layer formation. Arbizzani *et al.* [62] and Lazzari *et al*. [63] investigated the use of an activated carbon material that exhibits an average pore diameter of 3 nm with 50% of the structure being microporous (< 2 nm) and compared the results to that of carbon xerogels and cryogels that exhibit mesopores averaging 9, 15 and 20 nm. On normalising capacitance to mesopore

surface area the carbon xerogels and cryogels outperformed the activated carbon corresponding to the typical capacitance of a clean graphite electrode, i.e. 20 – 30 μF cm^{-2}, proving that most of the surface area of the carbon xerogels and cryogels is accessible to the RTIL electrolyte.

ACNFs were produced at different activation temperatures; 700, 750 and 800°C, for 30 minutes in 30% volume steam/N_2. The lowest temperature ACNF with surface area of 1200 m^2 g^{-1} gave specific capacitance of 175 F g^{-1}, however as activation temperature was increased the electrode resistance decreased from 14Ω to 5Ω. This was attributed to the increase in mesopore volume as activation temperature increased. [147]

Mesoporous carbons are also considered essential for the high discharge currents utilised by high power applications such as HEVs. It has been shown that porous carbons derived from polyvinyl alcohol (PVA) and magnesium citrate with surface area of 1300 m^2 g^{-1} and mesopores centred between 5 and 15 nm, were found to maintain 85% of the specific capacitance determined at low current density (1 mA cm^{-2}) when discharged at high current density (100 mA cm^{-2}). [148] Another study carried out on templated carbons with 3 pore regimes; (i) micropores, (ii) mesopores (~ 3 nm) and (iii) mesopores (~ 16 nm), assessed the effect of current density on specific capacitance in each pore regime. At low current rates all carbon samples had a specific capacitance of 200 F g^{-1}, however, as current density was increased the specific capacitance decreased in a different manner for each electrode. For regime (i), a sharp decrease in capacitance of 75% was observed. For regime (ii) the reduction in capacitance was slower but shows a continual decrease in capacitance with increasing current density. Regime (iii) plateaus at a minimum capacitance of 100 F g^{-1} at much lower current densities, and would allow for higher discharge rates without having a detrimental effect on capacitance. [149]

2.5.2 Porosity overview

The importance of identifying the optimum pore size for maximising capacitance has been highlighted in **Section 2.5.** Of the porous carbons identified in **Section 2.1**, activated carbon xerogels show up as the most promising materials, due to their controllable pore structure and relative low cost. They also exhibit high surface areas, high specific capacitance, and good electrical conductivity.

None of the studies mentioned above have the determined optimum pore size for use with RTIL electrolytes at ambient temperature, merely using them as solvent free probes at elevated temperature to reduce the effects of the high viscosities associated with RTILs on the capacitance performance. Other studies that have been published investigate only one or two electrolytes combined with either one electrode material, or several but with parameters other than pore size being varied [62-63,143-144]. This leaves a gap in the literature for a larger scale study identifying the optimum pore size for ambient temperature operation of RTIL electrolytes. In this study the aim was to produce six activated carbon xerogels with varying pore size distribution and test their capacitance performance with four RTILs that were identified as having promising attributes for EC manufacture.

2.6 Current Collector

The voltage of a carbon-based supercapacitor depends mainly on three factors:

1. The electrolyte potential window stability,
2. The active material potential window stability and
3. The current collector potential window stability.

The electrolyte working potential window is dependant on the type of electrolyte selected and has already been discussed in **Section 2.3**.

The active material working potential window (1) is determined by the nature of the active material used. For carbon based active materials that exhibit clean surfaces, i.e. no surface functionality, the carbon is electrochemically stable above the potentials reached for EDLC electrolytes. However, in the presence of surface functionality, the key point is the potential reached by the positive electrode during charging: it must be kept under the oxidation potential of the surface functionality if non-reversible Faradaic charge transfer is to be prevented. This highlights the importance of the activated carbon purity, which must be as high as possible: redox reactions associated with the presence of impurities can decrease this working potential window.

The current collector is an important part of the EC which is often neglected, both on a performance and cost basis. It ensures the active material polarisation through its electronic conductivity. There should be no Faradic reactions associated with the current collector in a carbon-based supercapacitor. It has to be stable in the potential range explored by the positive and negative electrode. Problems generally appear at the positive electrode, where high positive potentials can be reached at the end of a constant current charge, thus leading to the degradation of the current collector by anodic oxidation. Aluminium is the most commonly used current collector in organic electrolytes, due to the passive Al_2O_3 layer protecting the underlying metal. [150-151] In aqueous electrolytes such as sulphuric acid, stainless steels can be used. [150] Nickel can be used in alkaline solutions and in some cases gold is used to ensure current collector stability. [151]

It is the combination of the three factors mentioned on *Page 42* that control the nominal voltage of the EC, although for the case of carbon based ECs the electrolyte potential stability window is generally the controlling factor.[20,152-153] As mentioned above, a high cell voltage is not sufficient enough to reach high power: the series resistance must be as low as possible. [156] The equivalent series resistance (ESR) of an EC is the sum of various contributions, such as the electrolyte resistance, the active material resistance, and the active material/current collector interface resistance. Therefore a reduction in the resistance for any of the ECs component parts will result in an increase the power density according to *Equation 1.3*.

2.7 Objectives of this Research

To increase the energy density of ECs through the use of RTILs to enhance operating voltage (ΔV) whilst maintaining high capacitance by tailoring the pore size distribution and of the porous carbon electrodes.

Firstly 1-ethyl-3-methylimidazolium dicyanamide ($EMImN(CN)_2$, *Figure 2.2 (a)*) was selected as unlike many RTILs used as electrolytes, it does not contain fluorine and therefore cannot produce either fluorine or hydrogen fluoride by reaction, degradation or combustion, improving the already desirable safety benefits of RTILs. [126]

1-ethyl-3-methylimidazolium bis(trifluoromethylsulfonyl)imide (EMImTFSI) was of interest due to the low reported viscosity, high diffusivity and relatively high ionic conductivity. This cation anion combination was found to have the optimum properties for an electrolyte[131-133]. However, 1,2,-dimethyl-3-propylimidazolium bis(trifluoromethylsulfonyl)imide (DMPImTFSI, *Figure 2.2(b)*) was chosen for this study as a slight increase in the upper operating voltage was reported [125].

1-butyl-3-methylpyrrolidinium tris(pentafluoroethyl)trifluorophosphate ($BMPyT(f_5Et)PF_3$, *Figure 2.2 (c)*) was a new ionic liquid and was selected owing to a reported extremely large electrochemical window of 6.8 V total, 4.2 V anodic. [20] The physical and transport properties of the electrolyte were also largely untested.

Additionally, a fourth ionic liquid, 1-ethyl-3-methylimidazolium tetrafluoroborate ($EMImBF_4$, *Figure 2.2 (d)*), was tested due to its low viscosity, high conductivity and high capacitance reported in literature. [21]

Commercially utilised organic electrolyte 1M-tetraethylammonium tetrafluoroborate solution in anhydrous propylene carbonate (Et_4NBF_4-PC 1M) was studied for comparison purposes. The RTIL electrolytes have been characterised by Fletcher *et al.* [126].

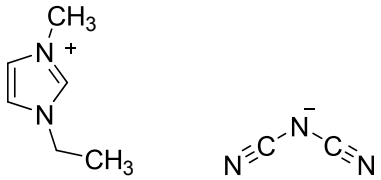

Figure 2.2 (a) – 1-ethyl-3-methylimidazolium dicyanamide.

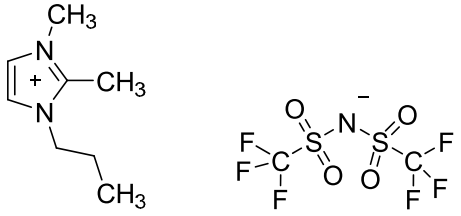

Figure 2.2 (b) – 1,2-dimethyl-3-propylimidazolium bis(trifluoromethylsulfonyl)imide.

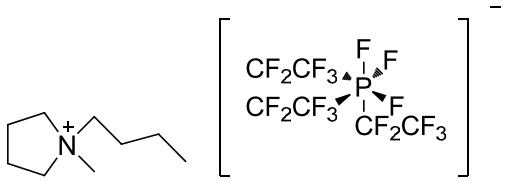

Figure 2.2 (c) – 1-butyl-1-methylpyrrolidinium tris(pentafluoroethyl) trifluorophosphate.

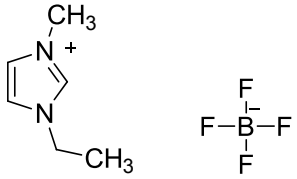

Figure 2.2 (d) – 1-ethyl-3-methylimidazolium tetrafluoroborate.

Although extensive studies have been carried out to determine the optimum pore size for use with aqueous and organic electrolytes.[139-144] None of the studies discussed above have determined optimum pore size for use with RTIL electrolytes at ambient temperature, merely using them as solvent free probes at elevated temperature to reduce the effects of the high viscosities associated with RTILs on the capacitance performance. Other studies investigate only one or two electrolytes combined with either one electrode material, or several but with parameters other than pore size being varied [62-63,142]. This leaves a gap in the literature for a larger scale study identifying the optimum pore size for ambient temperature operation of RTIL electrolytes.

Of the porous carbons identified above, activated carbon xerogels appear as the most promising materials, due to their controllable pore structure and relative low cost. They have also been shown to exhibit high surface areas, high specific capacitance in aqueous or organic media, and good electrical conductivity.

This studies aim was to produce six activated carbon xerogels with varying pore size distribution and test their capacitance performance with four RTILs that were identified as having promising attributes for EC manufacture. The six porous carbon materials were prepared by the pyrolysis and activation of organic resorcinol-formaldehyde gels. It was identified that the porous structure of the resultant xerogels could be controlled by varying resorcinol to catalyst ratio. The varying pore size distributions of the activated carbons were used to determine the optimum pore size for high power and energy performance.

3.0 Theory

3.1 Production of Activated Carbon

The manufacture of activated carbons involves two main steps: the carbonisation of the carbonaceous raw material at high temperatures (depending on precursor) and the activation of the carbonised product. Most carbonaceous materials can be converted into activated carbon, although the properties of the final product will be different, depending on the nature of the raw material used, the nature of the activating agent, and the conditions of the activation process. During carbonisation most of the non-carbon elements such as oxygen and hydrogen are eliminated as volatile gaseous products. The residual carbon atoms group themselves into sheets of condensed aromatic ring systems with a certain degree of planar structure. The arrangement of these aromatic rings is irregular and gives rise to pores in the structure. The pores can become blocked with tarry material or products of decomposition or at least partially blocked by disorganised carbon. [157]

Carbonisation alone does not yield a material with a high surface area due to the less developed pore structure. Activation of the carbonised material enhances the pore structure and converts the raw material into a form that contains the greatest possible number of randomly distributed pores of various shapes and sizes giving rise to high surface area product. [158,159]

3.1.1 Carbonisation

Carbonisation (or pyrolysis) involves thermal decomposition of the carbonaceous material, eliminating non-carbon elements and producing a fixed carbon mass and an undeveloped pore structure. The process is usually carried out below 1000ºC in a continuous stream of inert gas. The important parameters that determine the quality and the yield of the carbonised product are the rate of heating, the final temperature, the isothermal time in the final temperature, and the nature and physical state of the raw material.

Some carbon precursors (e.g., petroleum pitch, coal pitch, some polymers) pass through a fluid stage (referred to as mesophase) during carbonisation that allows

large aromatic molecules to align with each other and form a more extensive pre-graphitic structure. Upon further high-temperature treatment (>2500 ◦C), these carbons can be converted into highly ordered graphite and are referred to as graphitising carbons. [111] Other carbon precursors remain a solid phase during carbonisation, and the limited mobility of the crystallites leads to the formation of a rigid amorphous structure that consist of randomly-oriented graphene layers. [22] These materials cannot be readily converted to graphite by further high temperature treatment and are referred to as non-graphitising carbons. Non-graphitising carbons are produced from materials such as biomass e.g., wood, nut shells, etc., non-fusing coals and many thermosetting polymers e.g., polyvinylidene chloride (PVDC). The loss of volatiles and the retention of a rigid and complex molecular structure during the carbonisation of many non-graphitisable carbons can lead to a highly porous structure without the need for further activation.

For precursors with a lot of volatile matter, the temperature rise during the initial heating stage should be slow so that the gases can escape through the pores of the material without a collapse or deformation.

3.1.2 Activation

The objective of the activation process is to enhance the volume and to enlarge the diameters of the pores which were created during the carbonisation process and to create some new porosity. The precursor material and the carbonisation process largely determine the structure of the pores and their pore size distribution. Activation removes the disorganised carbon, exposing the aromatic sheets to the activating agents in the first phase and leads to increased microporous structure. In the latter phase of the reaction the significant effect is the widening of the existing pores or the formation of large-sized pores by the complete burnout of the walls between adjacent pores. This results in an increase in the transitional pores and macroporosity, and the micropore volume decreases. The extent of activation is reported as percentage burnoff of the carbon material. According to Dubinin and Zaverina, [160] a microporous structure is produced when the degree of burnoff is less than 50% and a macroporous structure is produced when the degree of burnoff is

greater than 75%. In between these values the structure is a combination of all pore types.

Activation can be divided into two main types: chemical activation and physical activation. In the chemical activation process, carbonisation and activation are carried out in a single step by carrying out the thermal decomposition of the precursor impregnated with a chemical activating agent. Physical activation involves gasification of the carbon produced from carbonisation with steam or carbon dioxide in high temperatures in the range of 800-1100ºC.

3.1.2.1 Chemical Activation

Chemical activation is usually carried out when the raw material is of wood origin. The starting material is impregnated with the activating agent in the form of a concentrated solution. The chemical impregnated material is then extruded and pyrolysed in a furnace between 400-600ºC under inert conditions. The carbonised product is cooled and washed to remove the activating agent, which can be recycled. On calcination, the impregnated chemicals dehydrate the precursor material, resulting in charring and aromatisation of the carbon structure and creation of a porous structure. The most widely used activating agents include hydrochloric acid, phosphoric acid, sulphuric acid, although carbonates of alkali metals and chlorides of calcium, magnesium and ferric iron may be used. The common feature of these activating agents is that they are dehydrating agents that influence the pyrolytic decomposition and inhibit the formation of tar.

3.1.2.2 Physical Activation

Physical activation is generally carried out at temperatures between 800-1100ºC in the presence of suitable oxidising gases such as steam, carbon dioxide, air or any mixture of these gases. The active oxygen in the activating agent basically burns away the more reactive portions of the carbon skeleton as CO and CO_2. The extent to which burnoff occurs depends on the nature of the gas employed and the temperature

of activation. The burning out of the carbon skeleton also occurs at different rates at different parts of the exposed surface.

Gasification of the carbonised material with steam and carbon dioxide occurs by the following endothermic reactions:

$$C + H_2O \rightarrow CO + H_2$$
$$C + CO_2 \rightarrow 2CO$$

The reaction of steam with carbon is accompanied by the water-gas formation reaction, which is catalysed by the carbon surface as

$$C + 2H_2O \rightarrow CO_2 + 2H_2$$

The rate of reaction with steam is retarded by the product H_2, which is strongly adsorbed on the active centres of the carbon surface and reduces the rate of activation. Activation with CO_2 is also retarded by H_2 and CO. The CO acts either by increasing the rate of the back reaction or by chemisorption on the active centres.

The high temperature activation of carbon in CO_2 is used to produce a material that has a maximum surface area and a minimum amount, or even lack, of surface oxygen functional groups provided that an inert atmosphere is used during cooling.

Activation with O_2 is exothermic, so that there is excessive burning and the reaction is difficult to control. Since there is always some local overheating, the product obtained is not always uniform. As the reaction is very aggressive, the burning is not just restricted to pores but also occurs on the surface of the grain, causing excessive weight loss. Therefore this method is rarely used.

3.2 Surface Area Characterisation

3.2.1. Gas Adsorption

Gas adsorption is used to probe the surface irregularities and pore interiors that are otherwise hidden from other methods of analysis. Gas adsorption can provide detailed information about the internal structure of the pores, their dimensions and volume and the pore size distribution and their contribution to the surface area of the material.

Adsorption on a clean solid surface will always occur, when the solid is exposed to vapour. [3] The amount adsorbed on the solid surface is dependant on the absolute temperature T, the pressure P, and the interaction potential E between the vapour (adsorbate) and the surface (adsorbent). Therefore, at some equilibrium temperature and pressure the volume V of gas adsorbed on a unit weight of adsorbent is given by: [161]

$$V = F(P, T, E) \qquad \textbf{Equation 3.1}$$

As the measurement temperature is usually kept constant this reduces to;

$$V = F(P, E) \qquad \textbf{Equation 3.2}$$

A plot of V versus P, at constant T, is referred to as the sorption isotherm of a particular vapour-solid interface. Adsorption isotherms are usually reported in terms of the relative pressure P/P_0, where P is the actual pressure of the adsorbate and P_0 is the saturation pressure.

Gas adsorption can be divided into two categories; chemical; and physical adsorption. Chemical adsorption is also known as irreversible adsorption and is characterised by large interaction potentials, which leads to high heats of adsorption close to that of chemical bonds. This means that chemical adsorption can be found to occur at temperature above the critical temperature of the adsorbate. It is useful in the case of catalyst characterisation as it is restricted to monolayer formation, the

[3] A vapour is defined here as a gas below its critical temperature and, therefore, condensable.

number of active sites on the catalyst can be quantified by the simply measuring the quantity of gas chemically adsorbed.

Physical adsorption is the most suitable method for determining the surface area characteristics. The heat of adsorption associated with physical adsorption is low with no destructive changes occurring to the surface during adsorption. Physical adsorption can also lead to multi-layer adsorption, if the pore size allows for it. Therefore, the pores can be filled by adsorbate and pore volume can be determined. As there is no activation energy to be overcome, physical adsorption is more rapid than chemical adsorption, however, low rates of diffusion in narrow pores lead to long equilibration times. At elevated temperatures, physical adsorption does not occur or sufficiently low to allow relatively clean surfaces to be prepared for more accurate surface area measurements. Physical adsorption is also fully reversible, allowing for both the adsorption-desorption isotherms to be studied, particularly important for materials exhibiting Type IV and V isotherms discussed below in **Section 3.2.2**.

3.2.2 Adsorption Isotherms

Although all adsorption isotherms are essentially unique, the majority of isotherms may be grouped into six types as outlined by the IUPAC, shown in *Figures 3.1 a-f.* [162,163]

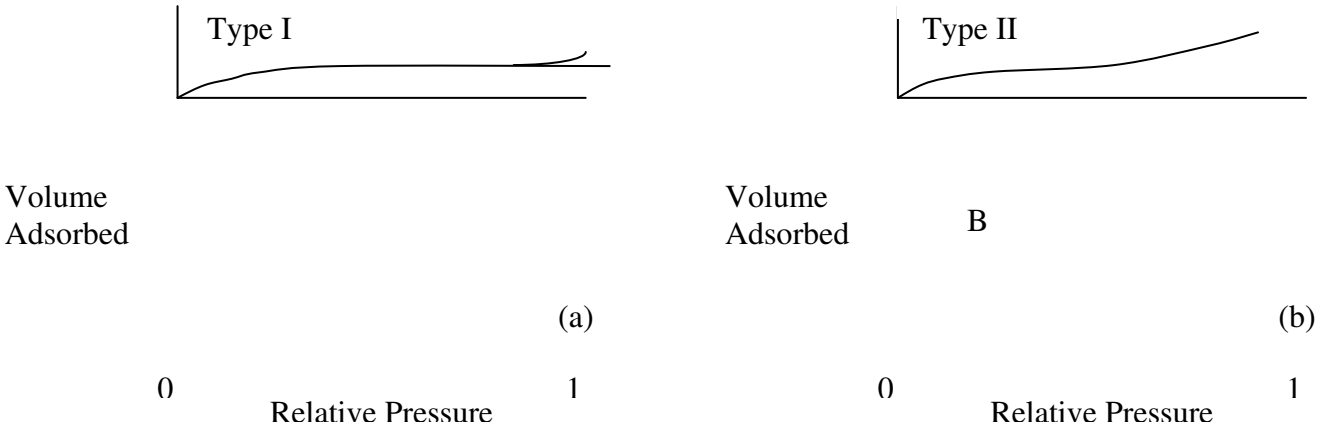

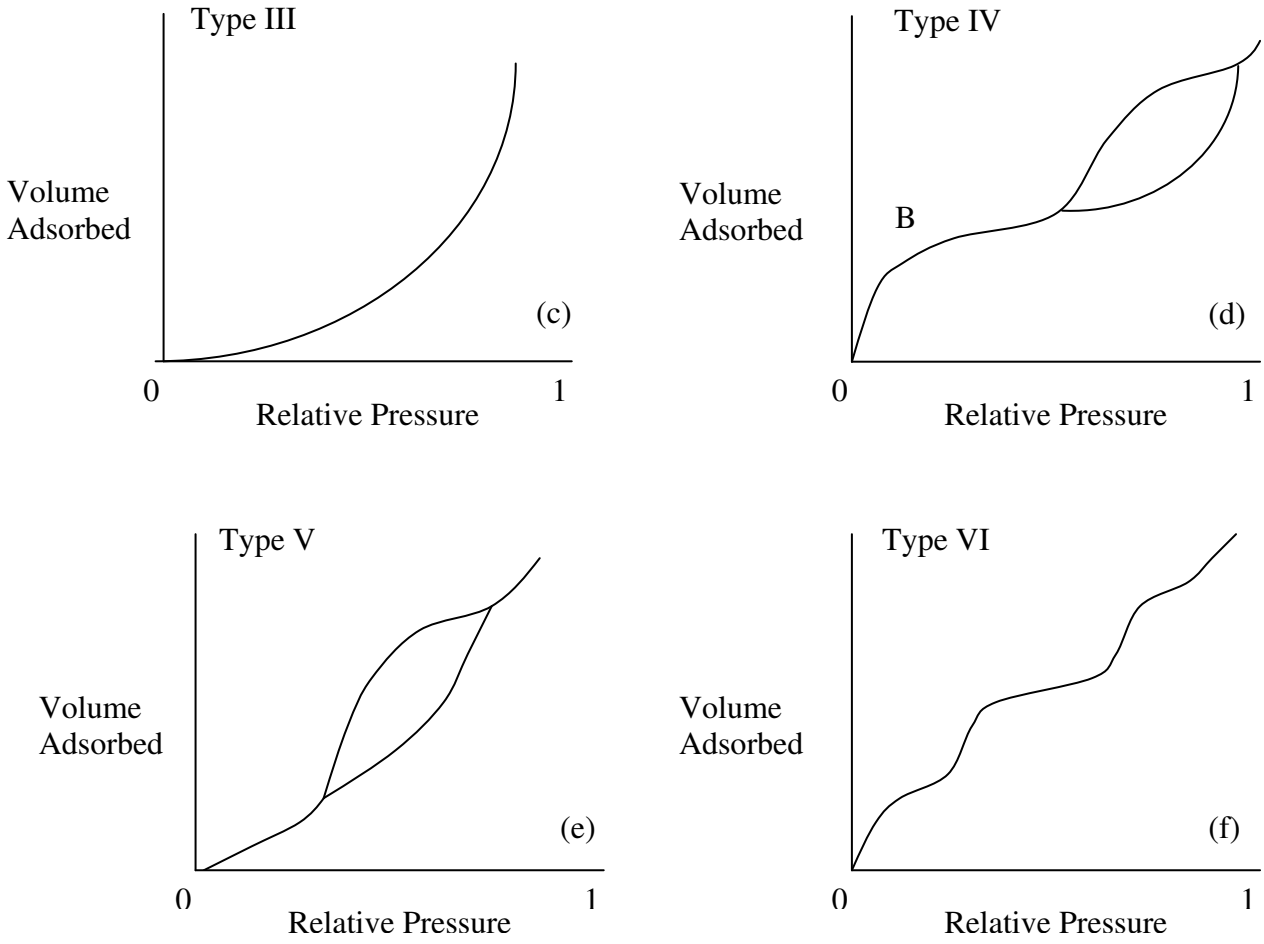

Figure 3.1 – IUPAC Classification of Adsorption-Desorption Isotherms; (a) Type I, (b) Type II, (c) Type III, (d) Type IV, (e) Type V, and (f) Type VI

The reversible *Type I* isotherm is characterised by a rapid initial amount adsorbed at low pressures followed by a flat region. In some cases the curve is reversible and the amount adsorbed approaches a limiting value. In others, the curve approaches the saturated vapour pressure line asymptotically and the desorption curve may lie above the adsorption curve. This shape is characteristic of micropore filling. This isotherm is applicable to physical adsorption in micropores, with wider application to chemisorption and the adsorption of solute from solution. In physical adsorption the restriction to a monolayer may be due to the presence of micropores with a pore size of a few adsorbate molecular diameters. Under these conditions, overlapping pore potentials compress adsorbate molecules into a smaller volume than they would otherwise occupy. The concept of surface area becomes meaningless and the limiting

amount adsorbed and the determined volumes will be higher than the true pore volumes. *Type I* isotherms may also occur for adsorption on high energy level surfaces.

The reversible *Type II* isotherm is obtained by adsorption on non-porous or macroporous powders and represents unrestricted monolayer-multilayer adsorption on a heterogeneous substrate. Monolayer completion is assumed at the point of inflection of the isotherm at point B.

The reversible *Type III* isotherms are convex to the relative pressure axis and exhibit distinct point B. *Type III* isotherms arise when the affinity between adsorbate and adsorbent is weaker than the affinity between the adsorbate molecules. This results in increased adsorption after the interfacial monolayer has formed.

A characteristic feature of the *Type IV* isotherms is the hysteresis loop. The desorption follows a different path to the adsorption curve, although the curve closes again at lower relative pressures. Hysteresis loops occur for multilayer adsorption and can associated with capillary condensation. This is where higher pressures are required to fill the pores with adsorbent than that at which desorption occurs. This type of isotherm is found with many mesoporous adsorbents.

Type V isotherms result from small adsorbate-adsorbent interaction and are similar to *Type III* isotherms. As with *Type IV*, the desorption branch of the isotherm differs from the adsorption branch due to the presence of mesopores.

Type VI isotherms arise with stepwise multiplayer adsorption on a uniform non-porous substrate. The step height represents the monolayer capacity for each adsorbed layer and may remain constant for two or three adsorbed layers. Examples include argon and krypton on graphitised carbon black at liquid nitrogen temperature.

The hysteresis loops obtained for *Type IV and V* isotherms can be further divided into types, to obtain a better understanding of the porous structure. The hysteresis loops are classified by IUPAC into four types; H1, H2, H3 and H4 as shown in *Figures 3.2 (a) – (d).* [164]

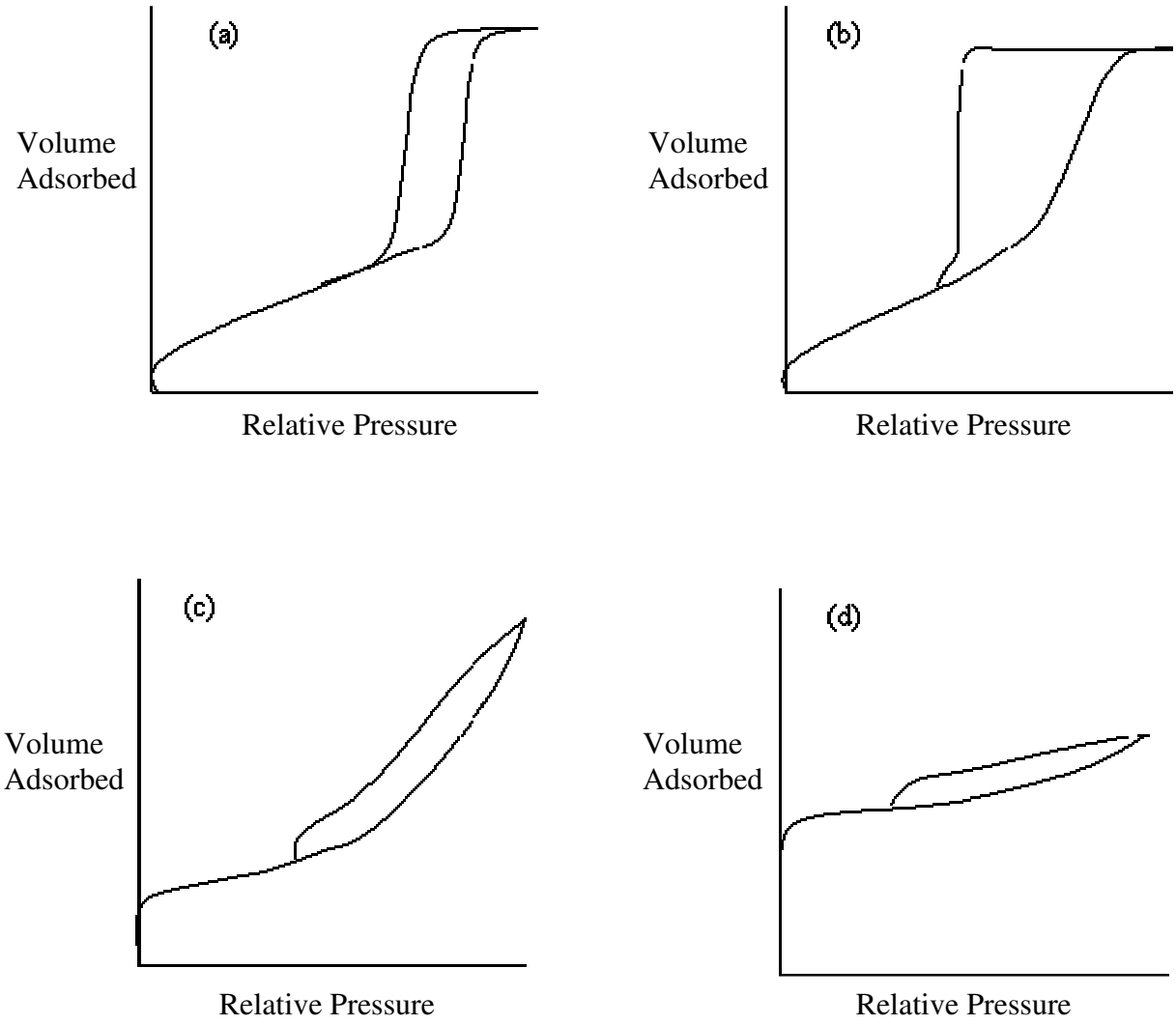

Figure 3.2 – IUPAC Classification of Adsorption-Desorption Hysteresis Loops; (a) Type H1, (b) Type H2. (c) Type H3 and (d) Type H4

The *Type H1* hysteresis loop has been attributed to porous materials known to be made up of agglomerates of relatively uniform spheres and therefore have a narrow pore size distribution.

The *Type H2* hysteresis loop is the most common, occurring for many materials. This means that *Type H2* hysteresis loops may occur for more than one distinct structure. One of the main defined features of materials exhibiting *Type H2* hysteresis is the presence of ink-bottle pores (thin neck and wide base). The IUPAC have suggested that *Type H2* hysteresis can also be attributed to networks of interconnected pores.

The *Type H3* hysteresis loops are attributed to aggregates of plate-like particles which results in slit shaped pores. This type of hysteresis is defined as having no limiting adsorption at high relative pressures.

The *Type H4* hysteresis loops are associated with narrow slit shaped pores, i.e. micropores.

3.2.3 Langmuir and BET Theories (Equilibrium Isotherms)

The success of kinetic theories for surface area analysis depends on their ability to predict the number of adsorbate molecules required to cover the solid with a single molecular layer. The other important factor is the cross-sectional area of each molecule or the effective area covered by each molecule adsorbed on the surface. That is, the surface area is a function of the number of molecules in a monolayer and the effective cross-sectional area of the adsorbate molecule.

The Langmuir isotherm [166] is represented by the Type I isotherm as shown in *Figure 3.1(a)* and is based on the main assumption that at equilibrium, the rates of adsorption and desorption of gas molecules are equal. To derive the theory Langmuir made many assumptions:

1. Adsorption cannot proceed beyond monolayer coverage.

2. All surface sites are equivalent and can accommodate, at most, one adsorbed atom.

3. The ability of a molecule to adsorb at a given site is independent of the occupation of neighbouring sites.

The Langmuir Equation for Type I isotherms:

$$\frac{P}{v} = \frac{1}{Kv_m} + \frac{P}{v_m} \qquad \textbf{Equation 3.3}$$

Where, P is the equilibrium pressure of adsorbate at the temperature of adsorption, v is the adsorbed gas quantity, and v_m is the monolayer adsorbed gas

quantity, and *K* is the Harkins – Jura constant. This gives rise to a straight line plot of *P/v* versus *P* of gradient $1/v_m$ and intercept $1/Kv_m$. Once v_m is obtained the surface area can be calculated using *Equation 3.2*.

$$S_{total} = N_m A = \frac{v_m \overline{N} A}{M} \qquad \textbf{Equation 3.4}$$

Where, $\overline{N}$ is Avogadro's number, N_m is the number of molecules, *A* is the adsorption cross-section, and *M* is the molecular weight of adsorbate.

As the assumptions above lead to an oversimplified model that cannot represent the Type II – V isotherms, it has not been used in this study. The Langmuir theory gave rise to the multilayer adsorption BET theory which is summarised below. The BET theory results in increased flexibility for the determination of surface area materials exhibiting Type II – V isotherms.

BET theory was developed by Stephen Brunauer, Paul Hugh Emmett, and Edward Teller and is an extension of the Langmuir theory for monolayer adsorption.[167] This lead to a model for multilayer adsorption with the following assumptions:

1. Gas molecules physically adsorb on solid in layers infinitely;
2. No interaction between each adsorption layer;
3. Langmuir theory applies to each layer;
4. The heat of adsorption for the first layer has a distinct value, while that of the subsequent layers is equal to the heat of condensation for the liquid adsorbate;
5. Adsorption-desorption can only occur at the exposed layer.

The resulting BET equation is expressed by:

$$\frac{1}{v\left[\left(\frac{P_0}{P}\right)-1\right]} = \frac{1}{v_m c} + \frac{c-1}{v_m c}\left(\frac{P}{P_0}\right) \qquad \textbf{Equation 3.5}$$

Where, *P* and P_0 are the equilibrium and the saturation pressure of adsorbates at the temperature of adsorption, *v* is the adsorbed gas quantity, and v_m is the monolayer adsorbed gas quantity, *c* is the BET constant, which is expressed by:

$$c = \exp\left(\frac{E_1 - E_L}{RT}\right)$$ **Equation 3.6**

E_1 is the heat of adsorption for the first layer, and E_L is that for the second and higher layers and is equal to the heat of condensation of the adsorbate.

Equation 3.5 gives rise to a straight line when $1/v[(P_0/P) - 1]$ is plotted versus P/P_0 for $0.05<P/P_0<0.3$, as demonstrated in *Figure 3.3*.

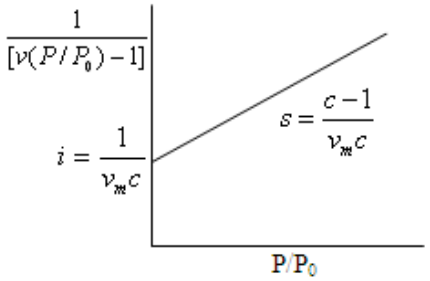

Figure 3.3 – BET Plot

The gradient and intercept of the line can be obtained using the following equations:

$$s = \frac{c-1}{v_m c}$$ **Equation 3.7**

and,

$$i = \frac{1}{v_m c}$$ **Equation 3.8**

The total surface area is then calculated as for the Langmuir theory, using *Equation 3.4*. Specific surface area can be calculated by dividing by sample weight, as in *Equation 3.9*.

$$S = \frac{S_{total}}{W}$$ **Equation 3.9**

3.2.4 Pore Size Distribution

3.2.4.1 The Barrett – Joyner – Halenda (BJH) Theory

The BJH theory is the most commonly used method of analysing the pore size distribution of porous materials that exhibit mesopores. [168] The BJH method was originally developed for relatively coarse porous adsorbents having a wide range of pore sizes. However, the procedure proved to be applicable to almost all types of mesoporous materials. The model considered the desorption process with a step-wise reduction in relative pressure from cylindrical pores in which capillary condensation has occurred (mesopores). It was assumed all pores of equal radius respond in the same way with respect to changes in the relative pressure and that at relative pressure close to unity $(P/P_0)_1$, all pores are filled with condensate. The largest pore[4] has diameter r_{p1}. Upon its surface is a physically adsorbed layer of molecules of statistical thickness t_1. Within this physically adsorbed layer is the inner capillary with radius r_k, from which evaporation occurs as P/P_0 is lowered.

[4] For simplicity Barrett *et al.* referred to all pores of equal radius as if they were one pore. For consistency this nomenclature has been maintained for this derivation.

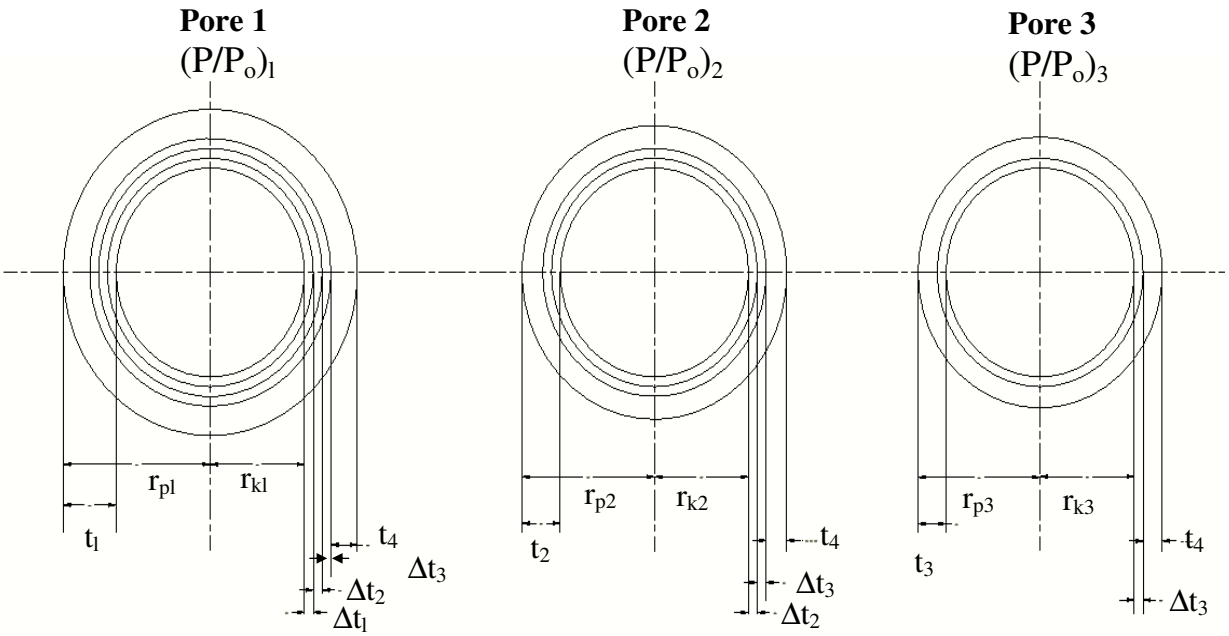

Figure 3.4 – Schematic of BJH Model for Pores Exhibiting Capillary Condensation

The thickness of the adsorbed layer and the radius of the inner capillary can be calculated using the Halsey equation (*Equation 3.10*) or the Harkins and Jura equation (*Equation 3.11*) and the Kelvin equation (*Equation 3.12*) respectively.

$$t = A\left[\frac{B}{\ln(P/P_0)}\right]^c \qquad \textbf{Equation 3.10}$$

$$t = \left[\frac{\alpha}{\beta - \log(P/P_0)}\right]^\delta \qquad \textbf{Equation 3.11}$$

$$\ln\left(\frac{P}{P_0}\right) = \frac{2\gamma\overline{V}}{r_k RT}\cos\theta \qquad \textbf{Equation 3.12}$$

Where, (P/P_0) is the relative pressure, $\overline{V}$ is the molar volume of the liquid adsorbate, γ is the surface tension of the liquid adsorbate, R is the universal gas constant, T is the absolute temperature and θ is the contact angle between the liquid and pore wall. *A, B, C, α, β* and *δ* represent constants that are dependant on the adsorbate.

At equilibrium, the relationship between the pore volume, V_{p1}, and the inner capillary volume, V_{k1}, is

$$V_{p1} = \frac{V_{k1} r_{p1}^2}{r_{k1}^2} \qquad \textbf{Equation 3.13}$$

However, V_{k1} is unknown. To obtain useful data it is necessary to incrementally reduce $(P/P_0)_1$ to $(P/P_0)_2$ ($(P/P_0)_1 = 1$ to $(P/P_0)_2 = 0.98$ for example). This process is represented in *Figure 3.4*. This will result in the desorption of a measurable volume of adsorbed gas, ΔV_1. The reduction in P/P_0 will result in the evaporation of capillary condensate from the largest pore and the reduction in thickness of the physically adsorbed layer by the amount Δt_1. This allows for *Equation 3.13* to be rewritten as

$$V_{p1_1} = R_1 \Delta V_1 \qquad \textbf{Equation 3.14}$$

$$\text{Where } R_1 = \frac{r_{p1}^2}{(r_{k1} + \Delta t_1)^2}$$

For the second pore, lowering $(P/P_0)_2$ to $(P/P_0)_3$ results in another volume of liquid desorbed. However this volume of liquid includes not only the evaporation of capillary condensate and the reduction in thickness of the physically adsorbed layer from the second pore, ΔV_2, but also the volume desorbed from the thinning of the physically adsorbed layer in the first pore, $V_{\Delta t2}$. This gives rise to

$$V_{p2} = R_2 (\Delta V_2 - V_{\Delta t2}) \qquad \textbf{Equation 3.15}$$

$$\text{Where } R_2 = \frac{r_{p2}^2}{(r_{k2} + \Delta t_2)^2}$$

From *Figure 3.4* it can be seen that

$$V_{\Delta t2} = \pi L_1 (r_{k1} + \Delta t_1 + \Delta t_2)^2 - \pi L_1 (r_{k1} + \Delta t_1)^2 \qquad \textbf{Equation 3.16}$$

where L_1 is the length of pore one (i.e. the largest pore).

As this is only for two steps in the desorption process, it is clear that as the number of pores involved increases such a calculation would become impractical. An alternative expression for $V_{\Delta t2}$ is

$$V_{\Delta t2} = \Delta t_2 A_{c1} \qquad \textbf{Equation 3.17}$$

where A_{c1} is the average area from which adsorbed gas is desorbed.
Equation 3.17 may be generalised to represent any one of the steps of the stepwise desorption in the form

$$V_{\Delta tn} = \Delta t_n \sum_{j=1}^{n-1} A_{cj} \qquad \textbf{Equation 3.18}$$

The summation is the sum of the average area in unfilled pores down to, but not including, the pore that was emptied of capillary condensate in the n^{th} desorption.
Generalising *Equation 3.15* and substituting *Equation 3.18* for $V_{\Delta tn}$ gives

$$V_{pn} = R_n \Delta V_n - R_n \Delta t_n \sum_{j=1}^{n-1} A_{cj} \qquad \textbf{Equation 3.19}$$

This equation is still unsatisfactory for computation of pore volume as A_c is not constant with each decrease in P/P_0. However the area of each pore is constant with decreasing P/P_0, and can be calculated from its volume relationship

$$A_p = 2\frac{V_p}{r_p} \qquad \textbf{Equation 3.20}$$

Therefore a method for computing ΣA_c from ΣA_p is required. The procedure which provides a method for this is illustrated in *Figure 3.5*.

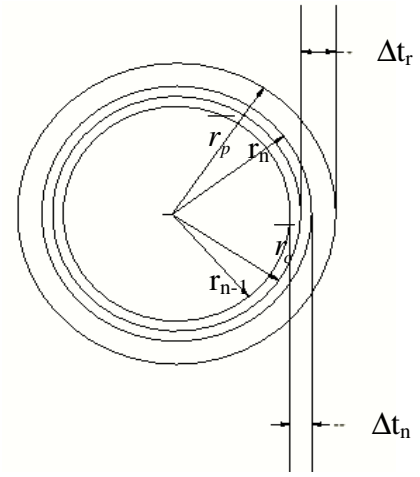

$$V_{\Delta t} = A_c \Delta t$$

$$A_c = A_p \left(\frac{\overline{r_p} - \overline{t_r}}{\overline{r_p}} \right) = A_p c$$

Figure 3.5 – Relation of Capillary Area to Actual Pore Area for nth Step of Desorption

Assuming that all capillaries emptied of their condensate during an incremental relative pressure decrease have an average radius, $\overline{r_p}$, between the radii corresponding to the upper and lower values of *P/P₀*. *Figure 3.5* represents the change in thickness *(Δtₙ)* of the physically adsorbed layer of a previously emptied pore of radius $\overline{r_p}$ during the *nth* desorption step. The capillary radius is r_{n-1} and after desorption it is r_n, giving an average value of $\overline{r_c}$. Since the capillary is concentric within the pore

$$\Delta t_n = A_p \left(\frac{\overline{r_c}}{\overline{r_p}} \right) \qquad \textbf{Equation 3.21}$$

Also $\overline{r_c} = \overline{r_p} - \overline{t_r}$, where $\overline{t_r}$ is the thickness of the physically adsorbed layer at the corresponding value of *P/P₀*. For convenience, ratio $\overline{r_c} / \overline{r_p} = (\overline{r_p} - \overline{t_r}) / \overline{r_p}$ has been defined as $c = (\overline{r_p} - \overline{t_r}) / \overline{r_p}$.

Therefore, *Equation 3.19* can be expressed as

$$V_{pn} = R_n \Delta V_n - R_n \Delta t_n \sum_{j=1}^{n-1} c_j A_{pj} \qquad \textbf{Equation 3.22}$$

Equation 3.22 provides a practical measure of pore volume distributions with respect to pore radii, with the following two assumptions that:

1. The pores are cylindrical, and
2. That the amount of adsorbate in equilibrium with the gas phase is retained by adsorbent *via* two mechanisms, physical adsorption on the pore walls and capillary condensation in the inner capillary volume.

To use *Equation 3.22* a functional relationship between P/P_0 and Δt and between P/P_0 and r_k must be obtained. Values of t as a function of P/P_0 can be obtained from the empirical Halsey or Harkins and Jura Equations 3.10 and 3.11 for nitrogen at 77K.

$$t(\text{Å}) = 3.54\left(\frac{-5.00}{\ln(P/P_0)}\right)^{0.333} \qquad \textbf{Equation 3.10}$$

$$t(\text{Å}) = \left(\frac{13.99}{0.034 - \log(P/P_0)}\right)^{0.5} \qquad \textbf{Equation 3.11}$$

Assuming cylindrical pores and that the liquid completely wets the adsorbed film i.e. θ is zero,[161] the Kelvin equation for nitrogen at 77K becomes

$$\ln(P/P_0) = \frac{-9.53}{r_k} \qquad \textbf{Equation 3.12}$$

Where γ is 8.85 x 10^{-3} N m^{-1}, $\bar{V}$ is 3.467 x 10^{-5} m^3 mol^{-1}, R is 8.314 J mol^{-} K^{-1} and T is 77K. This gives r_k in Å.

Once r_k and t have been obtained, r_p can be obtained from $r_p = r_k + t$. This gives rise to the relationship between r_p and P/P_0. For computation of *Equation 3.22,* $\overline{r_p}$ and the $\overline{r_k}$ corresponding to it at each P/P_0 increment are used, whereas Δt is an increment corresponding to the decrease in P/P_0. Values of $R = \overline{r_p}^2 \Big/ \left(\overline{r_k} + \Delta t\right)^2$ and $c = (\overline{r_p} - t_{\bar{r}}) / \overline{r_p}$ can be calculated as functions of $\overline{r_p}$ for incremental changes in pore radius. The increment is dependant on the size of the pores. Barrett *et al.*[168] suggested increments of 1 nm for pore radii in the range of 20 – 30 nm, 0.5 nm for 1 – 20 nm and 0.1 nm for 0.7 – 2.5 nm. The results of these calculations are given in *Table 3.1* for a sample activated carbon, which constitutes the actual working data of the procedure.

Table 3.1 – Numerical Values of Parameters Required for Computation of Pore Volume and Pore Area Distributions

P/P_0	r_k (Å)	t (Å)	Δt (Å)	$\overline{r_k}$ (Å)	r_p (Å)	$\overline{r_p}$ (Å)	R	c
0.969	307.00	19.23	3.65	378.99	326.22	400.05	1.09	0.95
0.943	163.01	15.57	1.80	188.19	178.58	204.66	1.16	0.92
0.919	112.65	13.77	1.28	126.92	126.42	141.33	1.22	0.90
0.893	84.11	12.49	0.90	92.58	96.61	105.53	1.28	0.88
0.868	67.17	11.59	0.71	72.99	78.76	84.94	1.32	0.86
0.842	55.52	10.88	0.59	59.81	66.40	70.99	1.38	0.85
0.816	46.92	10.29	0.48	50.08	57.21	60.61	1.44	0.83
0.791	40.62	9.80	0.42	43.09	50.42	53.11	1.48	0.81
0.765	35.66	9.39	0.37	37.69	45.05	47.27	1.56	0.80
0.740	31.60	9.02	0.33	33.28	40.62	42.46	1.61	0.79
0.714	28.24	8.69	0.29	29.63	36.93	38.46	1.65	0.77
0.688	25.46	8.39	0.27	26.66	33.86	35.19	1.72	0.76
0.661	23.06	8.12	0.24	24.05	31.18	32.29	1.76	0.75
0.636	21.09	7.88	0.22	21.96	28.97	29.96	1.82	0.74
0.611	19.34	7.66	0.21	20.10	26.99	27.86	1.90	0.73
0.586	17.81	7.45	0.19	18.48	25.26	26.03	1.90	0.71
0.561	16.47	7.26	0.18	17.07	23.73	24.42	2.05	0.71
0.535	15.26	7.08	0.17	15.80	22.34	22.97	2.04	0.69
0.510	14.17	6.90	0.16	14.67	21.08	21.65	2.12	0.68
0.485	13.19	6.74	0.16	13.63	19.93	20.45	2.19	0.67
0.460	12.29	6.58	0.15	12.71	18.87	19.37	2.27	0.66
0.435	11.46	6.43	0.14	11.83	17.89	18.34	2.36	0.65
0.410	10.70	6.29	0.14	11.05	16.98	17.41	2.44	0.64
0.385	9.99	6.15	0.14	10.32	16.14	16.53	2.53	0.63
0.360	9.34	6.01	0.12	9.62	15.35	15.69	2.65	0.62
0.338	8.78	5.89	0.13	9.08	14.67	15.03	2.71	0.61
0.313	8.20	5.75	0.13	8.47	13.96	14.29	2.73	0.59
0.288	7.66	5.62	0.13	7.91	13.28	13.60	2.83	0.58
0.263	7.15	5.50	0.13	7.39	12.64	12.95	2.95	0.57
0.239	6.67	5.37	0.12	6.89	12.04	12.33	3.19	0.57
0.216	6.21	5.25			11.46			

Using the parameters in *Table 3.1*, computation of *Equation 3.22* can be carried out via the step-by-step procedure outlined below. The results are shown in *Table 3.2*.

Table 3.2 – Computation of Pore Volume and Area Distribution for Activated Carbon

P/P_0	r_p (Å)	V_{ads} ($cm^3\ g^{-1}$)	V_{liq} ($cm^3\ g^{-1}$)	ΔV ($cm^3\ g^{-1}$)	$\overline{r_p}$ (Å)	$R\Delta V$ ($cm^3\ g^{-1}$)	$R\Delta t$ (Å)	A_p ($m^2\ g^{-1}$)	ΣcA_p ($m^2\ g^{-1}$)	$R\Delta t\ \Sigma cA_p$ ($cm^3\ g^{-1}$)	V_{pn} ($cm^3\ g^{-1}$)
0.969	326.22	418.22	0.6469	0.00110	400.05	0.0012	3.776	0.060	0.057	2.16E-05	0.00117
0.943	178.58	417.50	0.6458	0.00097	204.66	0.0011	2.090	0.109	0.158	3.31E-05	0.00109
0.919	126.42	416.88	0.6448	0.00066	141.33	0.0008	1.553	0.113	0.261	4.05E-05	0.00076
0.893	96.61	416.45	0.6442	0.00073	105.53	0.0009	1.151	0.176	0.416	4.79E-05	0.00088
0.868	78.76	415.98	0.6434	0.00067	84.94	0.0009	0.942	0.208	0.596	5.62E-05	0.00083
0.842	66.40	415.55	0.6428	0.00075	70.99	0.0010	0.816	0.291	0.843	6.88E-05	0.00096
0.816	57.21	415.07	0.6420	0.00099	60.61	0.0014	0.696	0.471	1.233	8.58E-05	0.00134
0.791	50.42	414.43	0.6410	0.00151	53.11	0.0022	0.615	0.844	1.923	1.18E-04	0.00211
0.765	45.05	413.45	0.6395	0.00262	47.27	0.0041	0.578	1.721	3.294	1.91E-04	0.00390
0.740	40.62	411.76	0.6369	0.00414	42.46	0.0067	0.532	3.124	5.746	3.06E-04	0.00635
0.714	36.93	409.08	0.6328	0.00565	38.46	0.0093	0.485	4.848	9.502	4.61E-04	0.00885
0.688	33.86	405.43	0.6271	0.00711	35.19	0.0122	0.469	6.925	14.752	6.92E-04	0.01155
0.661	31.18	400.83	0.6200	0.00770	32.29	0.0135	0.419	8.396	21.057	8.82E-04	0.01263
0.636	28.97	395.86	0.6123	0.00810	29.96	0.0148	0.409	9.864	28.324	1.16E-03	0.01362
0.611	26.99	390.62	0.6042	0.00817	27.86	0.0155	0.393	11.094	36.330	1.43E-03	0.01410
0.586	25.26	385.34	0.5960	0.00793	26.03	0.0151	0.365	11.722	44.783	1.63E-03	0.01347
0.561	23.73	380.21	0.5881	0.00769	24.42	0.0158	0.374	12.771	53.647	2.00E-03	0.01379
0.535	22.34	375.24	0.5804	0.00739	22.97	0.0151	0.352	13.230	62.853	2.21E-03	0.01290
0.510	21.08	370.46	0.5730	0.00704	21.65	0.0149	0.347	13.808	72.292	2.51E-03	0.01239
0.485	19.93	365.91	0.5660	0.00663	20.45	0.0146	0.342	14.253	81.859	2.80E-03	0.01175
0.460	18.87	361.62	0.5594	0.00641	19.37	0.0145	0.346	15.018	91.768	3.17E-03	0.01137
0.435	17.89	357.48	0.5529	0.00612	18.34	0.0144	0.341	15.674	101.918	3.48E-03	0.01093

0.410	16.98	353.52	0.5468	0.00591	17.41	0.0144	0.345	16.484	112.404	3.88E-03	0.01053
0.385	16.14	349.70	0.5409	0.00568	16.53	0.0144	0.345	17.305	123.205	4.25E-03	0.01014
0.360	15.35	346.03	0.5352	0.00505	15.69	0.0134	0.322	16.883	133.515	4.29E-03	0.00909
0.338	14.67	342.77	0.5302	0.00555	15.03	0.0151	0.362	19.852	145.478	5.26E-03	0.00980
0.313	13.96	339.18	0.5246	0.00542	14.29	0.0148	0.356	20.789	157.975	5.62E-03	0.00914
0.288	13.28	335.68	0.5192	0.00528	13.60	0.0150	0.360	22.123	171.012	6.16E-03	0.00880
0.263	12.64	332.26	0.5139	0.00523	12.95	0.0154	0.370	23.915	184.830	6.84E-03	0.00857
0.239	12.04	328.88	0.5087	0.00522	12.33	0.0167	0.398	26.593	199.584	7.94E-03	0.00873
0.216	11.46	325.50	0.5035								

Column 1, P/P_0 – the relative pressure corresponding to the selected radii, r_p.

Column 2, r_p (Å) – the values of the selected radii.

Column 3, V_{ads} ($cm^3\ g^{-1}$) – the volume of nitrogen adsorbed at the relative pressures given in column 1.

Column 4, V_{liq} ($cm^3\ g^{-1}$) – the liquid volume, calculated by multiplying the V_{ads} in column 3 by the conversion factor for liquid nitrogen at it boiling point, 0.001568.

Column 5, ΔV ($cm^3\ g^{-1}$) – this is the volume of liquid desorbed between two consecutive relative pressures (P/P_0) in column 1. It is obtained by successive subtraction of each volume listed in column 4 from the succeeding one. This column represents the distribution for uncorrected physical adsorption, i.e. it does not account for the thinning of the adsorbed layer in pores previously emptied of their capillary condensate that occurs for each additional decrease in relative pressure. The remainder of the calculations are carried out to give a corrected volume distribution.

Column 6, $\overline{r_p}$ (Å) – the radius which is the average of the radii of the largest and smallest pore represented by the P/P_0 increment in column 1.

Column 7, $R\Delta V$ ($cm^3\ g^{-1}$) – the ΔV calculated in column 5 is corrected for the additional thinning of the adsorbed layers that occurs with each decrease in P/P_0. Values of R are taken from *Table 3.1*.

Column 8, $R\Delta t$ (Å) – corrected decrease in the thickness of the physically adsorbed layer

Column 9, A_p ($m^2\ g^{-1}$) – the area of pores for $\overline{r_p}$ at P/P_0. Where $A_p = 2V_p/\overline{r_p} \times 10^4$ (multiplication factor accounts for change in units to $m^2\ g^{-1}$) and $V_p = R\Delta V$. The use of the uncorrected V_p is accounted for in column 10 with correction factor, *c*.

Column 10, ΣcA_p ($m^2\ g^{-1}$) – the cumulative corrected pore area which can be obtained by progressively summing cA_p, using A_p in column 9 and *c* calculated in *Table 3.1*.

Column 11, $R\Delta t\ \Sigma cA_p$ ($cm^3\ g^{-1}$) – this is the full correction term for calculation of pore volume as outlined by *Equation 3.22*. NOTE: ΣcA_p must be multiplied by 10^{-4} to give answer in $cm^3\ g^{-1}$.

Column 12, V_{pn} ($cm^3\ g^{-1}$) – this is the corrected pore volume for pores within the limits determined by $\overline{r_p}$ in column 6.

3.2.5 Micropore Analysis

3.2.5.1 Dubinin – Radushkevich Theory

Micropores have diameters that are only a few times greater than the gas adsorbate molecule diameter. Micropore filling is different from that described by the BET theory and therefore this theory is inappropriate for the analysis of micropores. Unlike mesoporosity, where the BET equation dominates, there are numerous theories currently in use for the description of micropore adsorption-desorption methods. [160-162] The more common methods of micropore analysis are the Dubinin-Radushkevich and Dubinin-Astakhov equations. [21, 145]

M. Dubinin derived the Dubinin – Radushkevich (DR) equation for determining the volume of micropores based on the theory that if the system is significantly below its critical temperature, the adsorbate will be in a liquid state within the micropores. According to Dubinin, if the pore diameter is comparable to the adsorbate molecule diameter, micropores are filled by volume rather layer-by-layer adsorption on the walls. Dubinin also assumed that to bring a molecule from the gas phase to the adsorbed film depends both on the adsorbate and adsorbent. To obtain a relation that is dependant only on the adsorbent, Dubinin introduced a coefficient, β, which is the affinity coefficient of the analysis gas at P_0 and E_0 which is the characteristic energy of the adsorbate. On the assumption that the pore size distribution is Gaussian, Dubinin – Radushkevich derived *Equation 3.23*, which determines the number of micropores in a material based at the relative pressure, P/P_0.

$$\frac{W}{\rho V_0} = \exp\left[-\left(\frac{RT}{E_0 \beta} \right)^2 \left[\ln\left(\frac{P_0}{P} \right) \right]^2 \right] \qquad \textbf{Equation 3.23}$$

Where, W (g) is the mass adsorbed at a relative pressure P/P_0 at temperature T (K), V_0 ($cm^3\ g^{-1}$) is the total micropore volume, ρ (g cm^{-3}) is density of the liquid adsorbate, and R (J $mol^{-1}\ K^{-1}$) is the universal gas constant, E_0 (J mol^{-1}) and β are as defined above.

For plotting purposes, *Equation 3.23* can be rearranged as in *Equation 3.24* where a plot of $ln(W)$ versus $[ln(P_0/P)]^2$ may yield a straight line with intercept of $ln(V_0\rho)$, from which the micropore volume can be determined.

$$\ln(W) = \ln(V_0\rho) - k_a\left(\frac{RT}{\beta}\right)^2\left[\ln\left(\frac{P_0}{P}\right)\right]^2 \qquad \textbf{Equation 3.24}$$

The DR equation has been found to apply for the adsorption of nitrogen, and organic adsorbents (e.g. benzene) over the relative pressure range 10^{-5} – 10^{-1} on a variety of microporous materials. Despite the DR theory being widely accepted and applied in the literature, DFT simulation has shown that nitrogen may actually freeze in the micropores at the experiment temperature of 77K. However, the DR theory allows for a qualitative comparison of micropore volume between samples, when tailored DFT models are not available.

3.2.5.2 Dubinin – Astakhov Theory

The Dubinin – Astakhov (DA) theory was developed to account for the varying pore size distributions that can be exhibited by porous materials making it more widely applicable. The equation is derived as for the DR equation. [160] The DR theory only corresponds to samples with relatively narrow pore size distributions, i.e. samples approximate to homogenous materials. The DA theory accounts for the varying pore size distribution, or increasing heterogeneity, by introducing a parameter, n, that describes the surface heterogeneity or degree of sharpness of the micropore size distribution. This yields the following Dubinin – Astakhov equation shown as *Equation 3.25*. All symbols are as *Equation 3.23.*

$$\ln(W) = \ln(V_0\rho) - \left(\frac{RT}{E_0\beta}\right)^n\left[\ln\left(\frac{P_0}{P}\right)\right]^n \qquad \textbf{Equation 3.25}$$

Where, R is 8.314 J mol^{-1} K^{-1}, β is 0.33 for nitrogen, T is 77K, and ρ is 0.807 g cm^{-3}.

A plot of $ln(W)$ versus $[ln(P_0/P)]^n$ over the relative pressure range 10^{-5} – 10^{-1}, may yield a straight line with intercept of $ln(V_0\rho)$, from which the micropore volume can be determined, as shown in *Figure 3.6*. The characteristic energy, E_0 (J mol^{-1}) is determined from the slope, s, of the plot where $s = (RT/\beta E_0)^n$.

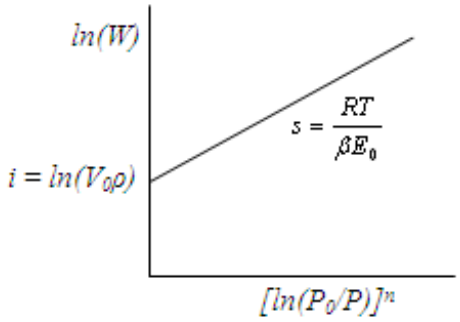

Figure 3.6 – Dubinin-Astakhov Plot

Large values of the heterogeneity parameter correspond to narrow pore size distributions, i.e. $n = 3$ can be equated to a narrow pore size distribution like that of molecular sieves. For zeolites, having an almost uniform pore size distribution, n lies between 3 – 6. Below $n = 3$, the heterogeneity increases and the pore size distribution becomes broader, with strongly activated carbons having n values in the region of 1.2 – 1.8. For this study DA was the preferred method as it accounts for wider pore size distributions, through the use the heterogeneity parameter n. In order to obtain an optimised heterogeneity parameter, n, a systematic search is carried out by recalculating the linear regression and selecting the value of n that gives the smallest standard error of the y-intercept. The exponent n is optimised to within 10^{-4} using the software ASAP2420.

Surface area and pore size characterisation was carried out with the BET, DA and BJH equations with nitrogen as the adsorbate, using software ASAP2420. These equations are the most commonly utilised throughout literature for the analysis of porous materials utilised for EC manufacture. [25-63, 140-151]

3.3 Thermal Gravimetric Analysis

Thermo gravimetric analysis (TGA) is defined as the study of the change in the mass as a function of temperature, time and/or atmosphere. TGA consists of two components; mass and temperature detection. The sample analysis can be carried out under a range of gaseous atmospheres dependant on the system being studied.

The weight-loss curve (weight-loss versus temperature) obtained can then be studied to determine temperature related characteristics of materials, for example, water content, volatile content, ash content and/or decomposition or combustion temperature. [169] The weight-loss curve for calcium oxalate is shown in *Figure 3.7.* [170] This example shows marked weight-loss at specific temperatures allowing for easy interpretation of the results. However, in some cases interpretation of the weight-loss curve is difficult. A derivative weight-loss curve (shown in *Figure 3.7*) can be used to determine the temperature(s) at which the highest weight loss occurs.

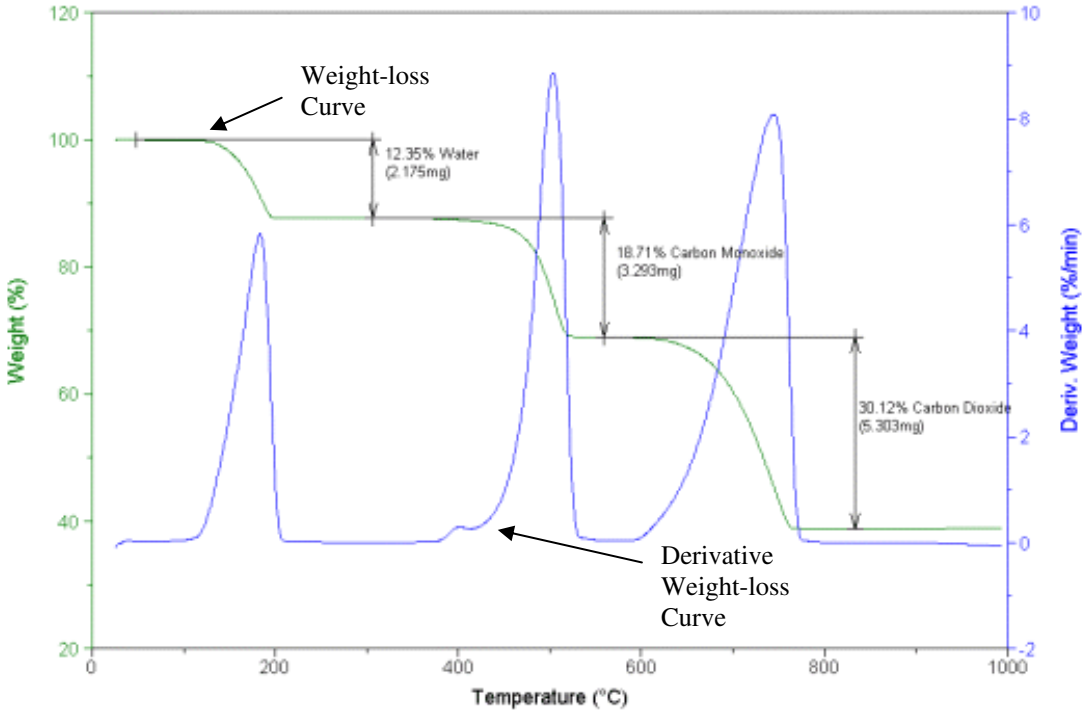

Figure 3.7 – Weight-loss and Derivative Weight-loss Curve for Calcium Oxalate

3.4 Spectroscopic Analysis

Infrared (IR), ultraviolet (UV), and nuclear magnetic resonance (NMR) spectroscopies involve the interaction of molecules with electromagnetic energy. The infrared region of the electromagnetic spectrum covers the range of approximately 8 x 10^{-7} to 10^{-4} m. However, only the mid-range is used in infrared spectroscopy (2.5 x 10^{-6} to 2.5 x10^{-5} m). Wavelengths within the infrared spectrum are usually given in micrometres and frequencies are expressed in wavenumbers ($\bar{\upsilon}$, cm^{-1}) rather than Hertz. [171,172]

$$\text{Wavenumber} \quad \bar{\upsilon} = \frac{1}{\lambda} \qquad \textbf{Equation 3.26}$$

where, λ is the wavelength (cm). Thus, the useful IR region is from 4000 cm^{-1} to 400 cm^{-1}.

Infrared spectroscopy (IR) reveals information about the vibrational states of a molecule. The vibrational spectrum produced is considered to be unique to the molecule. That is, a molecule can stretch or bend only at specific frequencies. Therefore, the IR spectrum can be used like a fingerprint for identification, either by comparing it with a known reference spectra or from first principles. The characteristics of the molecule can be determined from first principles as the structural features of a molecule produce characteristic and reproducible absorptions in the spectrum. This information can indicate whether there is backbone to the structure and, if so, whether the backbone consists of linear or branched chains. Next it is possible to determine if there are unsaturated bonds and/or aromatic rings in the structure. Finally, it is possible to deduce whether specific functional groups are present or not present.

The IR spectrum occurs due to the absorption of electromagnetic radiation at frequencies that correlate to the vibration of specific sets of chemical bonds within a molecule. The sum of the contributing energy terms is given by *Equation 3.27.* [172]

$$E_{total} = E_{electronic} + E_{vibrational} + E_{rotational} + E_{translational}$$ **Equation 3.27**

The translational energy relates to the displacement of molecules in space as a function of the normal thermal motions of matter. Rotational energy, which gives rise to its own form of spectroscopy, is observed as the tumbling motion of a molecule, which is the result of the absorption of energy within the microwave region. The vibrational energy component is a higher energy term and corresponds to the absorption of energy by a molecule as the component atoms vibrate about the mean centre of their chemical bonds. The electronic component is linked to the energy transitions of electrons as they are distributed throughout the molecule, either localized within specific bonds, or delocalized over structures, such as an aromatic ring. In order to observe such electronic transitions, it is necessary to apply energy in the form of visible and ultraviolet radiation (*Equation 3.28*): [171]

$$E = h\upsilon = \frac{h}{\lambda}$$ **Equation 3.28**

where, E is the energy of each individual photon, h is the Planck's constant 6.626 x 10^{-34} J s, and υ is the vibrational frequency.

The fundamental requirement for infrared activity, leading to absorption of infrared radiation, is that there must be a net change in dipole moment during the vibration for the molecule or the functional group being study.

To explain the origin of the characteristic frequencies that can be assigned to particular combinations of atoms within a molecule it is necessary to look to Hook's Law. The fundamental vibrational frequency, υ, of a molecule can be expressed as: [171]

$$\upsilon = \frac{1}{2\pi c}\sqrt{\frac{\kappa}{\mu}}$$ **Equation 3.29**

Where, κ is the force constant, c is the speed of light and μ is the reduced mass given by *Equation 3.30.*

$$\mu = \frac{m_1 m_2}{m_1 + m_2}$$ **Equation 3.30**

where m_1 and m_2 are the mass of the two atoms. This simple equation provides a link between the strength of the covalent bond between two atoms (or molecular sections), the mass of the interacting atoms and the frequency of vibration. Although simple in concept, there is a reasonably good fit between the bond stretching vibrations predicted and the values observed for the fundamentals.

To allow for ease of interpretation of the model it is necessary to describe the model in terms of a minimum set of fundamental vibrations. That is, base the model on the xyz coordinate axes. This leads to a molecule with N atoms having 3N degrees of freedom. 3 degrees of freedom are translational, 3 rotational degrees of freedom for a non-linear and 2 for a linear molecule. This gives 3N-6 vibrational degrees of freedom for a non-linear and 3N-5 for a linear molecule. These vibrations are bonding vibrations (number equals the number of chemical bonds), bending vibrations (change of bonding angles), torsional vibrations, out-of-plane vibrations, and others.

When a spectrum is recorded using a conventional, dispersive IR spectrometer, each data point reveals the transmitted light at the respective frequency. The signal provided by the FTIR technique, however, contains information about the complete spectrum of the probe. This signal has to be transformed from the *time-domain* into the *frequency-domain* in order to reveal the spectrum. This transformation is called *Fourier transformation*.

3.5 Electrochemical Measurements

In the field of EC development and testing, it is necessary to be able to qualitatively evaluate capacitance and its dependence on various experimental variables by direct instrumental measurements. All polarisable electrode interfaces with solutions or solid electrolytes exhibit a double layer capacitance.

3.5.1 Cyclic Voltammetry

A commonly applied procedure for study and evaluation of the behaviour of electrochemical capacitors is linear sweep voltammetry or, when applied in a repetitive mode, cyclic voltammetry. In this technique, the time and potential dependant current, I, are measured at a constant (or linear) sweep rate between a set potential difference, ΔV. [1] For a capacitor the response current *I(t)* to a linear voltage sweep is

$$I(t) = C\left(\frac{dV}{dt}\right) \equiv Cs \qquad \textbf{Equation 3.31}$$

Where *C* is the capacitance and *dV/dt* is the linear voltage sweep rate, sometimes denoted as *s*. The direction of the current will depend on the sign of *dV/dt*, which is periodically reversed in cyclic voltammetry at the voltage limits.

For an ideal electrochemical capacitor, its capacitance is independent of frequency, so the charge stored by a capacitor is proportional to the voltage imposed. Therefore for a constant sweep rate (mV s^{-1}), current response will remain constant and a rectangular shape will be obtained from a plot of current vs. potential as shown in *Figure 3.8*.

If the electrodes are ideally polarisable the rectangle for the anode and cathode charging currents should be symmetrical around the zero for the y-axis. If this is not the case the capacitance can be calculated by measuring the current response at varying sweep rates and plotting $\Delta I = I_a - I_c$ vs. *dV/dt* as shown in *Figure 3.9*. [173] Where I_a and I_c are the anodic and cathodic current, respectively.

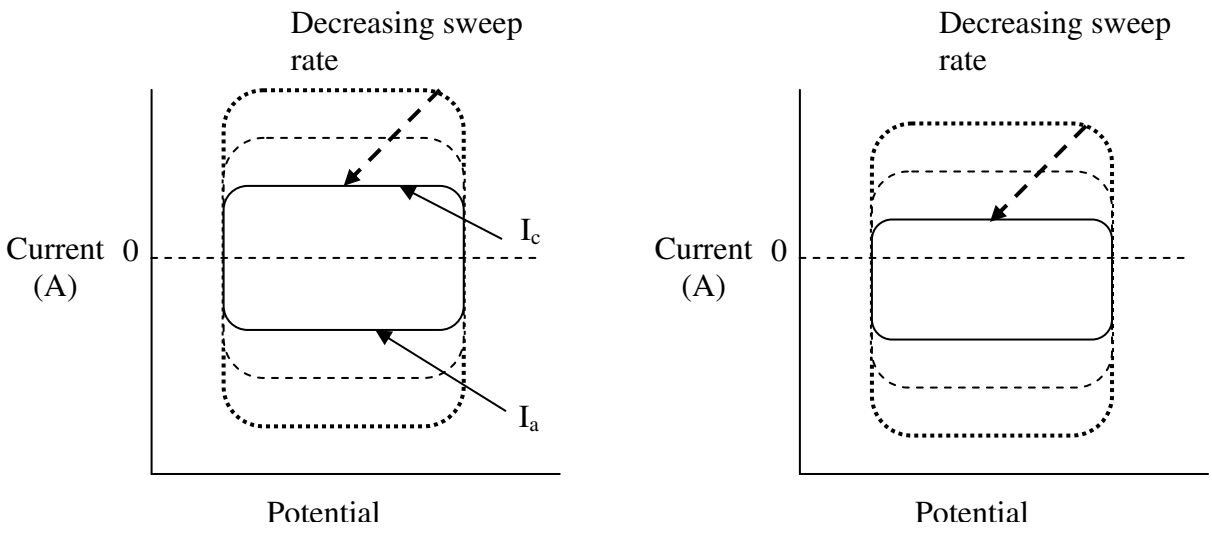

Figure 3.8 – Current-potential plots at different sweep rates for (a) an ideally polarisable interphase, and (b) a non-ideally polarisable interphase.

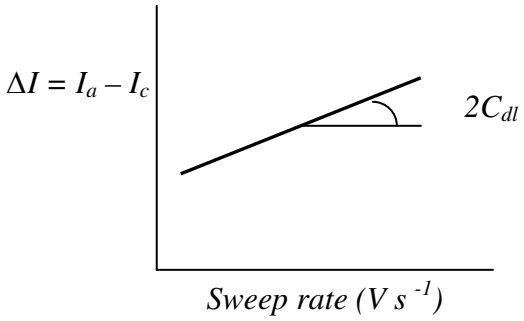

Figure 3.9 – Plot for capacitance calculation for non-ideally polarisable interphase

3.5.2 Galvanostatic Charge – Discharge

For interfacial charging at constant current density, I, the potential difference, ΔV, developed across the capacitor plates increases linearly with time as the charge builds up across the interface over some time interval Δt. [1] That is,

$$C = \frac{\Delta q}{\Delta V} \qquad \textbf{Equation 3.32}$$

And $$\Delta q = \int I \cdot dt \qquad \textbf{Equation 3.33}$$

Therefore $$C = \int I \cdot \frac{dt}{\Delta V} = I \cdot \frac{\Delta t}{\Delta V} \qquad \textbf{Equation 3.34}$$

It is this principle that is used in Galvanostatic Charge-Discharge (GC) cycling, where the EDLC is charged and discharged, over many cycles, to a set voltage at constant current density, and the cycle time is recorded for capacitance calculations. This technique gives information about the lifetime of the EDLC. The above equation only applies if the capacitance, C, is constant with potential. Often experimentally this is not the case, and so ΔV deviates from a linear dependence on time at constant current. C is therefore obtained as the reciprocal of the slope of the relationship between ΔV and Δt curve or differentially, at some point on it, as $(d\Delta V/dt^{-1})$ when C is not constant with ΔV. The measurable dependence of ΔV on time at a constant current is commonly referred to as the "charging curve".

This applies to an "ideally polarisable" electrode (as should be the case in EDLCs) where the current, I, simply passes charge in the interface without any Faradaic processes taking place. As long as that condition applies the electrode interface remains ideally polarisable and I is purely a double-layer charging current, I_{dl}.

In an EC where Faradaic processes are taking place, i.e. decomposition of the solution occurs at the electrodes, the double-layer continues to charge with the rise of ΔV, but the current I then becomes divided into two parts, I_{dl} and I_P, where I_P is the Faradaic current, which increases exponentially with ΔV when ΔV exceeds the thermodynamic reversible potential for solution decomposition at that electrode.

The charging curve takes the form as shown in *Figure 3.10* and as ΔV increases beyond its value corresponding to solution decomposition, the ΔV *vs.* Δt relation increasingly deviates from linearity as the I_P component becomes progressively larger and the electrode is behaving in an non-ideally polarisable way. [1]

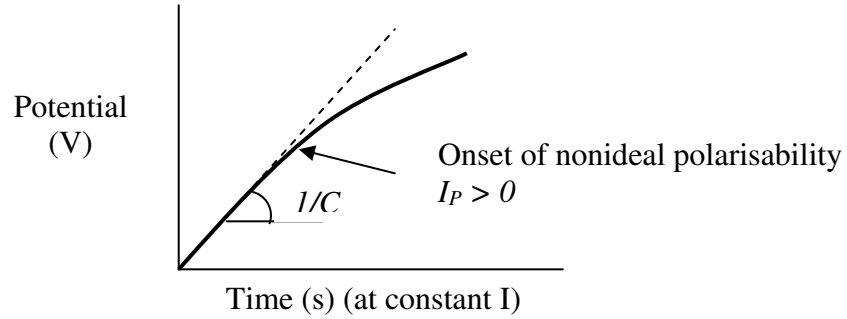

Figure 3.10– Constant current charging curve for an electrode interphase having double layer capacitance, C_{dl}, and Pseudocapacitance, C_P, represented as increase in Faradaic current, I_P.

3.5.3 Electrochemical Impedance Spectroscopy

The electrochemical techniques described in **Sections 3.3.1 and 3.3.2**, describe the characterisation of capacitance by measuring the current response to various changes of potential or, vice versa, changes of potential in response to a charging current. These techniques can classed as direct current (DC) type measurements. Another of characterisation is Electrochemical Impedance Spectroscopy (EIS). EIS is an AC technique which allows for characterisation, and isolation, of the resistances and double-layer capacitance as a function of frequency values for an EC cell by applying an AC potential and measuring the current response. It can be used to evaluate the capacitative behaviour of individual, two- or multi-electrode electrochemical devices.

In general, the impedance $Z(\omega)$ for a given imposed frequency is;

$$Z(\omega) = V(t) / I(t) \qquad \textbf{Equation 3.35}$$

This is analogous to Ohm's law, where $V(t) = V_0 \sin(\omega t)$ and $I(t) = I_0 \sin(\omega t + \phi)$ are the time variant voltages and currents that are modulated according to the frequency ω. $Z(\omega)$ may include Ohmic resistance (R), capacitive (C), and sometime inductive (L) elements. The elements of the equivalent circuits are dependent on frequency in *Table 3.3*: [1]

Table 3.3 – Elements of equivalent circuits and their respective dependences on frequency

Element	$Z(\omega)$
Resistor, R	$R\ (dR/d\omega = 0)$
Capacitor, C	$1/j\omega C = -j\omega C$
Inductor, L	$j\omega L$

In a series arrangement of *n* impedances [1]

$$Z_{total} = \sum_{i=1}^{n} Z_i \qquad \textbf{Equation 3.36}$$

while for a parallel arrangement

$$\frac{1}{Z_{total}} = \sum_{i=1}^{n} \frac{1}{Z_i} \qquad \textbf{Equation 3.37}$$

The use of EIS is particularly valuable, as it allows for the equivalent series resistance (ESR) and any other resistances associated with the EC system to be isolated and quantified. The evaluation of the ESR, for various electrode / electrolyte systems, is particularly important for device design and optimisation of power density, (as shown in *Equation 1.3*). The presence of pseudocapacitance can also be distinguished from that of the double-layer capacitance.

The analysis and interpretation of the data obtained from EIS is usually carried out via one of the following methods: [1]

1. Fitting the frequency-response data to data obtained from equivalent circuit models of varying complexity. The equivalent circuits should be able to simulate the behaviour of the real system and are usually composed out of the following equivalent circuit elements; Ohmic resistors, *R*; capacitances, *C*, or pseudocapacitances, C_P; and inductances, *L*. In addition to these, when diffusional impedance arises (e.g. that which occurs for porous electrode/electrolyte systems), a further special element, the Warburg impedance, W, must be included.
2. Interpretation of the frequency response behaviour in an analytical mathematical way based on electrochemical kinetic reaction mechanisms together with a double-layer capacitance.
3. A hardware simulation circuit is set-up and its impedance spectroscopy is compared with that obtained for the electrochemical systems being studied.

Method 1 (fitting equivalent circuits) is the most commonly used method for analysing EC systems, and will be used for the analysis of EIS data in this study.

3.5.3.1 Equivalent Circuits

The most basic equivalent circuits for ECs consists of 3 circuit components, (1) a double-layer capacitance, C_{dl}, a solution resistance for the electrolyte, R_S, and the ionic resistance which arises from the interparticle contact resistance, R_I. This gives rise to the circuit shown in *Figure 3.11*. [174]

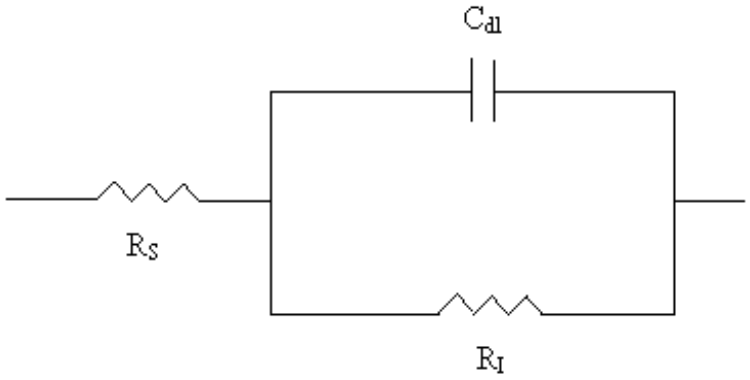

Figure 3.11(a) – Basic EC Equivalent Circuit

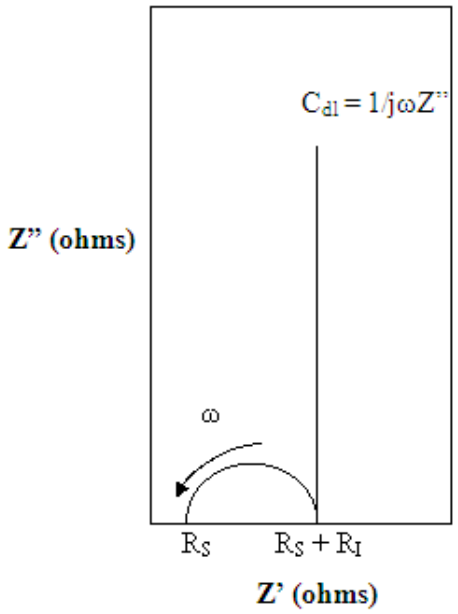

Figure 3.11(b) – Nyquist Plot for Equivalent Circuit shown in (a)

The complex plane impedance (Nyquist) plot is the result of plotting the imaginary impedance (Z") against the real impedance (Z') responses. For full mathematical derivation of how the equivalent circuit gave rise to the Nyquist plot shown in *Figure 3.11(b)* see *Page 491* in *Reference 1*.

The equivalent circuit above does not take into account the effect of porosity on the EIS data and therefore does not produce a reliable model to which the data can be fitted. Therefore the equivalent circuit must be more complex than that in *Figure 3.11(a).* The impedance behaviour of high surface area, porous carbons that provide large specific capacitance values, cannot be represented by a simple capacitance or even by a simple RC circuit. Work carried out by de Levie [175] on the electrochemical response of porous electrodes produced the "Transmission Line" model, as shown in *Figure 3.12*. The Transmission Line model consists of a network of parallel RC circuits (each a series RC combination) that represent the distribution of double-layer capacitance and internal resistance down a pore. The frequency response of the distributed circuit gives rise to a – 45° phase angle over a range of frequencies. This same frequency-response behaviour occurs for diffusion controlled processes as modelled by the Warburg impedance. The Warburg response (represented by W) arises when an electrochemical process is or becomes diffusion controlled. The Warburg response contains two components, a diffusion related capacitance and a diffusion related resistance, each of which is dependant on the square root of frequency. The Warburg response occurs at a 45° incline on the complex plane impedance plot. Although the transmission line model accounts for distribution down the pore, it assumes all pores are equal and therefore does not account for the pore size distribution found in porous electrodes.

ECs combining a porous electrode with a liquid electrolyte will give rise to both transmission line behaviour, due to the porous electrode, and diffusion behaviour, due to the liquid electrolyte. Therefore by simplifying the circuit and adding a Warburg component this allows for a more accurate model for fitting the frequency-response data. By removing the large number of RC circuits associated with the Transmission Line, this also makes the model more practical for use by engineers and materials scientists. The equivalent circuit is shown in *Figure 3.13(a)*. This circuit was developed by Randle and is known as the "Randles" circuit. [1,174] This is the most commonly utilised way of representing the impedance behaviour of an EC cell. [5,113, 176,177]

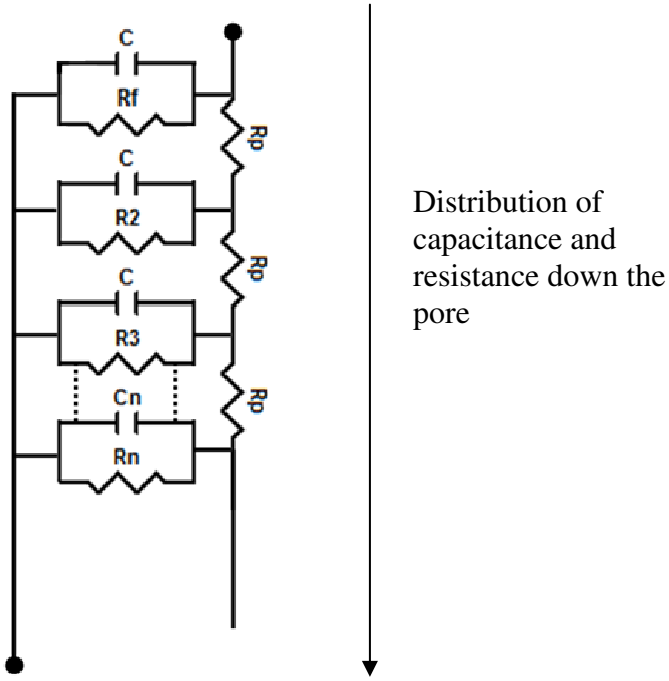

Figure 3.12 – Transmission Line Circuit Model

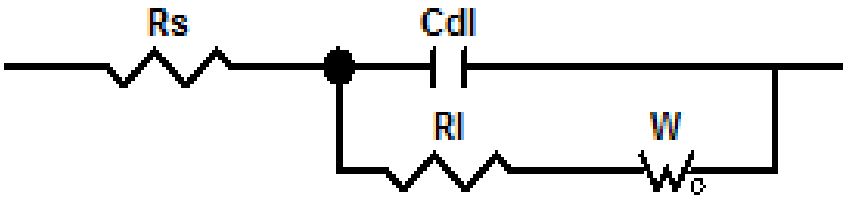

Figure 3.13(a) – Equivalent circuit for EDLC with porous carbon electrodes

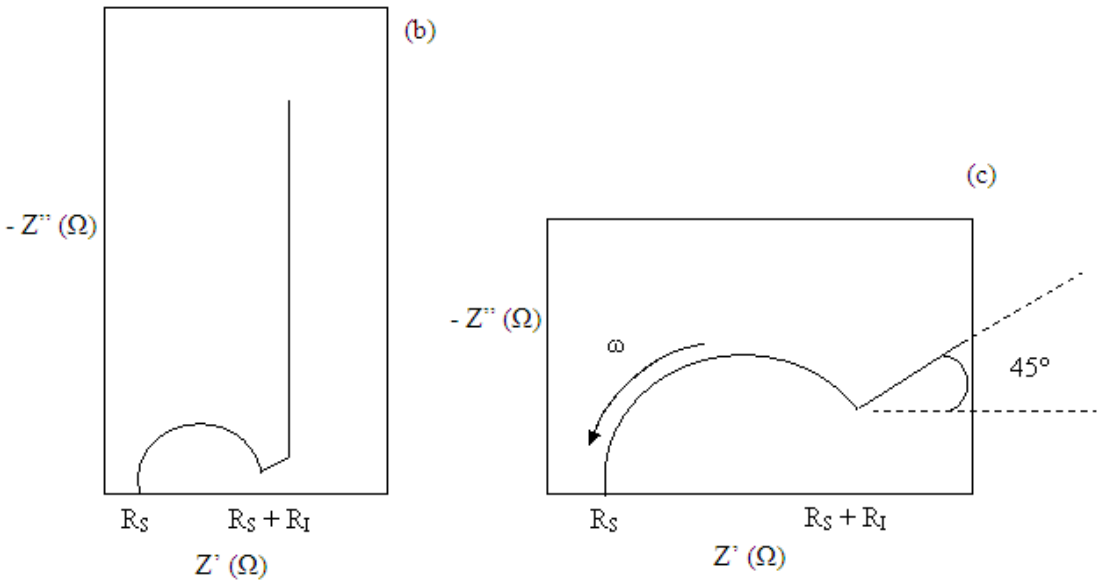

Figure 3.13 (b) – Nyquist Plot for Randles Equivalent Circuit Model; Equivalent to the complex plane impedance plot for porous carbon electrode/ liquid electrolyte system, with no Faradaic component. **(c) –** Expanded High Frequency Region

The complex plane (Nyquist) plot shown above in *Figure 3.13(b and (c)*, exhibits a single semicircle at high frequency which gives rise to a vertical line in the –Z" direction with decreasing frequency; the intercepts on the Z' axis are $R_S + R_I$ and R_S at high frequency. The vertical element of the plot corresponds to the impedance (Z") of a pure capacitor (C_1) as ω tends to zero.

For systems where conductivity across the electrode is high, $R_I \approx 0$ and the semi-circle disappears giving rise the Nyquist plot as shown in *Figure 3.14*.

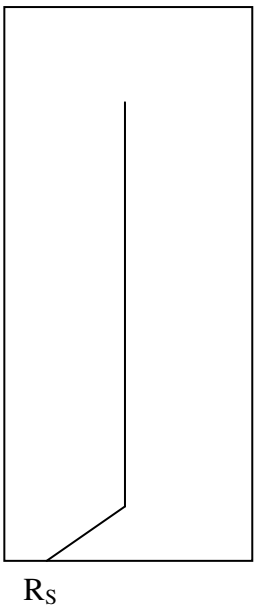

Figure 3.14 – Complex Plane (Nyquist) Plot for $R_I = 0$

The main flaw with the Randles Circuit is that although accounted for, the numerical data for the distributed capacitances and resistances across the electrode cannot be determined and it does not take into account self-discharge due to charge redistribution (discussed in **Section 3.7**). Bonert and Zubieta [178,179] proposed the 3-Branch model to allow for quantification of the distributed capacitance and resistances.

The circuit was developed for three main reasons:

1. To represent an EC with RC circuits, but to keep the number of RC elements low for practical reasons;
2. Include the non-linear voltage dependant capacitance that occurs due to charge redistribution only in one RC element;
3. Include a parallel leakage resistor, to represent self-discharge due to charge redistribution.

The equivalent circuit (shown in *Figure 3.15*) consists of three distinct RC time constants to cover the specified time range of 30 minutes. Each of the three branches has a distinct time constant differing from the others in more than an order of magnitude. The first (or immediate) branch consists the elements R_i, C_{i0}, and the

voltage dependant capacitor C_{i1} (in F V^{-1}), which represents the behaviour in the time range of seconds in response to a charge action. The second (or delayed) branch, with the parameter R_d and C_d, dominates the behaviour in the range of minutes. Finally, the third (or long-term) branch, with parameters R_l and C_l, dominates the behaviour for times longer than 10 minutes. A leakage resistor, parallel to the terminals, is added to represent the self-discharge.

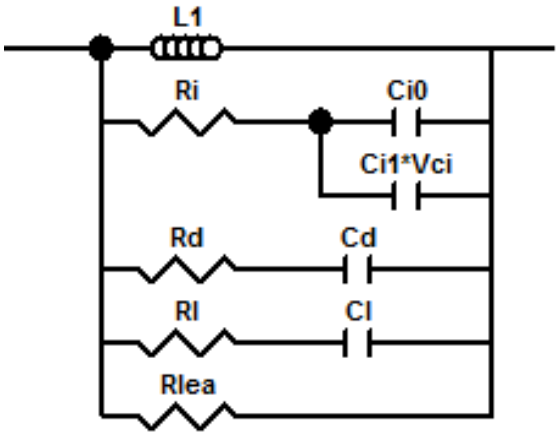

Figure 3.15 – 3 Branch Equivalent Circuit

Although this model allows for quantification of the distributed capacitance and resistance values, it does not take into account electrolyte diffusion and therefore may not be a good representation of systems involving liquid electrolytes.

3.6 Electrochemical Stability Window Measurement

3.6.1 Evaluation of Reduction and Oxidation Potential of RTILs

In considering RTILs for use as electrolytes for ECs, it is important to know the electrochemical stability toward a particular electrode. The electrochemical stability window (ESW) is defined as the potential range within which no oxidation or reduction of the electrolyte occurs. [16] As RTILs are organic, breakdown starts at the weakest covalent bond and is therefore specific to each RTIL. The ESW is strongly dependant on the electrode being used, with windows varying by as much as 3V from a tungsten working electrode to glassy carbon. [20] This difference makes it important for ESW measurements to be carried out in the electrode/electrolyte system they are intended for use in. The ESW is calculated by subtracting the reduction potential from the oxidation potential.

Cyclic voltammetry is usually used for determining the ESW of all types of electrolyte. The background for CV has already been outlined in **Section 3.3.1**. This method is simple but a number of factors must be taken into consideration; working electrode / reference electrode, differences in potential scan rate and/or cut-off current density. The ESW of RTILs is very sensitive to impurities with even 100ppm having a detrimental effect on the ESW. [16]

As the oxidation and reduction reactions of RTIL are not reversible, [180-182] the corresponding reduction or oxidation potential cannot be specifically obtained as would be possible for an electrochemically reversible system. *Figure 3.16* shows the voltammogram for RTILs. The oxidation and reduction current monotonically increase with increasing potential. Since no peak is observed even at high current density, a current density must be specified to evaluate the reduction or oxidation potential. This is known as the cut-off current density. The cut-off current density chosen is usually between 0.1 and 1 mA cm^{-2}, however, for capacitor applications this is usually lower as the cycling performance is strongly dependant on the stability of the electrolyte. [16]

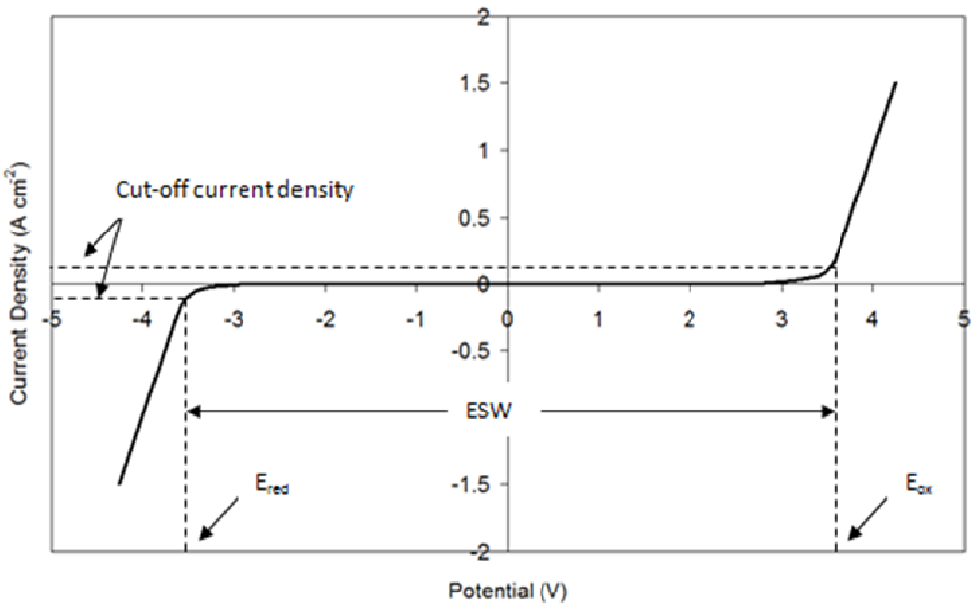

Figure 3.16 – Cyclic Voltammogram of RTILs as typically observed (Two separate voltammograms are indicated)

3.6.2 Reference Electrode

Reference electrodes are unpolarised electrodes often used to evaluate new materials for supercapacitor electrodes. The use of a reference electrode allows for evaluation of individual electrodes of the device. In the case of ESW measurement, this allows for isolation of oxidation and reduction processes at the individual electrodes. There are two systems that can be used; one is a three-compartment cell where the reference electrode is kept separate from the system being used but is connected through instrumentation, or a three-electrode cell where the third (reference) electrode can be inserted between two working electrodes, referred to as a quasi reference electrode. For both of these systems the potentials of each working electrode on charge, discharge or open circuit can be recorded against the potential of a compatible reference electrode. [1]

The problems that are associated with the use of reference electrodes become particularly apparent with the introduction of ionic liquids as electrolytes. This is due to the operating voltage of ionic liquids not being limited by a well defined solvent,

be it aqueous or organic. [183] Literature data on the electrochemical stability of ionic liquids is available for different working electrode materials, most commonly platinum, tungsten, glassy carbon and graphite and with different reference electrodes. This makes comparison of the data difficult due to different reference systems and in some cases systems are not electrochemically defined. For example, systems such as platinum, aluminum or silver wires immersed in the electrolyte being studied are known as quasi reference electrodes and the reference potential is not defined. [16, 20]

3.6.3 Effect of Water on Electrochemical Stability

Even in highly pure RTIL samples, water and oxygen are the main impurities due to them being highly soluble in the RTILs. As these molecules are electrochemically active at much lower potentials than the RTIL anions and cations, they lead to a significant reduction in the ESW of the RTILs, with 3 wt% water reducing the ESW by up to 2 V. [184] This makes it essential for the RTILs to be stored in a glove box with N_2 or Ar atmosphere with less than 50 ppm water.

3.7 Self-Discharge

ECs are required for storing energy over time periods ranging from seconds to several days. The main factor determining the retention energy, or capacitance, over time is the self-discharge rate. The self-discharge rate of an EC refers to the decrease in voltage across the cell that occurs when the EC is disconnected from a charging current or electrical load. In chemical cells such as batteries, the self-discharge rate is very low and the energy can be stored for much longer periods of time than for ECs, e.g. many months if not years. The reason for the higher discharge rate in ECs than in batteries is that charged ECs are in a state of high energy, i.e. thermodynamically unstable. The driving force for self-discharge is to attain a lower more stable state, as demonstrated in *Figure 3.17*. Batteries are less affected by self-discharge due to the thermodynamic potential present at open-circuit. [1]

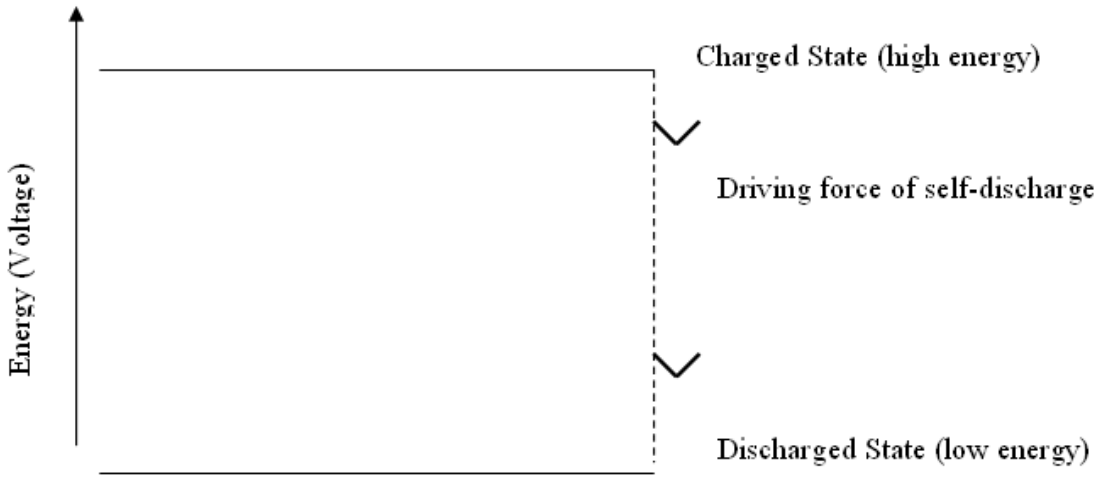

Figure 3.17 – Driving Force for Self-discharge

Self-discharge is dependant on the electrochemistry of the system, reagents and electrolytes. Temperature can also have a significant effect on the self-discharge rate.

If the electrodes of the EC are ideally polarisable self-discharge will not occur. ECs are able to self-discharge more readily than batteries, as ECs have an electrostatic potential difference, that is not stabilised by a thermodynamic or kinetic process and therefore any impurity may depolarise the potential. Self-discharge is the spontaneous decrease in voltage with time of a charged EDLC left on open-circuit.

The rate of self-discharge is dependant on the mechanism by which self-discharge occurs. When an EDLC is placed on open-circuit there is no external circuit through which electrons may pass and discharge the cell, and therefore self-discharge must take place through processes at the electrodes. Conway [1] proposed three mechanisms through which self-discharge can take place and derived models which predict the self-discharge profiles for each mechanism.

1. Faradaic reaction of a species which is either at high concentration in the cell e.g. when the EC is charged beyond the decomposition limit of the electrolyte or due to the oxidation/reduction of surface functionality attached to the surface of the carbon.

2. The electrode material or electrolyte contain impurities that are oxidisable or reducible over the potential range and the EC becomes non-ideally polarisable.

3. An internal ohmic leakage or 'short-circuit' due to faulty construction.

Case (1) where an activation-controlled Faradaic process occurs the voltage reduction (V_{SD}) versus log time would give a straight line:

$$V_{SD} = \frac{-RT}{\alpha T}\ln\frac{Fi_0}{RTC} - \ln\left(t + \frac{C\tau}{i_0}\right) \qquad \textbf{Equation 3.26}$$

And

$$V_{SD} = V_i - A\log(t+\tau) \qquad \textbf{Equation 3.27}$$

where R is the universal gas constant, T is the absolute temperature, α is the transfer coefficient, F is the Faraday constant, i_0 is the exchange current density, C is the capacitance, t is the time, τ is an integration constant, V_i is the initial charge voltage and A is a constant related to the Tafel slope.

If (1) became apparent due to water uptake in the electrolyte the resultant voltage would be independent of pore size distribution.

2) A diffusion controlled process results in voltage drop that is related to the square root of t:

$$V_{SD} = V_i - \frac{2zFAD^{1/2}\pi^{1/2}c_0}{C}t^{1/2} \qquad \textbf{Equation 3.27}$$

where D is the diffusion coefficient of the redox species, z is the charge, c_0 is the initial concentration and A is the electroactive area. This model is based on the Faradaic reaction of a species which has a low concentration in the EC and relies on diffusion to the electrode surface to react e.g. an Fe shuttle reaction.

For an internal ohmic leakage or 'short-circuit' the plot of lnV_{SD} vs. t would give a linear relationship:

$$\ln V_{SD} = \ln V_i - \frac{t}{RC} \qquad \textbf{Equation 3.28}$$

where R is the resistance of the ohmic contact.

4.0 Experimental

This chapter outlines the experimental procedures followed throughout the EDLC production process from resorcinol-formaldehyde gel production to test cell construction. This chapter also includes a discussion of the development of the process of construction and testing of EDLC test cells, in particular the fine-tuning of the electrodes to produce the good quality uniform electrodes required for EDLC manufacture.

4.1 Resorcinol – Formaldehyde Xerogel Preparation

Synthesis of resorcinol formaldehyde xerogels first requires the preparation of a hydrogel from the condensation polymerisation of resorcinol with formaldehyde in the presence of anhydrous sodium carbonate as a catalyst to facilitate the formation of resorcinol derivatives. [50] Solvent exchange is carried out to remove water from the structure and replace it with a solvent with a lower surface tension to reduce pore shrinkage during drying. Xerogel resins are produced specifically from vacuum drying of the wet gel. The materials and methods followed are outlined in the following sections.

Materials

Resorcinol (1,3-dihydroxybenzene) [$C_6H_4(OH)_2$, 98%] (R), formaldehyde [HCHO, 37% solution] (F), and sodium carbonate [Na_2CO_3, $\geq$ 99.5%] (C) were procured form Sigma-Aldrich Co., and acetone [C_3H_6O, 98%] were used as received. Distilled and deionised water was used in the preparation of all solutions.

From the literature [58, 59] it was identified that two gelation methods have been utilised for the production of resorcinol-formaldehyde gels for use in EC manufacture. Although the original method developed by Pekala [50] is still the most commonly utilised method of RF gel production, Zhu *et al.* [59] utilised an alternative procedure which exhibited a different gelation temperature profile. It was noted that Zhu *et al.* produced higher specific capacitances of 250 – 290 F g^{-1} than that achieved in other studies. To assess the effect of gelation temperature on the resultant

xerogel the two hydrogel preparation procedures were carried out. The two procedures are given in **Sections 4.1.1 and 4.1.2.** Gelation method 1 follows the original resorcinol-formaldehyde gelation method by Pekala[50,58]. Gelation method 2 follows the procedure utilised by Zhu *et al.* [59]

Apparatus

500 ml beaker

Magnetic Stirrer

Balance

100 ml measuring cylinder

20 ml pipette

1 l Duran Bottle

4.1.1 Gel Preparation Method 1 – RF100

R/F = 0.5 (molar ratio)

R/C = 100 (molar ratio)

R/W = 0.25 g ml^{-1}

22 g of resorcinol and 0.212 g of sodium carbonate catalyst were dissolved in 220 ml of de-ionised water in a 500 ml beaker. The mixture was stirred with a magnetic stirrer in a fume cupboard at room temperature (25 °C). Once the solids were dissolved, 32.43 ml of formaldehyde was added to the solution at room temperature. The mixture was stirred for 45 minutes. The solution was transferred to a 1 L glass flask and well sealed. It was kept in an oven at 90 °C for 72 hours to allow the gelation process to complete.

To assess the effect of R/C ratio, the procedure above was repeated for R/C ratios; 200, 300, 400, 500, 750, 1000 and 1500. The R/F ratio was kept constant at 0.5 and R/W at 0.1 g ml^{-1}.

4.1.2 Gel Preparation Method 2 – RF100

R/F = 0.5 (molar ratio)

R/C = 100 (molar ratio)

R/W = 0.1 g ml^{-1}

22 g of Resorcinol and 0.212 g of sodium carbonate catalyst were dissolved in 220 ml of de-ionised water in a 500 ml beaker. The mixture was stirred with a magnetic stirrer in a fume cupboard at room temperature. Once the solids were dissolved 32.43 ml of Formaldehyde was added to the solution at room temperature. The mixture was stirred for 45 minutes. The solution was transferred to a 1 L glass flask and well sealed. It was kept in an oven at 25 °C for 24 hours to allow the gelation process to start. After this time the temperature was increased to 60 °C for 72 hours. After this time the solution had turned to a dark pink opaque monolithic gel. To complete the gelation process the temperature was increased to 80 °C for 48 hours.

The procedure above was repeated for the following R/C ratios; 200, 300, 400, 500, 750, 1000 and 1500. R/F ratio and R/W ratio were kept constant.

4.1.3 Solvent Exchange

On completion of the gelation process, the monolithic hydrogels (for both methods) were broken down into approximate 5 mm pieces and twice the volume of acetone to aquagel was added for solvent exchange.[5] The gels were kept in a shaker at 125 rpm at 25 °C for 7 days. After 3 days the acetone was changed. After solvent exchange the acetone was drained from the soaked gels which were then ready for the drying stage.

[5] Acetone reduces pore shrinkage on drying due to a lower surface tension than that of water.

4.1.4 Vacuum Drying

Vacuum drying was carried out using a vacuum oven set to 60 °C. The vacuum oven was evacuated to maximum vacuum (-1 bar (g)) and held for 3 days. As it was not possible for the vacuum pump to be left running overnight for safety reasons, the heating was switched off and the gels cooled to prevent ambient drying overnight.

A solvent trap was used to collect the acetone vapour removed from the gels. This was emptied every 20 minutes for the first day to prevent back-flow into the oven or acetone vapour from entering the vacuum pump.

4.2 Carbon Xerogel Production

Carbonisation of approximately 4 g of each sample was carried out in a Carbolite model 2408 tubular furnace using a ceramic boat; an inert atmosphere was obtained with a flow of argon gas at 200 ml min^{-1} (shown in *Figure 4.1*). All samples were purged for 30 minutes in the furnace with argon prior to heating to ensure inert blanket. The heating cycle is summarised in *Figure 4.2.* The first two isothermal steps of the heating cycle were determined by thermal gravimetric analysis of xerogel samples (**Section 5.4**). The maximum carbonisation temperature was selected from studies carried out on the effect of carbonisation temperature on EC performance by Pekala *et al.* [58] and Kim *et al.* [60]

Figure 4.1 – Carbolite Furnace used for Carbonisation and Activation [185]

NOTE: Controlled cooling cannot be carried out cool down phase is included only for visual purposes. Samples were cooled overnight under argon.

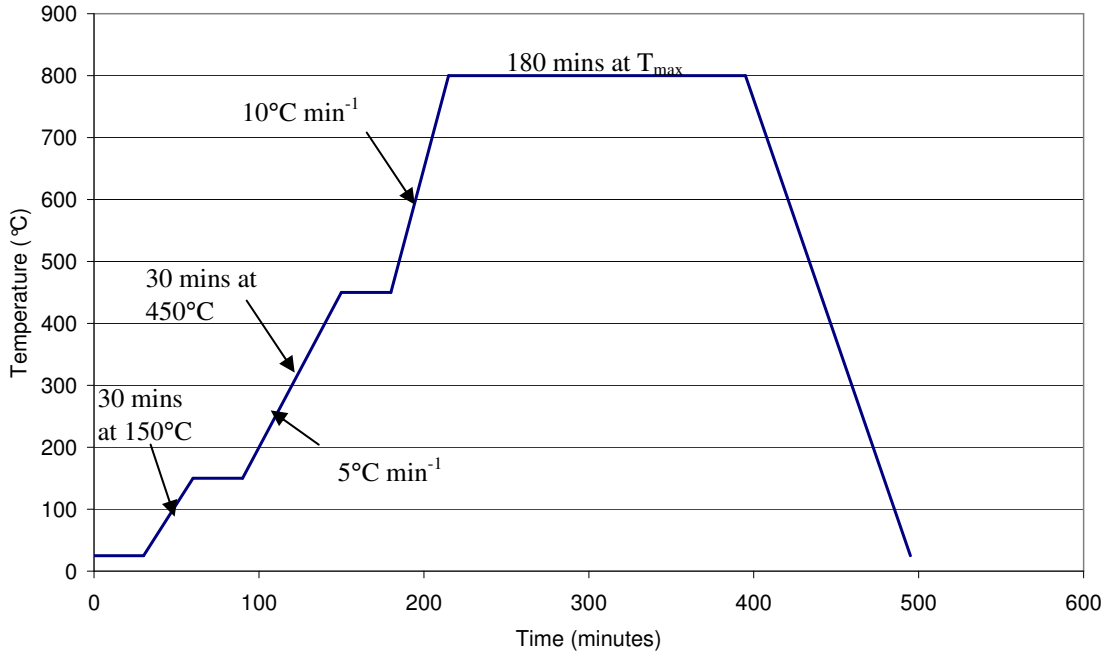

Figure 4.2 – Temperature Programme for the Carbonisation of Xerogels

4.3 Activated Carbon Xerogel Production

Activation was carried out post carbonisation to increase surface area and remove surface roughness from carbon. Activation was carried out in a tubular furnace as in **Section 4.2**. Purging of the samples in argon for 30 minutes was carried out as with carbonisation. To prevent oxidation before reaching the activation temperature, an inert atmosphere was maintained with a flow of argon gas at 200 ml min^{-1} while the furnace heated to the required activation temperature. The gas was then switched to 200 ml min^{-1} of carbon dioxide (99.8% CO_2) as the oxidising agent. Time for switching the gases at 800 °C was allowed either side of the 180 minute activation time. Activation procedure is summarised in *Figure 4.3*. The activation temperature was selected from studies carried out on the effect of activation temperature on EC performance by Pekala *et al*. [58].

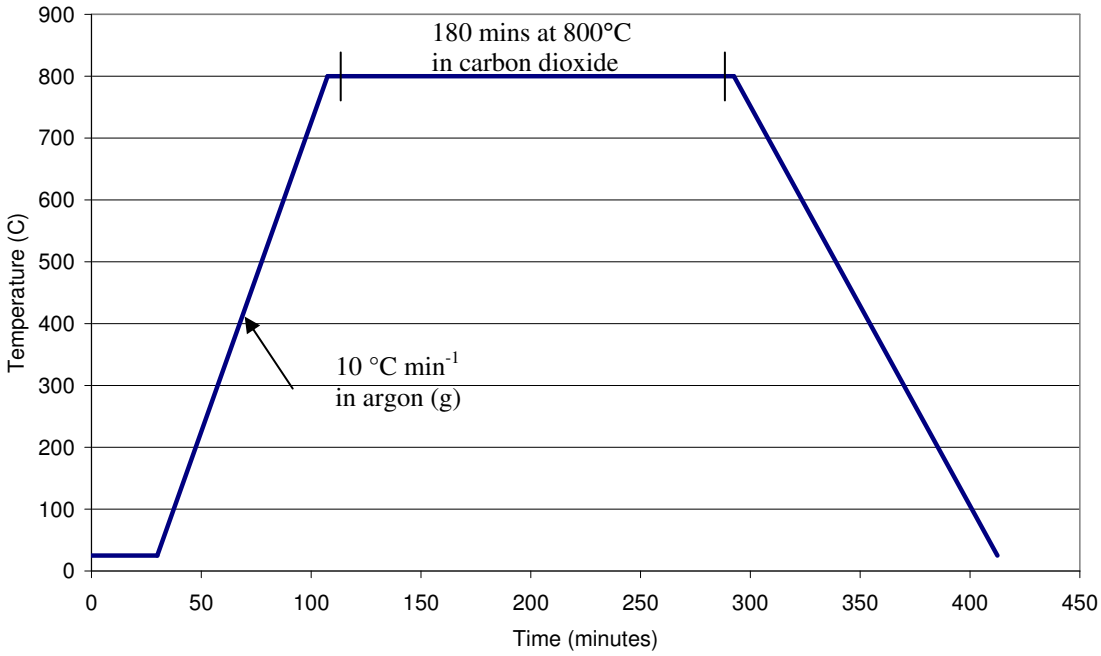

Figure 4.3 – Temperature Programme for Activation of Carbon Xerogels

4.4 Thermal Gravimetric Analysis

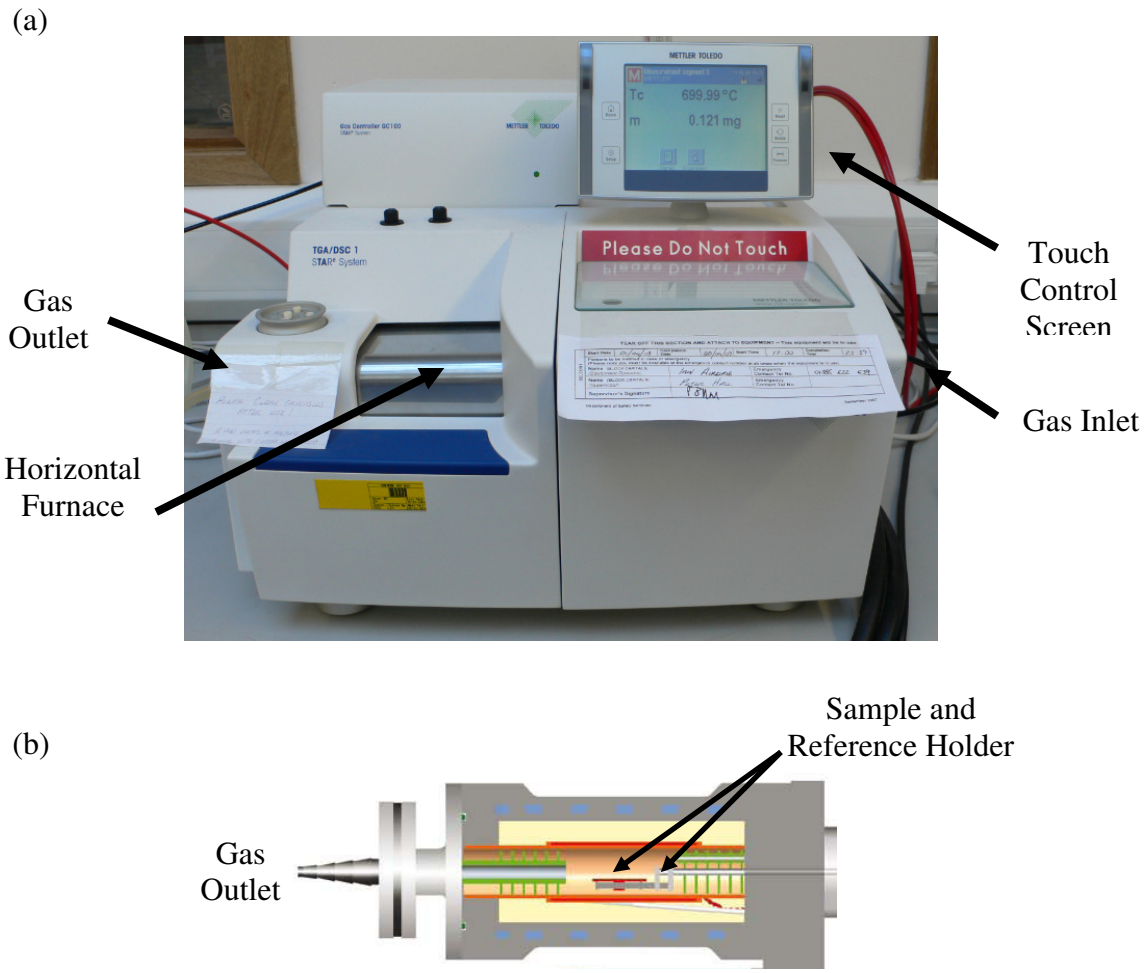

Figure 4.4 – Mettler Toledo Thermogravimetric Analyser (a) Photograph of Laboratory Equipment, (b) Schematic of Furnace [186]

Thermal gravimetric analysis (TGA) was carried out to assess the xerogel weight-loss with temperature during carbonisation. This weight-loss could then be used to determine the optimal carbonisation cycle.

The TGA thermal cycle was set to heat to 1000 °C at 10 °C min^{-1}. Nitrogen gas was supplied to the system at a constant flowrate of 50 ml min^{-1}. Degassing was carried out for 30 min, to remove oxygen from the furnace chamber. A blank run was carried out with the empty sample holders in place. This accounted for any changes in gas density with increasing temperature.

Approximately 15 mg of sample was weighed externally before being placed on the horizontal balance in the furnace chamber, as shown in *Figure 4.4*. The weight-loss with temperature was recorded.

4.5 FTIR Analysis

FTIR was carried out to determine the change in the functional groups of the RF xerogels on carbonisation, activation and cleaning of the activated carbons.

The samples were processed into potassium bromide (KBr) discs; the KBr and sample were ground together in a pestle and mortar and formed under 10 bar(g) pressure.

A background spectrum was run. The sample scan rate was set at 4 cm^{-1}, and 5 scans were run per sample. The spectrums were obtained between 4000 – 400 cm^{-1}.

4.6 Nitrogen Adsorption – Desorption at 77K

Nitrogen (N_2) adsorption – desorption at 77K analysis was carried out on a Micromeritics ASAP 2420 Analyser as shown in *Figure 4.5*.

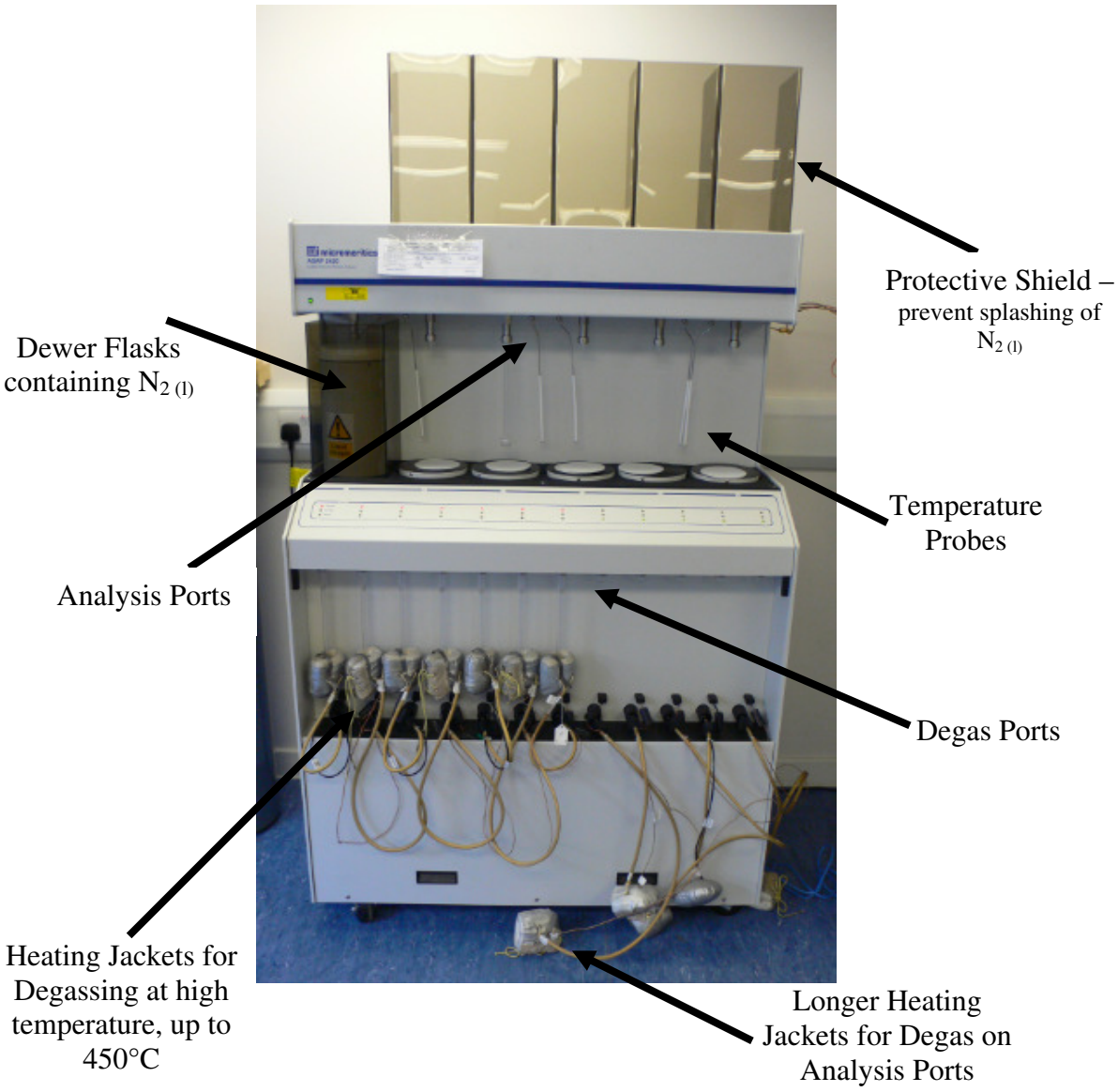

Figure 4.5 – Micromeritics ASAP 2420 Accelerated Surface Area and Porosimetry System

4.6.1 BET Analysis

Adsorption-desorption was carried out between 0.01 – 1.0 P/P_0 to give isotherm data for calculation of BET and BJH surface area and BJH pore size distribution. Calculations were obtained via Micromeritics ASAP 2420 software which was pre-programmed with the equations and parameters required for N_2 analysis using BET, BJH and DA models. To confirm the equations were able to provide an accurate fit to the experimental data, it was ensured the correlation coefficients were >0.99. Samples were analysed twice to ensure consistent results could be obtained and the ASAP 2420 was always maintained within the calibration limits.

Prior to analysis all samples were dried overnight in a vacuum oven at 90 °C. For quick analysis, a sample size equating to no more than 5 m^2 surface area was chosen. As the exact surface area of each sample was not known until after analysis, sample weights were as follows:

Xerogels – 0.2 – 0.25 g

Carbon – 0.1 g

Activated Carbon - <0.1 g

Composite Electrode <0.1 g

The sample was placed into the sample tubes and the samples were degassed (on degas ports shown in *Figure 4.5*) under a slow initial vacuum to 5mmHg, at room temperature, to remove the majority of physically adsorbed molecular species followed by the application of a fast vacuum to 10 μmHg. The samples were held 50 °C for 30 minutes then heated to 90 °C for xerogels and 120 °C for carbons, activated carbons and composite electrodes. The samples were held at the maximum temperature for 3 – 4 hours to remove all physically adsorbed species.

Liquid nitrogen was used as the cooling medium for analysis, contained in the Dewars shown in *Figure 4.5*. Adsorption of nitrogen proceeded from a helium/nitrogen mixture (helium being so far from its critical temperature that physical adsorption does not occur).

A 70-point adsorption-desorption method was used for the characterisations between relative pressures 0.05 – 1.0 – 0.05. The samples were reweighed after degassing to give "dry" sample weight. A filler rod was added to the sample tube after weighing to reduce volume of nitrogen required and therefore speed up

analysis. An isothermal jacket is added to the exterior of the sample tubes to keep temperature constant along the length of the tube.

4.6.2. Micropore Analysis

As the carbon xerogels, activated carbon xerogels and composite electrodes exhibited microporosity in the structure, adsorption-desorption was carried out from 10^{-6} – 1.0 P/P_0 to produce isotherms for the analysis of micropores. Incremental doses of 3 cm^3 g^{-1} were added up to relative pressure 0.05. Once this relative pressure was reached the samples carried on analysis from a relative pressure table between 0.05 – 0.95 – 0.1. Sample weights were as above for the activated carbon xerogel and composite electrode samples. Initial degassing was carried out as for BET analysis in **Section 4.6.1**. A second degassing step was carried out on the analysis ports. This is required for analysis of micropores to ensure that all adsorbed species are removed from the smallest pores and no material is re-adsorbed during transfer of samples from degas ports to analysis ports. The evacuation of the analysis ports was the same as for the degas ports. The samples are then heated to 150 °C and held at this temperature for 2 hours. Samples are not backfilled before analysis is commenced. No filler rods are used for micropore analysis; instead seal frits are added to the top of the sample tubes to prevent any particles from entering equipment under very low vacuum. Isothermal jackets are used as in BET analysis. (NOTE: due to low pressures and, therefore, long pressure stabilisation times involved with micropore analysis, measurements were found to take over 5 days).

4.7 Ball Milling

Milling was carried out using a High Energy Spex SamplePrep 8000M Mixer/Mill, shown in *Figure 4.6.*

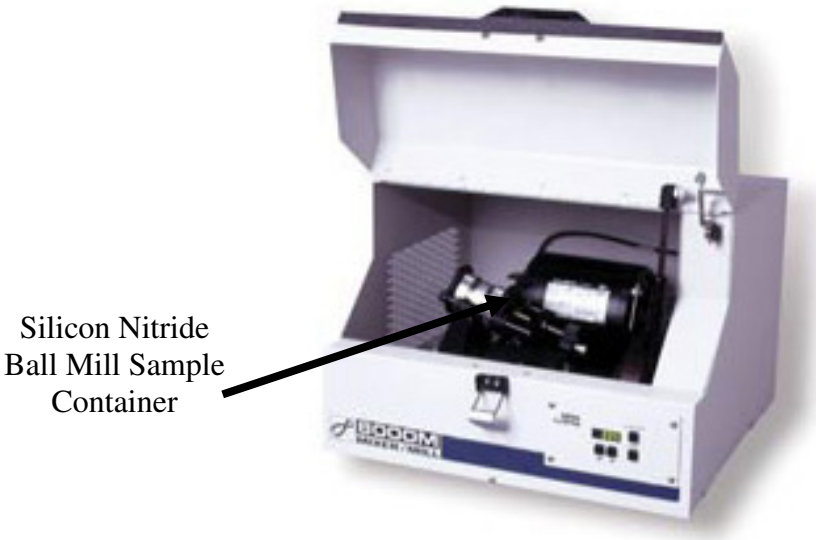

Figure 4.6 - High Energy Spex SamplePrep 8000M Mixer/Mill [187]

4.7.1 Milling of Xerogels

Milling of the xerogel samples was carried out to provide uniform particle size for carbonisation of samples. The silicon nitride ball mill was filled half full of xerogel and the xerogels were milled for 5 minutes.

4.7.2 Milling of Carbon and Activated Carbon Xerogels

As part of the development of the electrodes for EDLC manufacture, a milling study was carried. Ball milling of the samples is required to improve the processability of carbon materials for electrode manufacture, by reducing particle size. However, a side-effect of ball milling is the loss of surface area. This study assessed the effect of milling time on surface area and on particle size for electrode preparation.

Initially 1.5 g of the activated carbon xerogel samples produced from gelation method 1 were milled for 30 minutes. The surface areas were analysed before and

after milling and then electrodes were prepared from activated carbons xerogels from gelation method 1.

The next step was to mill the carbon xerogel samples prior to activation, it was hypothesised that milling prior to activation would impact the surface area less than after activation, as during activation the pore walls become thinner and therefore mechanical strength would be reduced. Two x 2 g samples of carbon xerogel were milled for 30 minutes and 60 minutes. The samples were then activated and electrodes formed. The surface area was measured before and after milling, and after activation. The quality of the electrodes was assessed for EDLC manufacture. The criteria for assessing the electrodes were; uniform film layer, strength of electrode on cutting, and flexibility of electrode discs.

4.8 Electrochemical Double Layer Capacitor Production

In order to produce good quality, reproducible EC results it was necessary to ensure that each step in the production of the final EC test cells was well considered. The first aim was to carry out an Electrode Preparation Study. The aim was to study the effect of electrode composition on the final electrode quality.

4.8.1 Electrode Preparation

The study can be divided into four groups; (1) Stirring Time, (2) Milling Time, (3) Substrate, and (4) Binder Type Variation.

Materials

Active carbon material
Cabot carbon black XC72 (conductivity enhancer)
Kynar® 2801 (binder)
DuPont 30-N PTFE 60% Suspension (binder)
Carboxymethylcellulose (CMC)
Glass microfibre separator
Aluminium foil 30 μm (current collector)

Preparation Procedure

Activated carbon xerogel, carbon black and binder were mixed with 1.5 ml acetone to form a paste, using at magnetic stirrer at 50 rpm. The paste was stirred for 4 hours to ensure the binder was evenly distributed, then spread to form a wet film with the applicator shown in *Figure 4.7* onto a substrate.

The stirring time was varied between 1 – 4 hour(s) to ensure that a completely uniform suspension was created.

To ensure that the activated carbon xerogel particle size was fine enough to form a uniform layer with a low quantity of Kynar 2801, additional studies were carried to look at the effect of milling the carbon xerogel for longer. The milling time of the carbon xerogels was increased from 30 to 60 minutes.

To assess the uniformity of the electrodes produced, the electrodes were studied by eye, looking for gaps in the electrode where light could shine through and the

distribution of weight was assessed by punching 1.33 cm^2 discs. If no light was visible through the electrode film and the weight distribution across the film was minimised to less than 2 mg across the film then this was deemed a uniform electrode.

The Binder Variation and Substrate studies are summarised in *Table 4.1*.

Table 4.1 – Electrode Binder and Substrate Study

Electrode	Composition	Solvent	Stirring Time	Thickness	Substrate
1	• 70% wt ACX– mill 30 min • 30 % wt Kynar 2801 (adapted from University of St. Andrews Battery electrodes)	Acetone	4 hrs	200 μm	Glass Plate
2	• 80% wt ACX– mill 30 min • 10% wt CB XC72 • 10% wt Kynar 2801 [188]	Acetone	4 hr	200 μm	Glass Plate
3	• 90% wt ACX– mill 30 min • 4% wt CB XC72 • 4% wt PTFE (60 % wt dispersion) • 2 % wt CMC [113]	Ethanol	4 hrs	200 μm	Glass plate
4	• 90% wt ACX– mill 30 min • 4% wt CB XC72 • 4% wt PTFE (60 % wt dispersion) • 2 % wt CMC	H_2O	4 hrs	200 μm	Glass plate
5	• 90% wt ACX– mill 30 min • 4% wt CB XC72 • 4% wt PTFE (60 % wt dispersion) • 2 % wt CMC	IPA	4 hrs	200 μm	Glass plate

6	• 90% wt ACX– mill 30 min • 4% wt CB XC72 • 6% wt PTFE (60% wt dispersion)	Ethanol	4 hrs	200 μm	Glass plate
7	• 80% wt ACX – mill 30 min • 10 % wt CB XC72 • 10 % wt Kynar 2801 (same as No. 6)	Acetone	4 hrs	200 μm	Glass plate
8	• 80 % wt ACX – mill 60 min • 10 % wt CB XC72 • 10 % wt Kynar 2801	Acetone	4 hrs	200 μm	Glass plate
9	• 80 % wt ACX– mill 60 min • 10 % wt CB XC72 • 10 % wt Kynar 2801	Acetone	4 hrs	170 μm	30 μm Al foil

4.8.1.1 Final Electrode Preparation Procedure

Electrode Composition:

80% wt ACRF100

10% wt Kynar 2801

10%wt Carbon Black

Procedure:

NOTE: The following method was used to prepare 200mg of electrode material.

160mg ACRF100, 20mg Carbon Black and 20mg of Kynar 2801 were mixed with 1.5 ml acetone to form a paste, using a magnetic stirrer at 50 rpm. The paste was stirred for 4 hours to ensure the Kynar 2801 binder was evenly distributed, then rolled to 170 µm thick film with the applicator shown in *Figure 4.7* onto 30 µm aluminium foil current collector.

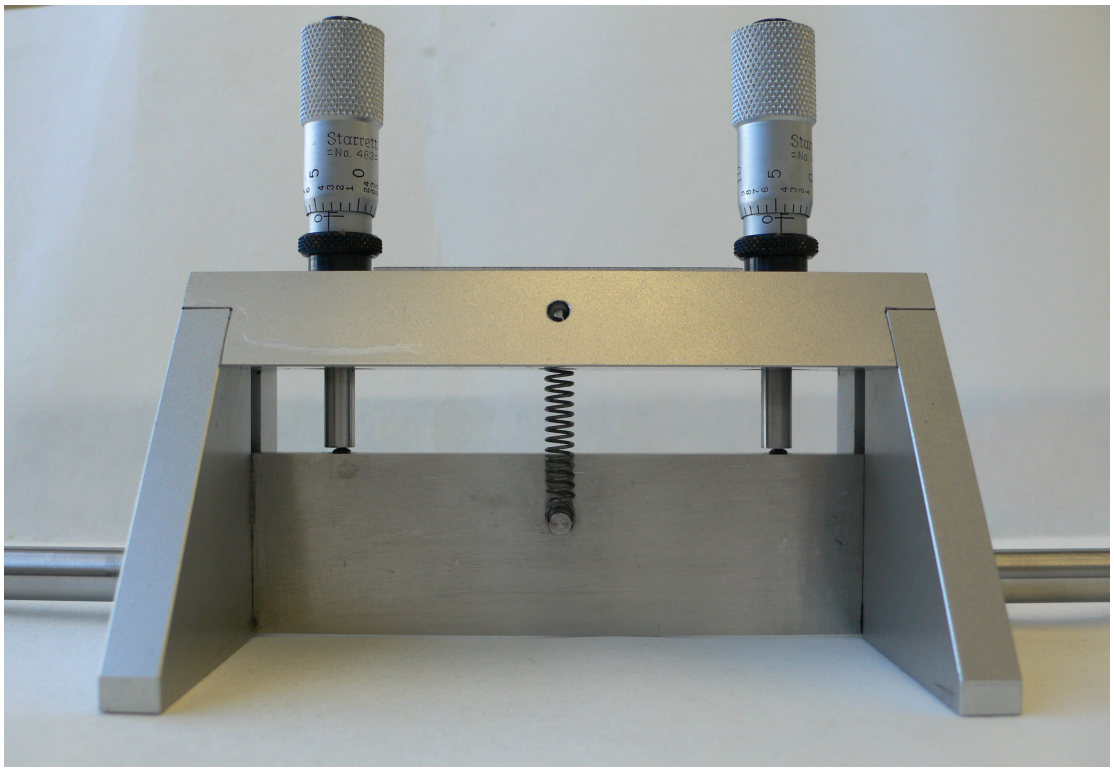

Figure 4.7. Variable thickness electrode slurry applicator.

The electrode was allowed to dry overnight in a vacuum oven at 90 °C. 1.33 cm^2 discs were punched and placed in a glove box under argon for EDLC preparation. To ensure reproducibility of the EC measurements, electrode weight was kept at 2.5 mg (excluding current collector weight). 1.33 cm^2 discs of separator were also punched.

4.8.2 Electrolytes

Room Temperature Ionic Liquid Electrolytes

- 1-ethyl-3-methylimidazolium tetrafluoroborate ($EMImBF_4$) [Sigma-Aldrich ≥99%],
- 1,2-dimethyl-3-propylimidazolium bis(trifluoromethylsulfonyl)imide (DMPImTFSI) [Sigma Aldrich ≥ 98%],
- 1-ethyl-3-methylimidazolium dicyanamide ($EMImN(CN)_2$) [Merck ≥ 97%]
- 1-butyl-3-methylpyrrolidinium tris(pentafluoroethyl)trifluorophosphate ($BMPyTf_5Et_3PF_3$) [Merck ≥ 97%].

Room temperature ionic liquid electrolytes were used as received.

Organic Electrolyte Preparation

1 Molar solution of Tetraethylammonium Tetrafluoroborate (Et_4NBF_4) was prepared as follows:

Materials

1. Et_4NBF_4 salt 99% Electrochemical grade Sigma Aldrich
2. Propylene carbonate 99.8%

Both procured from Sigma-Aldrich.

1.085 g of Et_4NBF_4 was dissolved in 5 ml of propylene carbonate under an argon atmosphere in the glove box.

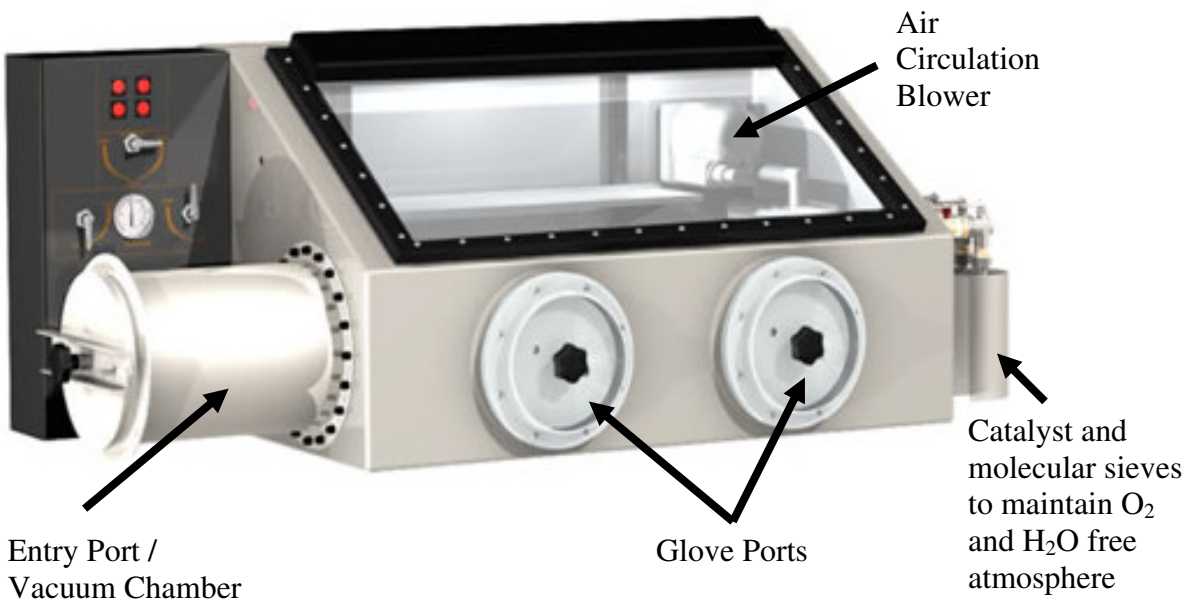

Figure 4.8 – Saffron argon atmosphere glove box

4.8.3 EDLC test cell production

All EDLC production was carried out in a glove box under argon. Two electrodes with the glass microfibre separator were placed into the sandwich type test cell shown in *Figure 4.9.* After placement of first electrode into test cell, the separator was added and soaked in electrolyte. After the addition of the second electrode the base plate was pressed in place to ensure contact between electrodes and separator. The test cell was reopened and placed under vacuum to remove gas from the pores and allow the electrolyte to enter the electrode structure. To ensure the test cells were sealed from the air during measurements they were covered in a layer of Parafilm. All EC test cells were repeated 3 – 6 times. The measurements for RF100-1 – RF200-1 were also repeated from initial gel preparation (**Section 4.1**) through to the EC test cell production, to ensure reproducibility of EC test cells studied. The variation in results was used for error calculations.

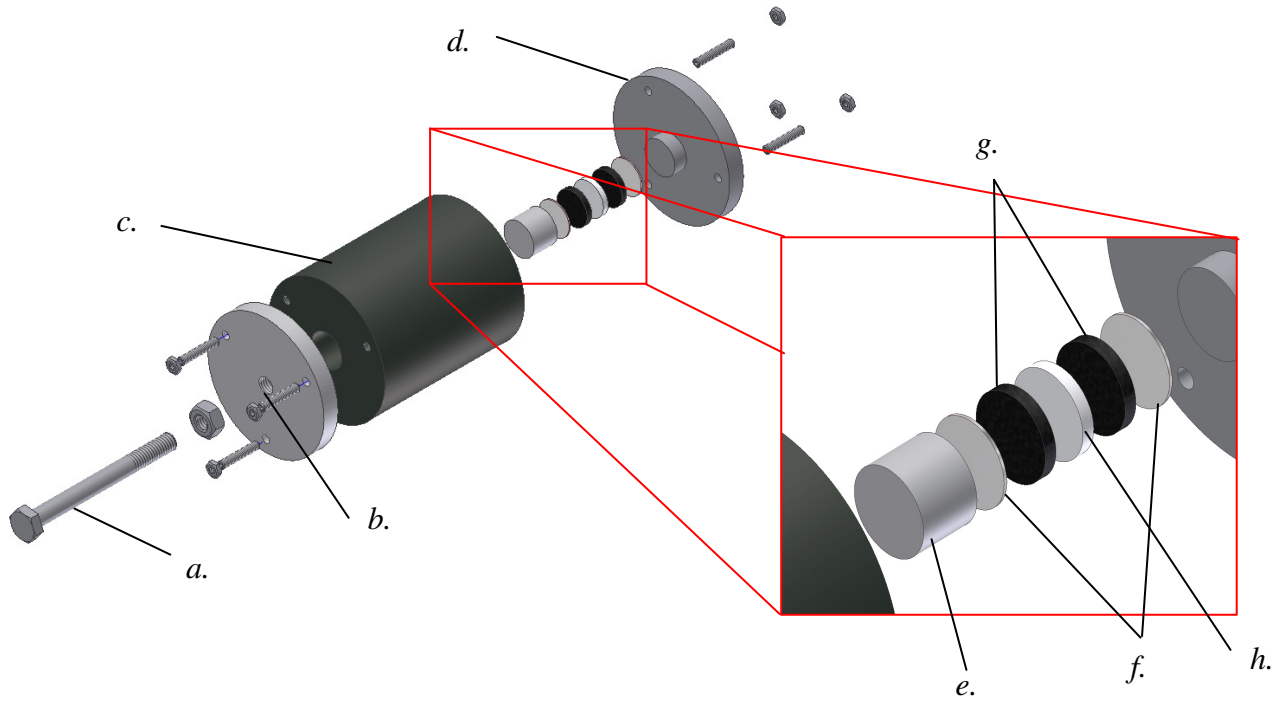

Figure 4.9 – Sandwich type symmetric capacitor cells were constructed with a pair of carbon electrodes (g) on aluminium foil (f) and a glass microfibre separator (h). The test cells consisted of an insulating PTFE body (c) that is resistant to corrosion by the electrolytes. The current collectors (d & e) are stainless steel with the upper current collector being controlled by a stainless steel plunger (a) which is sealed with a PTFE screw seal (b). The plunger moved independently from the current collector to prevent damage to the electrodes when tightened. Designed courtesy of Professor R. Slade of the University of Surrey.

4.9 Electrochemical Characterisation

For all electrochemical measurements one electrode of the capacitor was used as the positive electrode and the other as the negative electrode. The tests were carried out on Solartron Analytical 1400 Cell Test System, shown in *Figure 4.10*.

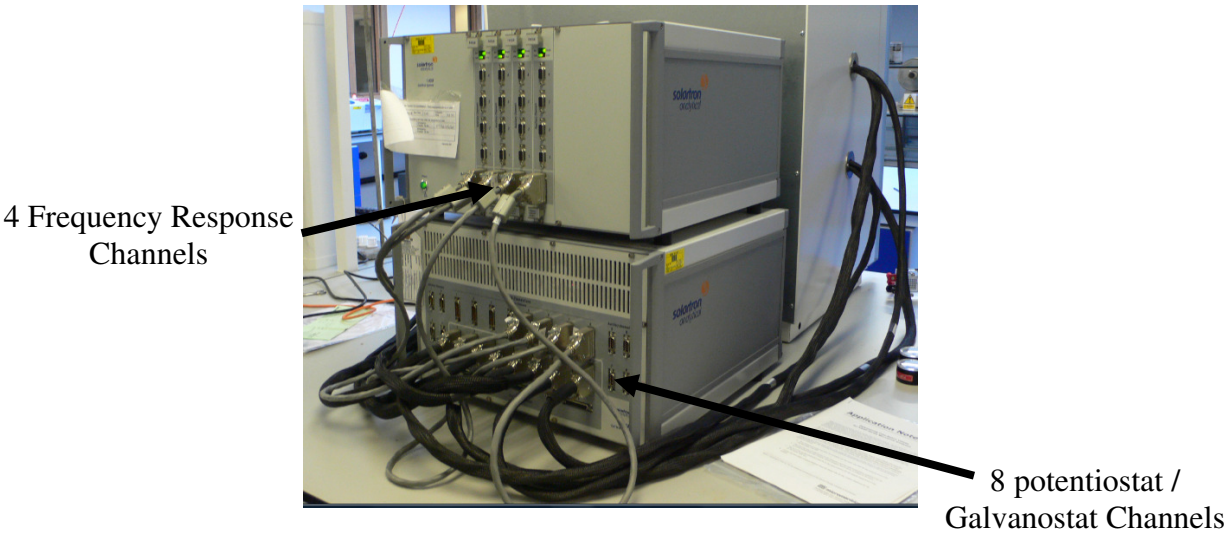

Figure 4.10 - 1470E Multichannel Potentiostat / Frequency Response Analyser

4.9.1 Electrochemical Stability Window (ESW) Measurement

The electrochemical stability window (ESW) of each electrolyte was determined by carrying out cyclic voltammetry. The electrodes were made as in **Section 4.8.1,** however, the active carbon material was replaced with a non-porous carbon xerogel. The use of carbon xerogel accounted for the difference between the composite electrodes used for EC measurements and the working electrodes used for the determination of ESW in the literature (as discussed in **Section 3.6**). Non-porous electrodes were used to prevent the increase in current (due to electrolyte decomposition) being disguised by the high ESR of porous electrodes. Cyclic voltammetry was carried out at a scan rate of 10 mV s^{-1} between 0 to 6 V vs. open circuit.

4.9.2 Galvanostatic Charge – Discharge (GC)

The EDLC test cells were constructed as above and were charged to V_{max} at 2, 4, 8, 16, 32, and 64 mA cm^{-2} and the time for charge-discharge for each cycle was recorded. The voltage range was set according to the upper voltage limit of the electrolyte determined from EC Window measurement. Specific capacitance of the electrode was obtained from $C = (I \times t) / (W \times \Delta V)$ where I is the discharge current, t is the discharge time, W is the mass of active material in one electrode, and ΔV is the potential difference during discharge.

4.9.3 Cyclic Voltammetry

The EDLC test cells were cycled 20 times between 0.2 and – 0.2 V vs open circuit potential at scan rates of 5, 10 and 25 mV s^{-1}. The current induced was measured for each cycle.

4.9.4 Electrochemical Impedance Spectroscopy

The electrochemical impedance spectrum was measured in the frequency range 100 kHz – 10 mHz. An AC amplitude of 10mV and a DC potential of 100 mV were applied. The specific capacitance can be calculated from the impedance plots according to $C = -1/(2\pi f \times Z'' \times m)$, where f, Z'' and m are the frequency, the imaginary impedance, and the mass of active material, respectively. The value of frequency dependant specific capacitance for the cell was derived at 0.01 Hz. The ESR is measured at 1 kHz.

4.9.5 Self – discharge Measurement

The self-discharge was measured by charging up to the full operating voltage for each electrolyte (as defined in *Table 6.1* in **Section 6.1**), via constant current charging at 2 mA cm^{-2}. The test cell is then switched to Open Circuit, where no current is applied, and the voltage recorded for 24 hours. The voltage lost over this period is used to determine the self-discharge rate for the electrode/electrolyte system.

5.0 Surface Area and Pore Size Distribution Characterisation

5.1 Variation in Gelation

From the literature [58,59] it was identified that two gelation methods have been utilised for the production of resorcinol-formaldehyde gels for use in EC manufacture. Each gelation method followed a different temperature profile. To determine the effect of varying the gelation temperature on the resultant xerogel, carbon and activated carbons, the variation in gelation time, and the resultant hydrogel characteristics were studied. The variation in hydrogel structure was studied qualitatively, by examining the colour and stiffness of the hydrogels.

The gelation time for the xerogels produced via method 1 was fast, with the start of gelation occurring within 1 hour of holding at 90 °C and full gelation having taken place after 24 hours. The gelation for method 2 did not appear to take place until the sample temperature was increased from 25 °C to 60 °C. After 24 hours at 25 °C the solution had changed from a colourless solution to a uniform, transparent, yellow/brown solution. Full gelation had occurred after 24 hours at 60 °C. No further gelation appeared to occur after the temperature was turned up to 80 °C.

On increasing the R/C ratio, for both methods, it was found that the resultant hydrogel structure changes. For method 1, at R/C 100 the hydrogels are hard transparent red ‘jelly-like’ monoliths, and the hydrogels remain the same colour up to R/C 400, however, the stiffness of the monoliths reduces as the R/C ratio is increased. The colour of the hydrogels changes at R/C 500 where it changed to a lighter, opaque, orange with the texture of soft rubber. R/C 750 had the same colour and texture, but was again softer than R/C 500. Gelation did not occur above R/C 750 for method 1. The hydrogels produced via method 2, followed the same pattern, however all gels were softer than the method 1 counterpart. For method 2, gelation occurred to a limited extent at R/C 1000 and 1500. The hydrogels produced were dark opaque orange, powdery in texture, with very low water content, and yielded 70% less xerogel over the other R/C ratios.

The reduction in stiffness with increasing R/C ratio indicates that the degree of cross-linking decreases with increasing R/C ratio, which is consistent with that found in the literature. [50,189] The implications for EC manufacture due the reduction in stiffness will be discussed further in **Section 5.3 Ball Milling Study**.

5.2 Effect of Catalyst Ratio on Resultant Xerogel, Carbon and Activated Carbon Structure

It has been assumed in this study that the parameters applied in the computation of the BJH pore size distribution are equally applicable to the xerogels, carbons and activated carbons. However, as the primary objectives were to compare the effects of production parameters on the resultant pore structure of the xerogels and the effects of carbonisation and activation on the pore structure of the carbons. Comparisons between the gels and carbons are purely qualitative in nature and as such are not affected by pore model parameters.

5.2.1 Resorcinol – Formaldehyde Xerogels

The aim of this section was to study the influence of the gelation method and catalyst ratio on the porous structure of the resorcinol-formaldehyde xerogels, carbon and activated carbons. To determine the surface area and pore size distributions of the porous materials produced, N_2 adsorption-desorption at 77K was carried out on Micromeritics ASAP 2420. The surface area and pore size distribution were determined using the BET and BJH equations through Micromeritics ASAP 2420 standard software. The adsorption-desorption isotherms for the xerogels, carbon xerogels and activated carbon xerogels are shown in *Figures 5.1 – 5.2, 5.5 – 5.6,* and *5.9 – 5.10*, respectively. The BJH pore size distributions are shown in *Figure 5.3 – 5.4, 5.7 – 5.8 and 5.11 – 5.12*, respectively. The surface area, pore volume, and average pore diameters are summarised in *Tables 5.1 – 5.3*.

It is known from the literature [43,189] that the structure of resorcinol-formaldehyde xerogels can be controlled by varying the reactant ratios, the largest effect of which is for varying the resorcinol to catalyst ratio (R/C). In this study the aim was to determine the effect of varying pore size on EC performance; to do this the catalyst ratio was increased from R/C 100 to R/C 750.

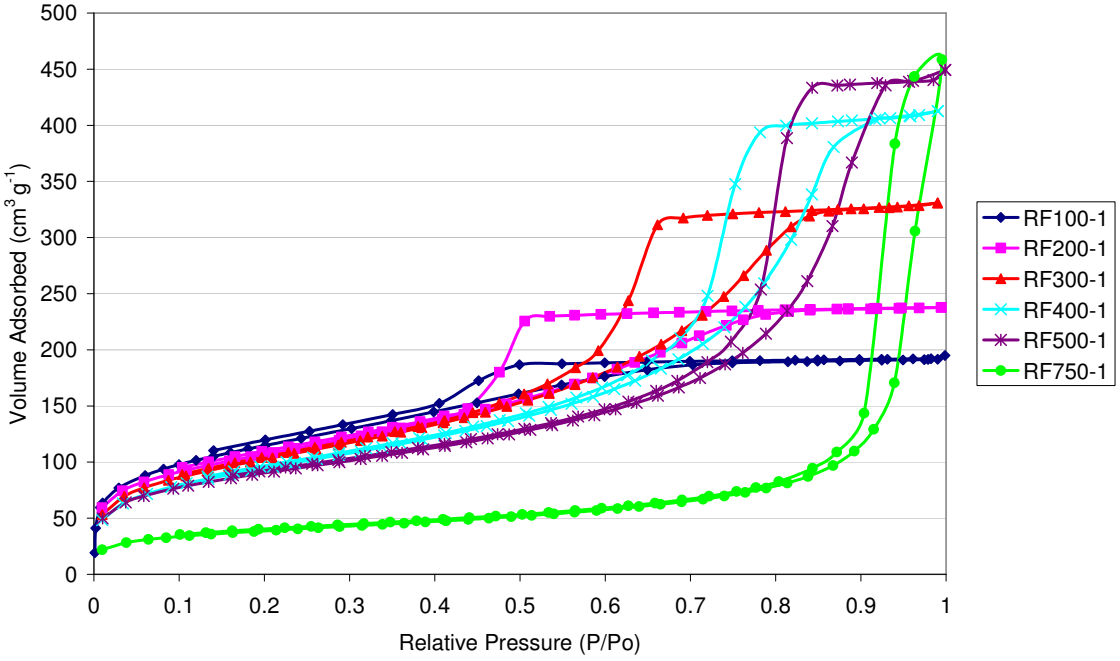

Figure 5.1 – Xerogel Method 1 - Adsorption – desorption Isotherms at 77K

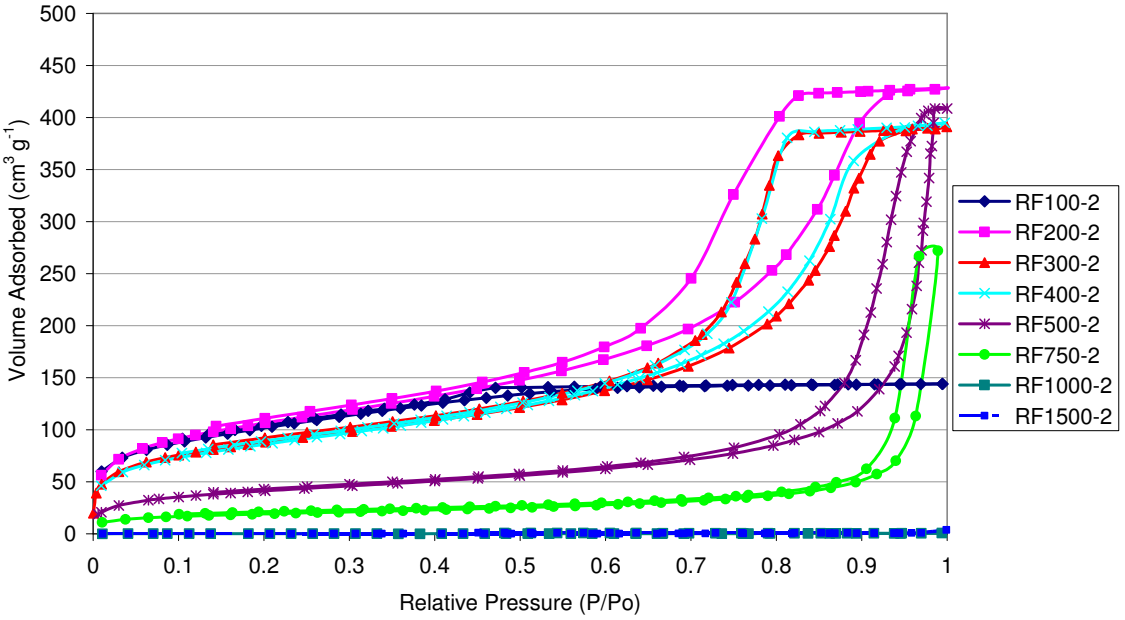

Figure 5.2 – Xerogel Method 2 - Adsorption – desorption Isotherms at 77K

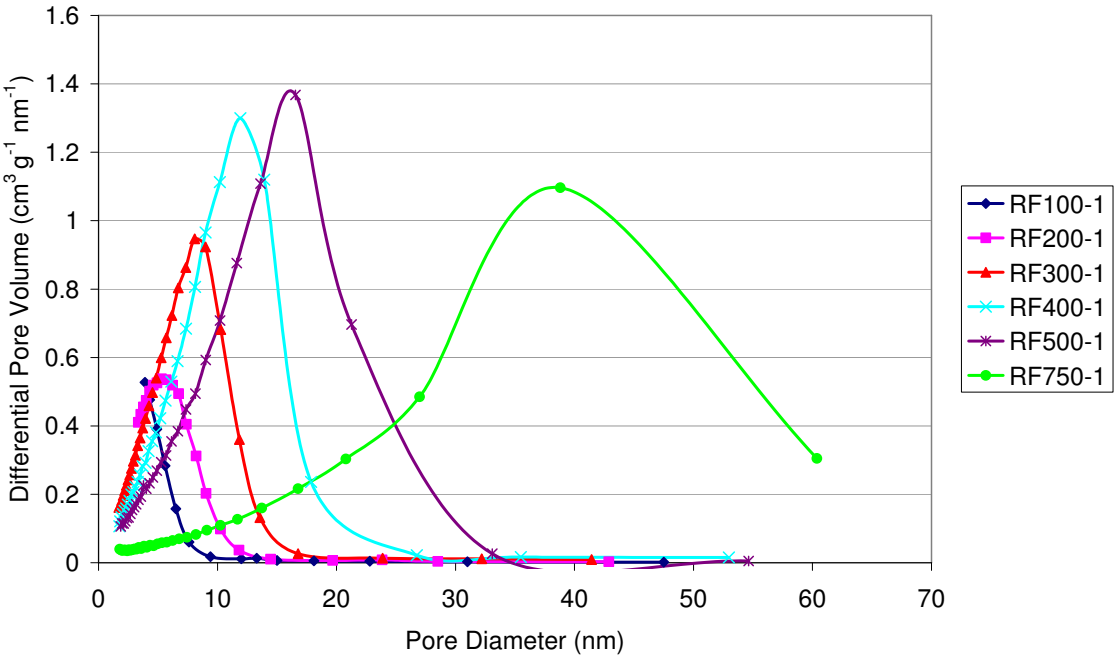

Figure 5.3 – Xerogel Method 1 –Pore Size Distributions

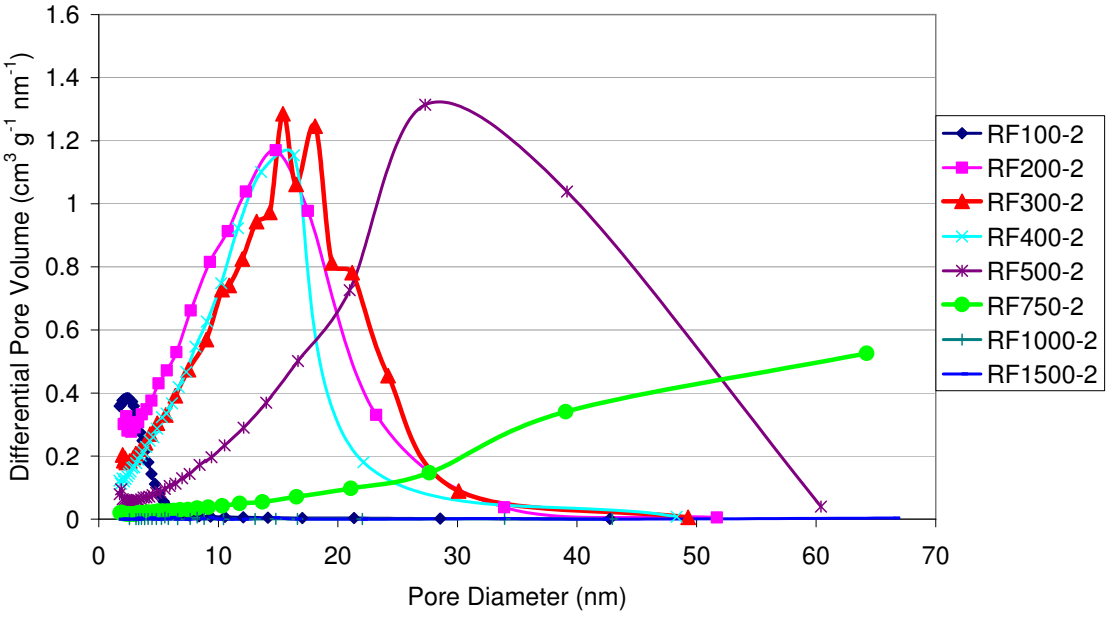

Figure 5.4 – Xerogel Method 2 –Pore Size Distributions

The results in *Figures 5.3 and 5.4* and *Table 5.1* demonstrate that with an increase in R/C ratio for both gelation methods, the volume of micropores was reduced and the volume and size of mesopores increased. The surface area increased between R/C 100 and R/C 200 before decreasing with increasing R/C ratio. The isotherms for RF100-1 and RF100-2 exhibit the highest absorbed volume of N_2 at relative pressures below 0.4. This indicates the xerogels with the highest volume of micropores. The isotherms exhibit a very small hysteresis loop at pressures above 0.4 indicating a small volume of the porous structure was made up of mesopores 0.151 and 0.14 cm^3 g^{-1}, respectively. The isotherms follow a Type IV isotherm with lower adsorption at low relative pressures and a higher volume N_2 adsorbed and a hysteresis loop at higher relative pressures (see **Section 3.2.2** and **Footnote 6**). [149-151], [6] The isotherms, for both gelation methods, demonstrate that as R/C ratio was increased the volume N_2 adsorbed at lower relative pressures was reduced. That is, the volume of micropores was reduced with increasing R/C ratio, with the largest drop in volume occurring between R/C 500 and R/C 750. The hysteresis loop continues to move to higher relative pressures for R/C 200 – 750 indicating an increase in the size of mesopores making up the structure. For method 1, the volume adsorbed at higher relative pressures also increased indicating an increase in the pore volume. For method 2, the volume adsorbed at higher relative pressures marginally changes for samples RF300-2 – RF500-2, indicating the pore volume was not influenced to the same extent by R/C ratio as with method 1, this may be due to the presence of larger mesopores. A decrease in the volume adsorbed occurred for method 2 RF750-2, indicating a decrease in mesopore volume. The isotherm for RF750 (for both gelation methods) exhibits a depressed hysteresis loop indicating that some of the pores are out with the limits of the analysis and extend into the macroporous range. The hysteresis loops can be further divided into types (as outlined in **Section 3.2.2**).

The hysteresis loops for the RF xerogels method 1 RF100-1 – RF500-1 and method 2 RF100-2 – 400-2 follow the Type H2 hysteresis for adsorbents with complex pore structures made up of interconnected networks of pores of varying size and shape

[6] Hysteresis loops occur for multilayer adsorption and can be associated with capillary condensation. This is where higher pressures are required to fill the pores with adsorbent than that at which desorption occurs.

and/or ink-bottle pores. For xerogels method 1 RF750-1, and method 2 RF500-2 and RF750-2, the hysteresis loops change to Type H3, which occur for aggregates of plate-like particles and/or slit shaped pores. [165] From *Table 5.1* it can also be seen that as the (R/C) ratio was increased, the average pore size and the width of the pore size distribution (*Figures 5.3 and 5.4*) of the RF xerogels gradually increases. This change in structure coupled with the change in hysteresis suggests that cross-linking is reduced with increasing R/C ratio. This reduction in cross-linking may be related to the polymerisation process that forms the RF hydrogels. The reaction mechanism occurs in two stages; first the catalysed addition of resorcinol to formaldehyde and second the condensation of hydroxyl-methyl derivative. [189] The catalyst aids in the ionisation of the resorcinol molecules, and therefore, the formation of the monomer groups of resorcinol and formaldehyde. These monomers cross-link to form nanometre size clusters, which make up the final hydrogel. The degree of cross-linking and final cluster size is also affected by the concentration of catalyst. When the R/C ratio is low (i.e. high catalyst concentration) the two stage reaction proceeds quickly resulting a large number of small diameter clusters. When the R/C ratio is high (i.e. low catalyst concentration) the reaction proceeds slowly, resulting in the formation of fewer clusters. As there are fewer clusters attracting the monomers as they are created, these clusters are able to grow, resulting in large particle formation. Therefore, decreases in the catalyst concentration result in less cross-linkage and a more disordered structure which could result in plate-like particles as opposed to more spherical particles that may be formed at low R/C ratio. [50,191] This is consistent with that found by Horikawa *et al.* [57] where on increasing R/C ratio from 200 to 1000 it was found via small angle x-ray scattering (SAXS) that the primary particles changed from being spherical to disc shaped.

Both gelation methods follow the same incremental increase in pore size for increasing R/C ratio up to R/C 750, however, the xerogels produced via method 2 resulted in a less ordered structure with wider pore size distributions and higher average pore size at each equivalent R/C ratio than that obtained for method 1. This indicates that the longer gelation time reduces the degree of cross-linkage and the lower temperature slows cluster formation leading to a less ordered structure. The surface areas for R/C 100 and R/C 200 for method 2 are comparable to that obtained

for method 1 (within the experimental error), above R/C 200 the surface area, for method 2, continually reduces further below that of the method 1 equivalent. The surface area for method 2 RF500-2 and RF750-2 is 50% lower than that of method 1 RF500-1 and RF750-1. The lack of variation in surface area for R/C 100 and R/C 200 indicates that for low R/C ratio the catalyst concentration is sufficiently high to overcome the effects of a slower gelation time. Although gelation had occurred for method 2 at R/C 1000 and R/C 1500, the xerogels produced are non-porous and the yield was 70 % lower. This indicates that few clusters were formed and the concentration of monomers was too low to facilitate particle growth.

Table 5.1 – Surface Area and Pore Size Characterisation of Xerogels

Sample	$S A_{BET}$ ± 10 ($m^2 g^{-1}$)	$P V_{Total}$ ± 0.02 ($cm^3 g^{-1}$)	$PV_{micropore}$ ± 0.02 ($cm^3 g^{-1}$)	$PV_{mesopore}$ ± 0.02 ($cm^3 g^{-1}$)	% Micropore	% Mesopore	D_{av} ± 0.1 (nm)
Gelation Method 1							
RF100-1	355	0.175	0.024	0.151	13.4	86.6	2.7
RF200-1	380	0.318	0.013	0.305	4.1	95.9	4.0
RF300-1	370	0.538	0.016	0.522	3.0	97.0	6.2
RF400-1	315	0.668	0.018	0.650	2.7	97.3	9.1
RF500-1	265	0.744	0.021	0.724	2.8	97.2	12.5
RF750-1	135	0.700	0.012	0.688	1.8	98.2	25.0
Gelation Method 2							
RF100-2	350	0.159	0.019	0.140	11.9	88.1	2.2
RF200-2	385	0.699	0.017	0.682	2.4	97.6	6.7
RF300-2	310	0.625	0.018	0.605	2.9	97.1	8.4
RF400-2	305	0.580	0.010	0.570	1.8	98.2	8.1
RF500-2	150	0.632	0.008	0.624	1.3	98.7	17.0
RF750-2	65	0.417	0.007	0.410	1.7	98.3	32.0
RF1000-2	0.26	0.001	-	0.001	0	100	14.9
RF1500-2	0.31	0.006	-	0.006	0	100	32.3

5.2.2 – Carbon Xerogels

Figures 5.5 – 5.6 and 5.7 – 5.8 show the N_2 adsorption-desorption isotherms and pore size distribution, respectively, for methods 1 and 2 carbon xerogels. The surface area, pore volume, and average pore diameters are summarised in *Table 5.2*.

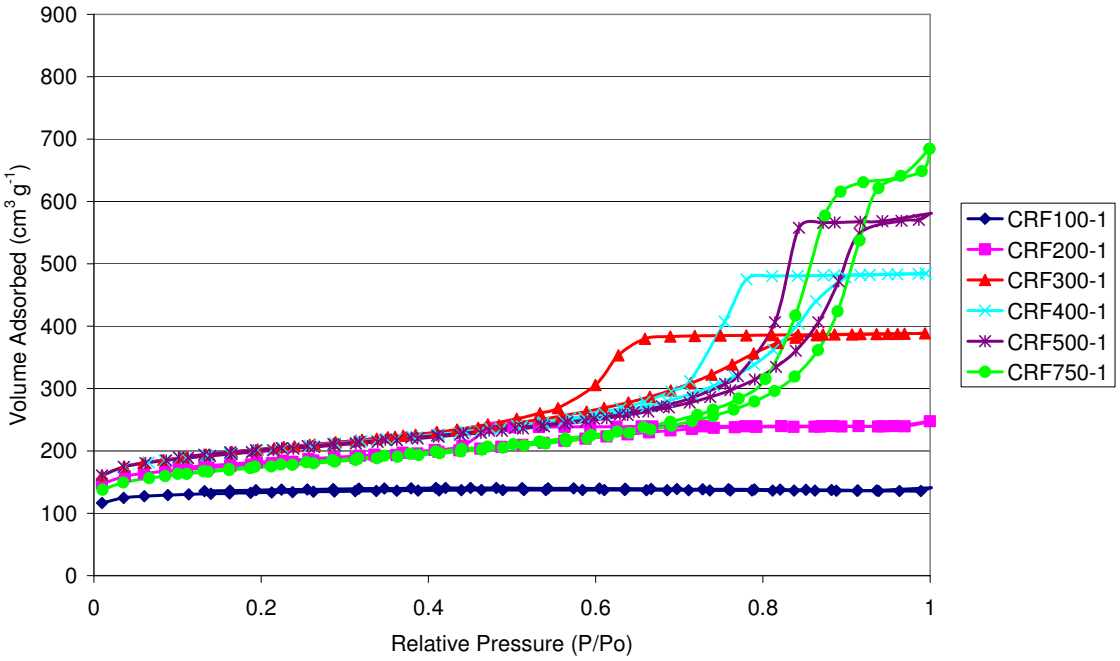

Figure 5.5 – Carbon Xerogel Method 1 - Adsorption – desorption Isotherms at 77K

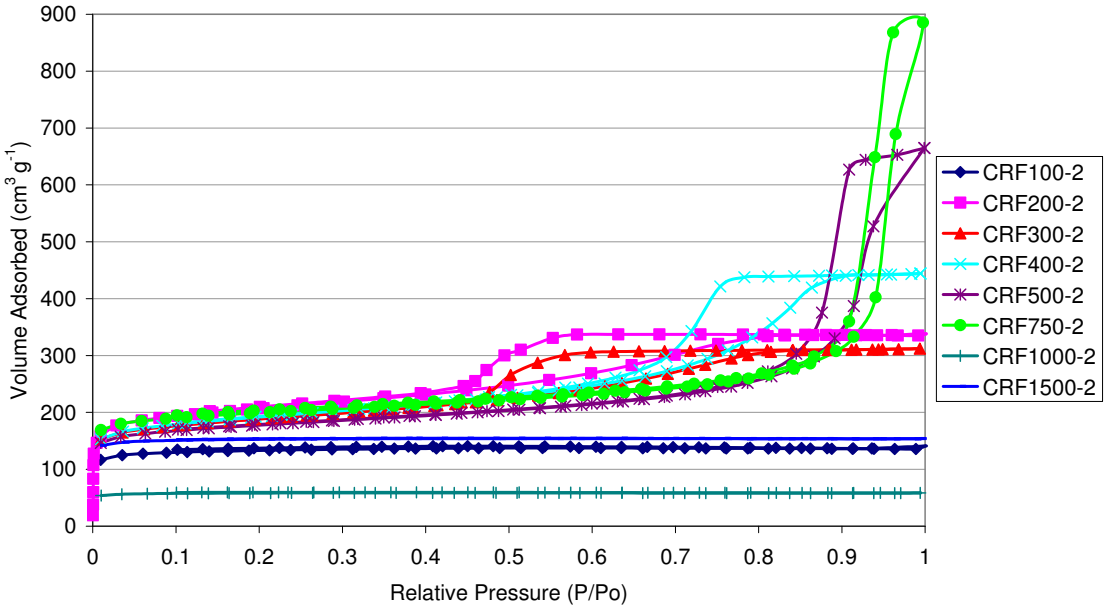

Figure 5.6 – Carbon Xerogel Method 2 - Adsorption – desorption Isotherms at 77K

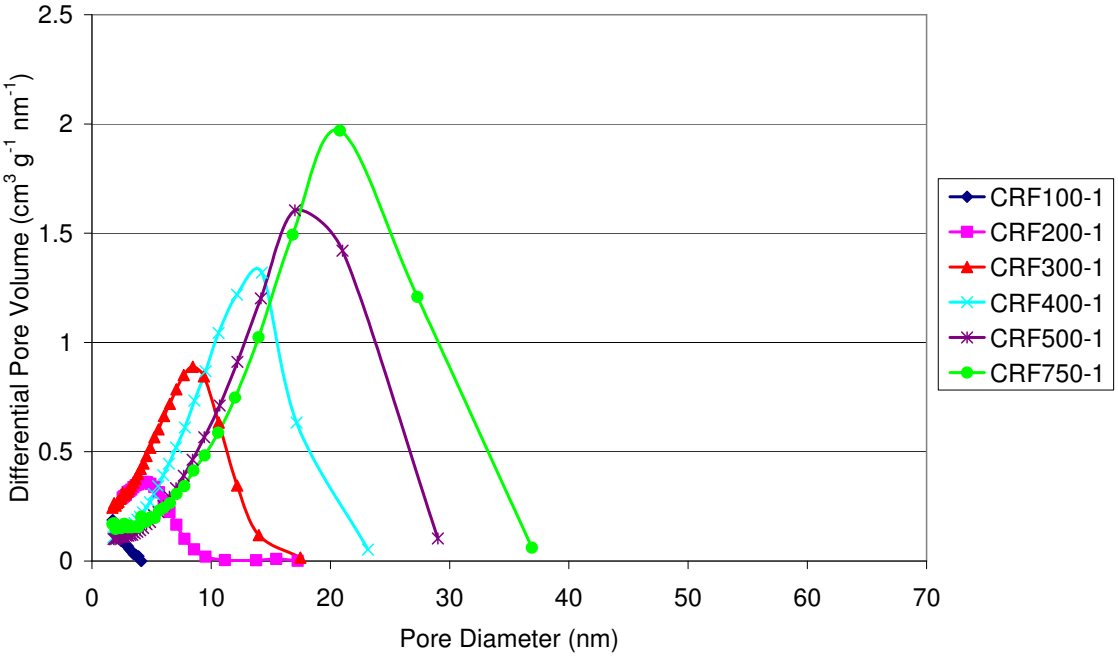

Figure 5.7 – Carbon Xerogel Method 1 –Pore Size Distributions

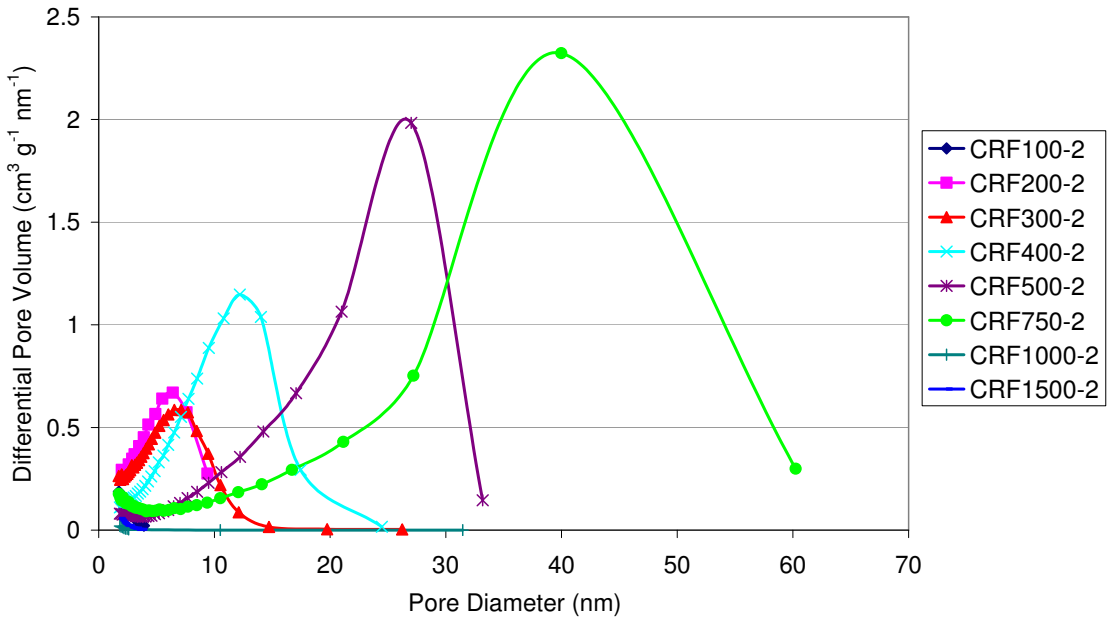

Figure 5.8 – Carbon Xerogel Method 2 –Pore Size Distributions

On carbonisation the functional groups in the RF xerogel structure are removed, enriching carbon and creating microporosity in the structure. [22,191] This was most apparent for CRF1000-2 and CRF1500-2 produced via gelation method 2, where the initial xerogels were non-porous and on carbonisation the surface area increased to 175 and 462 $m^2 g^{-1}$, respectively. The walls of the mesopores in the structure appear to be widened with largest mesopores being burned away leading to a smoothing effect which results in a narrower pore size distribution. For gelation method 1 the peak in surface area occurs at 655 $m^2 g^{-1}$ for CRF300-1 and for gelation method 2 the peak occurs at 650 $m^2 g^{-1}$ for CRF500-2. This indicates a further difference in the structures of the carbons produced via the two different gelation methods. A higher pore volume is reached for method 2 of 1.229 $cm^3 g^{-1}$ compared with 0.951 $cm^3 g^{-1}$ for method 1; however the pore size distribution is still wider for method 2 than for method 1.

The isotherms for CRF100-1 and CRF100-2 now follow a Type I isotherm for microporous solids, with most of the mesoporosity having been removed during carbonisation. Although a large volume of microporosity has been created in the structure, the removal of the mesoporosity leads to only a small increase in the surface area. The isotherms for CRF1000-2 and CRF1500-2 also follow the Type I isotherm. The isotherms for CRF200 – CRF750 (for methods 1 and 2) continue to exhibit the mesoporous Type IV isotherm. The hysteresis loops become depressed due to the increased volume N_2 adsorbed at lower relative pressure, due to the increase in the microporosity.

The largest difference in surface area occurs for method 2 CRF750-2, where the BET surface area increases from 65 $m^2 g^{-1}$ for the xerogel to 630 $m^2 g^{-1}$ for the carbon. The new microporosity is the main contributor to surface area, while the increase in pore volume from 0.417 to 1.392 $cm^3 g^{-1}$ can be attributed to the mesoporosity.

As R/C ratio increases the micropore volume only increases marginally by comparison with the mesopore volume. The main reason for this is micropores don't contribute to pore volume to the same extent mesopores do, therefore, increases in microporosity result in an increase in surface area without significant increases to pore volume. The mesopore volume increases with increasing R/C ratio; that is, the

carbon xerogels go from predominantly microporous at R/C 100 to predominantly mesoporous at R/C 750. The increase in volume for each increase in R/C ratio is a result of the increase in pore size.

Table 5.2 – Surface Area and Pore Size Characterisation of Carbon Xerogels

Sample	$S A_{BET}$ ± 5 ($m^2 g^{-1}$)	PV_{Total} ± 0.02 ($cm^3 g^{-1}$)	$PV_{micropore}$ ± 0.02 ($cm^3 g^{-1}$)	$PV_{mesopore}$ ± 0.02 ($cm^3 g^{-1}$)	% Micropore	% Mesopore	D_{av} ± 0.1 (nm)
Gelation Method 1							
CRF100-1	410	0.212	0.176	0.036	83.2	16.8	2.2
CRF200-1	615	0.424	0.197	0.227	42.4	53.6	3.5
CRF300-1	655	0.637	0.178	0.459	27.9	72.1	4.9
CRF400-1	640	0.788	0.184	0.604	23.4	76.6	6.9
CRF500-1	640	0.918	0.189	0.729	20.6	79.4	8.9
CRF750-1	580	0.951	0.219	0.732	23.0	77.0	16.0
Gelation Method 2							
CRF100-2	707	0.527	0.188	0.339	35.7	64.3	4.4
CRF200-2	670	0.962	0.188	0.774	19.5	80.5	3.9
CRF300-2	605	0.510	0.177	0.333	34.6	65.4	4.3
CRF400-2	640	0.685	0.174	0.511	25.4	74.6	7.2
CRF500-2	650	1.229	0.210	1.019	17.1	82.9	9.8
CRF750-2	630	1.392	0.222	1.170	16.0	84.0	20.7
CRF1000-2	175	0.088	0.085	0.003	96.6	3.4	2.1
CRF1500-2	460	0.228	0.223	0.005	97.8	2.2	2.1

5.2.3 Activated Carbon Xerogels

Figures 5.5 – 5.6 and 5.7 – 5.8 show the N_2 adsorption-desorption isotherms and pore size distribution, respectively, for methods 1 and 2 carbon xerogels. The surface area, pore volume, and average pore diameters are summarised in *Table 5.3*.

While the purposes of carbonisation was to enrich the carbon content, create initial porosity, and begin the process of creating an ordered structure, by removing volatiles from the structure, activation is used to enhance the porosity and remove disordered carbon from the structure. Activation carves away at the carbon surface, widening existing pores and opening any closed porosity that exists in the carbon structure. The carving away of pore walls results in the loss of larger pores where the carbon walls are thinner. [191] Activation leads to the carbon structure becoming more ordered, thus enhancing the conductivity, essential for use as EC electrodes.

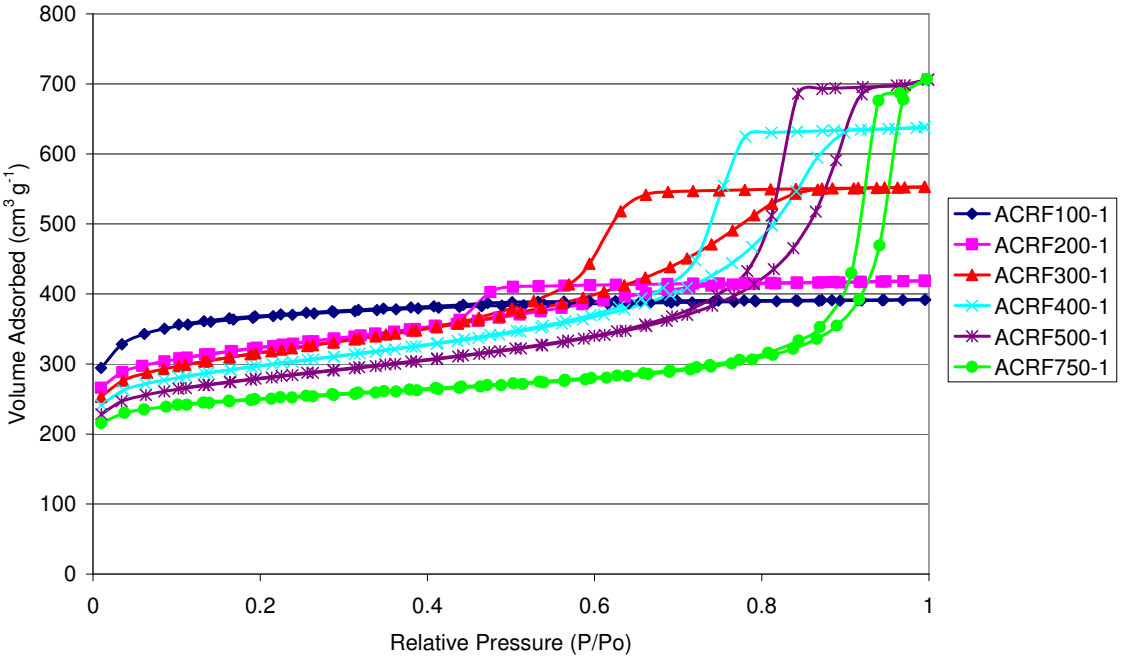

Figure 5.9 – Activated Carbon Xerogel Method 1: Adsorption – desorption Isotherms at 77K

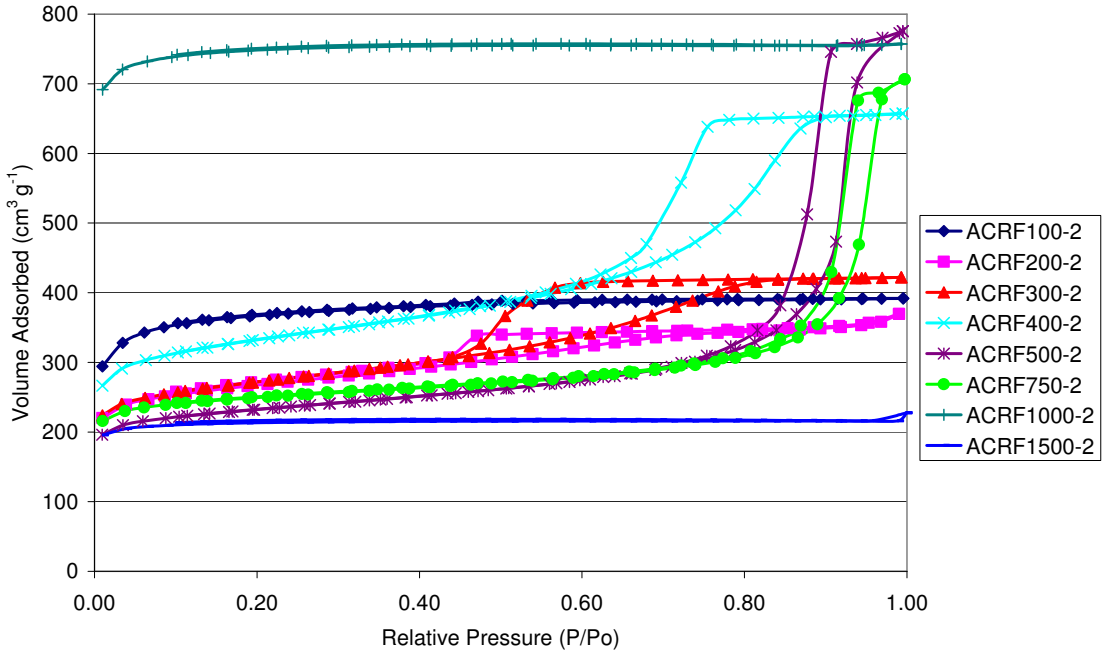

Figure 5.10 – Activated Carbon Xerogel Method 2 - Adsorption – desorption Isotherms at 77K

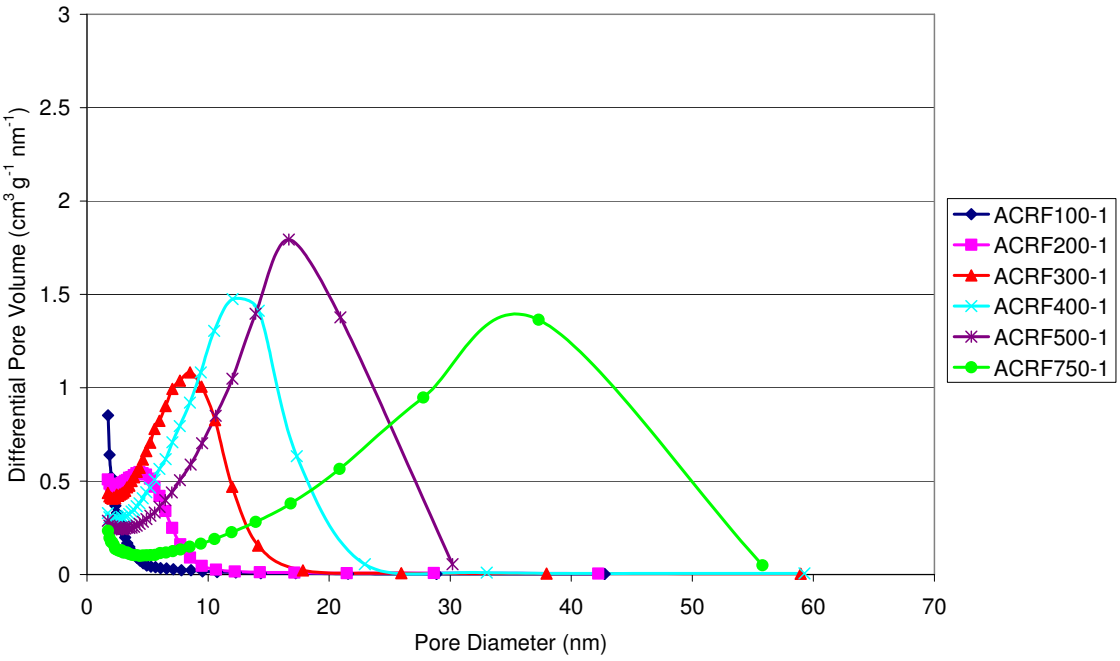

Figure 5.11 – Activated Carbon Xerogel Method 1 –Pore Size Distributions

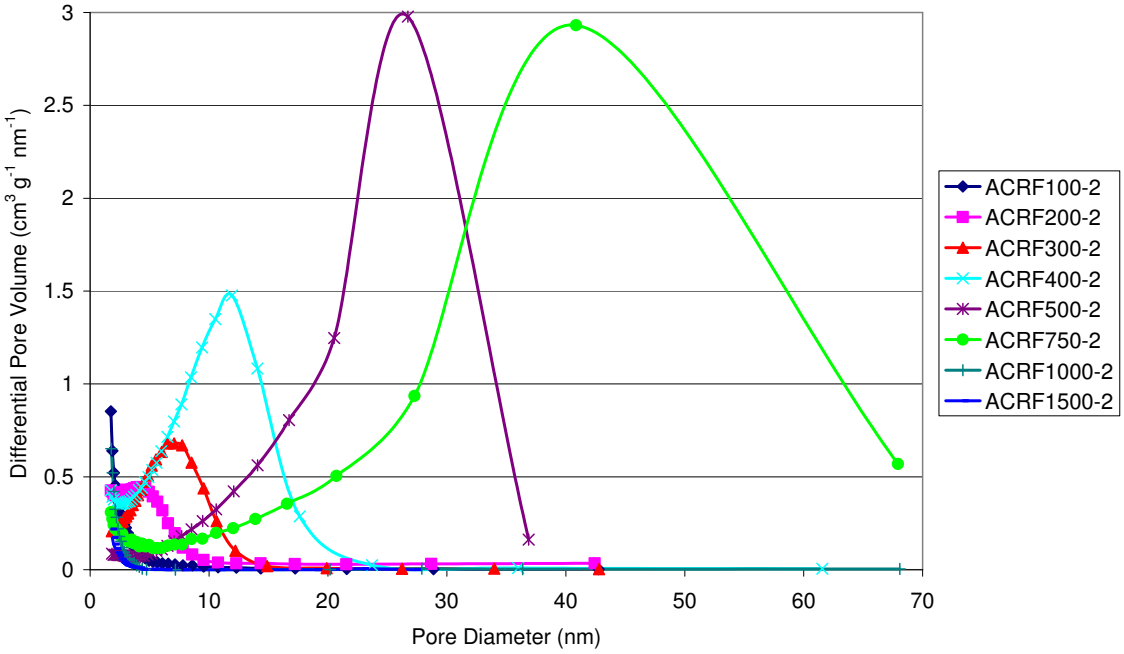

Figure 5.12 – Activated Carbon Xerogel Method 2 –Pore Size Distributions

The volume of N_2 adsorbed increases over the full range of relative pressures, indicating both micro- and mesoporosity have been enhanced for all of the activated carbon samples. Microporosity is enhanced due to the opening of closed porosity, and mesoporosity due to the widening of the existing pores. A large increase in surface area and total pore volume occurs for all samples.

The isotherms for methods 1 and 2 – ACRF100 still follow the Type I isotherm for microporous materials with no hysteresis at higher pressures. Method 2 ACRF1000-2 and ACRF1500-2 also follow the microporous Type I isotherm. The lack of increase in pore size may indicate that these samples contained a higher quantity of disordered carbon that had blocked the porosity and the activating agent (in this case CO_2) has removed this material, but the activation time was not long enough to start any sizeable widening of the pores. The large increase in surface area for ACRF1000-2, from 175 $m^2 g^{-1}$ to 2250 $m^2 g^{-1}$, indicates that there may have been significant volume of closed porosity in the structure resulting in an activated carbon with over 12 times the surface area of the original carbon, unlike ACRF1500-2 where the surface area only increased by 1.4 times that of the carbon. The reason for

the higher quantity of tar in these samples may be due to the micropores not allowing for the volatiles to be liberated from the materials quickly enough and instead become trapped in the structure on cooling. [22]

From *Table 5.3*, the increase in mesopore volume for all samples and decrease in average pore size (in particular for ACRF750), confirms that the smaller pores of the carbon xerogels are widened and the largest pores are removed on activation.

The highest total pore volume coupled with a relatively high surface area occurs for method 2 ACRF750-2. This unique combination can be attributed to the disordered structure of ACRF750-2; i.e. the large pore volume occurs as the pore size distribution continues into the macroporous region, whereas the high surface area occurs due to the high volume of micropores.

Although the combination of the characteristics found for method 2 ACRF750-2 may be desirable for some applications, a more ordered structure was desired for EC testing and all further measurements were continued using the method 1 xerogels, which overall exhibited a narrower pore size distribution. Another factor in the decision to discontinue use of the method 2 xerogels was that the strength of the structure was lower than for method 1 xerogels. As the porous structure had to be able to withstand milling to fine particles, method 1 xerogels were again preferred.

Table 5.3 – Surface Area and Pore Size Characterisation of Activated Carbon Xerogels

Sample	$S A_{BET}$ ± 5 ($m^2 g^{-1}$)	$P V_{Total}$ ± 0.02 ($cm^3 g^{-1}$)	$PV_{micropore}$ ± 0.02 ($cm^3 g^{-1}$)	$PV_{mesopore}$ ± 0.02 ($cm^3 g^{-1}$)	% Micropore	% Mesopore	D_{av} ± 0.1 (nm)
Gelation Method 1							
ACRF100	1135	0.612	0.455	0.157	74.3	25.7	2.4
ACRF200	1025	0.670	0.327	0.343	48.8	51.2	3.3
ACRF300	1010	0.901	0.302	0.599	33.5	66.5	4.7
ACRF400	950	1.034	0.297	0.738	28.7	71.3	6.6
ACRF500	890	1.134	0.285	0.849	25.1	74.9	8.5
ACRF750	775	1.114	0.303	0.811	27.2	72.8	14.9
Gelation Method 2							
ACRF100	1110	0.524	0.377	0.147	71.9	28.1	2.9
ACRF200	860	1.112	0.266	0.846	23.9	76.1	3.9
ACRF300	870	0.685	0.274	0.411	40.0	60.0	4.2
ACRF400	1060	1.065	0.332	0.734	31.1	68.9	5.9
ACRF500	670	1.143	0.235	0.908	20.6	79.4	22.7
ACRF750	930	1.734	0.343	1.391	19.8	80.2	32.9
ACRF1000	2260	1.168	1.086	0.082	93.0	7.0	2.2
ACRF1500	645	0.352	0.305	0.047	86.7	13.3	3.5

Due to the more disordered structure and therefore wider pore size distribution of the activated carbon xerogels produced via method 2, it was decided to continue all further studies with the xerogels produced via method 1.

5.3 Milling Study

5.3.1 Effect of Milling Time on Activated Carbon

To produce uniform composite electrodes for EC manufacture it is necessary to produce activated carbons with small enough particle size to allow for even distribution of materials when mixed with the binder and conductivity enhancer. The reduction in particle size is carried out through ball milling the samples. The aim of this study was to obtain particles small enough for uniform electrode manufacture whilst maintaining the porous characteristics of the activated carbon xerogels. In this section the effect of ball milling on the porous structure of the activated carbon xerogels is studied. The surface area and pore size distribution of the activated carbon xerogels milled for 0 – 30 minutes are shown in *Figures 5.13 and 5.14*. The data is summarised in *Table 5.4*. As will be discussed in **Section 5.8 Electrode Development**, ball milling for 30 minutes was not sufficient to provide a small enough particle size for uniform electrode production and ball milling of the activated carbon xerogels would lead to further destruction of the surface area. It was decided to mill the carbon xerogel before activation for 60 minutes and determine the effect this had on the resultant activated carbon xerogel.

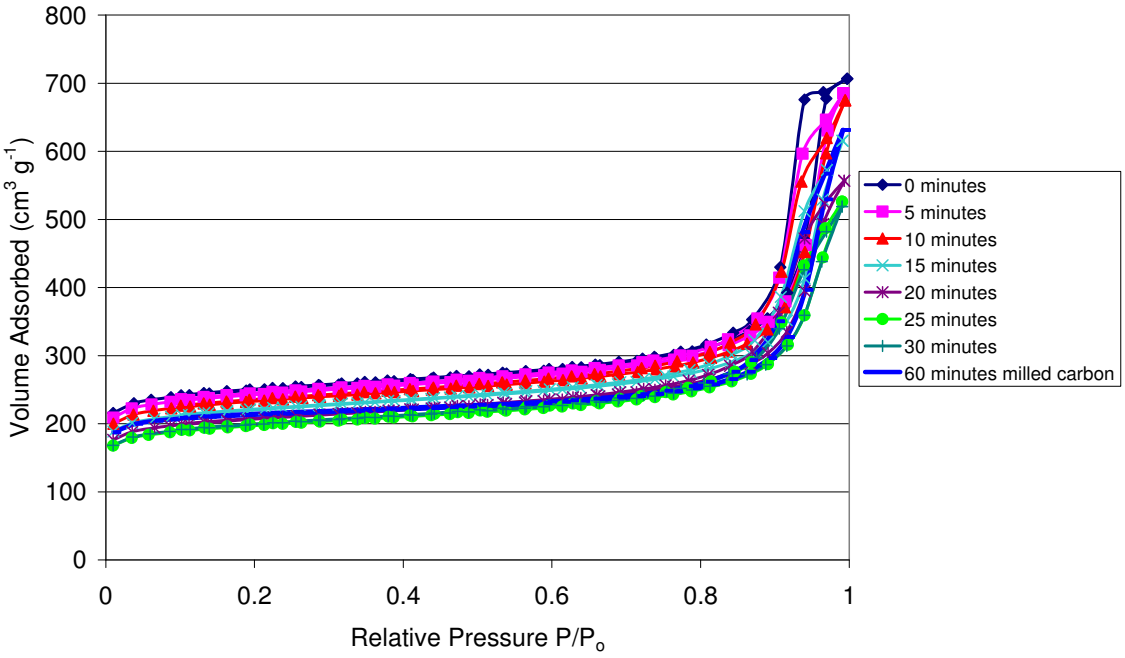

Figure 5.13 – Effect of Ball Milling on Surface Area of Activated Carbon Xerogels

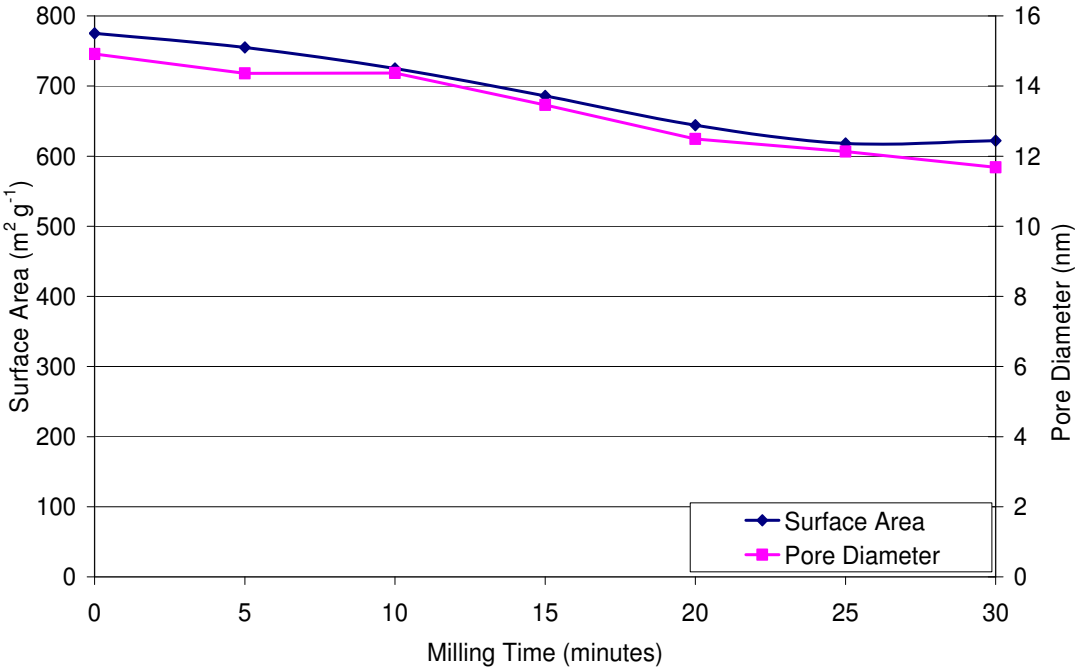

Figure 5.14 – Surface Area and Average Pore Diameter of Milled Activated Carbon Xerogels

The isotherms shown in *Figure 5.13* follow the Type IV isotherm for mesoporous solids. *Figure 5.14* indicates that the surface area and average pore diameter decrease with increasing milling time. The sample milled for 5 minutes displays an increase in the pore size distribution with pores of up to 80 nm being created, shown in *Figure 5.15*. This may have been caused by the breakdown of the walls between smaller pores, creating larger pores. After this initial increase, the width of the pore size distribution decreases until at 25 minutes it reduces below that of the original activated carbon xerogels to 65 nm. The pores most affected by the milling process were the largest mesopores in the structure. This can be seen from *Table 5.4* and *Figure 5.15* where there is less difference in the pore volume (less than 0.03 cm^3 g^{-1}) of micropores, whereas the pore volume of mesopores reduces by up to 0.1 cm^3 g^{-1}. The reduced effect of ball milling on micropores may be due to the thicker pore walls associated with micropores [191] reducing the destruction of the porosity.

The surface area of the sample is reduced by 25 % after 30 minutes of milling. By milling the carbon before activation the loss is reduced to 19 %, equivalent to the milling of the activated carbon xerogels for between 15 and 20 minutes. This indicates that this is the best method for maintaining the porous characteristics, whilst improving the processability of activated carbons for manufacture of EC electrodes.

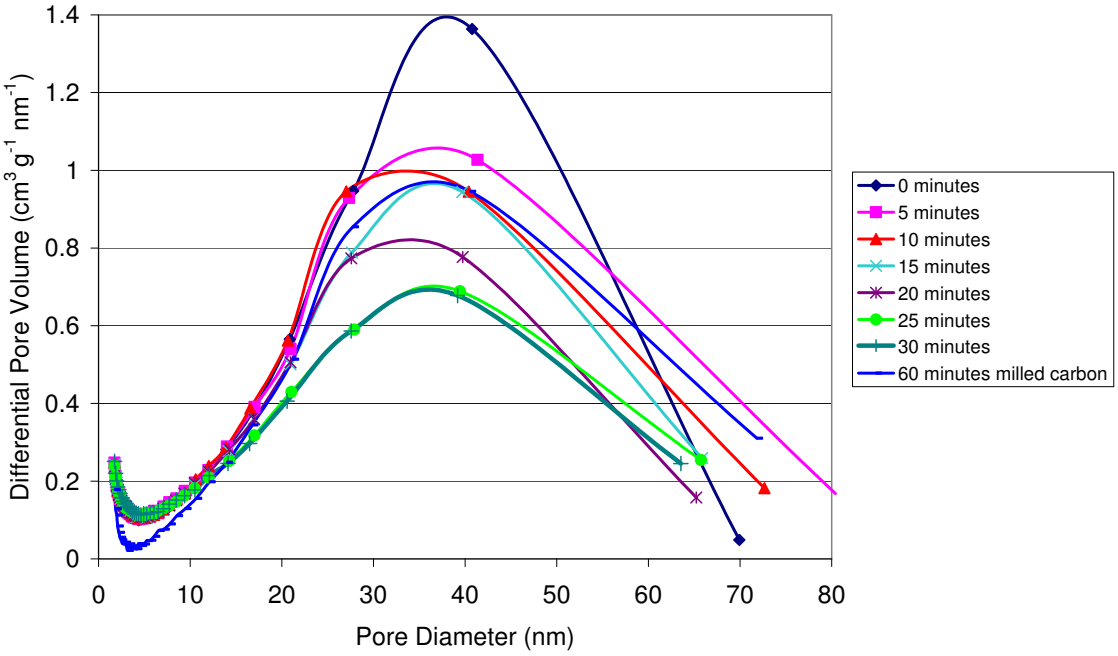

Figure 5.15 – Effect of Ball Milling on Pore Size Distribution of Activated Carbon Xerogels

Table 5.4 – Effect of Milling on Surface Area and Pore Size of Activated Carbon Xerogel

Sample	S A $_{BET}$ ± 5 (m^2 g^{-1})	P V_{Total} ± 0.02 (cm^3 g^{-1})	$PV_{micropore}$ ± 0.02 (cm^3 g^{-1})	$PV_{mesopore}$ ± 0.02 (cm^3 g^{-1})	% Micropore	% Mesopore	D_{av} ± 0.1 (nm)
0 min	780	1.114	0.303	0.811	27.2	72.8	14.9
5 min	770	1.080	0.291	0.789	27.0	73.0	14.4
10 min	740	1.064	0.276	0.788	26.0	74.0	14.4
15 min	690	0.970	0.259	0.711	26.7	73.3	13.4
20 min	645	0.879	0.241	0.638	27.4	72.6	12.5
25 min	620	0.830	0.228	0.602	27.5	72.5	12.1
30 min	620	0.819	0.229	0.590	27.9	72.1	11.7
Carbon 60 min	650	0.993	0.277	0.716	27.9	72.1	14.1

5.3.2 Milling of Carbon Xerogels before Activation

In this section the effect of milling the carbon xerogels before activation on the final pore structure is studied, to determine the most effective method of producing fine milled activated carbon xerogels for use in composite EC electrodes.

Table 5.5 summarises the results for the same sample (i.e. from one batch of xerogel), where milling was carried out on the carbon xerogels for 30 and 60 minutes prior to activation. This was then compared to the results of the activated carbon xerogels milled for 30 minutes. Activation was carried out as for the activated carbon samples in **Section 5.2.3**.

From *Table 5.5* it may be proposed that milling the activated carbon xerogel has the most detrimental effect on the porosity of the structure with the loss of the highest amount of surface area and pore volume. The reason for this high loss could be attributed to the nature of activation. As discussed in **Section 5.2.3** activation leads to the thinning of the pore walls, and whilst enhancing porosity, it may reduce the wall thickness of the porous network. To prevent the loss of surface area and pore volume through milling, the effect of milling on the carbon xerogel with subsequent activation to enhance the porosity was studied.

The results for the carbon xerogels milled for 30 and 60 minutes display little difference between the surface area, pore volume and average pore size for the two samples. From this it could be suggested that an extra 30 minutes of milling does not destroy any more of the porosity. It also may indicate that the carbon xerogels are able to withstand milling well with only a 1 % reduction in the surface area and an increase in pore volume over the non-milled carbon xerogel. This implies that activation leads to activated carbon xerogels with lower mechanical strength than the equivalent carbon xerogel.

The surface area for the activated carbon xerogel milled for 30 minutes was higher than that milled for 60 minutes and also higher than that of the non-milled sample. This could be attributed to the increase in particle surface area created by milling, which allowed the CO_2 to access the surface more readily, leading to an increase in the surface area and pore volume. The lower surface area for the activated carbon xerogel milled for 60 minutes even though it had a smaller particle size, may

be due to complete oxidation of some of the carbon smallest particles resulting in a reduced surface area.

Table 5.5 – Summary of Milling before and after Activation

Sample	S A $_{BET}$ ± 5 (m^2 g^{-1})	P V_{Total} ± 0.02 (cm^3 g^{-1})	$PV_{micropore}$ ± 0.02 (cm^3 g^{-1})	$PV_{mesopore}$ ± 0.02 (cm^3 g^{-1})	% Micropore	% Mesopore	D_{av} ± 0.1 (nm)
Non-milled AC	870	0.685	0.274	0.411	40.0	60.0	4.3
Milled AC 30 min	770	0.628	0.241	0.387	38.4	61.6	4.5
Non-milled C	605	0.510	0.177	0.333	34.6	65.4	4.3
Milled C 30 min	600	0.525	0.177	0.348	33.8	66.2	4.7
Milled C 60 min	600	0.523	0.174	0.349	33.3	66.7	4.7
Act. Milled C 30 min	1065	0.835	0.341	0.494	40.8	59.2	4.2
Act. Milled C 60 min	830	0.693	0.268	0.425	61.3	38.7	4.7

5.3.3 Activated Milled Carbon Xerogels

From **Section 5.3.2** (and further in **Section 5.8**) it was concluded that milling the carbon xerogels for 60 minutes before activation, produced more desirable materials characteristics for EC electrode manufacture. In this section the effect of milling and R/C ratio is studied.

NOTE: The R/W ratio was also increased to 0.25 g/ml to improve the carbon xerogels resistance to ball milling. [192] Above R/W 0.25 g/ml the material did not produce small enough particle sizes on milling.

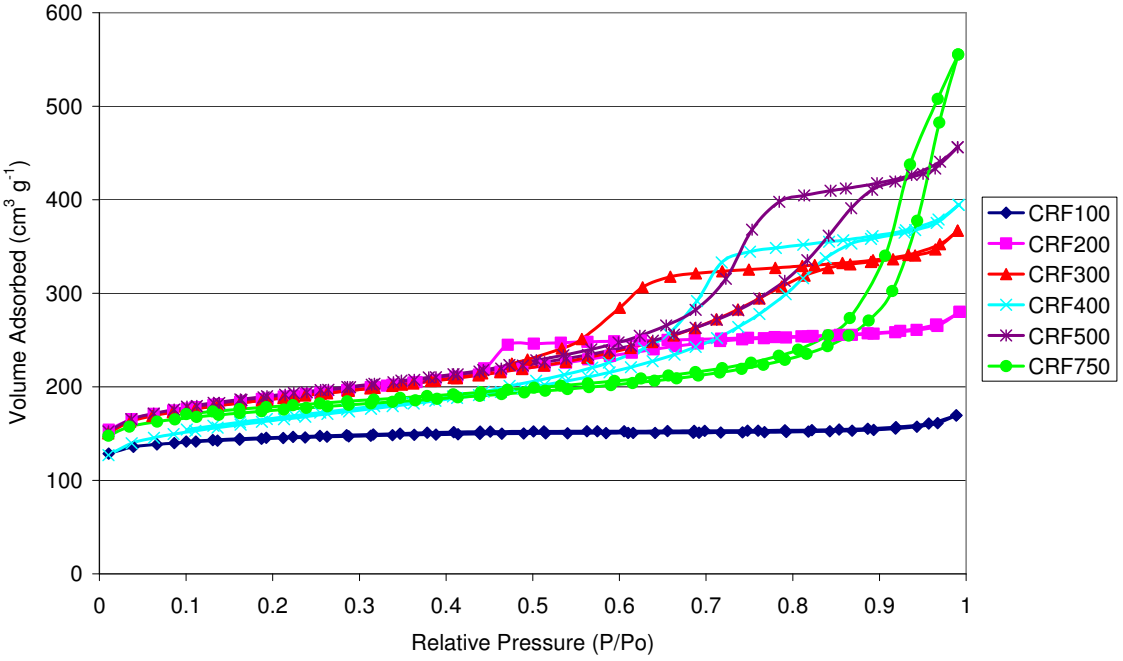

Figure 5.16 – Milled Carbon Xerogel Method 1 - Adsorption – desorption Isotherm at 77K

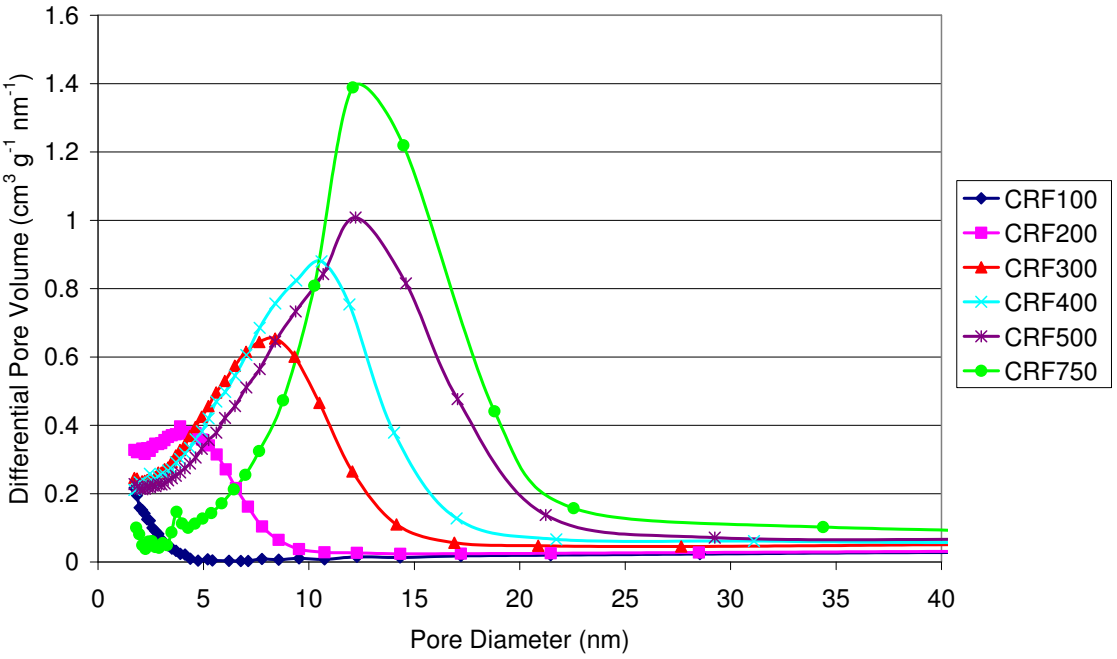

Figure 5.17 – Milled Carbon Xerogel Method 1 –Pore Size Distribution

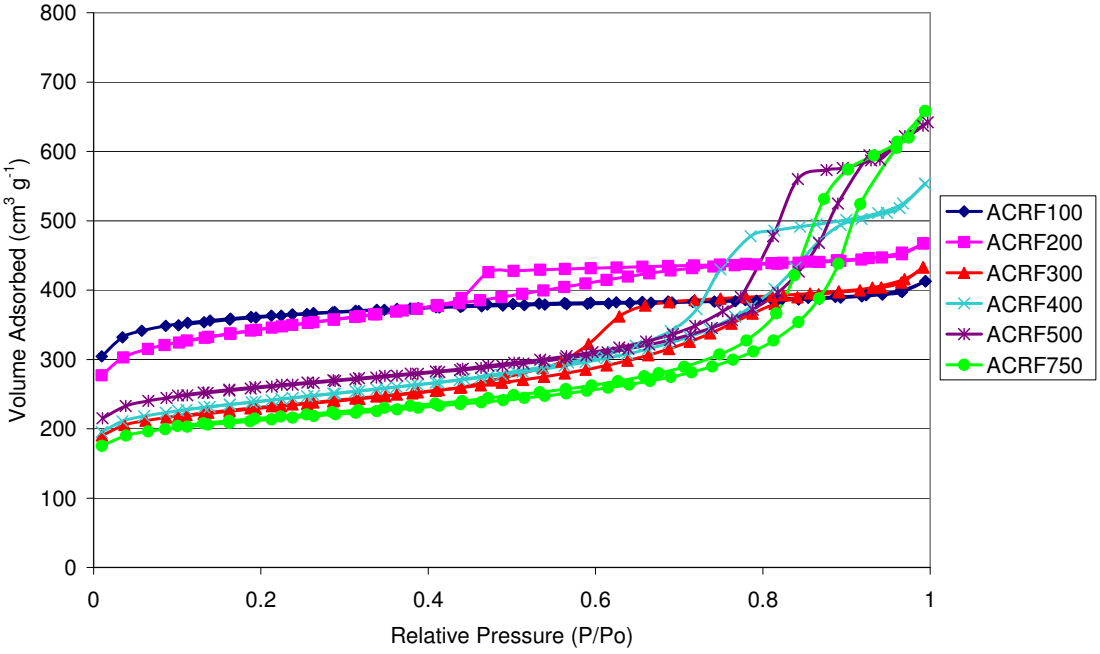

Figure 5.18 – Activated Milled Carbon Xerogel Method 1 - Adsorption – desorption Isotherm at 77K

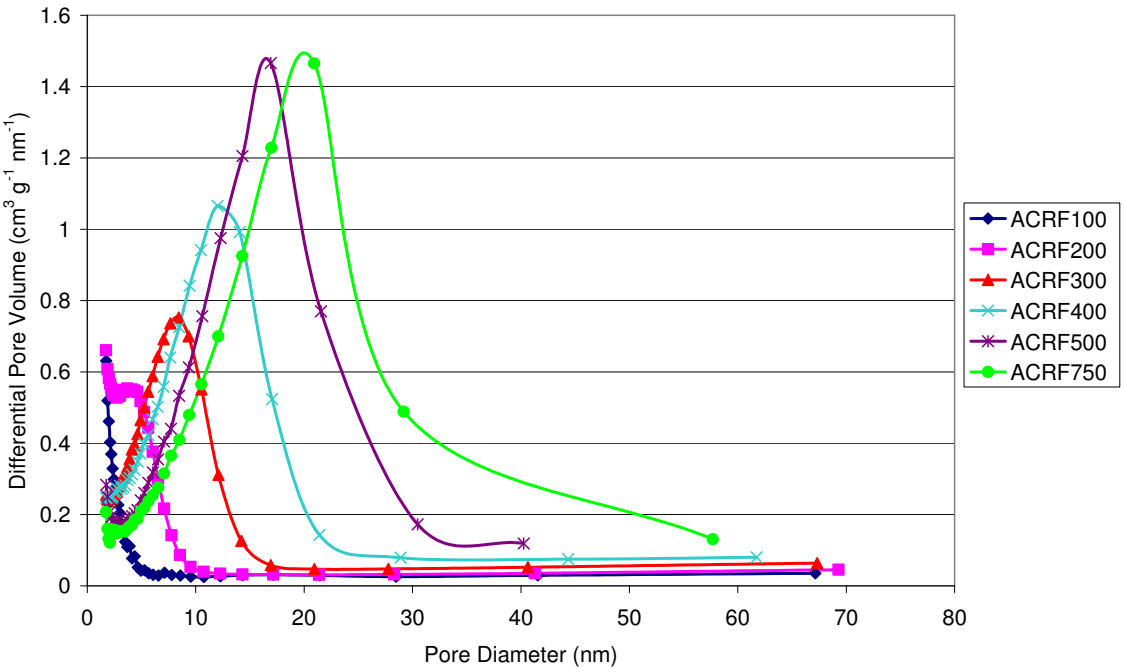

Figure 5.19 – Activated Milled Carbon Xerogel Method 1 –Pore Size Distribution

Figures 5.16 and 5.18 show the N_2 adsorption-desorption isotherms at 77K and *Figures 5.17 and 5.19* show the BJH pore size distribution for the milled carbon xerogels and activated milled carbon xerogels, respectively. The characterisation of the samples is summarised in *Table 5.6*. Comparing *Figures 5.9 and 5.18*, it can be seen that ACRF100 is the least affected by the milling process and that the effect of milling increases with increasing R/C ratio. Where, the largest reduction in surface area and pore size occur at ACRF750. This is due to the high proportion of large pores that make up the porous structure.

The activation of the carbons milled for 60 minutes leads to a significantly narrower pore size distribution than the non-milled activated carbon. This narrower pore size distribution is advantageous for EC manufacture as the error in determining the optimum average pore size is reduced.

Table 5.6 – Milled carbon and Activated Milled Carbon Results

Sample	S A $_{BET}$ ± 5 (m^2 g^{-1})	PV_{Total} ± 0.02 (cm^3 g^{-1})	$PV_{micropore}$ ± 0.02 (cm^3 g^{-1})	$PV_{mesopore}$ ± 0.02 (cm^3 g^{-1})	% Micropore	% Mesopore	D_{av} ± 0.1 (nm)
Carbon							
CRF100	445	0.262	0.188	0.074	71.7	28.3	3.8
CRF200	605	0.449	0.181	0.268	40.3	59.7	3.9
CRF300	600	0.597	0.176	0.421	29.5	70.5	5.5
CRF400	610	0.738	0.176	0.562	23.9	76.1	7.0
CRF500	570	0.796	0.187	0.609	23.5	76.5	9.6
CRF750	540	0.906	0.202	0.704	22.3	77.7	16.6
Activated Carbon							
ACRF100	1120	0.642	0.462	0.180	71.8	28.2	3.2
ACRF200	1090	0.746	0.298	0.448	39.9	60.1	3.5
ACRF300	840	0.719	0.254	0.465	35.4	64.6	6.0
ACRF400	905	0.894	0.272	0.658	29.3	70.7	8.5
ACRF500	970	0.969	0.299	0.671	30.8	79.2	10.6
ACRF750	670	1.052	0.224	0.829	21.3	78.7	16.9
Composite Electrode							
ACRF100	470	0.276	0.221	0.055	80.1	19.9	1.5
ACRF200	630	0.473	0.216	0.257	45.7	54.3	4.7
ACRF300	520	0.485	0.171	0.314	35.2	64.8	6.6
ACRF400	570	0.672	0.173	0.499	25.7	74.3	9.9
ACRF500	730	0.837	0.206	0.631	24.6	75.4	10.4
ACRF750	490	0.924	0.155	0.789	16.8	83.2	16.9

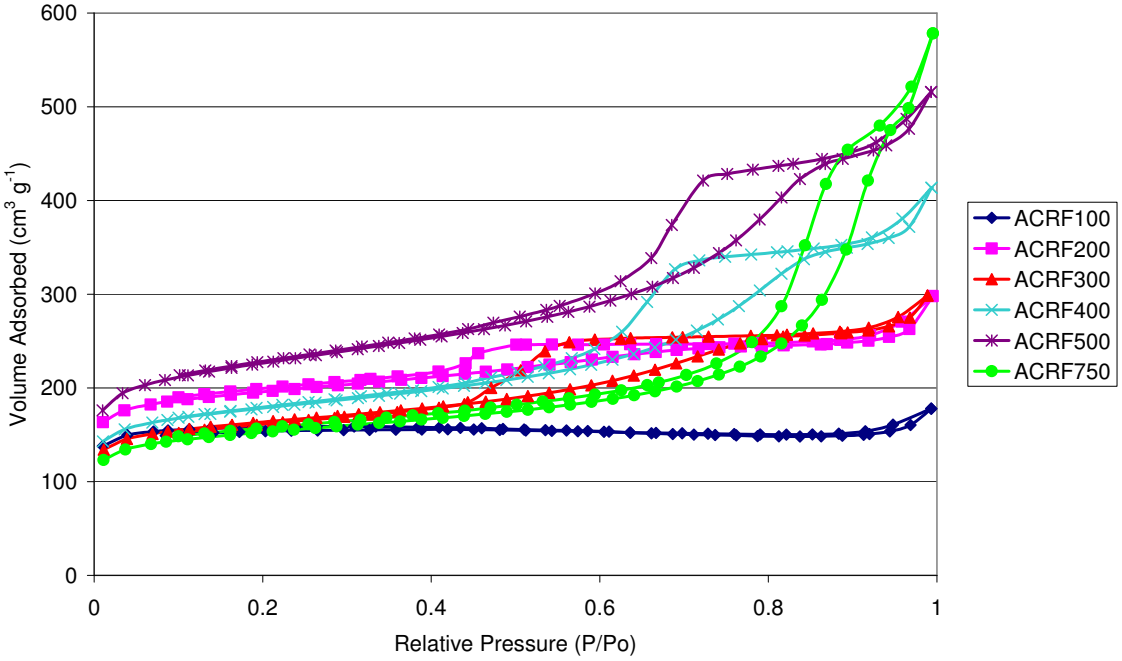

Figure 5.20 – Composite Electrode – Adsorption – desorption Isotherm at 77K

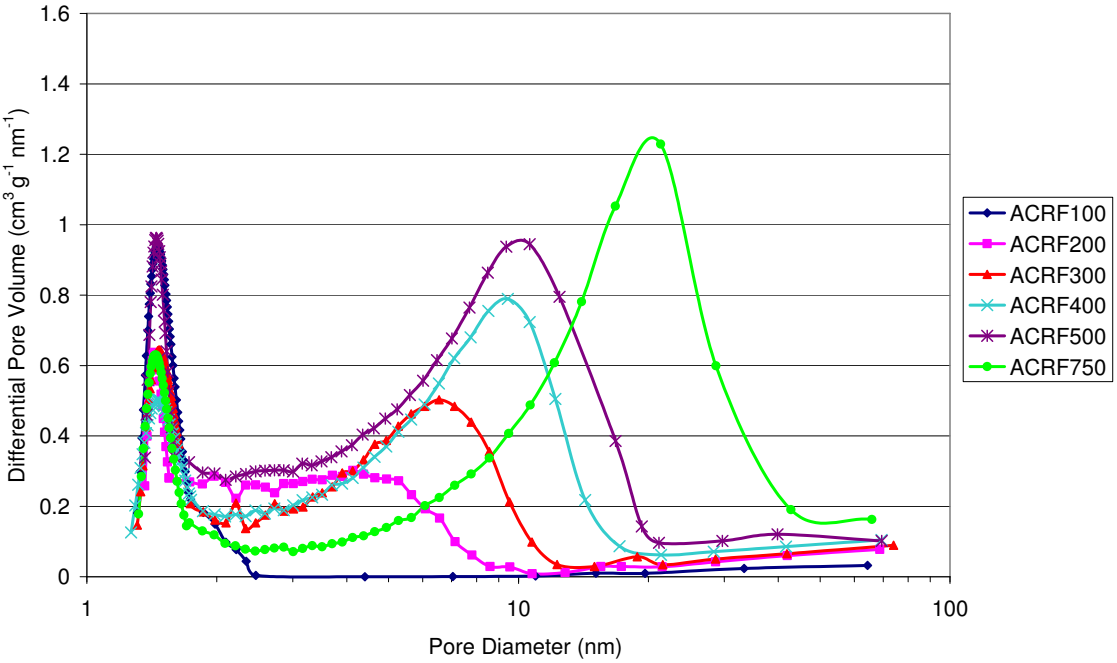

Figure 5.21 – Composite Electrodes – Pore Size Distribution

The double hysteresis loops in *Figure 5.20* that occur for ACRF300 – ACRF500 indicate that on adding the binder and carbon black larger pores are created, not from pores in the activated carbon xerogel network, but possibly introduced from the gaps between the activated carbon, carbon black and binder particles.

Figure 5.19 shows the BJH pore size distribution for the samples discussed above. The graph confirms the information drawn from the isotherms that as the R/C ratio increases the volume and size of mesopores increase. The graph also displays how well the activated carbon xerogels can be tailored to the size of pore required.

These samples were all tested for use in EC electrodes using Electrochemical Characterisation techniques to confirm the structure most suitable for good EC performance. To determine the effect of the addition of the Kynar 2801 binder and Cabot Carbon Black XC72, further surface area and pore size distribution characterisation was carried out. *Figure 5.21* shows the micro- and mesopore size distribution for the composite electrodes with a summary of the results in *Table 5.6*. The results indicate that smaller pores are blocked over larger pores, and as a consequence the largest reduction in surface area occurs for ACRF100. The reduction in BET surface area continues to decrease as the average pore size increases reaching a minimum for ACRF500. The small mesopores for ACRF100 are blocked and as result the average pore size reduces to 1.5 nm from 2.5 nm. The opposite effect is seen for the mesoporous samples, where an increase in the average pore size occurs.

5.4 Thermogravimetric Analysis

The results for the thermogravimetric analysis (TGA) of the resorcinol-formaldehyde (RF) xerogels are shown in *Figures 5.22 and 5.23*. All RF xerogels display the same behaviour on heating in nitrogen indicating that the catalyst ratio used during synthesis does not affect the carbonisation characteristics of the RF xerogels. The carbonisation process can be divided into 4 stages as shown in *Figure 5.22*. The first stage, occurring at 150°C, can be attributed to the removal of residual water from the sample. The second stage starts at 450°C, where the C – O bonds break, resulting in the removal of oxygen from the carbon structure and the initiation of the carbonisation of the RF xerogels. The third stage involves the removal of hydrogen from the structure and occurs at 600°C, where the C – H bonds break. In the forth stage, carbonisation of the RF gels is complete and the weight of the sample becomes constant. This can be seen to occur above 800°C. These results are consistent with those obtained by Lin *et al.* and Mirzaeian *et al*. [189,193]

As the surface area reaches a peak for carbonisation at 800°C [60,193], to ensure that carbonisation was complete at this temperature TGA was carried out by holding the sample at 800°C for 3 hours to ensure carbonisation was complete after this time. *Figure 5.24* proves that the weight becomes constant; indicating carbonisation at this temperature is complete.

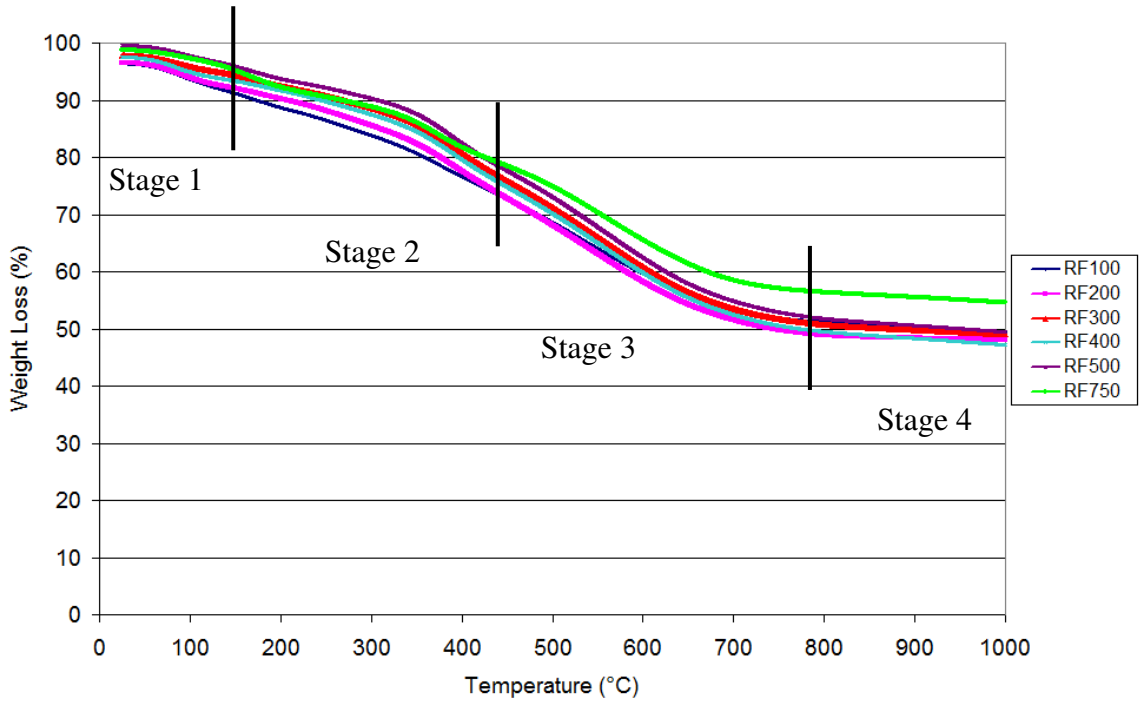

Figure 5.22 – Thermogravimetric Analysis of RF Xerogels; Weight Loss

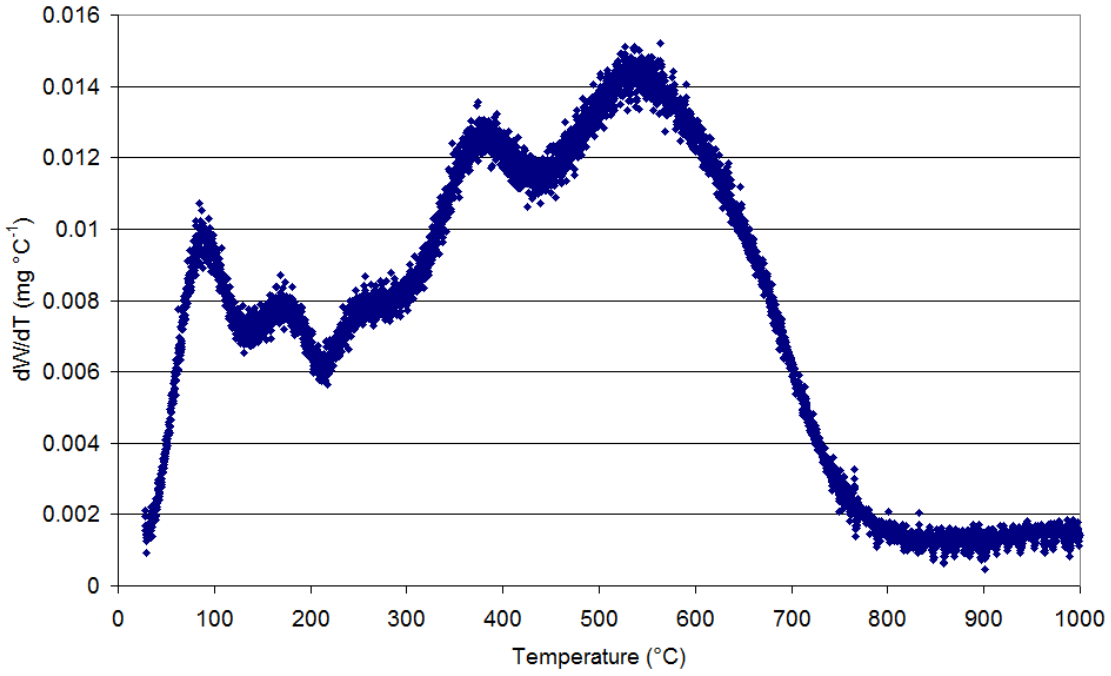

Figure 5.23 – Derivative Thermogravimetric Analysis of RF Xerogels

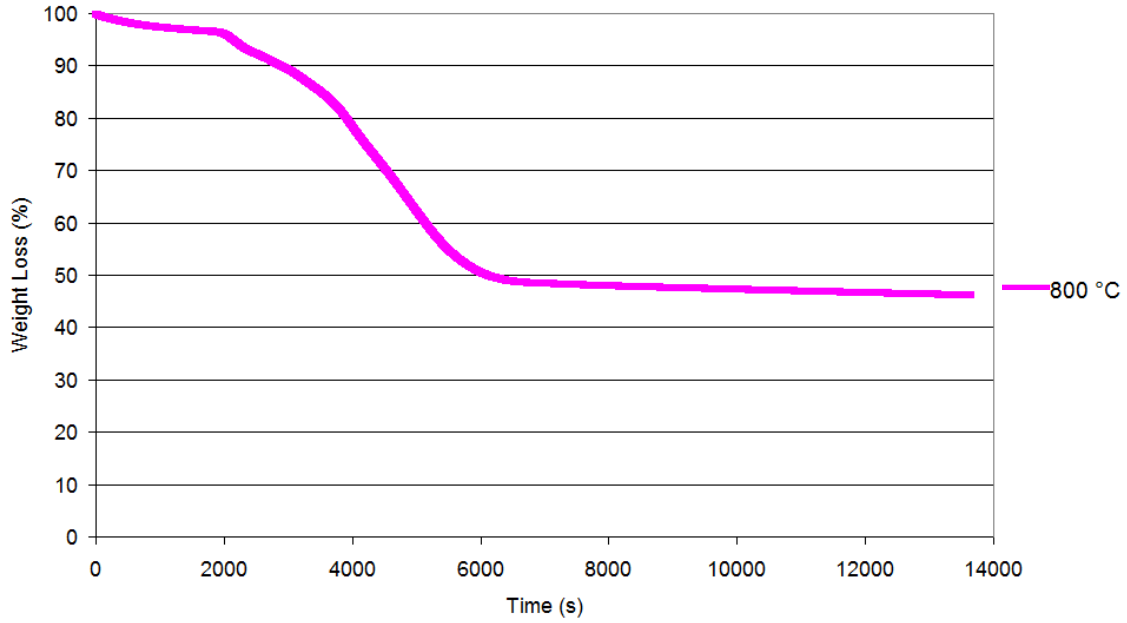

Figure 5.24 – Weight Loss for Carbonisation at 800°C

5.5 Fourier Transform Infrared (FTIR)

Figure 5.25 shows the FTIR spectra for the RF gel, carbon, activated carbon and cleaned activated carbon samples for R/C 200. NOTE: all wavelengths have been rounded to whole numbers.

For the RF gels the strong, broad peak that starts at approximately 3600 cm^{-1}, is due to phenolic O – H stretching, indicating OH – OH – OH as a result of intramolecular H-bonding. The peak at 1610 cm^{-1} can arise due to C = C – C aromatic ring stretching of both 1,2,4- and 1,2,6-trisubstituted aromatic ring structures. Peaks arising at 1500 and 1475 can be attributed to 1,2,4- and 1,2,6-trisubstituted, 1,2,4,6-tetrasubstituted aromatic ring stretching and the peak at 1450 cm^{-1} is due to CH_2 asymmetric bending. The peaks that occur at 1260 and 1220 cm^{-1} can be attributed to C – O stretching in ether groups confirming the presence of the alky-ether groups of the RF xerogels. The peaks that occur between 1220 and 1000 cm^{-1} can be attributed to in-plane C – H stretching. Below 900 cm^{-1}, the peaks can be attributed to out-of-plane C – H bending. These results were consistent with those found by Pekala and Lin *et al.* [50, 189]

The strength of the peaks at 1610 and 1475 cm^{-1} indicate that 1,2,4- and 1,2,6-trisubstituted aromatic ring are abundant in the structure as would be expected with phenolic resins produced from resorcinol-formaldehyde precursors.

After carbonisation it can be seen that no detectable surface functionality has been left in the structure. On activation with $CO_{2(g)}$ surface functionality has been introduced to the carbon surface and can be seen to be present in low concentrations due to weak peaks at 3650, 1680 and 1250 cm^{-1} which indicate the presence of acidic surface functionality often associated with the use of $CO_{2(g)}$ as the activating agent. The peaks are due to O – H stretching, C = O and C – O, respectively. On cleaning the activated carbon in an inert atmosphere of $Ar_{(g)}$, this surface functionality is removed proving the cleaning procedure was effective.

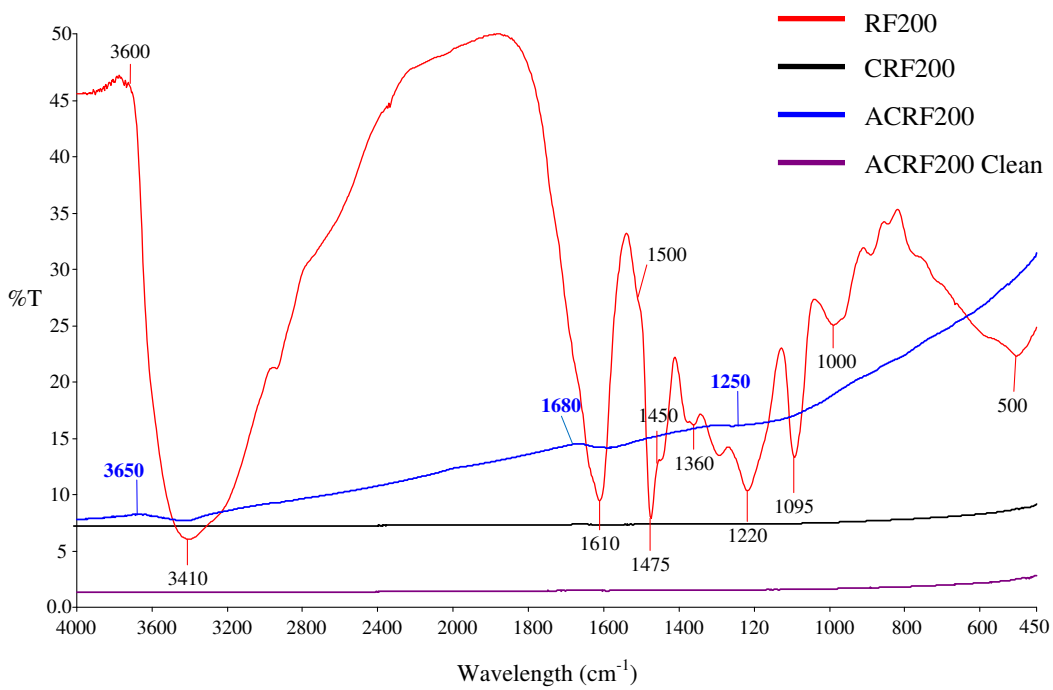

Figure 5.25 – FTIR Analysis of Xerogel, Carbon, Activated Carbon and Clean Activated Carbon

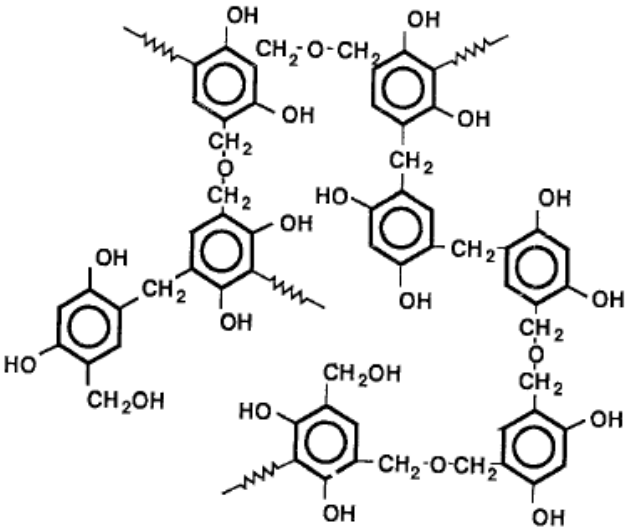

Figure 5.26 – Structure of Resorcinol – Formaldehyde Xerogel

5.6 Microanalysis

Table 5.7 – Microanalysis of RF Xerogels, Carbons and Activated Carbons

Sample	Carbon %	Hydrogen %	Nitrogen %	Oxygen %
Xerogel				
RF100	58.10	3.92	<0.3	37.98
RF200	59.78	4.83	<0.3	35.39
RF300	60.69	4.14	<0.3	35.17
RF400	60.54	3.59	<0.3	35.87
RF500	60.99	3.49	<0.3	35.52
RF750	61.42	4.42	<0.3	34.16
Carbon				
CRF100	81.04	1.7	Trace	17.26
CRF200	82.02	1.52	Trace	16.46
CRF300	83.61	1.16	Trace	15.23
CRF400	83.31	1.35	Trace	15.34
CRF500	86.11	1.34	Trace	12.55
CRF750	91.50	2.51	Trace	5.99
Activated Carbon				
ACRF100	65.63	2.89	Trace	31.48
ACRF200	82.86	2.01	Trace	15.13
ACRF300	80.90	1.89	Trace	17.21
ACRF400	81.94	1.53	Trace	16.53
ACRF500	79.63	1.49	Trace	18.88
ACRF750	82.42	1.20	Trace	16.38

The results from microanalysis are shown in *Table 5.7* for method 1 xerogel, carbon and activated carbon samples. All samples were prepared under the same carbonisation and activation conditions.

Microanalysis proves that the RF xerogels contain approximately the same wt % of each component with only a 5% increase in % carbon from RF100 to RF750, indicating that although surface area characterisation has shown a significant change in physical structure for increasing R/C ratio the component ratios remain little changed. The reduction in oxygen content and increase in hydrogen and carbon content with increasing R/C ratio indicate that the degree of cross-linking decreases

i.e. reduction in number of ether bridges occurs. The results indicate the RF xerogels contain a small quantity of nitrogen. This may be attributed to impurities in the reagents which were removed on carbonisation.

Carbonisation of the RF xerogels results in an increase in the relative carbon content of the samples and removal of hydrogen and oxygen from the structure. The samples still contain significant quantities of oxygen and hydrogen and this is attributed to the presence of the C – O – C ether bridges between the resorcinol molecules that are only fully removed on graphitisation of the carbon xerogels, which only occurs above 2000°C. The lowest degree of cross-linking was expected to occur at R/C 750, the microanalysis result for CRF750 confirms the lack of ether bridges as it has a substantially lower oxygen content than the results for lower R/C ratios. The overall reduction in % carbon content that occurs upon activation can be attributed to the removal of the disordered or 'free' carbon left in the structure after carbonisation. The largest decrease in carbon content occurs for ACRF100 due to this sample containing the largest number of ether bridges. On activation a large increase in surface area also occurs indicating a large part of the carbon structure was due to 'free' disordered carbon that is easily removed during activation.

5.7 Yield

In this section the influence of xerogel R/C ratio on the yield from carbonisation and activation is studied. The % Yield from carbonisation and activation is summarised in *Table 5.8* below, where

$$\%Yield = \left(\frac{InitialWeight - FinalWeight}{FinalWeight} \right) * 100$$

$$\%Burn - off = (100\% - \%Yield)$$

NOTE: Burn-off is reported for activation processes, not carbonisation.

Table 5.8 – Yield for Carbonisation and Activation of RF Xerogels

Sample	% Yield	
	Method 1	**Method 2**
Carbon		
CRF100	51.2	51.4
CRF200	48.9	51.6
CRF300	51.4	52.2
CRF400	49.6	49.4
CRF500	49.8	51.5
CRF750	50.1	47.2
CRF1000	-	48.8
CRF1500	-	49.2
Activated Carbon		
ACRF100	55.9	74.2
ACRF200	74.2	88.5
ACRF300	82.4	63.9
ACRF400	84.8	24.3
ACRF500	87.5	27.9
ACRF750	88.2	26.3
ACRF1000	-	80.0
ACRF1500	-	84.7

The yield for carbonisation was constant at 50% ± 1.5% of the original RF xerogel mass for all R/C ratios, which is consistent with that found for phenolic resins [191]. However, the burn-off for activation varies with R/C ratio. For method 1, the increase in R/C ratio results in an increase in the Yield, i.e. a reduction in the %

Burn-off from 44 to 12%. From earlier discussion it was suggested that the lower R/C ratio carbon contained a higher quantity of tar, left in the structure from carbonisation. The higher % weight loss for those samples considered to contain high quantity of tar may provide evidence for this suggestion, as the tar is being more easily removed and/or may be heavier than that of the disordered carbon removed at higher R/C ratios.

The % Burn-off for the method 2 Activated Carbon Xerogels exhibits no pattern for R/C ratio and the difference between the % Burn-off for ACRF400 - ACRF750 is significantly lower (> 50 %) than that for the other method 2 samples. This could indicate a large quantity of disordered carbon was contained in these samples, which was removed during activation. This may explain the larger degree of burn-off for this sample than that of ACRF100 - 300. Method 2 ACRF500 and ACRF750 exhibit the largest pores making the surface easily accessed by the CO_2 gas, allowing for a higher degree of burn-off than those with smaller pores.

5.8 Electrode Study

There were various stages in the development of good quality electrodes for EC manufacture. The study can be divided into four groups; (1) Stirring Time, (2) Binder Type Variation, (3) Substrate, and (4) Milling Time. *Table 5.9* summarises the results.

The stirring time was varied between 1 – 4 hour(s) to ensure that a completely uniform suspension was created. It was determined that the binder, Kynar 2801, took 4 hours of stirring to be evenly distributed in the composite electrode suspension. Stirring between 1 – 3 hours left some of the Kynar 2801 un-dispersed.

Due to difficulty forming non-brittle, flexible electrodes with only 10 % wt Kynar 2801, a study into other binders was carried out. However, it was found that Kynar formed the best suspension with the activated carbon xerogels.

To ensure that the activated carbon xerogel particle size was fine enough to form a uniform layer with a low quantity of Kynar 2801, additional studies were carried to look at the effect of milling the carbon xerogel for longer. The milling time of the carbon xerogels was increased from 30 to 60 minutes. The finer activated carbon xerogel particles improved the uniformity of the electrode and improved flexibility of the electrode. It was found when passed through a series of sieves from 100 to 38 μm the sample milled for 60 minutes was not able to pass through the 50 μm sieve, whilst the sample milled for 30 minutes passed through the 50 μm sieve but not through the 35 μm sieve. This indicates a particle size of < 50 μm allowed for improved dispersion and contact with the Kynar 2801. However, the electrodes were still found to be brittle around the edges of the circular discs when cut.

The next step was to find a way to produce electrodes that were strong enough to be cut into disc electrodes using Kynar 2801 as the binder. It was found that spreading the electrode slurry directly onto the Al foil current collector, as opposed to a glass plate, reduced the brittleness and improved the flexibility of the electrode. An added advantage of this technique is the improved contact of the electrode and current collector.

The best quality electrodes were produced from:

Composition: 80 % wt Activated Carbon Xerogel (milled carbon 60 minutes)
10 % wt Carbon Black Cabot XC72
10 % wt Kynar 2801

Solvent: Acetone

Mixing Time: 4 hours

Electrode Thickness: 170 μm

Substrate: Al Foil 30 μm

Table 5.9 – Summary of Electrode Study

Electrode	Composition	Solvent	Stirring Time	Thickness / Substrate	Comments	Next Steps
1	• 70% wt ACX– mill 30 min • 30 % wt Kynar 2801 (adapted from University of St. Andrews Battery electrodes)	Acetone	4 hrs	200 µm / glass Plate	The electrode was good quality. i.e. strong and flexible. However, the binder content was too high for use as EC electrode.	• Reduce Quantity of Binder
2	• 80% wt ACX– mill 30 min • 10% wt CB XC72 • 10% wt Kynar 2801 [188]	Acetone	4 hr	200 µm / glass Plate	Electrode allowed for good, uniform distribution on glass plate, but, the electrode was too brittle to lift from the glass plate.	• Try other type of binder's compatibility with ACX.
3	• 90% wt ACX– mill 30 min • 4% wt CB XC72 • 4% wt PTFE (60 % wt dispersion) • 2 % wt CMC [113]	Ethanol	4 hrs	200 µm / glass plate	The electrode did not form a uniform layer due to binder clumping.	• Try dispersion in H_2O, as PTFE is already suspended in 60 %wt H_2O.
4	• 90% wt ACX– mill 30 min • 4% wt CB XC72 • 4% wt PTFE (60 % wt dispersion) 2 % wt CMC	H_2O	4 hrs	200 µm / glass plate	Activated carbon xerogel was not dispersed.	•Try ethanol as the dispersion medium.

5	• 90% wt ACX– mill 30 min • 4% wt CB XC72 • 4% wt PTFE (60 % wt dispersion) • 2 % wt CMC	IPA	4 hrs	200 µm / glass plate	Same result as Electrode 3.	• CMC was removed from next electrode to ensure this was not the cause of the clumping as PTFE was already in a dispersed solution
6	• 90% wt ACX– mill 30 min • 4% wt CB XC72 • 6% wt PTFE (60% wt dispersion)	Ethanol	4 hrs	200 µm / glass plate	PTFE not dispersed.	• Discontinue use of PTFE as binder and CMC as auxiliary binder.
7	• 80% wt ACX – mill 30 min • 10 % wt CB XC72 10 % wt Kynar 2801 (same as No. 6)	Acetone	4 hrs	200 µm / glass plate	The electrode formed uniform layer onto the glass plate, however, it could not be removed from the glass in a solid film.	• Mill carbon for longer to improve particle dispersion.
8	• 80 % wt ACX – mill 60 min • 10 % wt CB XC72 10 % wt Kynar 2801	Acetone	4 hrs	200 µm / glass plate	The finer ACX particles improved the uniformity and flexibility of the electrode. However, the electrodes were still found to be brittle around the edges of the circular discs when cut.	• Try spreading directly onto Al foil current collector
9	• 80 % wt ACX– mill 60 min • 10 % wt CB XC72 • 10 % wt Kynar 2801	Acetone	4 hrs	170 µm/ 30 µm Al foil	The electrode was uniformly distributed onto Al foil and could be cut into disc electrodes.	• Electrode could be cut into disc electrodes without any cracking.

6. Results and Discussion – Electrochemical Measurement

6.1 Electrochemical Stability Window

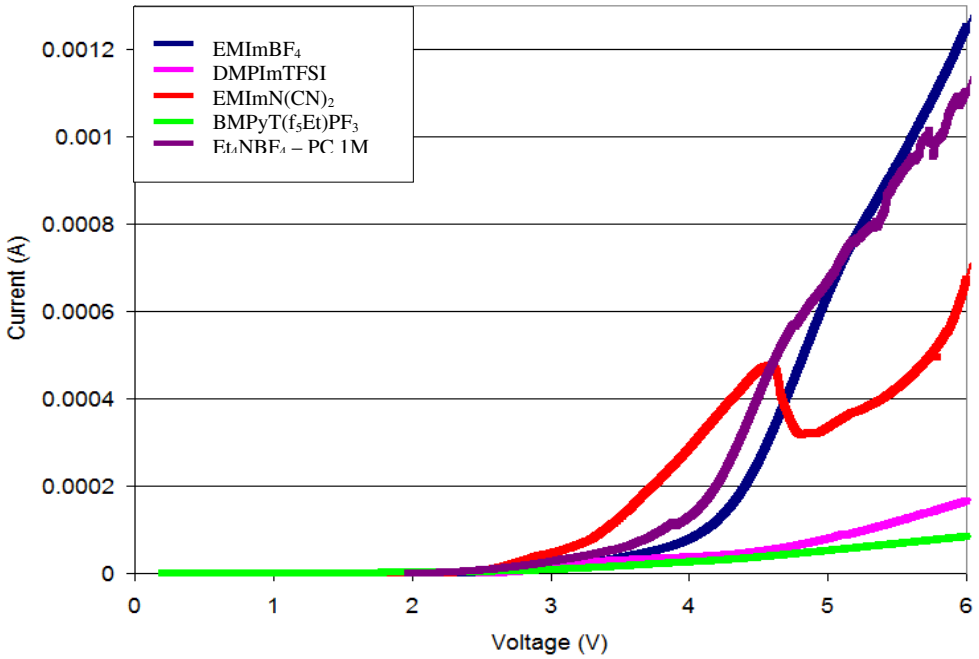

Figure 6.1 – Electrolyte Electrochemical Stability Window

Figure 6.1 shows the electrochemical stability windows (ESWs) for each of the electrolytes from 0 – 6 V. Electrolytes $EMImBF_4$, $EMImN(CN)_2$ and Et_4NBF_4 – PC 1M, show a sharp increase in current at the point of decomposition indicating that any accidental over charging during operation would result in rapid decay of capacitance performance. Electrolytes DMPImTFSI and $BMPyT(f_5Et)PF_3$ produce a much lower current above the stable voltage window.

Table 6.1 shows the breakdown voltage determined when the current increase from 0V reached 0.02 mA. This value was chosen from the known breakdown voltage of the commercially utilised organic electrolyte Et_4NBF_4-PC 1M. The degradation starts at the weakest covalent bond for all electrolytes. The large stability window of $T(f_5Et)PF_3$ anion (3.7 V) could be attributed to the ethyl groups on the anion (*Figure 2.2(c)* in **Section 2.7**) having a shielding effect on the bonds within the anion leading to an enhanced ESW. The relatively low increase in current may be due to the different bonds strengths leading to differing breakdown voltages for each

bond. The larger stability window (3.2 V) for the BF_4 (*Figures 2.2(d)* **Section 2.7**) anion over that of the anions $N(CN)_2$ (2.2 V) (*Figures 2.2(a)* **Section 2.7**) and TFSI (2.9 V) could be attributed to the increased strength of the σ B-F bonds.[194] However, as all bonds are equivalent a large increase in current occurs at the breakdown voltage. The low current increase for TFSI may arise as a result of similar shielding effects as discussed for $T(f_5Et)PF_3$. However, the reduced operating voltage of 2.7 V may be a result of the reduced shielding effect of the smaller methyl groups and more open configuration of the anion which can be seen in *Figure 2.2(b)* in **Section 2.7**. The lower voltage window for $N(CN)_2$ than for the other anions discussed above may be attributed to the lower bond strength of the carbon to nitrogen bond, by comparison with the bond strength of fluorine to carbon or boron. [194]

The results obtained for the ESW of the RTILs under investigation, emphasises an important issue that is not immediately obvious from RTIL/EC literature. Higher operating voltages of up to 6 V are claimed in the literature, [16, 20] on working electrodes such as tungsten. However, when tested using the electrode materials (i.e. carbon xerogels) under investigation a large reduction in operating voltage occurs. Despite not reaching the highest voltages claimed, RTIL electrolytes DMPImTFSI , $EMImBF_4$, and $BMPyT(f_5Et)PF_3$ all exhibit higher operating voltages than the conventional organic electrolyte and should therefore allow for up to a two-fold increase in energy density if capacitance were to remain constant.

The operating voltage for each electrolyte was reduced by 0.2V below the maximum stable voltage.

Table 6.1 – Electrochemical Stability Windows of Electrolytes

Electrolyte	**Maximum Electrolyte Stability Voltage (V) ± 0.1**	**Maximum EDLC Operating Voltage (V)**
$EMImBF_4$	3.2	3.0
DMPImTFSI	2.9	2.7
$EMImN(CN)_2$	2.7	2.5
$BMPyT(f_5Et)PF_3$	3.7	3.5
Et_4NBF_4 – PC 1M	2.7	2.5

6.2 Galvanostatic Charge - Discharge

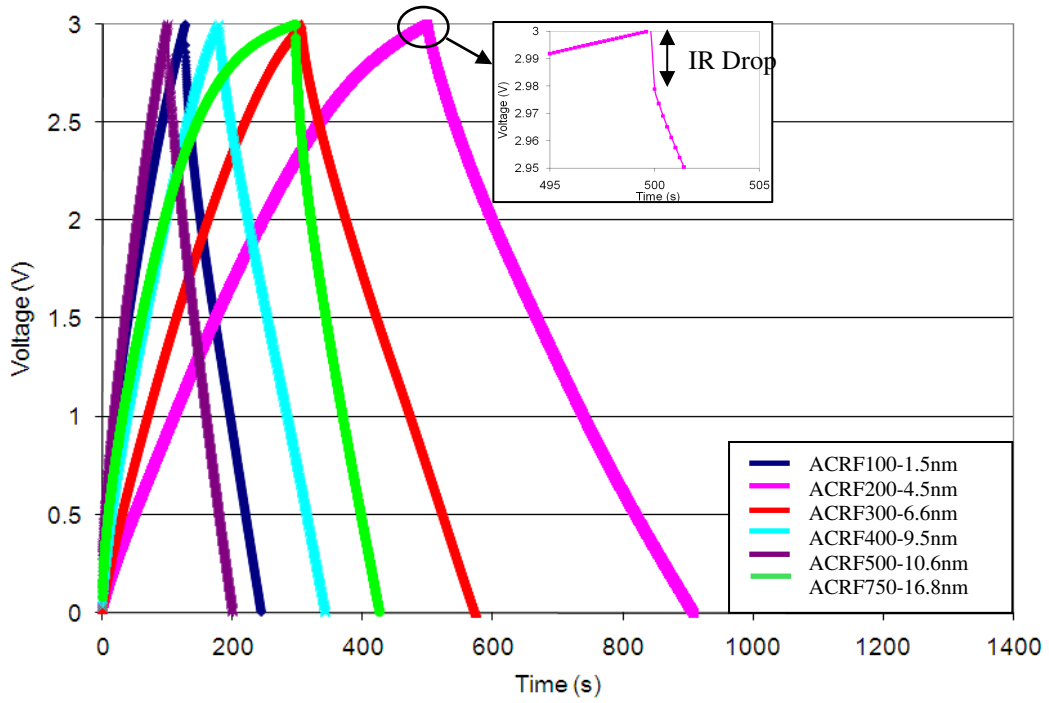

Figure 6.2 – Galvanostatic Charge – Discharge $EMImBF_4$

Figure 6.2 shows Galvanostatic charge-discharge (GC) results at 2 mA cm^{-2} for $EMImBF_4$ and *Figures A1.1 – A1.4* in *Appendix A* show the Galvanostatic charge-discharge (GC) results at 2 mA cm^{-2} for all other electrolytes studied, when the cells were cycled between 0 V and the maximum operating voltage as defined in *Table 6.1*. *Table 6.2* summarises the capacitance results obtained for current densities 2, 4, 8, 16, 32 and 64 mA cm^{-2} for each electrolyte tested.

For all test cells at low discharge current, the response of the capacitor can be seen to approach the ideal linear charge-voltage relationship. At higher current rate, the total impedance of the cell gives rise to an initial drop of the discharge voltage, known as the *IR* drop as indicated in *Figure 6.2*. This increases with increasing current density. The voltage drop can be used to calculate the equivalent series resistance (ESR) of the cells according to $V = IR$. The low capacity values observed at higher current rates are associated with the low mobility of the ions which results in the ions being unable to transfer from the bulk to the pore wall rapidly enough to form the double-layer at increased current rates. The effect of pore size on this trend will be discussed later in **Section 6.2.2**.

Table 6.2 – Capacitance for GC at Varying Current Rate [7]

Sample	2mA cm^{-2} ± 0.1 ($F\ g^{-1}$)	4mA cm^{-2} ± 0.1 ($F\ g^{-1}$)	8mA cm^{-2} ± 0.1 ($F\ g^{-1}$)	16mA cm^{-2} ± 0.1 ($F\ g^{-1}$)	32mA cm^{-2} ± 0.1 ($F\ g^{-1}$)	64mA cm^{-2} ± 0.1 ($F\ g^{-1}$)
Electrolyte: $EMImBF_4$						
ACRF100-1.5nm	67.8	19.8	16.1	13.3	11.5	10.2
ACRF200-4.5nm	140.1	117.5	103.4	91.2	78.5	32.7
ACRF300-6.6nm	116.6	99.0	93.4	88.0	81.9	76.2
ACRF400-9.5nm	70.2	61.6	55.3	49.2	43.8	39.4
ACRF500-10.5nm	66.3	62.2	54.2	52.7	48.3	35.2
ACRF750-16.5nm	57.3	49.5	44.8	38.6	31.0	23.2
Electrolyte: DMPImTFSI						
ACRF100-1.5nm	13.2	10.6	8.2	6.6	5.6	2.3
ACRF200-4.5nm	104.3	98.7	92.2	81.6	63.0	33.4
ACRF300-6.6nm	71.4	69.0	64.9	60.3	53.9	44.5
ACRF400-9.5nm	42.5	40.8	37.8	34.4	29.6	25.3
ACRF500-10.5nm	34.5	31.2	28.6	24.7	21.4	19.0
ACRF750-16.5nm	18.6	17.2	15.2	13.0	9.7	1.8
Electrolyte: $EMImN(CN)_2$						
ACRF100-1.5nm	6.3	4.8	4.2	4.1	4.7	6.0
ACRF200-4.5nm	26.8	15.0	9.8	7.4	7.1	7.1
ACRF300-6.6nm	63.2	58.6	54.2	49.6	45.6	41.0
ACRF400-9.5nm	55.5	40.7	38.2	36.7	35.7	37.7
ACRF500-10.5nm	44.4	32.6	30.6	29.3	28.6	30.2
ACRF750-16.5nm	38.6	34.5	31.8	29.7	28.3	27.8
Electrolyte: $BMPyT(f_5Et)PF_3$						
ACRF100-1.5nm	3.3	2.9	2.6	2.1	0.5	-
ACRF200-4.5nm	41.7	29.4	17.5	6.9	0.6	-
ACRF300-6.6nm	16.8	16.8	15.3	13.8	11.9	10.2
ACRF400-9.5nm	19.9	18.2	16.5	13.9	10.6	-
ACRF500-10.5nm	24.8	20.6	16.2	12.0	8.9	-
ACRF750-16.5nm	6.2	6.3	5.9	5.5	5.1	-
Electrolyte: Et_4NBF_4 – PC 1M						
ACRF100-1.5nm	51.8	48.0	44.5	40.9	37.0	24.5
ACRF200-4.5nm	100.3	96.9	91.3	89.8	86.8	75.3
ACRF300-6.6nm	51.5	45.8	42.4	39.7	37.5	35.1
ACRF400-9.5nm	47.7	44.8	43.3	42.0	40.6	39.0
ACRF500-10.5nm	45.9	44.5	43.1	41.5	39.8	38.0
ACRF750-16.5nm	16.9	13.2	12.6	12.5	12.1	12.2

[7] The hyphenated sample name includes the average pore width for the composite electrodes as outlined in Table 5.6 on Page 146.

6.2.1 Variation of Capacitance with Pore Size

From traditional capacitor theory for a parallel plate capacitor the relationship between capacitance and surface area should follow *Equation 1.1.*

$$C = \varepsilon_o \varepsilon_r \left(\frac{A}{d} \right) \qquad \textit{Equation 1.1}$$

Where, ε_0 is relative permittivity of vacuum, ε_r is the dielectric constant at the interphase, A is the surface area of electrode and d is the thickness of the double layer. If it is assumed that $\varepsilon_r\varepsilon_0/d$ is constant for each electrolyte and carbon electrode sample then capacitance and surface area should exhibit a linear relationship. *Figure 6.3* shows the specific capacitance with respect to the activated carbon electrode BET surface area for all electrolytes and activated carbon xerogels studied. The results show no systematic trends between surface area and specific capacitance, showing that the traditional capacitor theory does not hold for these experiments. Explanations for this deviation can be drawn from the literature. Huang *et al.* [146] proposed that the traditional model only holds for macroporous carbon materials and developed new models for mesoporous and microporous carbon materials, shown in *Equations 2.1a-b and 2.2 (***Section 2.5***)* respectively. However, the new models can only be applied when the structure of the nanoporous carbon can be considered unimodal. As, all of the activated carbon xerogels produced in this study exhibit a bimodal pore structure of both micro and mesoporosity with this extending into macroporosity at high R/C ratio, this accounts for the deviation from the expected linear relationship. Another study from Wang *et al.* [195] examined the effect of activated carbon pore structure on the performance of aqueous EDLCs. To determine if the capacitance showed a linear relationship with surface area the activated carbon samples were divided into two groups based on their pore structure. Group I includes the samples that mainly contain micropores, small mesopores (2 – 5 nm), and macropores; Group II includes those mainly containing micropores, small mesopores (2 – 5 nm) and larger diameter mesopores (5 – 30 nm). It was found that both groups of carbons show a linear relation between the specific capacitance and the BET area, separately. They found that the slope of the linear line for Group I samples was steeper than for Group II. These studies confirm that capacitance is not only dependant on surface area, but also on the porous structure of the carbons electrodes.

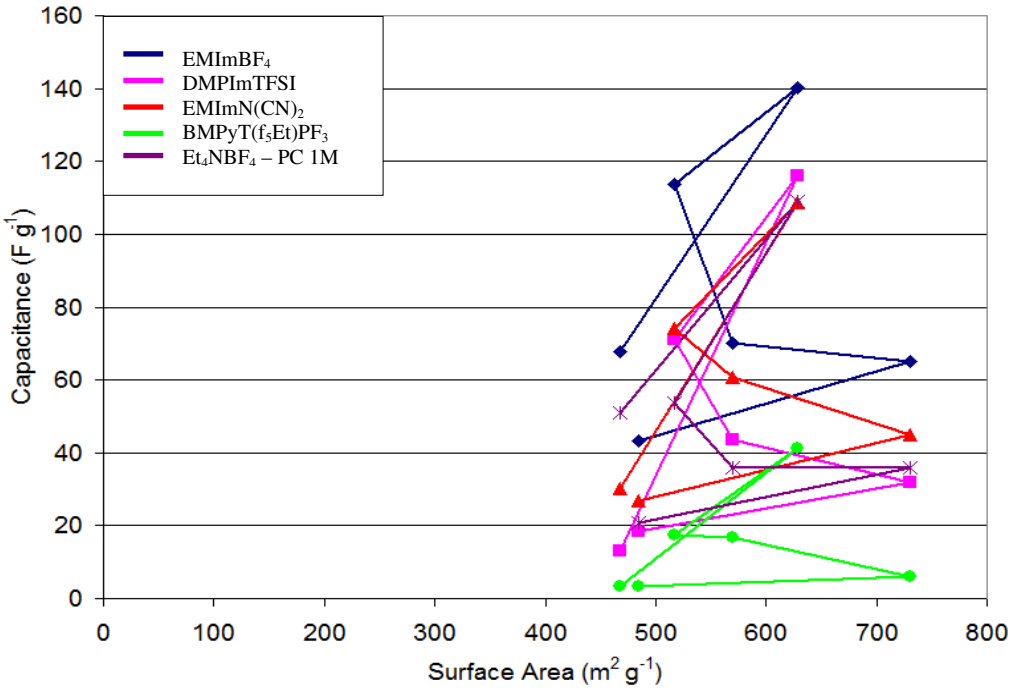

Figure 6.3 – Specific Capacitance vs. Surface Area

Another explanation for the results not obeying *Equation 1.1* could be based on the assumption that the thickness of the double-layer, *d,* is constant. This assumption may not hold for different size pores as the pores that provide the best fit for the ions will result in a smaller *d* than those that are left with empty pore volume. As no systematic trend in capacitive behaviour was shown for surface area, a comparison of average pore size of the electrodes and capacitance was carried out.

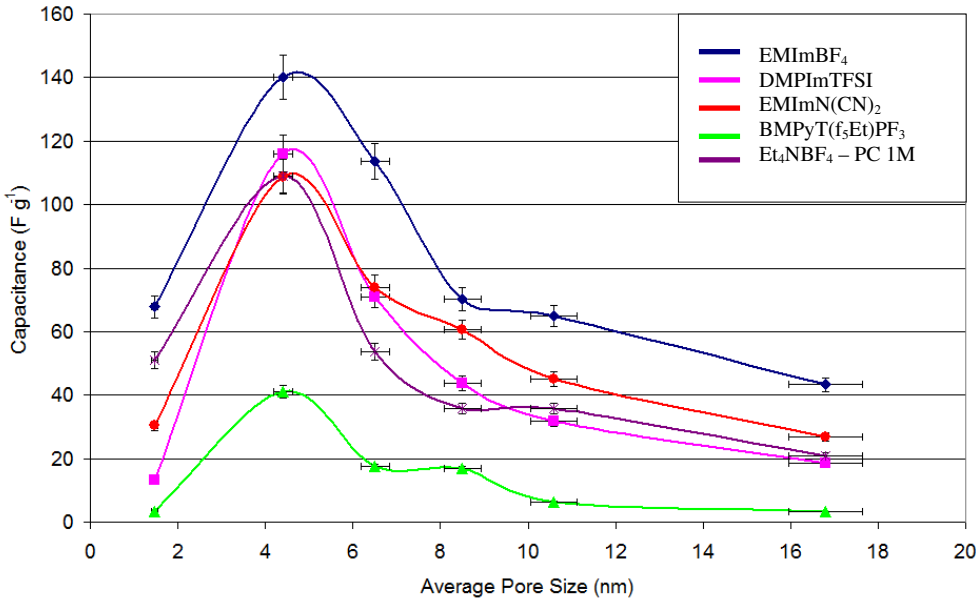

Figure 6.4 – Specific Capacitance vs. Pore Size

Figure 6.4 shows the change in specific capacitance of the six activated carbon samples with increasing pore size. Arbizzani *et al.* [62] assumed that increasing pore size whilst maintaining surface area enhances capacitor performance by providing wider pathways for ion transport, therefore reducing the resistance of the system. If this assumption were true then an increased value of normalised capacitance could be expected to occur with increasing pore size. However, a maximum specific capacitance was obtained for activated carbon electrode ACRF200-4.5nm for all electrolytes tested, i.e. activated carbon xerogel with d_{av} = 3 nm. For pores sizes greater or less than 4.5nm the specific capacitance was found to reduce. The high capacitance may be a result of the increased surface for double-layer formation as a result of ACRF200-4.5nm exhibiting a higher electrode surface area (640 m^2 g^{-1}) than the other composite electrodes (with the exception of ACRF500-10.6nm which exhibits the highest surface area of 730 m^2 g^{-1}). The decrease in specific capacitance that occurs above and below ACRF200-4.5nm may be related to the decrease in surface area that occurs with increasing pore size. However, ACRF100-1.5nm exhibits a lower specific capacitance than would be expected for the surface area (510 m^2 g^{-1}), which may indicate that the full surface of the electrode is not participating in double-layer charge storage.

To obtain a better understanding of the relationship between pore size, ion size and capacitive performance, the capacitance was normalised to the surface area of the composite electrodes, shown in *Figure 6.5*. The dimensions of the RTIL ions used for this study are shown in *Table 6.3*. The graph follows a similar trend to that of the specific capacitance vs. pore size in *Figure 6.4*.

As the normalised capacitance for ACRF100-1.5nm remains lower than the maximum normalised capacitance, the results continue to indicate that the full surface area present in the electrode is not being utilised for double-layer formation. The optimum capacitance performance still occurs at ACRF200-4.5nm for all electrolytes, indicating that this pore size allows for the best double-layer formation. That is, at this pore size the pores are large enough for the ions to access a large percentage of the surface area but small enough to allow for double-layer formation on the walls of the pore without excess electrolyte entering the pores, as shown in *Figure 6.6*. An excess of electrolyte in the pores may result in a significant increase in the double-layer thickness, d, or decrease in the dielectric constant, ε_r, of the electrolyte. This effect will be referred to as pore flooding. If the ions are able to fill the pore efficiently, i.e. without empty pore volume, this would also explain the large increase in capacitance for this activated carbon sample. For $EMImBF_4$ a small reduction in normalised capacitance is seen from ACRF200-4.5nm (0.223 F m^{-2}) to ACRF300-6.6nm (0.220 F m^{-2}). This could suggest that the small increase in pore size has not reduced ε_r and/or increased d for this electrolyte to same degree as with the other RTILs. This may be attributed to the higher bulk conductivity and weaker interaction from the anion and cation for this particular RTIL. [16]

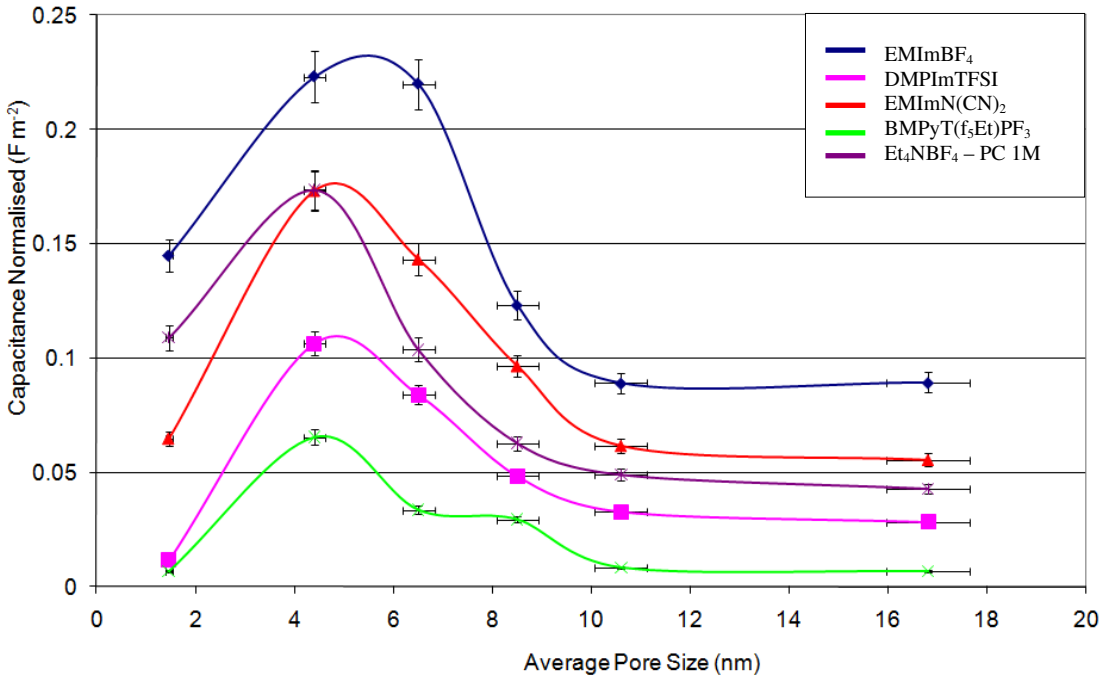

Figure 6.5 – Surface Area Normalised Capacitance vs. Pore Size

As the pore size increases, the normalised capacitance decreases and appears to plateau at ACRF500-10.6nm. This indicates that above this pore size the higher specific capacitance (F g^{-1}(carbon)) for ACRF500-10.6nm than ACRF750-16.5nm for all electrolytes (*Figure 6.4 and Table 6.2*) is due to the increased surface area. That is, the capacitance is independent of pore size and the traditional capacitor model described in *Equation 1.1* holds for large mesopores. These results may provide contradictory evidence to the models proposed by Huang *et al* [146], i.e. the traditional model only holds for macropores. The reduction in capacitance with increasing pore size could be attributed to a decrease in ε_r and electrolyte conductivity, or increase d that may occur as a result of pore flooding (excess electrolyte entering pores). Pore flooding may cause "solvation" of the anions with the cations or more likely ion pairing (demonstrated in *Figure 6.7*) where the attraction of the anion to the cation is greater than the attraction to the pore wall resulting in a higher concentration of neutral ion pairs. Large pores that become flooded with electrolyte may also create a situation where the ions in the pore compete for participation in the double-layer, with adsorbed ions exchanging with non-adsorbed ions in the same pore, as demonstrated in *Figure 6.6*. This could

weaken the strength of the double-layer causing an increase in *d*, which would result in a lower capacitance than would be expected based on surface area.

Comparing the low capacitance obtained for pore size < 2 nm and that obtained for pore sizes > 10 nm, it can be seen that for the electrolytes DMPImTFSI and BMPyT(f_5Et)PF_3, the normalised capacitance of ACRF100-1.5nm (0.028 and 0.003 F m^{-2} respectively) is lower than the normalised capacitance of ACRF500-10.6nm (0.044 and 0.006 F m^{-2} respectively) and ACRF750-16.5nm (0.038 and 0.005 F m^{-2} respectively). However, the decrease in capacitance can be attributed to different porous characteristics of the electrodes. ACRF100-1.5nm is 85 % vol. microporous with a peak pore size at 1.5 nm. The dimensions of the RTIL ions used for this study are shown in *Table 6.3*. Since the anion sizes of TFSI and T(f_5Et)PF_3 are 1.132 nm and 1.042 nm, respectively, the anions will have limited access to the full surface of the electrode, this results in a lower capacitance. For the other electrolytes studied ACRF100-1.5nm shows higher normalised capacitance than for ACRF500-10.6nm and ACRF750-16.5nm, indicating that the electrolytes are able to access the larger micropores of the electrode resulting in better performance for ACRF100-1.5nm. However, as the charge/discharge rate increases, electrolyte penetration may become hindered and could result in less surface area being accessed. As a consequence, the formation of an effective double-layer could fail notably at high current density causing the energy and power density of the EDLCs drop. This will be discussed further in **Section 6.2.2**.

Table 6.3 – Ionic Liquid Cation and Anion Dimensions

(Data Courtesy of Dr C. Arrouvel of the University of Bath)

Cations	**Length (nm)**	**Width (nm)**	**Breadth (nm)**
1-ethyl-3-methylimidazolium ($EMIm^+$)	0.948	0.676	0.537
1,2- dimethyl-3-propylimidazolium ($DMPIm^+$)	1.135	0.773	0.549
1-butyl-1-methylpyrrolidinium ($BMPy^+$)	1.275	0.771	0.663
Anions			
Tetrafluoroborate (BF_4^-)	0.515	0.515	0.515
bis(trifluoromethylsulfonyl)imide ($TFSI^-$)	1.132	0.838	0.553
Dicyanamide ($N(CN)_2^-$)	0.755	0.43	0.34
tris(pentafluoroethyl)trifluorophosphate ($T(f_5Et)PF_3^-$)	1.042	1.042	0.652

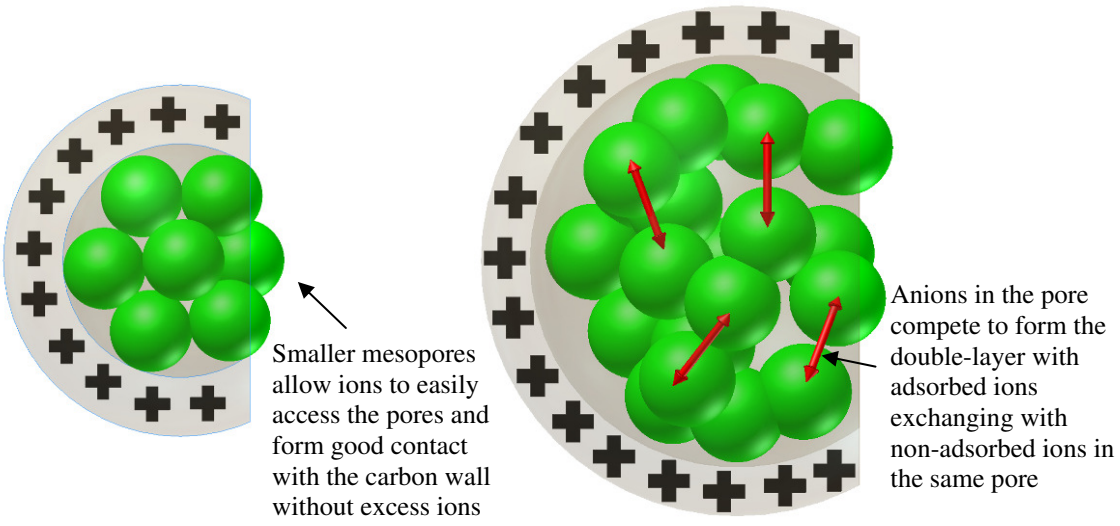

Figure 6.6 – Proposed mechanism of pore flooding leading to ions at double-layer and bulk exchanging

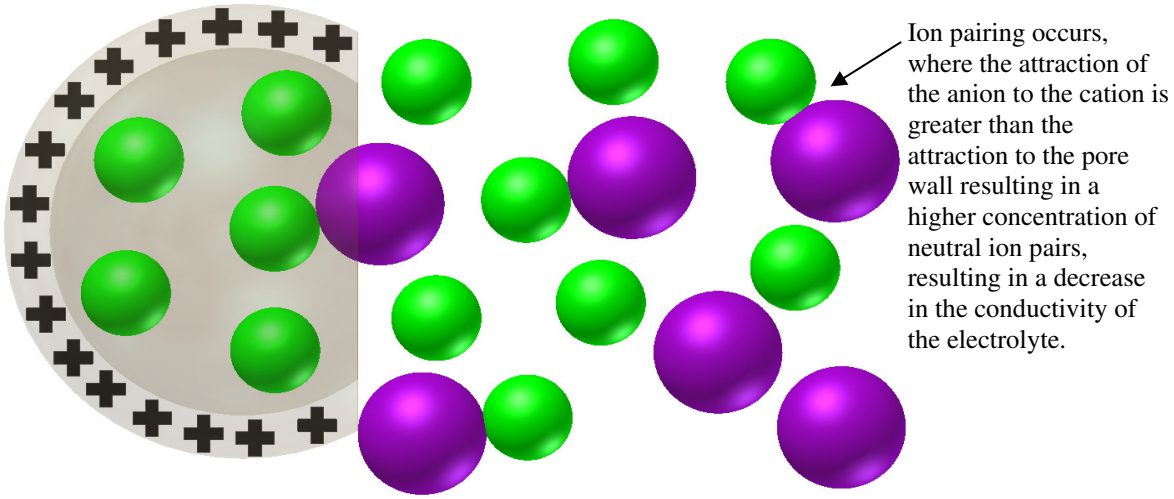

Figure 6.7 – Proposed mechanism of pore flooding leading to ion pairing in RTIL electrolytes

6.2.2 Variation of Rate Performance with Pore Size

Although obtaining maximum capacitance is the main aim for most EC research, consideration must be given to the performance of the capacitors at high charge/discharge rate. The performance of the capacitors at high current density also gives an indication of the resistance of the cell, as high resistance becomes more apparent at higher current density according to the voltage drop *V= IR*. *Figures 6.8 and 6.9* show the rate capability of RTIL EMImBF$_4$ with the six activated carbon samples and the capacitance at maximum discharge current normalised to that at low discharge current for all electrolytes tested. RTIL BMPyT(f$_5$Et)PF$_3$ does not allow for charging at the highest current density due to the high viscosity and low conductivity. [126] The microporous sample ACRF100-1.5nm exhibits a poor rate capability, retaining only 30% of the specific capacitance obtained at 2 mA cm^{-2} when the current density is increased to only 4 mA cm^{-2}. Indicating the mass transfer of the ions becomes limited and they are presumably unable to access the pores/double-layer rapidly enough to access the surface area of the electrode with increasing discharge rate. As a consequence, the formation of the double-layer fails at high current density resulting in low capacitance. The hindering of ion transfer also results in an increase in resistance leading to poor power performance at high discharge rate. Indicating micropores are detrimental to mass transfer kinetics of the system.

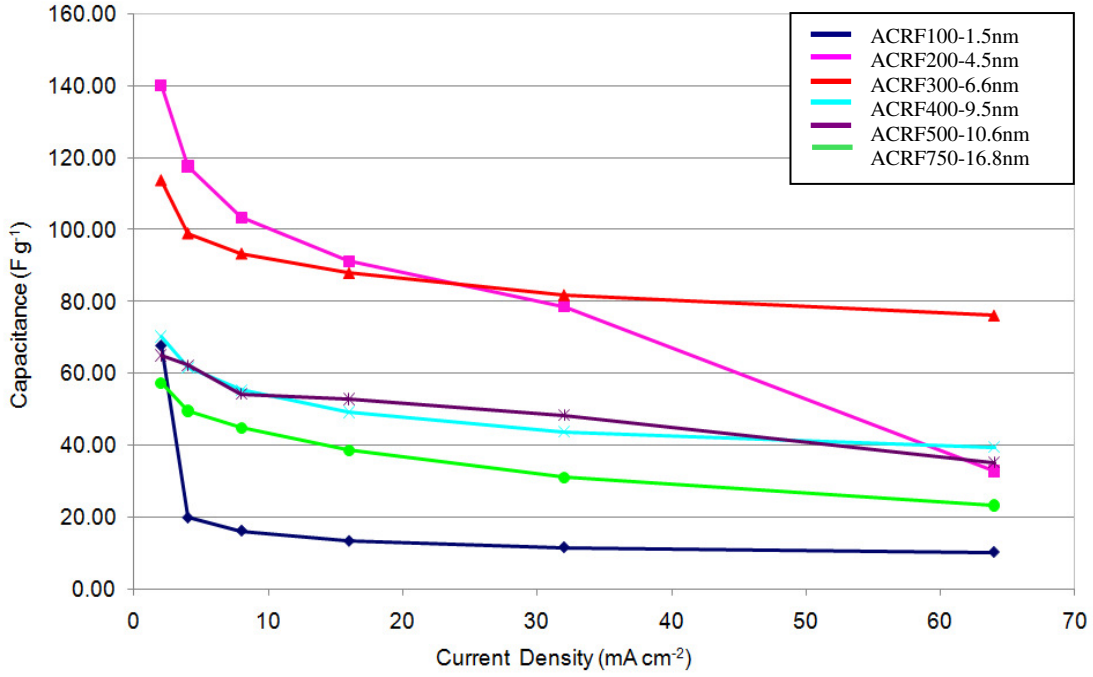

Figure 6.8 – Specific Capacitance vs. Current Density for $EMImBF_4$

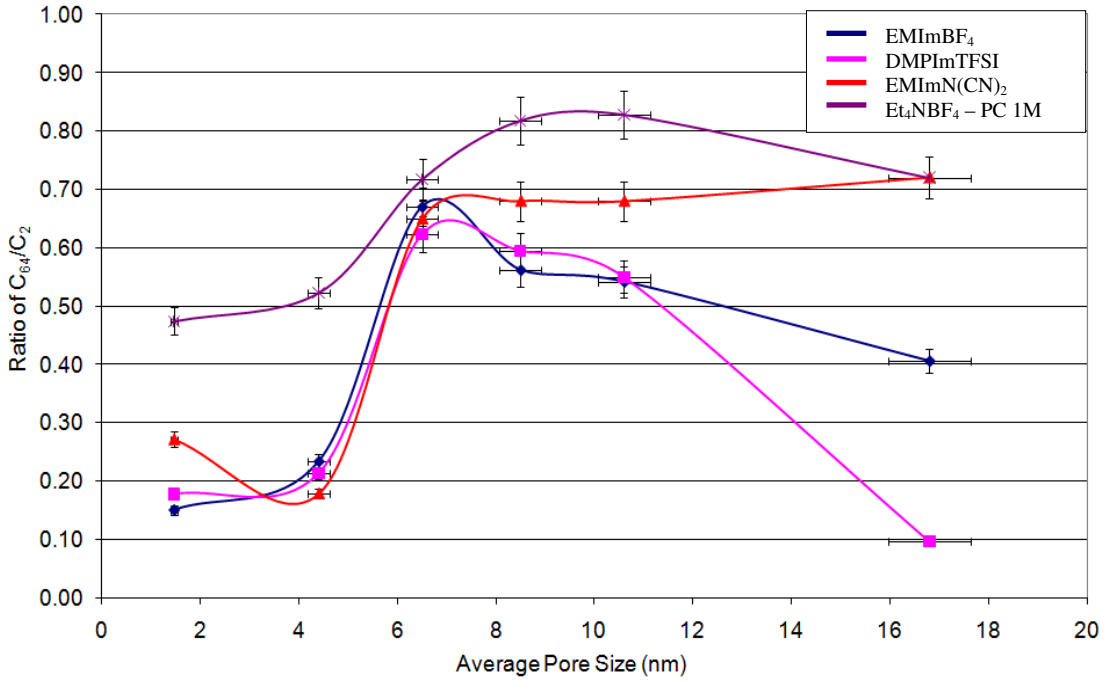

Figure 6.9 – Current Density Ratio vs. Pore Size

Even though the pores of ACRF200-4.5nm are large enough to allow for easy ion access, a large reduction in capacitance with increasing current density occurs. This can be attributed to more than one factor. ACRF200-4.5nm still exhibits a large volume of micropores and so suffers from the same problems as ACRF100 at higher current densities. As mentioned above the high capacitance of ACRF200 could be due to the mesopores being efficiently filled with little empty pore volume left within each pore. At higher current density the pores will not have time to fill efficiently (as demonstrated in *Figure 6.10*), and the capacitance of ACRF200-4.5nm will be affected more than those that are not efficiently filled even at low charge-discharge rates; and the last reason could be due to "gate" effects at the pore opening, either due to the pore shape being that of an ink bottle or due to partial blocking by other particles in the composite electrode. However due to activation of the samples, gate effects associated with narrow ink bottle pore openings should have been reduced. ACRF300-6.6nm provides the best rate capability for all the RTIL electrolytes, indicating that the larger mesopores allow the ions to access the pores from the bulk and return to their initial state quickly enough, improving dynamic performance of the EDLCs. This shows that the material chosen for EDLC application will be dependant on the requirement for high charge rates or high capacitance.

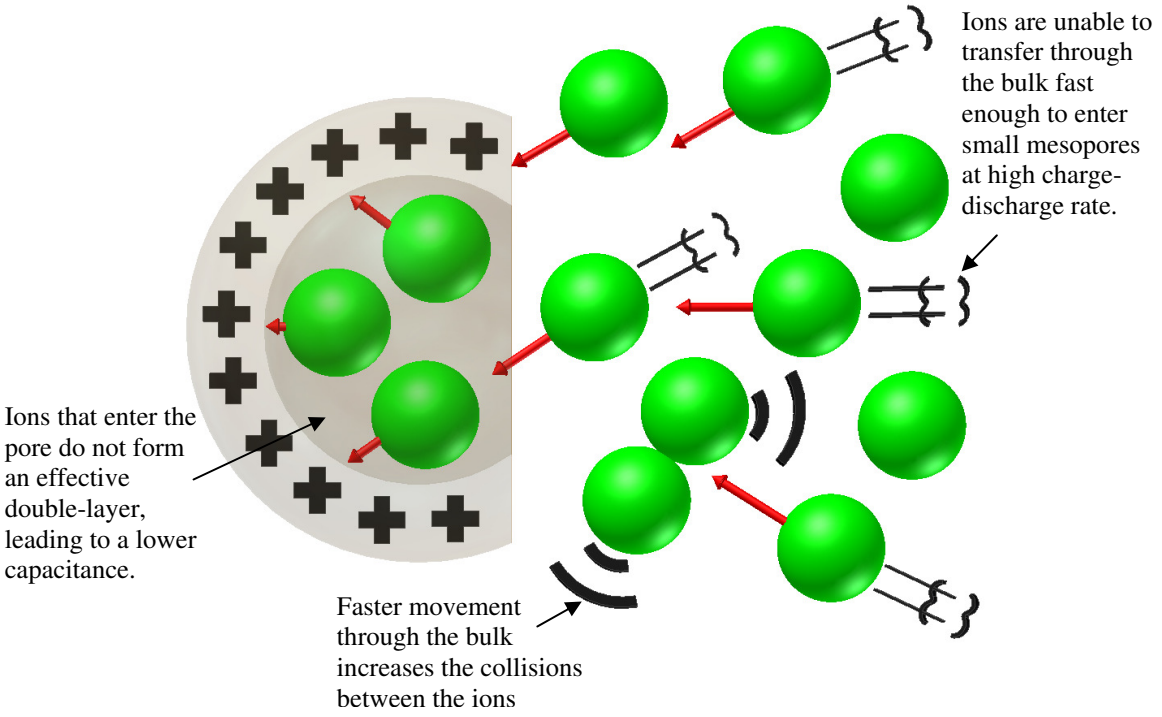

Figure 6.10 – High Charge-Discharge Rate Schematic for ACRF200

Above ACRF300-6.6nm, the rate capability for $EMImBF_4$, DMPImTFSI and $BMPyTf_5Et_3PF_3$ reduces. For organic electrolyte Et_4NBF_4 – PC 1M, the rate capability peaks at ACRF400-9.6nm before reducing at the larger pore diameters. The increase in the optimum pore diameter could be due to the large solvation shell surrounding the organic electrolyte ions (1.35 nm[199]). This contributes to the hypothesis that at larger pore sizes the double-layer formation is hindered resulting in poor performance. The rate performance of RTIL $EMImN(CN)_2$ becomes constant in samples above ACRF300-6.6nm, indicating this RTIL's conductivity is not affected when the pores become flooded with electrolyte. This could also be attributed to an already low capacitance, as a consequence of the low concentration of $N(CN)_2^-$ due to formation of the neutral dimmer $(CN)_2N – N(CN)_2$ on overcharging. [196]

6.2.3 Literature comparison

The results obtained in **Sections 6.2.1 and 6.2.2** apparently contradict recent developments indicating that microporosity is the best way to optimise the capacitance of ECs. This is true on the basis that a larger surface area and lower pore volume are only possible through the use of microporosity, which would result in the highest specific and volumetric capacitances. However, the studies that make these claims [139-144] carried out the electrochemical measurements at very low current density (0.1 - 6 A g^{-1}) and the capacitance variation with increasing current density was not reported. That is, the capacitance was only reported for the lowest current density where the capacitance is highest. This study operated in the range of 1 – 32 A g^{-1}. The reduced current densities utilised in the above studies [139-144] were sufficiently low that any limitations that may occur due to slow mass transfer in micropores were not apparent.

Measurements at the optimum pore size found in these studies were not carried out due to the materials constraints of forming controlled porosity centred at 0.7nm. However, poor rate performance for the microporous carbon ACRF100-1.5nm and ACRF200-4.5nm was found. This suggests that pores small enough to cause ion distortion or desolvation may not allow for high charge-discharge rates.[140] The capacitance values obtained in the literature [141] are also only marginally higher (160

F g^{-1}) than that found in this study (140 F g^{-1}). The studies carried out on the distortion of ions in pores utilised RTILs at elevated temperature of 60°C and very low scan rate to specifically allow for any kinetic restrictions imposed by the viscosity of the RTILs to be disregarded. [144] It has also recently been demonstrated by Aurbach *et al.*[199] that pores small enough to cause ion desolvation, result in the ions becoming trapped in the pores. This causes a large increase in the ESR which is not viable for the implementation of ECs.

6.2.4 Variation of Capacitance with Ionic Liquid Electrolyte

As values of dielectric constant at the interface are not available for RTILs, and to allow for analysis of the capacitive performance of different RTIL electrolytes, the ions can be termed as "soft" or "hard" ions depending on where the delocalised charge is situated, as outlined by Lazzari *et al.* [63]. The EMIm cation is a "soft" ion due the charge delocalised on the imidazolium aromatic ring, this increases the dielectric constant as the ion - ion attraction is lower. BMPy is a "hard" cation due to the stronger charge situated on the sp^3 nitrogen atom. Consequently, the RTIL utilising this cation exhibits stronger ion – ion interaction and a lower ε_r due to lower volume of dissociated ions. The effect of the "soft" and "hard" cations on the mass transport properties can be seen, with the BMPy based ionic liquid exhibiting the highest viscosity (0.221 Pa.s@ 25°C) and lowest conductivity. [16, 126]

Viscosity is not the only factor to affect the conductivity of the electrolytes; ionic size must be taken into account. That is, a small anion coupled with a "soft" cation will produce the highest conductivity. The best capacitive performance was obtained for $EMImBF_4$ as shown in *Table 6.2*; this electrolyte combines the "soft" EMIm cation with the small "weakly coordinating" anion BF_4. This combination, based on the theory given above (determining degree of dissociation in the absence of dielectric constant values), gives rise to the RTIL with the apparent highest ε_r of those tested in this study. The small BF_4 symmetrical anion (0.515 nm) also allows for the highest density of ions to form at the double layer and for the smallest *d,* thus increasing the capacitance. The small ion size coupled with the lower viscosity (0.037 Pa.s@ 25°C) and relatively high conductivity results in the best performance. [16, 17]

DMPImTFSI provides the next best capacitive performance. The TFSI anion is weakly charged as the negative charge is delocalised across the two trifluoromethylsulphonyl groups, which should result in a relatively high ε_r. [182] The reduction in the capacitance for DMPImTFSI may be partially attributed to the increase in viscosity to 0.108 Pa.s @ 25°C due to the bulkier DMPIm cation. Studies in the literature may be used to confirm this hypothesis [113, 183]. It was shown in these studies that the RTIL combining the EMIm cation with the TFSI anion exhibits a low viscosity (for an RTIL) of 0.034 Pa.s @ 25°C [24] and provided high specific capacitance of 160 F g^{-1}. [143] The lower capacitance could also result from the reduced density of ions at the double-layer and an increase in *d* due to the larger ions involved.

The initial conclusion from the diminishing capacitance of the $EMImN(CN)_2$ would be the electrolyte is surpassing the stable voltage with each charge-discharge cycle. This could be justified as the fluorine bonds of the other electrolytes are stronger and able to withstand cycling at high voltage where the dicyanamide cannot. However, as the capacitance can be seen to reach a minimum capacitance with no further degradation, this suggests that another factor may be affecting the performance of this electrolyte. The dicyanamide anion is known to undergo irreversible oxidation forming a neutral dimmer $(CN)_2N - N(CN)_2$ on over charging. [196] The strong van der Waals forces associated with the dicyanamide ions may also cause charge to be weakened leading to ion-pairing and therefore the adsorption of the ions to the pore wall is reduced resulting in a diminishing capacitance.

The poor capacitance performance of $BMPyT(f_5Et)PF_3$ could be attributed to the very high viscosity (0.221 Pa.s @ 25°C), reducing the mobility of the ions and resulting in a weaker interaction between the electrode and electrolyte ions in the double-layer. However, the orientation of the ion under the applied electric field and its stereochemistry are also important for double-layer thickness. The ethyl groups of $T(f_5Et)PF_3$ and the strong interaction with the cation hinder the reorientation of the anion on charge/discharge, leading to poor performance at high current rates and an increased *d* compared with that estimated from the anion size. As a consequence the capacitance performance of this electrolyte is poor for all activated carbons analysed, despite it having a higher operating voltage than the other RTIL electrolytes.

The capacitance of the organic electrolyte was expected to exhibit a higher capacitance than the RTILs, however, due to the large solvation shells (1.35 nm [199]) associated with organic electrolytes the ion density at the double-layer is reduced and the *d* is not the diameter of the anion (BF_4) as for RTIL $EMImBF_4$, but the diameter of the ions plus that of the propylene carbonate solvent molecule. Therefore, the capacitance is lower than expected for the electrolyte based on low viscosity and high conductivity of solution.

Figure 6.11 shows the relationship between the electrolyte viscosity and the capacitance performance. The graph shows that the trend for viscosity and capacitance does not follow a linear pattern, particularly in the lower viscosity region. This confirms the discussion above, both that ion size is a contributing factor in determining capacitance performance, and that the electrolytes $EMImN(CN)_2$ and Et_4NBF_4 – PC 1M have lower capacitances than would be expected from their comparatively low viscosities of 0.024 and 0.004 Pa.s @ 25°C, respectively.

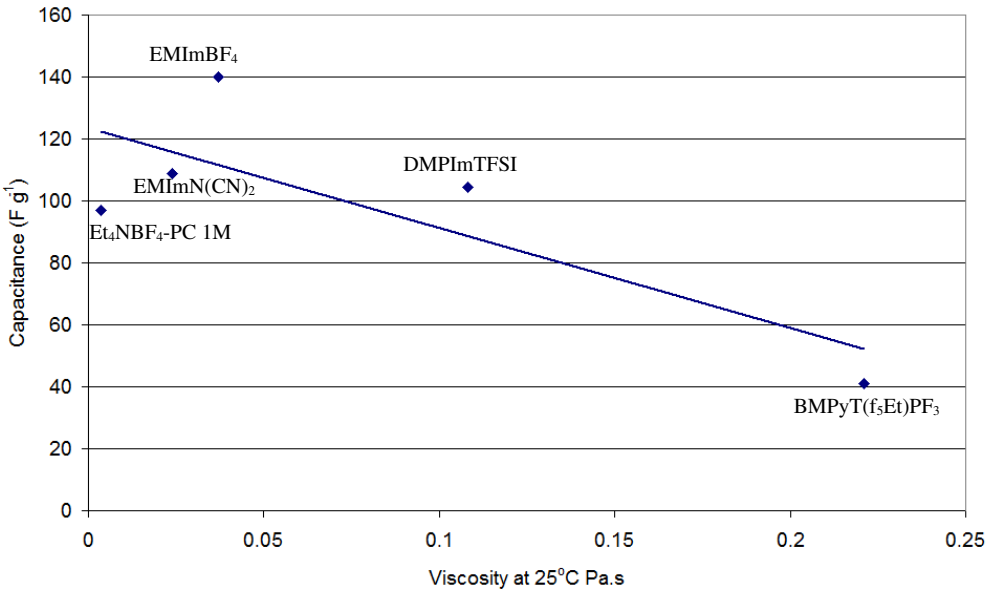

Figure 6.11 – Effect of Viscosity on Capacitance Performance

6.3 Electrochemical Impedance Spectroscopy

The electrochemical impedance spectroscopy results are summarised in *Table 6.4*. *Figure 6.12* shows the Nyquist complex plane plot obtained for $EMImBF_4$ and *Figures A2.1 – A2.4* in *Appendix A* show impedance results for all other electrolytes and activated carbons studied. As previously outlined in **Section 3.3.3**, electrolyte resistance (R_S) was estimated from the crossover point of the highest frequency with the real part of the impedance and ionic resistance (R_I) was estimated from the diameter of the semicircle. The equivalent series resistance (ESR) was recorded at 1 kHz, which was used for the calculation of power density (P_{max}) as in *Equation 1.3*. The *ESR* of an EC is the sum of various contributions, such as the electrolyte resistance, the active material resistance, the binder and carbon black resistance, and the active material/current collector interface resistance.

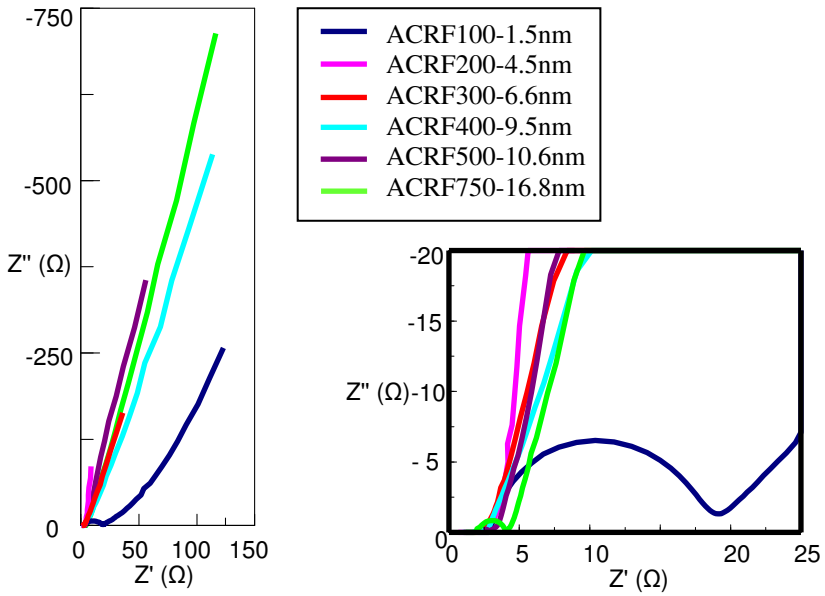

Figure 6.12 – (a) Nyquist Plot for $EMImBF_4$, (b) Expanded high frequency region

Table 6.4 – Frequency Dependant Capacitance and Resistances

Sample	Capacitance @ 10 mHz ± 5% ($F\ g^{-1}$)	ESR @ 1 kHz ± 0.1 Ω	Ionic Resistance ± 0.1 Ω	Electrolyte Resistance ± 0.1 Ω	AC Power Density ± 100 $W\ kg^{-1}$
Electrolyte: $EMImBF_4$					
ACRF100-1.5nm	51.5	18.0	16.1	2.9	78100
ACRF200-4.5nm	92.6	2.1	0.5	1.8	665500
ACRF300-6.6nm	61.0	2.1	0.6	2.0	662400
ACRF400-9.5nm	45.3	3.9	0.3	2.3	360400
ACRF500-10.5nm	32.3	4.1	1.0	3.0	342400
ACRF750-16.5nm	37.5	10.2	8.8	1.7	137600
Electrolyte: DMPImTFSI					
ACRF100-1.5nm	16.9	17.6	9.3	8.6	51800
ACRF200-4.5nm	65.6	15.5	6.1	9.6	82100
ACRF300-6.6nm	49.9	12.7	3.2	9.5	79900
ACRF400-9.5nm	33.1	14.8	2.8	12.1	76800
ACRF500-10.5nm	28.5	22.9	9.5	14.1	61300
ACRF750-16.5nm	15.2	41.6	23.0	20.3	27400
Electrolyte: $EMImN(CN)_2$					
ACRF100-1.5nm	26.5	1.2	0.1	1.1	822100
ACRF200-4.5nm	82.8	5.6	2.8	2.9	139600
ACRF300-6.6nm	47.2	2.1	0.8	1.3	468400
ACRF400-9.5nm	36.8	2.1	0.9	1.2	468900
ACRF500-10.5nm	35.9	2.2	1.0	1.2	436800
ACRF750-16.5nm	26.9	4.0	2.0	2.0	242700
Electrolyte: $BMPyT(f_5Et)PF_3$					
ACRF100-1.5nm	2.8	27.3	8.1	19.2	70180
ACRF200-4.5nm	23.5	34.0	10.2	24.2	45000
ACRF300-6.6nm	16.5	18.4	4.3	14.1	139000
ACRF400-9.5nm	15.8	24.2	2.7	21.4	79300
ACRF500-10.5nm	12.6	34.4	12.2	23.1	22700
ACRF750-16.5nm	5.6	34.9	8.5	27.3	32900
Electrolyte: Et_4NBF_4 – PC 1M					
ACRF100-1.5nm	40.9	3.1	0.4	2.5	320400
ACRF200-4.5nm	96.1	3.5	0.6	2.7	144800
ACRF300-6.6nm	50.4	2.7	-	2.5	421300
ACRF400-9.5nm	40.8	2.5	0.4	2.4	528100
ACRF500-10.5nm	43.0	3.0	0.4	2.5	470600
ACRF750-16.5nm	13.9	4.1	2.1	2.0	237800

Overall the results obtained for EIS confirm those for GC measurements, however, the lower capacitance for EIS than for GC is due to the full surface available for double-layer formation not being utilised until very low frequencies are attained. Due to the high surface area of the activated carbons, the full surface is still not fully accessed at 10 mHz. The complex plane plot consists of a small semicircle at high frequencies followed by a vertical spike at low frequencies indicating pure double layer behaviour.

6.3.1 Variation of Resistance with Ionic Liquid Electrolyte

From *Table 6.4*, it can be seen that the electrolytes give rise to a large variation in resistance. The order of R_S from lowest to highest is $EMImN(CN)_2$ > $EMImBF_4$ > Et_4NBF_4 – PC 1M > DMPImTFSI > $BMPyT(f_5Et)PF_3$.

As R_S is only associated with the resistance of the electrolyte itself, it would be expected to be little affected by the variation in pore size. From *Table 6.4* it can be seen that R_S remains relatively constant with variation in pore size. The ionic resistance, R_I, can be seen to vary with pore size and the causes of this variation will be discussed later in **Section 6.3.2.**

Figure 6.13 shows the effect of viscosity on the capacitance, R_S and ESR for ACRF200. It was observed that both R_S and ESR increase with increasing viscosity following close to a linear relation. The graph also demonstrates an improved correlation of resistance to viscosity over that which was drawn between capacitance and viscosity with the R^2 increasing to 0.932 and 0.958 for ESR and R_S, respectively, from 0.637 for specific capacitance. Although the general trend for decreasing capacitance with increasing viscosity is still apparent.

The impedance results in *Table 6.4* show that producing the highest capacitance does not equate to providing the lowest ESR. This in turn influences the maximum power density (P_{max}) of the electrolytes, with the most marked effect on DMPImTFSI. This electrolyte gives rise to the second highest GC capacitance of 104 F g^{-1} for ACRF200-4.5nm making it the desirable choice over $EMImBF_4$, due to the high current spikes that occur on overcharging for $EMImBF_4$. However, due to the high resistances (ACRF200-4.5nm R_S = 9.6 Ω and ESR = 15.5 Ω) combined with a

lower operating voltage of 2.7 V, the maximum power density achieved is 82.1 kW kg^{-1}. This is lower than that of BMPyT(f_5Et)PF_3 which displayed the lowest GC capacitance for ACRF200-4.5nm of 41 F g^{-1}. Due to the increased operating voltage of 3.5 V, a maximum power density of 139 kW kg^{-1} was achieved for ACRF300-6.6nm.

For all electrolytes studied, the ionic resistance, R_I, reaches a minimum for optimum pore size, however, the pore size which this occurs at differs for each electrolyte. At this optimum pore size the ions are able to travel less hindered during charge-discharge before the effect of 'pore flooding' reduces the efficiency of the system. For the RTIL electrolytes the pore size where the minimum R_I occurs increases with increasing viscosity. This indicates that the resistance is more highly related to the viscosity of the electrolyte than to anion size. The $N(CN)_2^-$ anion is 0.25 nm greater than BF_4^-, if the anion dictated the optimum pore size the optimum would occur at a lower pore size for BF_4^- than for $N(CN)_2^-$. However, the lowest R_I of 0.1 Ω occurs in microporous carbon ACRF100-1.5nm for $EMImN(CN)_2$, whereas for $EMImBF_4$, the lowest R_I of 0.5 Ω occurs for ACRF200-6.6nm where no semi-circle appears, indicating close to ideal behaviour. For DMPImTFSI and BMPyT(f_5Et)PF_3 the minimum R_I = 2.8 and 2.7 Ω, respectively, occurs for the larger pore size of ACRF400-9.6nm.

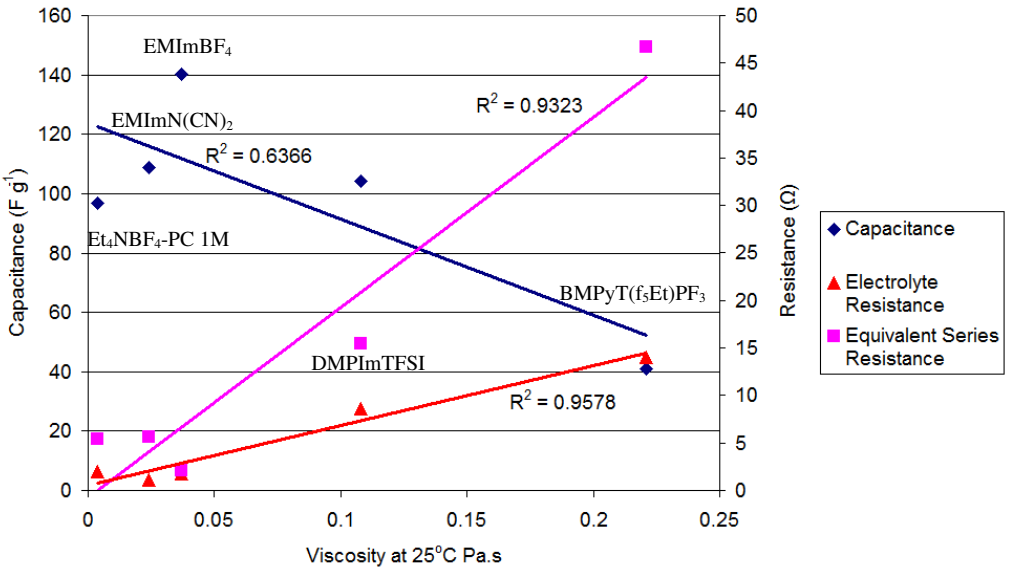

Figure 6.13 – Effect of Viscosity on Capacitance and Equivalent Series Resistance

6.3.2 Variation of Resistance with Pore Size

The higher values of ESR and R_I exhibited by ACRF100-1.5nm for all electrolytes studied (except EMImN$(CN)_2$) could be attributed to the high volume of inaccessible micropores contained within the structure. The ESR and R_I reduce as the ions access more of the electrode structure until the pores reach the optimum diameter, as discussed above, for lowest resistance. Above this pore diameter, 'pore flooding' results in an increase in ESR and R_I as the ion swapping at the double-layer (*Figure 6.6*) or ion pairing (*Figure 6.7*) increase d and/or decrease ε_r. This could be responsible for the lower capacitance and increase in the ESR and R_I as charged ions must compete (either with each other or with neutral pairs) for space inside the pores. ACRF300-6.6nm and ACRF400-9.6nm exhibit lower R_I (and ESR) values than ACRF200-4.5nm for all electrolytes, except EMImBF_4 where the lowest R_I occurs for ACRF200-4.5nm. This could be due to more rapid mass transfer within the larger pores of the structure. Above this pore size the increase in ESR and R_I may be a result of decrease in ε_r / conductivity within the pores. The absence of a semi-circle (i.e. low R_I) for EMImBF_4 for ACRF200-4.5nm and ACRF300-6.6nm indicates close to ideal behaviour due to high conductivity across the electrode. This shows that the ε_r of the electrolyte in the pores of the two carbon samples is higher than for the larger pore sizes, adding to the proposed theory of 'pore flooding'.

A distinction can be made between the high ESR of ACRF200-4.5nm and that which occurs with increasing pore size. The higher ESR than would be expected for ACRF200-4.5nm (due to the high capacitance performance) can be attributed to the high degree of microporosity still occurring in the structure. The angle of the capacitive component from the complex plane impedance (Nyquist) plot can be used to determine the ideal nature of the double-layer. Deviation from 90° occurs when the interface is not ideally polarisable. It can be seen from *Table 6.5* that ACRF200-4.5nm exhibits the closest to 90° from the x-axis, indicating d is at a minimum for sample. As pore size is increased the angle increases. This may be attributed to a decrease in ε_r and increase in d.

Table 6.5 –Angle of Capacitive Component of Nyquist Plot

Electrolyte / Sample	$EMImBF_4$	DMPImTFSI	$EMImN(CN)_2$	$BMPyT(f_5Et)PF_3$	Et_4NBF_4 – PC 1M
ACRF100	124°	134°	99°	119°	104°
ACRF200	95°	99°	112°	112°	92°
ACRF300	107°	103°	98°	107°	105°
ACRF400	109°	105°	93°	100°	100°
ACRF500	105°	112°	94°	100°	100°
ACRF750	105°	110°	95°	97°	106°

6.3.3 Electrochemical Impedance Spectroscopy Data Fitting Models

To obtain useful data from EIS, equivalent circuits must be utilised that best describe the behaviour of the system. The EIS data discussed above is fitted using the Randles circuit as shown in **Section 3.2.2**. To ensure that this was the best fit model, the data obtained was run through the Randles circuit model and another model suggested in the literature; the 3-branch model as suggested by Bonert and Zubieta, [178,179] (pictured in **Section 3.2.2**). As the modelling software could not accommodate the voltage dependant capacitance in the original 3-Branch model this was removed and replaced by a non-voltage dependant component, as shown in *Figure 6.14*.

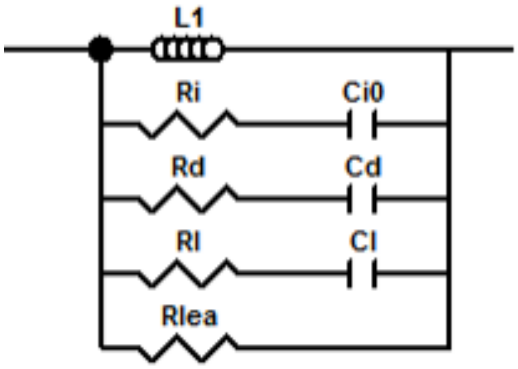

Figure 6.14 – Modified 3-Branch Model

Where, R_i and C_{i0} are the resistance and capacitance at the pore opening, R_d and C_d are the intermediate resistance and capacitance, and, R_l and C_l are the resistance and capacitance at the base of the pore. R_{lea} is the leakage resistance and can be related to the self-discharge of the system.

Each model was run for ACRF200 with all electrolytes. The results for the modified 3-Branch Model are shown in *Table 6.6* and the Nyquist Plots for the Randles circuit and 3-Branch Model are shown in *Figures 6.15* and *6.16* respectively.

For comparison purposes, for each model the same readings as used on the experimental data were recorded from each Nyquist Plot of the fit results and are shown in *Table 6.7*. It can be seen from this data that no one model gives best fit for all electrolytes. The greatest %errors occur for $EMImBF_4$ for the ionic resistance, R_I,

of 16, 20 and 30% for the Randles, 3-Branch and 3-Branch with Warburg circuits, respectively. This is due to the formation of the semi-circle associated with R_I which is not present in the experimental data.

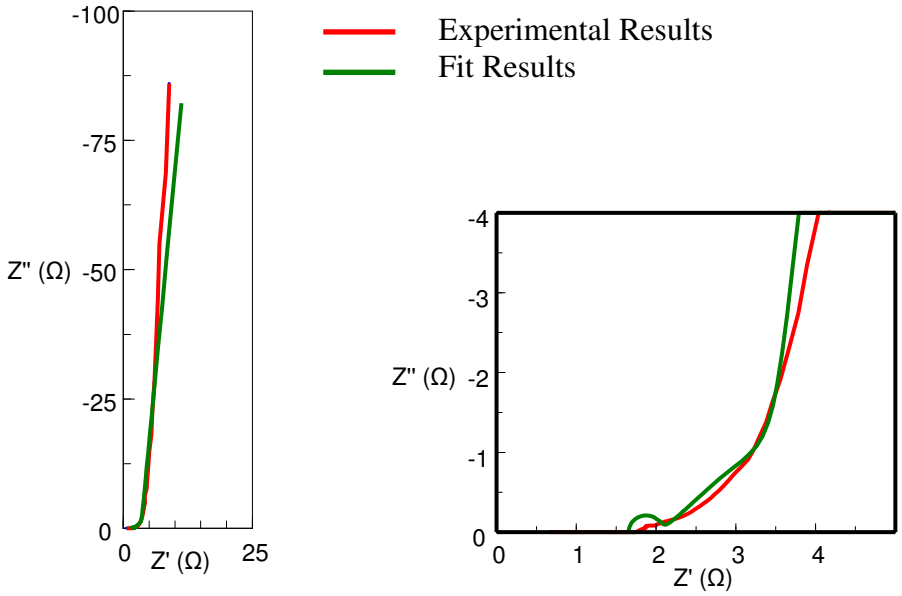

Figure 6.15 – Nyquist Plot Fit Results for Randles Circuit for ACRF200/EMImBF$_4$

Table 6.6 – ACRF200 Fit Results for Modified 3-Branch Model[8]

Parameter \ Electrolyte	EMImBF$_4$	DMPImTFSI	EMImN(CN)$_2$	BMPyT(f$_5$Et)PF$_3$	Et$_4$NBF$_4$ – PC 1M
R_i (Ω)	5.8 ± 7.5%	46.25 ± 8.4%	15.9 ± 6.7%	123.9 ± 7.7%	19.0 ± 8.3%
C_{i0} (F)	$5x10^{-3}$ ± 20.0%	$1x10^{-3}$ ± 23.7%	$2x10^{-3}$ ± 19.0%	$7x10^{-4}$ ± 21.3%	$2x10^{-3}$ ± 24.0%
R_d (Ω)	3.9 ± 6.9%	26.5 ± 3.8%	9.2 ± 3.1%	101.9 ± 4.9%	7.8 ± 2.8%
C_d (F)	0.2 ± 2.8%	0.1 ± 5.4%	0.1 ± 3.1%	0.03 ± 6.8%	0.2 ± 3.0%
R_l (Ω)	6.9 ± 9.9 %	26.8 ± 8.2%	5.75 ± 5.8%	44.1 ± 11.7%	10.3 ± 8.1%
C_l (F)	$9x10^{-6}$ ± 26.0%	$3x10^{-7}$ ± 17.4%	$5x10^{-7}$ ± 9.7%	$5x10^{-7}$ ± 11.7%	$3x10^{-7}$ ± 15.1%
R_{lea} (Ω)	682.9 ± 45.9%	515.6 ± 28.6%	272.7 ± 13.1%	785.4 ± 14.6	799.3 ± 53.2%

[8] Errors are associated with fit of model to the experimental data.

Table 6.7 – Fit Results for EIS Circuits

Electrolyte / Model	$EMImBF_4$		DMPImTFSI		$EMImN(CN)_2$		$BMPyT(f_5Et)PF_3$		Et_4NBF_4 – PC 1M	
Electrolyte Resistance										
	R (Ω)	Error	R (Ω)	Error	R (Ω)	Error	R (Ω)	Error	R (Ω)	Error
Experimental	1.78	N/A	9.59	N/A	2.85	N/A	24.16	N/A	2.74	N/A
Randles	1.66	6.7%	10.10	5.3%	2.85	0	23.77	1.6 %	2.72	0.9 %
3-Branch	1.73	2.8%	10.14	5.7%	2.87	0.7 %	23.90	1.1 %	2.77	1.1 %
3-Branch w/Warburg	1.61	9.6%	10.08	5.1%	2.85	0	23.78	1.6 %	2.75	0.3 %
Ionic Resistance										
	R (Ω)	Error	R (Ω)	Error	R (Ω)	Error	R (Ω)	Error	R (Ω)	Error
Experimental	0.50	N/A	6.10	N/A	2.75	N/A	10.81	N/A	1.85	N/A
Randles	0.40	20.0%	5.31	12.9%	2.53	8.0%	8.63	20.2%	0.58	10.0%
3-Branch	0.58	16.0%	6.17	1.2%	2.85	3.6%	10.91	0.9%	0.66	3.2%
3-Branch w/Warburg	0.35	30.0%	5.56	8.9%	2.65	3.6%	9.96	7.9%	0.63	2.2%
Capacitance										
	C ($F\ g^{-1}$)	Error	C ($F\ g^{-1}$)	Error	C ($F\ g^{-1}$)	Error	C ($F\ g^{-1}$)	Error	C ($F\ g^{-1}$)	Error
Experimental	92.58	N/A	65.57	N/A	82.81	N/A	23.52	N/A	96.10	N/A
Randles	97.94	5.8%	69.20	5.5%	84.88	2.5%	26.52	12.8%	95.53	0.6%
3-Branch	89.01	3.9%	63.92	2.5%	78.28	5.5%	25.17	7.0%	94.87	1.3%
3-Branch w/Warburg	95.76	3.4%	67.78	3.4%	85.05	2.7%	25.77	9.6%	98.73	2.7%

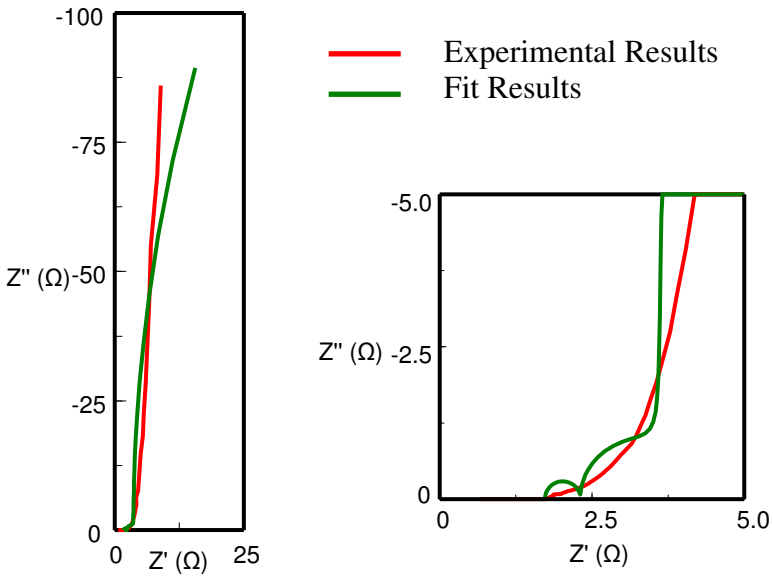

Figure 6.16 – Nyquist Plot for Results for 3-Branch Circuit for ACRF200/EMImBF$_4$

Although the 3-Branch model provides a good fit to the experimental data for the high frequency semi-circle, it does not take into account diffusion (modelled as a Warburg component). In *Figure 6.16* a second semi-circle is formed before capacitor behaviour is followed, where a 45° angle tail should occur due to diffusion at the double-layer. On adding a Warburg component in parallel to the initial capacitance (shown in *Figure 6.17*) the model fits closely with the high and intermediate frequency range experimental data. However, the % error was found to increase to ~ 1000% for the R_{lea} parameters in the model.

The advantage of the 3-Branch model is that it gives an indication of the distributed resistance and capacitance down the pores. However, the simplified Randles circuit still matches closest to the experimental results with the lowest %error for all components of the model. This verifies the use of this model for the RTIL systems studied.

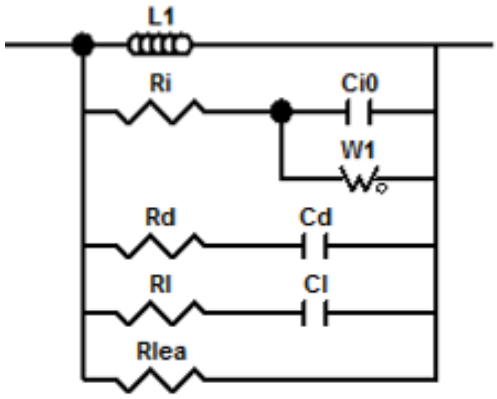

Figure 6.17 – 3-Branch Model with Added Warburg Component

6.4 Cyclic Voltammetry

As mentioned in *Section 3.2.3*, for an ideal EC, the voltammogram of current vs. voltage should form a rectangular plot. The behaviour may deviate from ideal due to charging beyond highest stable voltage, pseudocapacitance, high resistance and/or low capacitance. *Figures 6.18* and *6.19* show the current vs. voltage results for $EMImBF_4$ for ACRF100-1.5nm – ACRF750-16.8nm and ACRF200-4.5nm//$EMImBF_4$ for varying scan rate, respectively. *Table 6.8* shows the results for all electrolytes and activated carbons studied. *Figures A3.1 – A3.4* show the current vs. voltage graphs for all other electrolytes studied.

The cyclic voltammograms confirm the results from charge-discharge measurements, with the optimum capacitance occurring for ACRF200 for all electrolytes. The order of electrolyte capacitance from highest to lowest is $EMImBF_4$ > DMPImTFSI> Et_4NBF_4 – PC 1M > $EMImN(CN)_2$ > $BMPyT(f_5Et)PF_3$.

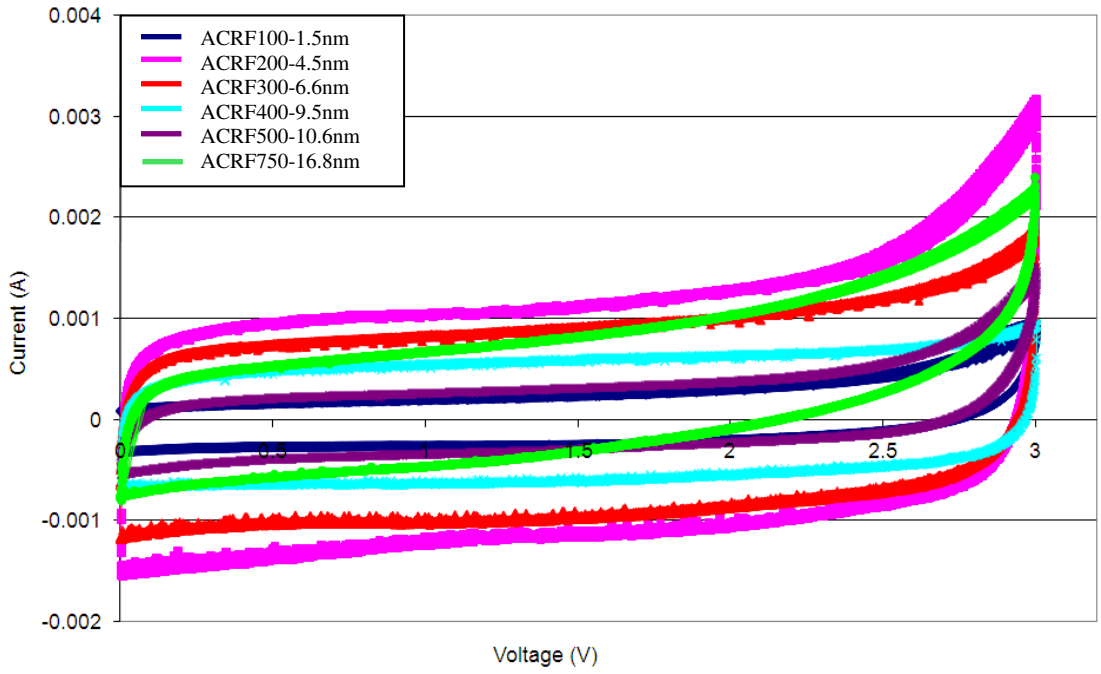

Figure 6.18 – Cyclic Voltammogram $EMImBF_4$ for Varying Pore Size

To determine if pseudocapacitance is occurring, the voltammograms were studied for an apparent increase in current at the reaction voltage. The results from cyclic voltammetry confirm that the EC cells were operating purely as double-layer capacitors (DLCs), as no deformation of the voltammograms can be seen to occur at intermediate potentials in *Figure 6.17* and *Figures A3.1 – A3.4* due to pseudocapacitance, the activated carbon xerogel/RTIL systems studied can be considered to operate purely as DLCs.

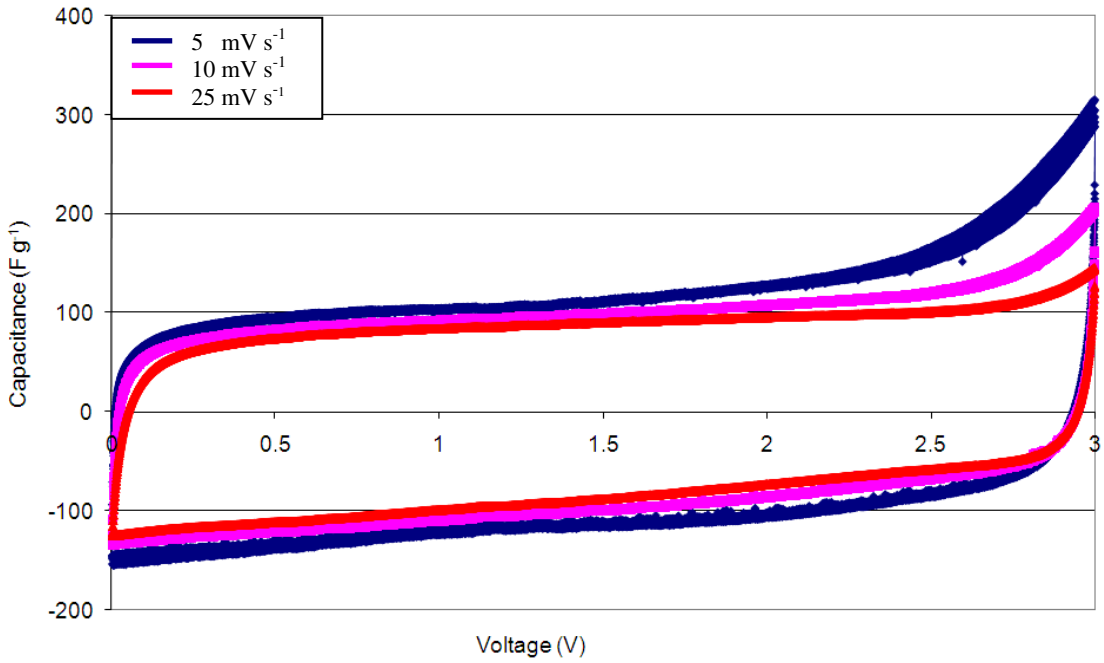

Figure 6.19 – Capacitance Cyclic Voltammogram for ACRF200-4.5nm / $EMImBF_4$ at Varying Scan Rate

The closest to ideal behaviour would be expected to occur for the high capacitance / low resistance EC cell consisting of ACRF200-4.5nm//$EMImBF_4$. The EC cells with the lowest resistance i.e. EMImCN and Et_4NBF_4 – PC 1M, would also be expected to give rise to the most rectangular voltammograms. However, as can be seen from a comparison of *Figure 6.18* above and *Figures A3.1 – A3.4* in *Appendix A*, the closest to ideal behaviour is for the EC cell ACRF200//DMPImTFSI. Deviation from ideal behaviour can be seen to occur for $EMImBF_4$ (*Figure 6.18*) above 2.5 V, in particular for ACRF200. This indicates that this electrolyte may be

decomposing below the determined ESW as shown in *Table 6.1*. This may be attributed to the higher percentage of surface area accessed and therefore utilised by this electrolyte of the activated carbons. This may lead to the full surface of the electrode not being charged at a uniform rate. This could result in concentrations of high charge where the voltage at these points exceeds that of the ESW. Thus, the potential window within which it is possible to charge-discharge the high surface area carbon electrodes appears narrower than the ESW determined with the non-porous carbon xerogel electrodes. From *Figure 6.19* at higher scan rates the voltammogram can be seen to fit more closely with ideal behaviour. This return to more ideal behaviour at higher scan rates is due to a lower percent of the surface area being utilised for double-layer formation resulting in the Faradaic contribution seen at low scan rates to be omitted. $EMImN(CN)_2$ shows a large deviation from ideal due to the decomposition of the electrolyte that occurs as discussed in *Section 6.2.3*. Due to the decomposition of the electrolyte, after each cycle a drop in the current attained occurs. This also occurs, to a lesser extent, for $EMImBF_4$. This reduction of the ESW may have occurred for all electrolytes studied, however, as shown in *Figure 6.1* $EMImBF_4$ and $EMImN(CN)_2$ give rise to the steepest increase in current on decomposition, causing the decomposition to become evident on the cyclic voltammograms.

Table 6.8 – Capacitance for CV at Varying Scan Rates

Sample	C @ 5 mV s^{-1} ± 0.1 ($F\ g^{-1}$)	C @ 10mV s^{-1} ± 0.1 ($F\ g^{-1}$)	C @ 25mV s^{-1} ± 0.1 ($F\ g^{-1}$)
Electrolyte: $EMImBF_4$			
ACRF100-1.5nm	67.9	37.9	21.7
ACRF200-4.5nm	114.7	100.4	91.6
ACRF300-6.6nm	113.4	102.6	95.3
ACRF400-9.5nm	75.3	67.6	58.2
ACRF500-10.5nm	59.9	50.1	42.1
ACRF750-16.5nm	52.4	39.7	24.3
Electrolyte: DMPImTFSI			
ACRF100-1.5nm	43.7	36.9	37.2
ACRF200-4.5nm	113.3	111.7	104.1
ACRF300-6.6nm	90.8	82.7	76.3
ACRF400-9.5nm	57.4	52.7	48.7
ACRF500-10.5nm	44.9	41.2	36.8
ACRF750-16.5nm	25.6	22.9	20.5
Electrolyte: $EMImN(CN)_2$			
ACRF100-1.5nm	-	-	-
ACRF200-4.5nm	-	-	-
ACRF300-6.6nm	68.6	52.0	42.2
ACRF400-9.5nm	62.5	57.3	47.0
ACRF500-10.5nm	48.0	43.6	36.0
ACRF750-16.5nm	56.6	37.6	31.9
Electrolyte: $BMPyT(f_5Et)PF_3$			
ACRF100-1.5nm	3.6	1.9	1.3
ACRF200-4.5nm	43.7	29.8	16.8
ACRF300-6.6nm	23.0	21.6	18.7
ACRF400-9.5nm	22.6	22.3	20.0
ACRF500-10.5nm	22.4	20.4	19.4
ACRF750-16.5nm	5.9	5.5	5.1
Electrolyte: Et_4NBF_4 – PC 1M			
ACRF100-1.5nm	48.6	43.4	12.1
ACRF200-4.5nm	89.9	79.8	72.5
ACRF300-6.6nm	62.7	59.8	55.4
ACRF400-9.5nm	50.9	47.7	44.9
ACRF500-10.5nm	43.5	38.3	34.1
ACRF750-16.5nm	21.5	16.0	13.1

6.5 Lifespan Cycling

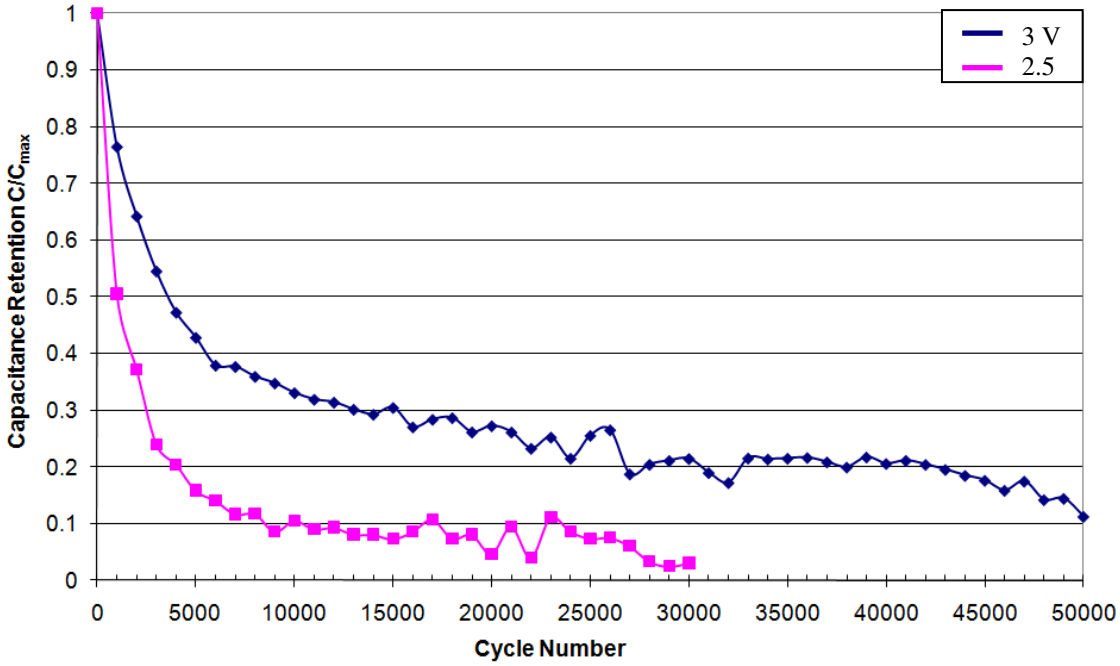

Figure 6.20 – Cycling Performance of ACRF200 with EMImBF$_4$

Figure 6.20 shows the cycling performance of ACRF200 with RTIL EMImBF$_4$ for 50,000 charge-discharge cycles at the maximum operating voltage of 3 V and at the lower voltage of 2.5 V. The results show that cycling at the lower voltage of 2.5 V increases the life of the EDLC by 5 times (after 50,000 cycles). However, although the performance is greatly improved by cycling at the lower voltage a large decrease in performance of 90% still occurs. As cycling at a lower voltage only marginally improved the lifetime of the ECs, other factors must be affecting their longevity. Although the ECs are sealed with a thick layer of Parafilm, this does not guarantee the uptake of oxygen or water from the environment does not occur. Also, the electrolytes used are never 100% pure and so impurities other than water in the electrolytes may also reduce the cycle life of the ECs.

Further cycling measurements were carried out on ACRF200-4.5nm that had been cleaned in an argon atmosphere at 750 °C to assess the effect the surface functionality has on the cycle life of the EC cells. It can be seen (*Figure 6.21*) that at 3 V and 2.5 V the clean carbon does not improve the performance of the EC cells

indicating that the problem is due to electrolyte degradation and not due to redox reactions with the surface functional groups. To confirm that the poor cycling ability of the EC cells is caused by the decomposition of the electrolyte the next best performing electrolyte was cycled 5,000 times, as this was the period over which the largest decrease in capacitance occurs. It can be seen in *Figure 6.22* that after 5,000 cycles DMPImTFSI allows for 3 times the capacitance retention by comparison to $EMImBF_4$ at 3 V. As the operating voltage of the DMPImTFSI EC cell was 2.7 V i.e. lower operating voltage than $EMImBF_4$, an improvement in the cycling performance could be attributed to the stability of the electrode materials at the lower voltage. If this was the case, i.e. capacitance decay due to destruction of the electrode material at high operating voltages, the decay in performance should sit between the EC cells at 2.5 V and 3 V. However, it is comparable with the EC cell cycled at 2.5V further confirming that electrolyte degradation is the main cause of capacitance decay.

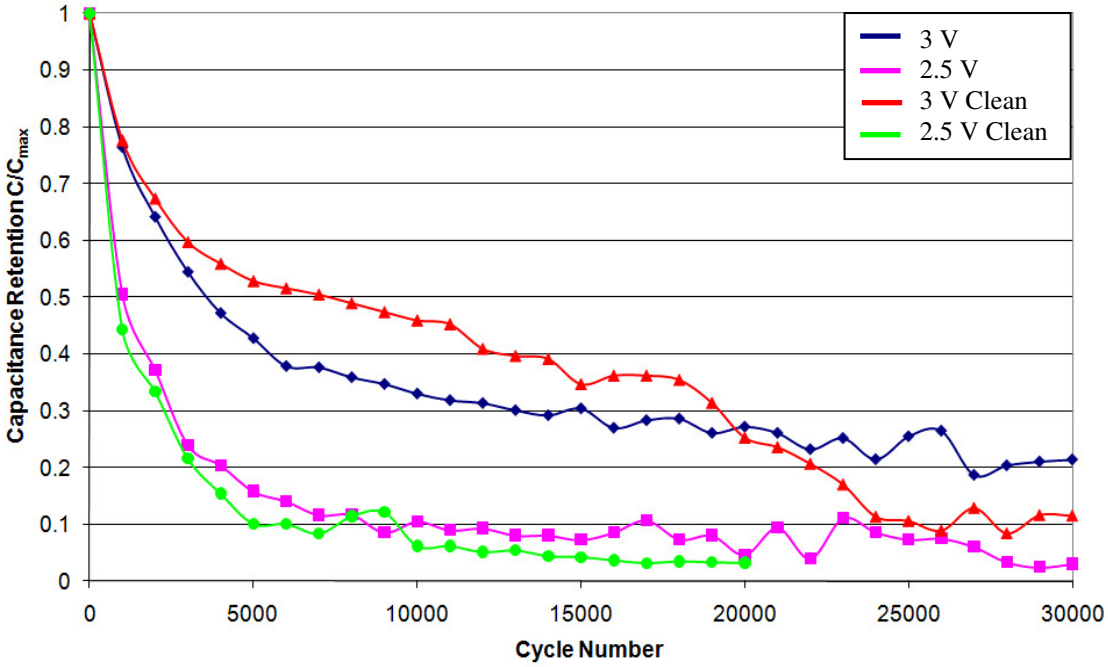

Figure 6.21 – Effect of Surface Functionality on Cycling Performance

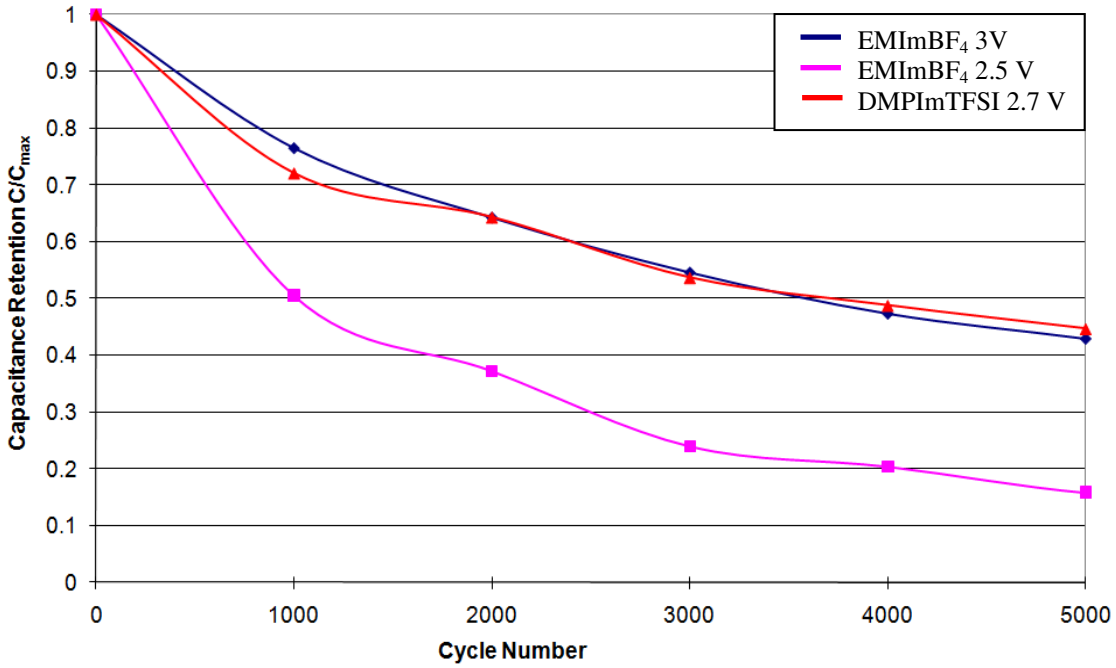

Figure 6.22 – Effect of Electrolyte on Cycling Performance

Since, the cycling performance of ECs is affected by all components of the cells including the current collector, the poor cycling performance may be attributed to degradation of the current collector. The current collector ensures polarisation of the active material through its electronic conductivity. Aluminium was used in this study and is the most commonly used current collector in organic and RTIL electrolytes, due to the passive Al_2O_3 layer protecting the under-lying metal. [151, 152] However, this alumina layer can continue to build up on the surface of the untreated aluminium foil after long periods of cycling leading to electron transfer being blocked.

The cycling stability of RTIL based EC cells could be improved by the treatment of the aluminium current collector, prior to electrode manufacture. The treatment procedure was initially developed by Simon *et al.* [150,151] to reduce the ESR by improving the contact interface between the current collector and the electrode. However, by improving the current collector/electrode interface the cycling ability of the ECs can be improved. [150, 151] This treatment could improve the cycling ability of the ECs of this study when combined in a hermetic system.

6.6 Self-discharge

The self-discharge rate is the reduction of stored voltage when the EC is no longer under a loading current.

6.6.1 Factors Influencing Self-discharge Behaviour of RTILs

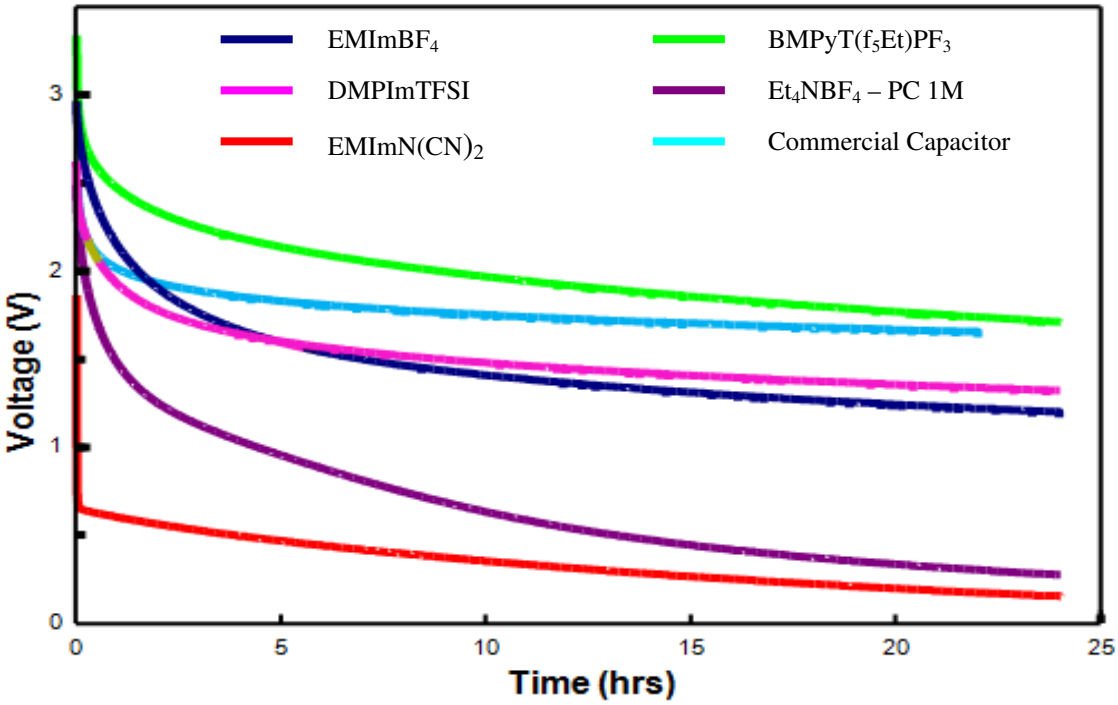

Figure 6.23 – Self-discharge over 24 hours for ACRF200 and Commercial EC BCAP0010 P270

The self-discharge for ACRF200-4.5nm for all electrolytes studied and the commercial EC (Maxwell BCAP0010 P270) is shown in *Figure 6.23* and the self-discharge for $EMImBF_4$ for varying pore size (i.e. R/C ratio) is shown in *Figure 6.25* (graphs for all electrolytes can be seen in *Appendix A, Figures A4.1 – A4.4*). The 'resting voltage'[9] peaks at ACRF200-4.5nm which produced the highest capacitance

[9] The 'resting voltage' in this case is the final voltage after OC for 24 hrs.

for all electrolytes. As the self-discharge rate was in the order of slowest to fastest for RTILs DMPImTFSI < BMPyT(f_5Et)PF_3 < EMImBF_4 < EMImN$(CN)_2$ the discharge rate for RTILs appears to be attributed to two factors; initial capacitance (i.e. quality of the double-layer) and viscosity of electrolyte. For the organic electrolyte Et_4NBF_4 – PC 1M, the self-discharge can be deemed independent of initial capacitance, as although the capacitance was still high at 100 F g^{-1}, the self-discharge rate is also very high with 0 V being reached for ACRF100-1.5nm, ACRF500-9.6nm and ACRF750-16.8nm after 24 hrs. A plateau out to a constant voltage, as with the RTILs, was not found to occur. This poor retention of capacitance can be attributed to the highly mobile ions in the solvent. The final voltage for the RTILs studied was found to be highest for BMPyT(f_5Et)PF_3 at 1.71 V. This indicates that the initial voltage also plays a role in determining the 'resting voltage'. [200] The results show that the electrolytes which provide a high capacitance due to lower viscosity and higher ion mobility suffer from higher rates of self-discharge than those that exhibit mass transfer limitations. *Figure 6.24* shows the effect of viscosity on the self-discharge rate. These results suggest that charge redistribution may be the cause of the self-discharge of the activated carbon/RTIL systems being studied.[10] As charge redistribution relies on the charge on the carbon being countered by electrolyte ions, the limitation is the rate of ion diffusion in the pores. Therefore, the more viscous RTILs hinder the ion diffusion and the result is a lower rate of self-discharge.

Table 6.8 – Self-discharge over 24 Hours for ACRF200 and Commercial EC BCAP0010 P270

Electrolyte	Initial Voltage, V_i (V)	Final Voltage, V_{SD} after 24hrs OC (V)	% Voltage Reduction
EMImBF_4	3.0	1.20	60
DMPImTFSI	2.7	1.42	47
EMImN$(CN)_2$	2.5	0.42	83
BMPyT(f_5Et)PF	3.5	1.71	51
Et_4NBF_4 – PC 1M	2.5	0.27	89
Commercial	2.5	1.66	34

[10] Charge redistribution occurs when a potential gradient is formed throughout pores on charging. On switching to open-circuit there will be a redistribution of charge throughout the pores until the charge is equal across the full electrode surface.

Table 6.9 – Final Resting Voltage after 24 Hours

Sample	$EMImBF_4$ (V)	DMPImTFSI (V)	$BMPyT(f_5Et)PF_3$ (V)	$EMImN(CN)_2$ (V)	Et_4NBF_4-PC 1M (V)
ACRF100-1.5nm	1.06	0.29	0.43	0	0
ACRF200-4.5nm	1.20	1.32	1.71	0.15	0.27
ACRF300-6.6nm	0.98	1.42	0.64	0.42	0.06
ACRF400-9.5nm	1.01	1.19	0.87	0.37	0.16
ACRF500-10.5nm	0.97	1.42	0.97	0.40	0
ACRF750-16.5nm	1.02	0.99	0.84	0.54	0

The dependence of self-discharge rate on electrolyte viscosity and double-layer quality suggests that charge redistribution may be responsible for the voltage reduction in the ECs tested. Charge redistribution affects porous electrodes due to significant migration and diffusion limitations down into the pores during charge-discharge, as a result of the high electrolyte resistance. A mathematical evaluation of the potential and current distribution in porous electrodes was carried out by de Levie, [175] known as the Transmission Line model. This evaluation showed that the electrode processes do not proceed evenly throughout the thickness of a porous electrode, largely due to the *IR* drop in the solution within the pores, resulting in faster electrode processes at the mouth of the pore, closer to the counter electrode, versus those that occur at the base of the pore. [201] That is, the external surface of the electrode will charge-discharge faster than the surfaces within the pores. As a result, of this pore effect, when a porous electrode is charged there will be a distribution of potentials across the electrode pores. As the system is switched to open-circuit these potentials will equilibrate as the charge redistributes evenly over the electrode surface. [202] The potential at the tip of the pore, where the potential is measured, will fall during this charge redistribution, and may appear as a rapid, initial self-discharge.

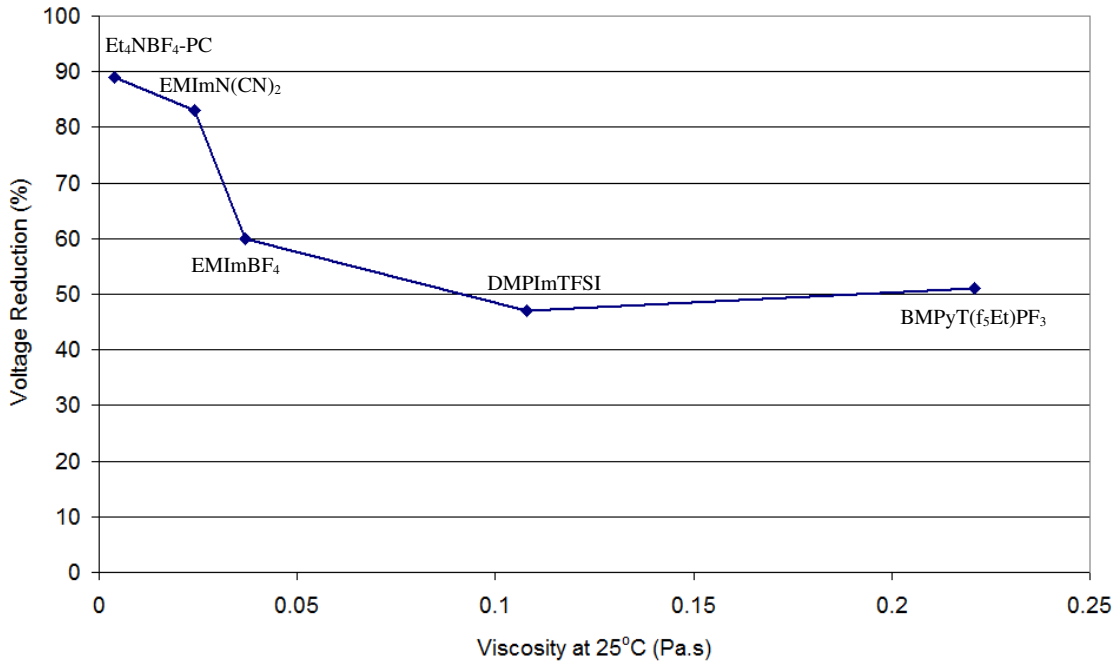

Figure 6.24 – Effect of Viscosity on Self-discharge Rate

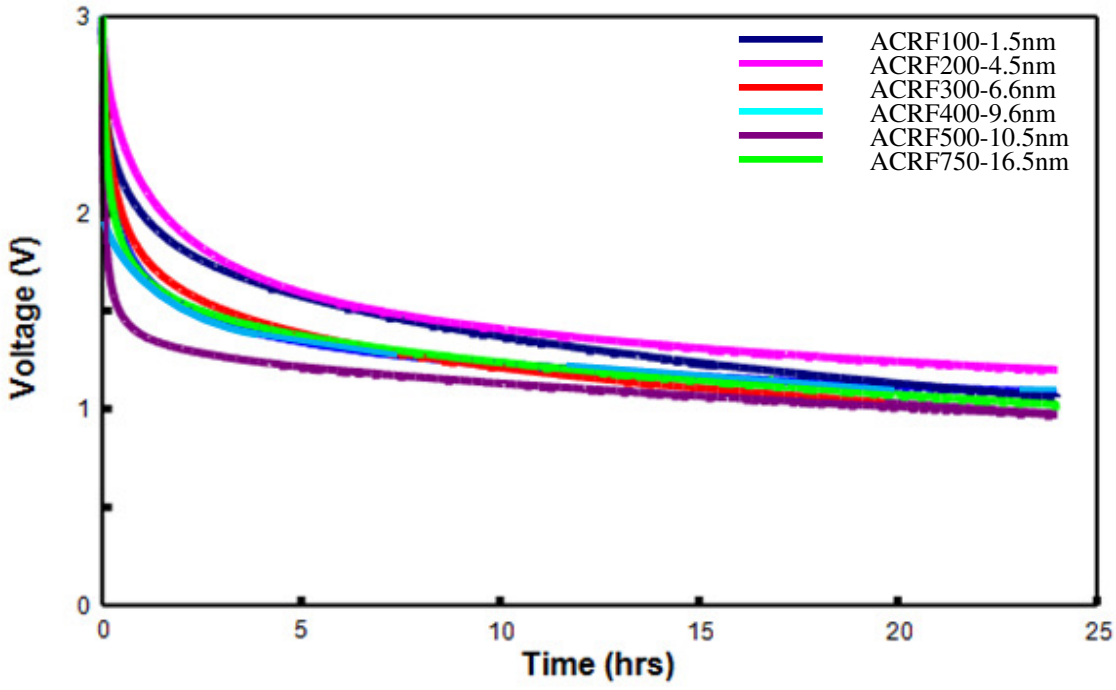

Figure 6.25 – Variance of Self-discharge with Pore Size for $EMImBF_4$

From *Table 6.9,* it can be seen that ACRF100-1.5nm exhibits the lowest resting voltage and therefore highest self-discharge rate over the 24 hour measurement period. This may be attributed to the earlier hypothesis that ions have poor access to the micropores at higher charge, leading to the capacitance being obtained mainly from double-layer formation on the external surface area of the carbon where the fastest discharge occurs. This results in a high degree of distribution occurring before equilibrium is attained across the electrode. ACRF200-4.5nm retains the highest capacitance (through retaining voltage) for all electrolytes, due to the highest initial capacitance and the smallest pore size accessible to the electrolyte ions giving rise to a more even distribution of charge in the pores during charging i.e. the pores are require less equilibration after charging is ceased. Above this pore diameter, the pore size increase results in a larger charge gradient in the pores giving rise to a higher self-discharge rate and a lower 'resting voltage'. This may be due to the volume available for redistribution / equilibration of charge being increased, resulting in increased redistribution of charge for equilibrium to be attained. The mechanisms suggested for 'pore flooding' discussed earlier in *Section 6.2.1* and illustrated in *Figures 6.6 and 6.7* also facilitates self-discharge at higher pore diameters. The mechanism of ion transfer *(Figure 6.6)* in the double-layer will increase self-discharge rate by ferrying the charge away from the double-layer and the ion pairing *(Figure 6.7)* will reduce the concentration of polarisable ions creating a greater concentration gradient facilitating diffusion from the double-layer.

6.6.2 Analysis of Self-Discharge Mechanisms

To confirm that charge redistribution is the main factor affecting the self-discharge for RTILs, the mechanisms for self-discharge as modelled by Conway (as outlined in *Section 3.6*) were fitted to the data obtained.

For self-discharge mechanism (1), *Figure 6.26* shows the self-discharge voltage vs. log (t), which should form a straight line if Faradaic processes were present. The plot shows that for all electrolytes (except $EMImN(CN)_2$) a plateau corresponding to the integration constant, τ, occurs before the self-discharge potential falls linearly with log (t) indicating that a Faradaic process is responsible for the self-discharge of the ECs studied. However, although Conway *et al.* [202] concluded that the linear fall in

potential with log (t) is due to a Faradaic activation controlled process, Black *et al.* [204] recently proved using a transmission line model circuit (consisting of eight parallel sections, with each section consisting of a capacitor and resistor in series, where no Faradaic processes are present) that the same profile is obtained. This indicates that this profile not only represents a Faradaic process but also a redistribution of charge through a porous electrode. As a result of this, the Conway model for activation-controlled mechanisms cannot be used for highly porous electrodes as charge redistribution will occur down the length of the pore. As no Faradaic processes were observed in the cyclic voltammograms in *Section 6.4*, the self-discharge profiles can be attributed to charge redistribution in the pores of the activated carbon xerogels. This could also explain the increase in self-discharge with increasing pore size. The larger pores require a higher degree of distribution before equilibrium is attained, thus resulting in a reduced final 'resting voltage' after 24 hrs. If mechanism (1) in (*Section 3.6*) became apparent due to water uptake in the electrolyte, the resultant voltage would be independent of pore size distribution. It would be expected that if self-discharge mechanisms (2) and (3) were in effect for each carbon sample, the self-discharge would occur at the same rate. However, as already discussed above for each electrolyte / activated carbon xerogel system a different 'resting voltage' is attained. For mechanism (2) and (3) the plots of V_{SD} *vs.* $t^{1/2}$ and *log* (V_{SD}) *vs. t* do not show a linear decrease with time, proving that there are no diffusion limited reaction occurring from charged impurities in the electrolyte or electrode and that the self-discharge is not due to faulty construction.

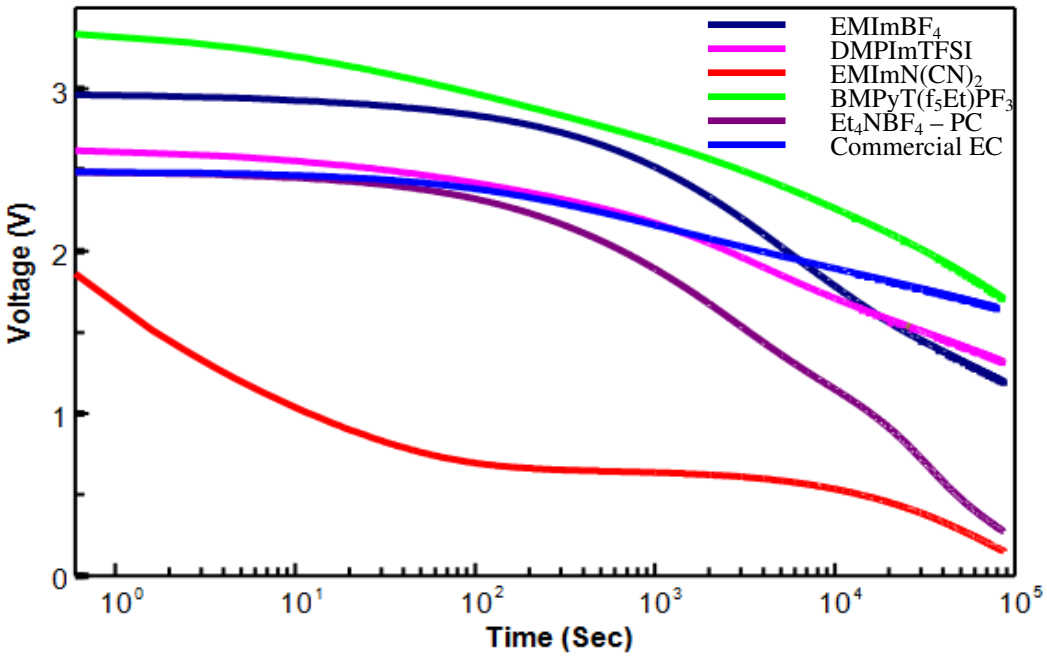

Figure 6.26 – Self-discharge voltage vs. log (t)

6.6.3 Measures to Counteract Self-Discharge

Black *et al.* [204] proved that adding a hold step during the charging of the highly porous carbon electrodes used for ECs reduces the effect of charge redistribution on self-discharge. However, it was found that for aqueous systems a hold step of 50hrs was required to minimise self-discharge due to charge redistribution, as the self-discharge rate for aqueous solutions is very high. Since the self-discharge rate of RTILs is slower, this indicates that the hold step required would be much shorter. Although in practical applications the use of a hold step may not be the most appropriate way to deal with self-discharge. A more practical solution would be to apply a small float current to counteract the self-discharge. If the ECs are not in use for long periods of time, this float current may also inadvertently act a hold step.

6.7 Energy and Power Density

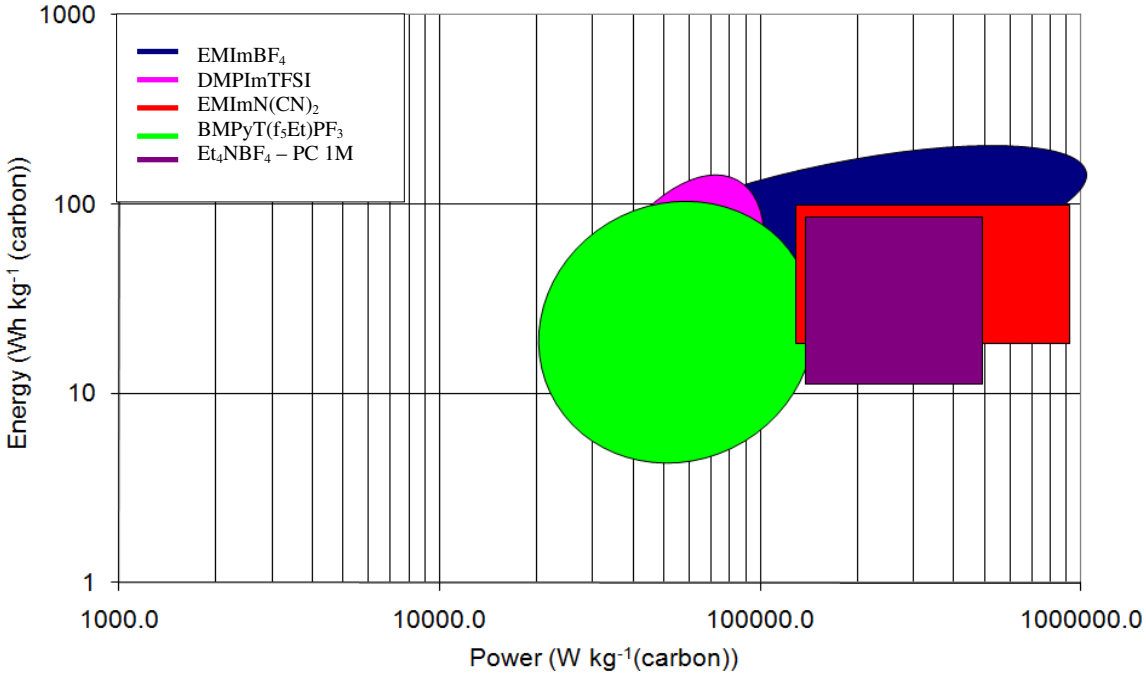

Figure 6.27 – Ragone Plot of Maximum Energy and Power Density

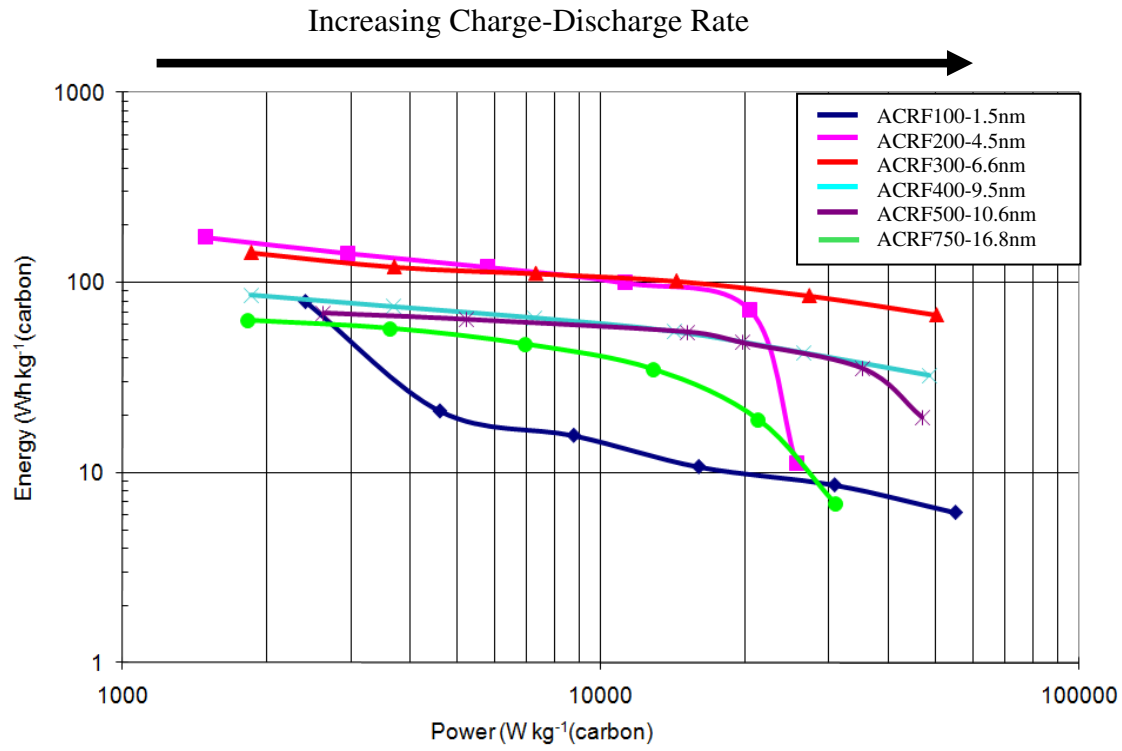

Figure 6.28 – Ragone Plot of Operating Energy and Power Density for $EMImBF_4$

Figure 6.27 represents a traditional Ragone Plot showing the maximum energy and power density taken from GC and EIS measurements, respectively, and *Table 6.10* summarises the results. *Figure 6.28* shows the operating energy and power density results for $EMImBF_4$ for varying R/C ratio and increasing charge-discharge rate. The maximum power was obtained using the ESR from EIS measurements, whilst the maximum energy, operating energy and operating power were determined from GC measurements.

Figure 6.27 shows that the highest power and energy density occurred for $EMImBF_4$ of 665.5 kW kg^{-1} and 175 Wh kg^{-1}, showing that the high capacitance coupled with the lower resistance and higher operating voltage of 3 V gives rise to the best energy and power performance. The lowest power and energy densities of 227 kW kg^{-1} and 10.5 Wh kg^{-1} occurred for ACRF70-16.8nm//$BMPyT(f_3Et)_3PF_3$, indicating that the higher operating voltage of 3.5 V is not sufficiently high enough to overcome the poor capacitance performance and high resistance. The lower resistance of $EMImN(CN)_2$, leads to better power density over electrolytes DMPImTFSI, $BMPyT(f_3Et)_3PF_3$ and Et_4NBF_4 – PC 1M.

Figure 6.28 shows the operating energy and power density results for $EMImBF_4$ for varying R/C ratio and increasing charge-discharge rate. The energy density was calculated from GC capacitance as for *Figure 6.27* and the power density was the operating energy per unit discharge time. Ragone plots for the all electrolytes are shown in Appendix A in *Figures A5.1 – A5.4*.

Figure 6.28 shows that ACRF100-1.5nm appears to give rise to a higher power density than ACRF200-4.5nm at high charge-discharge rate density, therefore the use of this type of Ragone Plot without other data would not be advisable as the wrong conclusions may be drawn. The energy and power density of ACRF200-4.5nm can be seen to reduce at higher charge-discharge rates, while the power density for ACRF300-6.6nm continues to increase. This shows that if high charge-discharge rate were a desired characteristic, ACRF300-6.6nm would be the better material choice, confirming the conclusions drawn in **Section 6.2.2,** that ACRF200-4.5nm is the best choice for low charge-discharge rates and ACRF300-6.6nm is the best choice for high charge-discharge rates.

As the energy and power density are calculated based on the capacitance and resistance values obtained from GC measurements, the results follow the pattern for increasing pore size. Where the higher pore sizes result in reduced energy and power performance.

Table 6.10 – Maximum Energy and Power Density

R/C Ratio	GC Capacitance ($F\ g^{-1}$)	Energy Density ($Wh\ kg^{-1}$)	ESR @ 1 kHz (Ω)	AC Power Density ($W\ kg^{-1}$)
Electrolyte: $EMImBF_4$				
ACRF100-1.5nm	51.5	84.8	18.0	78056
ACRF200-4.5nm	92.6	175.2	2.1	665460
ACRF300-6.6nm	61.0	94.6	2.1	662388
ACRF400-9.5nm	45.3	87.8	3.9	360411
ACRF500-10.5nm	32.3	69.4	4.1	342387
ACRF750-16.5nm	37.5	54.1	10.2	137557
Electrolyte: DMPImTFSI				
ACRF100-1.5nm	16.9	13.3	17.6	51781
ACRF200-4.5nm	65.6	117.6	15.5	82101
ACRF300-6.6nm	49.9	72.3	12.7	79934
ACRF400-9.5nm	33.1	43.0	14.8	76756
ACRF500-10.5nm	28.5	33.9	22.9	61315
ACRF750-16.5nm	15.2	18.8	41.6	27389
Electrolyte: $EMImN(CN)_2$				
ACRF100-1.5nm	26.5	26.3	1.2	822092
ACRF200-4.5nm	82.8	94.4	5.6	139594
ACRF300-6.6nm	47.2	64.2	2.1	468375
ACRF400-9.5nm	36.8	60.2	2.1	468938
ACRF500-10.5nm	35.9	31.1	2.2	436804
ACRF750-16.5nm	26.9	23.4	4.0	242715
Electrolyte: $BMPyT(f_5Et)PF_3$				
ACRF100-1.5nm	2.8	5.5	27.3	70176
ACRF200-4.5nm	23.5	56.7	34.0	45022
ACRF300-6.6nm	16.5	29.6	18.4	139018
ACRF400-9.5nm	15.8	11.6	24.1	79280
ACRF500-10.5nm	12.6	28.5	34.4	32896
ACRF750-16.5nm	5.6	10.5	34.9	22692
Electrolyte: Et_4NBF_4 – PC 1M				
ACRF100-1.5nm	40.9	44.9	3.1	320384
ACRF200-4.5nm	96.1	84.2	3.5	144751
ACRF300-6.6nm	50.4	46.8	2.7	421302
ACRF400-9.5nm	40.8	44.7	2.5	528100
ACRF500-10.5nm	43.0	31.0	3.0	470545
ACRF750-16.5nm	13.9	14.7	4.1	237792

7.0 Conclusions

7.1 Overview

This study has identified that the pore size is an important factor for optimising capacitance performance of carbon-based / RTIL ECs. To study the effect of pore size on EC performance, activated carbon xerogels were produced by varying the R/C ratio. The R/C molar ratios used were R/C 100, 200, 300, 400, 500, 750, 1000, and 1500. The R/F and R/W ratios were kept constant at R/F 0.5 (molar) and R/W 0.25 g/ml. The effect of gelation method on the resultant xerogel structure was also studied to ensure the most favourable production process was followed.

It was noted that for Gelation method 1, R/C ratios above 750 did not yield any hydrogel, whereas for Gelation method 2, gelation occurred to a limited extent. It was observed that with increasing R/C ratio, the volume of micropores reduced and the volume and size of mesopores increased, with the average pore diameter increasing; from 2.7 nm for RF100 to 25 nm for RF750 for Gelation method 1; and from 6.7 nm to 31 nm for Gelation method 2. A reduction in surface area with increasing R/C ratio was also recorded; 355 $m^2 g^{-1}$ to 133 $m^2 g^{-1}$ for Gelation method 1; and 383 $m^2 g^{-1}$ to 65 $m^2 g^{-1}$ for Gelation method 2. The hydrogels produced at RF1000 and 1500 for Gelation method 2, were found to be non-porous. The xerogels produced via Gelation method 2 exhibited a wider pore size distribution than those for Gelation method 1.

On carbonisation the functional groups in the RF xerogel structure are removed, enriching the carbon content and creating microporosity in the structure. This is most apparent for CRF1000 and CRF1500 produced via Gelation method 2, where the initial xerogels were non-porous and on carbonisation the surface area increased to 175 and 462 $m^2 g^{-1}$, respectively, with 97% of the structure situated in the microporous region. CRF100 for Gelation method 1 became microporous with most of the mesoporosity having been removed by carbonisation. An overall reduction in average pore diameter occurred, over that of the xerogel equivalents, due to the development of microporosity and removal of the largest mesopores. The average pore diameter was still found to increase with increasing R/C ratio; from 2.2 nm for

RF100 to 16 nm for RF750 for Gelation method 1; and from 4.4 nm to 20.7 nm for Gelation method 2.

On activation the surface area was enhanced increasing the surface area range; Gelation method 1 from 1135 $m^2 g^{-1}$ for ACRF100 to 775 $m^2 g^{-1}$ for ACRF750. The results also showed a significant ordering of the structure on activation, resulting in a narrowing of the pore size distributions. For Gelation method 1 the surface area was shown to decrease with increasing R/C ratio, whereas the pore volume increased with increasing R/C ratio due to the increase in the size of pores in the structure. The range of the pore size distribution was found to increase from 2 - 5 nm for ACRF100 to 5 - 30 nm for ACRF750.

Gelation method 2 does not show such clear patterns with increasing R/C ratio, for this reason, coupled with wider (less controlled) pore size distributions, it was decided to continue further studies with the activated carbon xerogels produced via Gelation method 1.

The next study examined the effect of ball milling on the structure of the activated carbons for use as electrode materials. The main purpose of ball milling was to reduce the particle size of the activated carbon xerogels to improve the ease of production of the composite electrodes. The aim of this study was to obtain particles small enough for uniform electrode manufacture whilst maintaining the porous characteristics of the activated carbon xerogels. It was concluded that the best milling technique was to mill the carbon xerogels for 60 minutes before activation. This resulted in the least destruction of the porosity, as the carbons walls were stronger than the activated materials.

The addition of binder (Kynar 2801) and conductivity enhancer (Carbon Black XC72), results in the blockage of pores resulting in a reduction in the surface area for all samples. The results indicate that smaller pores are blocked over larger pores, and as a consequence the largest reduction in surface area occurs for ACRF100. The reduction in BET surface area continues to decrease as the average pore size increases reaching a minimum for ACRF500. The small mesopores for ACRF100 are blocked and as result the average pore size reduces to 1.5 nm from 2.5 nm. The opposite effect is seen for the mesoporous samples, where an increase in the average pore size occurs. Overall it was determined the activated carbon xerogel composite

electrodes provided a good basis for the determination of the pore diameter for optimum capacitance performance for the RTIL electrolytes 1-ethyl-3-methylimidazolium tetrafluoroborate, ($EMImBF_4$), 1,2,-dimethyl-3-propylimidazolium bis(trifluoromethylsulfonyl)imide (DMPImTFSI), 1-ethyl-3-methylimidazolium dicyanamide ($EMImN(CN)_2$, 1-butyl-3-methylpyrrolidinium tris(pentafluoroethyl)trifluorophosphate ($BMPyT(f_5Et)PF_3$), and organic electrolyte 1M-tetraethylammonium tetrafluoroborate in propylene carbonate (Et_4NBF_4-PC 1M).

From electrochemical stability window measurements the following upper operating voltages were determined; $EMImBF_4$ – 3 V, DMPImTFSI – 2.7 V, $EMImN(CN)_2$ – 2.5 V and $BMPyT(f_5Et)PF_3$ – 3.5 V and Et_4NBF_4-PC 1M – 2.5 V.

To assess the capacitance performance of the activated carbon xerogels, Galvanostatic charge-discharge (GC) was used. The effect of pore size on both the optimum capacitance and optimum rate performance was studied. It was found that the pore size for optimum capacitance and optimum rate performance differs. The optimum capacitance was obtained for the activated carbon xerogel ACRF200-4.5nm for all electrolytes studied. Whereas, the optimum rate capability occurred at higher pore diameters, as the increase in pore size allows for improved mass transfer to and from the pore. The optimum rate capability for $EMImBF_4$, DMPImTFSI, $EMImN(CN)_2$ and $BMPyT(f_5Et)PF_3$ was obtained for ACRF300-6.5nm. For organic electrolyte Et_4NBF_4 – PC 1M, the performance peaks at ACRF400 due to the larger diameter of the solvated ions. The maximum capacitance values obtained for $EMImBF_4$, DMPImTFSI, $BMPyT(f_5Et)PF_3$, $EMImN(CN)_2$, and Et_4NBF_4-PC 1M under Galvanostatic charge-discharge at 2 mA cm^{-2}, were 140, 105, 41, 27, and 109 F g^{-1}, respectively. Above the optimum pore size for rate capability, a reduction in capacitance occurred. This was attributed to the reduction in conductivity of the electrolyte and increase in double-layer thickness, *d*, that occurred due to the pores becoming flooded with electrolyte. Below the optimum pore size electrolyte access to the pores is limited.

The results obtained in this study apparently contradict recent developments indicating that microporosity (d_{av}=0.7nm) is the best way to optimise the capacitance of ECs. This difference was attributed to the electrochemical measurements in those

studies [139-144] being carried out at very low current density (0.1 - 6 A g^{-1}). For this study it was determined that these current densities are too low to assess the influence slow mass transfer kinetics would have on the capacitance performance. Although the capacitance measurements were carried out at increasing current density, the capacitance was not reported. The capacitance values obtained in the literature [141] are also only marginally higher (160 F g^{-1}) than that found in this study (140 F g^{-1}). The studies carried out by Largeot *et al.* on the distortion of ions in pores utilised RTILs at elevated temperature of 60°C and very low scan rate to specifically allow for any kinetic restrictions imposed by the viscosity of the RTILs to be disregarded.[143] Whereas, this study operated in the range of 1 – 32 A g^{-1}, which led to an amplification of the slow mass transfer associated with RTILs. This may be the cause of the increase in optimum average pore diameter determined here.

The next investigation carried out looked at the variation in capacitance with RTIL electrolyte. It was found that the performance of the electrolytes was of the order $EMImBF_4$ > DMPImTFSI > $BMPyT(f_5Et)PF_3$ > $EMImN(CN)_2$. The electrolyte that provided the best performance was $EMImBF_4$. This was due to stability at a higher voltage allowing for longer discharge cycles, good conductivity and relatively low viscosity in comparison with the other electrolytes tested. The capacitance of the organic electrolyte Et_4NBF_4-PC 1M, was found to be lower than $EMImBF_4$ and DMPImTFSI. The capacitance for $EMImBF_4$, DMPImTFSI, and $BMPyT(f_5Et)PF_3$ produced a linear trend with electrolyte viscosity, however, $EMImN(CN)_2$ and Et_4NBF_4 – PC 1M deviated from the linear trend. This deviation confirmed that ion size was also a determining factor in the capacitance performance.

Electrochemical Impedance Spectroscopy (EIS) was used to study the resistive components of the EC test cells. The variation of ESR and R_I with pore size followed a different pattern from that found for the variation of capacitance with pore size. Higher values of ESR and R_I were found for ACRF100-1.5nm than ACRF200-4.5nm – 400-9.5nm for electrolytes $EMImBF_4$, DMPImTFSI and $BMPyT(f_5Et_3)$. This was attributed to the high volume of inaccessible micropores. The ESR and R_I reduced as the ions apparently accessed more of the electrode structure until the pores reached the optimum diameter for lowest resistance. ACRF300-6.5nm and ACRF400-9.5nm exhibited lower ionic resistance (and therefore ESR) values than ACRF200-4.5nm

for all electrolytes (except $EMImBF_4$) due to more rapid mass transfer within the larger pores of the structure. Above this pore size (ACRF500-10.5nm and 750-16.5nm) the conductivity within the pores is reduced due a possible reduction in the dielectric constant, ε_r, which may result in an increase in resistance. The absence of a semi-circle for $EMImBF_4$ for ACRF200-4.5nm and ACRF300-6.5nm indicates close to ideal behaviour due to high conductivity across the electrode. It was observed that for the electrolyte resistance (R_S) there was little change with variation in pore size.

The R_S and ESR increased with increasing viscosity following close to a linear relation (R^2 0.958 and0.932 respectively). The correlation between viscosity and ESR was higher than for viscosity and capacitance at 0.637. This indicated that the resistance was more highly related to the viscosity of the electrolyte than to anion size.

Cyclic Voltammetry (CV) was used to study the electrochemical behaviour for Faradaic reactions; both those resulting from pseudocapacitance; and decomposition of electrolyte due to overcharging. As no deformation of the voltammograms was seen at intermediate potentials, it was confirmed that the cells were not participating in Faradaic reactions for pseudocapacitance. However, the voltammograms showed decomposition of the electrolytes $EMImBF_4$ and $EMImN(CN)_2$ due to overcharging. This was attributed to the high surface areas of the activated carbon xerogel electrodes compared with the non-porous samples used for ESW determination.

The cycling performance of the EC test cell ACRF200-4.5nm/$EMImBF_4$ was studied by GC over 50,000 cycles, for operating voltages of 3 V (V_{max}) and 2.5 V (V_{max} – 0.5 V). It was found that the cycle life was extended by 5 times when the operating voltage was reduced from 3 to 2.5 V. However, the cycle life was still poor with only 20% capacitance retention. The poor cycle life was partially attributed to electrolyte decomposition. To ensure that surface functionality on the activated carbon xerogels was not the cause of the poor cycle life, measurements were carried out on cleaned carbons. The cycle life of the clean carbons was not extended, confirming no Faradaic reactions were occurring. The next step was to confirm that electrolyte decomposition was the cause of the poor cycle life, not electrode degradation. DMPImTFSI was cycled at 2.7 V (V_{max}) and found to show similar cycling performance to $EMImBF_4$ cycled at 2.5 V. If poor cycling performance had

been caused by electrode degradation, the higher operating voltage and large ion size for DMPImTFSI would have resulted in a lower cycling performance than for $EMImBF_4$ at 2.5 V. This indicated that the electrolyte was decomposing on cycling due to impurities in the test cells, e.g. water egress from the environment, and contaminants in the electrolytes.

The self-discharge behaviour of the EC test cells was studied over 24 hours. It was found that the main cause of self-discharge for the RTILs was due to charge redistribution. The extent to which charge redistribution occurred was found to be influenced by two factors; initial capacitance and viscosity of the electrolyte with the order of self-discharge (slowest to fastest) DMPImTFSI < $BMPyT(f_5Et)PF_3$ < $EMImBF_4$ < $EMImN(CN)_2$. The self-discharge of the organic electrolyte was found to be independent of both those factors due to the highly mobile ions in the solvent.

The energy and power density for the EC test cells was studied through the use of Ragone plots. It was found that the best power and energy density was obtained for $EMImBF_4$ and ACRF200-4.5nm of 665.5 kW kg^{-1} and 175 Wh kg^{-1}. The energy and power density of ACRF200-4.5nm was be seen to reduce at higher charge-discharge rates, while the power density for ACRF300-6.5nm continued to increase. This shows that if high charge-discharge rate were a desired characteristic, ACRF300 would be the better material choice, confirming the conclusions drawn from GC measurements that ACRF200-4.5nm is the best choice for low charge-discharge rates and ACRF300-6.5nm is the preferable for high charge-discharge rates.

As the energy and power density are calculated based on the capacitance and resistance values obtained from GC measurements, the results were found to follow the pattern for increasing pore size. Where the higher pore sizes result in reduced energy and power performance.

7.2 Implications for EC Manufacture

1. Overall, the electrolyte that provided the best performance was $EMImBF_4$; this was due to stability at a higher voltage allowing for longer discharge cycles, good conductivity and relatively low viscosity by comparison with the other electrolytes tested.

2. ACRF200-4.5nm provides the highest capacitance due to pore size being large enough for electrolyte ions to access the pore and provide a tight enough fit for the double-layer thickness, *d*, to the be at its lowest.

3. ACRF300-6.5nm provides the best charge-discharge rate capability due to the larger mesopores improving the dynamic performance of the system.

4. The combination of ACRF200-4.5nm/$EMImBF_4$ provides a system with a higher maximum operating voltage than the currently available AC/organic electrolyte systems.

5. DMPImTFSI gives rise to the second highest capacitance and energy density of 118 Wh kg^{-1} making it the desirable choice over $EMImBF_4$, due to the concerns raised over the safety of $EMImBF_4$. High current spikes that occur on overcharging of the $EMImBF_4$, indicate that hydrogen fluoride will be easily liberated from the cell on moderate overcharging that may occur during operation.

6. There is not one material or one pore size that is optimum for all applications. The applications of ECs can be divided into two main categories: power supply and memory back-up, the former requiring high discharge current and the latter requiring high-energy low current rate.

7.3 Further Studies

It was identified in **Section 5.8** that particles < 50 µm produced the most flexible electrodes. However, it was also shown that the ball milling required to obtain this particle size led to a reduction in the surface area. One way to solve this issue would be the production of RF gel spheres < 50 µm. Due to the versatility of the RF gels this may be a possible production route.

The optimum pore size for both capacitance performance and rate performance were identified in **Sections 6.2.1 and 6.2.2** respectively. To maximise the specific capacitance at these pore sizes increased activation could be carried out to enhance the surface areas.

It was identified in **Section 6.5**, that the cycling performance of the RTIL electrolytes was very poor. Significant improvements could be made to the EC test cell design to ensure water and oxygen egress is prevented. However, from a large scale implementation viewpoint, the more important issue raised was with the stabilty of the current collector. This could be improved through the use of stable coatings.

From the **Section 2.3** it was identified that surface modifcation to the carbon materials could improve wettability of the electrode in the electrolyte through the introduction of hydrophilic or hydrophobic surface groups. Thus, improving the EC performance. For RTILs there is an apparent lack of research in this area.

7.4 Concluding Remarks

This study has identified that the pore size is an important factor for optimising capacitance performance of carbon-based / RTIL ECs. It also identified the importance of studying the porosity characteristics of the composite electrodes as well as those of the active materials under investigation. The best capacitance performance of 140 F g^{-1} was obtained for composite electrode with average pore size 4.5nm, i.e. activated carbon xerogel with d_{av} = 3.5nm. The best dynamic performance of 70% capacitance retention was achieved with composite electrode with average pore size of 6.5nm, i.e. activated carbon xerogel with d_{av} = 6 nm. A maximum energy density of 175 Wh kg^{-1} and power density of 665.5 kW kg^{-1} were obtained for the activated carbon sample with average pore diameter 3.5 nm and RTIL electrolyte $EMImBF_4$ at an operating voltage of 3 V. This was an improvement over the commercially utilised organic electrolyte Et_4NBF_4-PC 1M which obtained a maximum energy and power density of 84 Wh kg^{-1} and 528.1 kW kg^{-1} respectively.

This study contradicts the literature stating that micropores (<1nm) enhance capacitance, by showing that mesopores of 3.5 – 6 nm provide the best performance at high charge-discharge rate, when combined with RTILs. This has implications in the manufacture of ECs for high power and energy applications, where mesoporous materials combined with RTILs may provide superior performance.

RTIL $BMPyT(f_5Et)PF_3$ exhibited the highest voltage of the RTILs studied, however, it did not reach the high voltages claimed by the suppliers Merck[22]. Despite the unattainable large increase in operating voltage, RTIL $EMImBF_4$ still outperforms the organic electrolyte Et_4NBF_4-PC 1M for all electrochemical measurements carried out, increasing capacitance, energy density, power density and reducing ESR. Although the RTILs use as high voltage electrolytes may be disappointing, the benefits of RTILs lie not in their abilty to increase the operating voltage, and therefore energy density, but in the safety improvements that can be made. The safety of the devices is improved over that of volatile and flammable organic electrolytes, where there are concerns of potential explosion under extreme conditions, e.g. during vehicle accidents.

8.0 References

[1] 'Electrochemical Supercapacitors Scientific Fundamentals and Technological Applications', B.E. Conway, Kluwer 1999, ISBN 0-306-45736-9,

[2] T. Markel, A. Brooker, T. Hendricks, V. Johnson, K. Kelly, B. Kramer, M. O'Keefe, S. Sprik and K. Wipke, *J.Power Sources*, 2002, **110**, 255-266

[3] A. Burke, *J. Power Sources,* 2000, **91,** 37 – 50

[4] Observatory NANO - http://www.observatorynano.eu/project/document/2028/

[5] R. Kotz, M. Carlen, *Electrochim. Acta*, 2000, **45**, 2583 – 2498

[6] R. Carter, A. Cruden, *IEEE International Symposium on Power Electronics, Electrical Drives, Automation and Motion,* 2008, **1-3**, 727-732

[7] E. Frackowiak, F. Beguin, *Carbon*, 2001, **39**, 937 – 950

[8] Y. Zhang, H. Feng, X. Wu, L. Wang, A. Zhang, T. Xia, H. Dong, X. Li, L. Zhang, *Hydrogen Energy*, 2009, **34**, 4889 – 4899

[9] A Time Before Telephones – www.telcomhistory.org

[10] H. E. Becker, US Patent 2,800,616 (to General Electric Co.) (1957)

[11] H. Von Helmholtz. *Ann. Phys. (Leipzig)*, 1853, **89**, 211 – 233

[12] G. Gouy, *Ann. Phys. (Paris),*1917, **7** , 129 – 184

[13] O. Stern, Zeit. Elektrochem., 1924, **30**, 508 – 516

[14] O. Barbieri, M. Hahn, A. Herzog, R. Kötz, *Carbon*, 2005, **43**, 1303 – 1310

[15] J. S. Wilkes, M. J. Zaworotko, *Chem. Comm.*, 1992, **13**, 965 – 967

[16] 'Electrochemical Aspects of Room Temperature Ionic Liquids' edited by H. Ohno, John Wiley & Sons, 2005, ISBN 0-471-64851-5

[17] L.J. Vimmerstedt, and C. J. Hamel, Current Status of Environmental, Health and Safety Issues of Electrochemical Capacitors for Advanced Vehicle Applications, Technical Report, April 1, 1997 http://www.cartech.doe.gov/pdfs/B/138.pdf

[18] P. R. Gifford, J. B. Palmisano, *J. Electrochem. Soc.* 1987, **134**, 610 – 614

[19] Merck KGaA, Darmstadt, Germany. 2007. www.merck-chemicals.com

[20] A. M. Galinski, A. Lewandowski, I Stepniak, *Electrochimica Acta*, 2006, **51**, 5567 – 5580

[21] 'Recent Advances in Supercapacitors' edited by V. Gupta, Transworld Research Network, 2006, ISBN 81-7895-233-5

[22] 'Activated Carbon: Surface Chemistry and Adsorption from Solution', J. S. Mattson, Marcel Dekker 1971, ISBN 978-08247-1443-7

[23] H. Shi, *Electrochimica Acta*, 1995, **41**, 1633 – 1639

[24] D. Qu and H. Shi, *J. Power Sources*, 1998, **74**, 99 – 107

[25] S. Wen, M. Jung, O-S. Joo and S. Mho, *Current Appl. Phys.,* 2005, **6**, 1012 – 1015

[26] S.B Sinnott and R. Andrews, *Crit. Rev. Solid State Mater. Sci.*, 2001, **26**, 145 – 249

[27] E. Frackowiak, K. Metenier, V. Bertagna and F. Beguin, *Appl. Phys. Lett*., 2000, **77**, 2421 – 2423

[28] Q. L. Chen, K. H. Xue, W. Shen, F. F. Tao, S. Y. Yin and W. Xu, *Electrochimica Acta*, 2004, **49**, 4157 – 4161

[29] T. Bordjiba, M. Mohamedi and L. H. Dao, *Advanced Materials*, 2008, **20**, 815 – 819

[30] W.Lu and D.D.L.Chung *Carbon* 1997, **35**, 427 – 435

[31] X. Zhao, A.A. Koos, B.T.T. Chu, C. Johnston, N. Grobert, P. S. Grant *Carbon,* 2009, **47**, 561 – 569

[32] C. Merino, P. Sato, E. Vilaplana-Ortego, J. M. Gomez de Salazar, F. Pico and J. M. Rojo, *Carbon*, 2004, **43**, 551 – 557

[33] X. Y. Tao, X. B. Zhang, L. Zhang, J. P. Cheng, F. Liu, J. H. Luo, Z. Q. Luo and H. J. Heise, *Carbon*, 2004, **44**, 1425 – 1428

[34] J. Leis, A. Perkson, M. Arulepp, P. Nigu and G. Svenson, *Carbon*, 2002, **40**, 1559 – 1564

[35] J. Chmiola, G. Yushin, R. Dash and Y. Gogotsi, *J. Power Sources*, 2006, **158**, 765 – 772

[36] A. Janes, L. Permann, M. Arulepp and E. Lust, *Electrochem. Comm.,* 2004, **6**, 313 – 318

[37] M. Arlupp, J. Leis, M. Latt, F. Miller, K. Rumma, E. Lust and A. F. Burke, *J. Power Sources*, 2006, **146**, 1460 – 1466

[38] W. Xing, S. Z. Qiao, R. G. Ding, F. Li, G. Q. Lu, Z. F. Yan and H. M. Cheng, *Carbon*, 2006, **44**, 216 – 224

[39] M. Sevilla, S. Alvarez, T. A. Centeno, A. B. Fuertes, F. Stoeckli, *Electrochimica Acta*, 2007, **52**, 3207 – 3215

[40] K.S. Novoselov, A. K. Geim, S. V. Morosov, D. Jiang, Y. Zhang, S. V. Dubonos, I. V. Grigorieva, A. A. Firsov, *Science*, 2004, **306**, 666 – 669

[41] S. Stankovich, D. A. Dikin, R. D. Piner, K. A. Kohlhaas, A. Kleinhammes, Y. Jia, Y. Wu, S. T. Nguyen, R. S. Ruoff, *Carbon*, 2007, **45**, 1558 – 1565

[42] A. Reina, J. Xiaoxing, J. Ho, D. Nezich, H. Sun, V. Bulovic, M. S. Dresselhaus, J. Kong, *Nano Lett*. 2009, **9**, 30 – 35

[43] J. Campos-Delgado, J. M. Romo-Herrera, X. Jia, D. A. Cullen, H. Muramatsu, Y. A. Kim, T. Hayashi, Z. Ren, D. J. Smith, Y. Okuno, T. Ohba, H. Kanoh, K. Kaneko, M. Endo, H. Terrones, M. S. Dresselhaus, M. Terrones, *Nano Lett*., 2008, **8**, 2773 – 2778

[44] C. Berger, Z. Song, X. Li, X. Wu, N. Brown, C. Naud, D. Mayou, T. Li, J. Hass, A. N. Marchenov, E. H. Conrad, P. N. First, W. A. de Heer, *Science*, 2006, **312**, 1191 – 1196

[45] Q. Kuang, S. Xie, Z. Jiang, X. Zhang, Z. Xie, R. Huang, L. Zheng, *Carbon*, 2004, **42**, 1737 – 1741

[46] S. Park, R. S. Ruoff, *Nat. Tech.*, 2009, **4**, 217 – 224

[47] M. D. Stoller, S. Park, Y. Zhu, J. An, R. S. Ruoff, *Nano Lett*., 2008, **8**, 3498 – 3502

[48] Y. Chen, X. Zhang, P. Yu, Y. Ma, *J. Power Sources*, 2010, **195**, 3031 – 3035

[49] Y. Wang, Z. Shi, Y. Huang, Y. Ma, C. Wang, M. Chen, Y. Chen, *J. Phys. Chem. C.*, 2009, **113**, 13103 – 13107

[50] R. W. Pekala, *J. Materials Science*, 1989, **24**, 3221 – 3227

[51] W. Li, S. Guo, *Carbon*, 2000, **38**, 1520 – 1523

[52] R. W. Pekala, C. T. Alviso, X. Lu, J. Gross, J. Fricke, *J. Crystalline Materials,* 1995, **188**, 34 – 40

[53] G. C. Rubens, R.W. Pekala, *J. Non-Cryst Solids,* 1995, **186**, 219 – 231

[54] G. Biesmans, A. Martens, T. Woignier, J. Phalippou, *J. Non-Cryst Solids,* 1998, **225**, 64 – 68.

[55] J. K. Lee, G. L. Gould, W. Rhine, *J. Sol-Gel Sci. Technology*, 2009, **49**, 209 – 220

[56] N. Job, A. Théry, R. Pirard, J. Marien, L. Kocon, J. Rouzaud, F. Beguin, J. Pirard, Carbon, 2005, **43**, 2481 – 2494

[57] T. Horikawa, J.Hayashi, K. Muroyama, *Carbon*, 2004, **42**, 1625 – 1633

[58] R. W. Pekala, J. C. Farmer, C. T. Alviso, T. D. Tran, S. T. Mayer, J. M. Miller, B. Dunn, *J. Non-Cryst Solids,* 1998, **225**, 74 – 80

[59] J. Li, X. Wang, Y. Wang, Q. Huang, C. Dai, S. Gamboa, P. J. Sebastian, *J. Non-Cryst Solids,* 2008, **354**, 19 – 24

[60] S. J. Kim, S. W. Hwang, S. H. Hyun, *J. Materials Science*, 2005, **40**, 725 – 731

[61] Y. Zhu, H. Hu, W. Li, X. Zhang, *Carbon*, 2007, **45**, 160 – 165

[62] C. Arbizzani, S. Beninati, M Lazzari, F. Soavi, M. Mastragostino, *J. Power Sources,* 2007, **174**, 648 – 652

[63] M. Lazzari, M. Mastragostino, F. Soavi, *Electro. Commun.,* 2007, **9**, 1567 – 1572

[64] M. V. Fedorov, A. A. Kornyshev, *J. Phys. Chem. B*, 2008, **112**, 11868 – 11872

[65] Y. Shim, H. J. Kim, *ACS Nano*, 2010, **4**, 2345 – 2355

[66] G. Bo, Z. Xiaogang, Y. Changzhou, L. Juan, Y. Long, *Electrochimica Acta*, 2006, **52**, 1028 – 1032

[67] I-H. Kim, K-B. Kim, *J. Electrochem. Soc*., 2006, **153**, A383 – A389

[68] J. B. Goodenough, '*Progress in Solid-State Chemistry'*, ed. N. Reiss, 1971, Volume 5,

[69] D.J. Ham, R. Ganesan, J.S. Lee, *Int. J. Hydrogen Energy*, 2008, **33**, 6865 – 6872

[70] M-S. Wu, Y-A. Huang, C-H. Yang, J-J. Jow, *Int. J. Hydrogen Energy*, 2007, **32**, 4153 – 4159

[71] X-H. Yang, Y-G. Wang, H-M. Xiong, Y-Y. Xia, *Electrochim. Acta*, 2007, **53**, 752 – 757

[72] S-L. Kuo, N-L. Wu, *Electrochem. Solid State Lett*., 2007, **10**, A171 – 175

[73] Z. J. Lao, K. Konstantinov, Y. Tournaire, S. H. Ng, G. X. Wang, H. K. Lui, *J. Power Sources,* 2006, **162**, 1451 – 1454

[74] D. Choi, G. E. Blomgren, P.N. Kumta, *Adv. Mater*., 2006, **18**, 1178 – 1182

[75] S. Desplobain, G. Gautier, J. Semai, L. Ventura, M. Roy, *Phys. Status. Solid. (C),* 2007, **4**, 2180 – 2184

[76] M. Jayalakshmi, and K. Balasubramanian, *Int. J. Electrochem. Sci.,* 2008, **3**, 1196 –1217

[77] K. R. Prasad, N. Miura, *J. Power Sources*, 2004, **135,** 354 – 360

[78] K. R. Prasad, N. Miura, *Electrochem. Commun*., 2004, **6**, 1004 – 1008

[79] W. Dong, D.R. Rolison, B. Dunn, *Electrochem. Solid-State Lett*., 2000, **3**, 457 – 459

[80] T. Kudo, Y. Ikeda, T. Watanabe, M. Hibino, M. Miyayama, H. Abe, K. Kajita, *Solid State Ionics*, 2002, **152**, 833 – 841

[81] G.X. Wang, B.L. Zhang, Z.L. Yu, M.Z. Qu, *Solid State Ionics*, 2005, **176**, 1169 – 1174

[82] H.P.Wong, B.C. Dave, F. Leroux, J. Harreld, B. Dunn, L.F. Nazar, *J. Mater. Chem*., 1998, **8**, 1019 – 1027

[83] M.J. Parent, S. Passerini, B.B. Owens, W.H. Smyrl, *J. Electrochem. Soc*., 1999, **146**, 1346 – 1354

[84] S. Passerini, J.J. Ressler, D.B. Le, B.B. Owens, W.H. Smyrl, *Electrochim. Acta*, 1999, **44**, 2209 – 2217

[85] S. Suzuki, M. Hibino, M. Miyayama, *J. Power Sources*, 2003, **124**, 513 - 517

[86] A. Dobley, K. Ngala, S. Yang, P.Y. Zavalij, M.S. Whittingham, *Chem. Mater.*, 2001, **13**, 4382 – 4386

[87] J.S. Sakamoto, B. Dunn, *J. Electrochem. Soc.*, 2002, **149**, A26 – A30

[88] H.Y. Lee, J.B. Goodenough, *J. Solid State Chem.*, 1999, **148**, 81 – 84

[89] Ravinder N. Reddy, Ramana G. Reddy, *J. Power Sources*, 2006, **156**, 700 – 704

[90] Ravinder N. Reddy, Ramana G. Reddy, *J. Power Sources*, 2004, **132**, 315 – 320

[91] T. Watanabe, Y. Ikeda, T. Ono, M. Hibino, M. Hosoda, K. Sakai, T. Kudo, *Solid State Ionics*, 2002, **151**, 313 – 320

[92] M. J. Parent, S. Passerini, B. B. Owens, W. H. Smyrl, *J. Electrochem. Soc.*, 1999, **146**, 1346 – 1350

[93] W. Dong, J. Sakamoto, B. Dunn, *J. Sol-Gel Sci. Technol.*, 2003, **26**, 641 – 649

[94] H. Kim, B. N. Popov, *J. Power Sources*, 2002, **104**, 52 – 61

[95] J. H. Park, J. M. Ko, O. O. Park, *J. Electrochem. Soc.*, 2003, **150**, A864 – A867

[96] K.-W. Nam, E.-S. Lee, J.-H. Kim, Y.-H. Lee, K.-B. Kim, *J. Electrochem. Soc.*, 2005, **152**, A2123 – A2129

[97] C.-C. Hu, W.-C. Chen, K.-H. Chang, *J. Electrochem. Soc.*, 2004, **151**, A281 – A290

[98] I.-H. Kim, J.-H. Kim, K.-B. Kim, *Electrochem. Solid-State Lett.*, 2005, **8**, A369 – A372

[99] I.-H. Kim, J.-H. Kim, Y.-H. Lee, K.-B. Kim, *J. Electrochem. Soc.*, 2005, **152**, A2170 – A2178

[100] C. C. Hu, T. W. Tsou, *J. Power Sources*, 2003, **115**, 179 – 186

[101] K. W. Nam, W. S. Yoon, K. B. Kim, *Electrochim. Acta*, 2002, **47**, 3201 – 3209

[102] C. C. Hu, C. C. Wang, *J. Electrochem. Soc*., 2003, **150**, A1079 – A1084

[103] R. N. Reddy, R. G. Reddy, *J. Power Sources*, 2003, **124**, 330 – 337

[104] J. K. Chang, Y. L. Chen, W. T. Tasai, *J. Power Sources*, 2004, **135**, 344 – 353

[105] J. Deng, X. Xing, W. Zhang, Y. Peng, J. Wang, X. Long, P. Li, A. S. C. Chan, *Eur. Polym. J.*, 2002, **38**, 2497 – 2501

[106] T. Shinomiya, V. Gupta, N. Miura, *Electrochim. Acta*, 2004, **51**, 4412 – 4419

[107] V. Gupta, N, Miura*, J. Power Sources*, 2006, **157**, 616 – 620

[108] V. Gupta, N, Miura, *Electrochim. Acta*, 2006, **52**, 1721 - 1726

[109] K. Kinoshita, *Carbon: Electrochemical and Physicochemical Properties*, Wiley Interscience, New York, 1988

[110] T. J. Bandosz and C. O. Ania, *Activated Carbon Surfaces in Environmental Remediation*, *Chapter 4 – Surface Chemistry of Activated Carbon and it Characterisation*. Elsevier 2006

[111] A. G. Pandolfo, and A. F. Hollenkamp, *J Power Sources*, 2006, **157**, 11 – 27

[112] B. Fang, and L. Binder, *J. Phys. Chem. B*, 2006, 110, 7877 – 7882

[113] B. Fang, and L. Binder, *J. Power Sources*, 2006, **163**, 616 – 622

[114] D. Lozano-Castelló, D. Cazorla-Amorós, A. Linares-Solano, S. Shiraishi, H. Kurihara, A. Oya, *Carbon*, 2003, **41**, 1765 – 1775

[115] D. Hulicova, J. Yamashita, Y. Soneda, H. Hatori and M. Kodama, Chem. Mater., 2005, **17**, 1241 – 1247

[116] M. Olivares-Marin, J. A. Fernandez, M. J. Lazaro, C. Fernandez-Gonzalez, A. Marcias-Garcia, V. Gomez-Serrano, F. Stoeckli, T. A. Centeno, *Mater.*

Chem. Phys., 2009, **114**, 323 – 327

[117] P. Kilaru, G. A. Baker and P. Scovazzo, *J. Chem. Eng. Data*, 2007, **52**, 2306 – 2314.

[118] K. Kim, C. Lang, Moulton, R. and P.A. Kohl, *J. Electrochem. Soc.,* 2004, **1518**, A1168 – A1172.

[119] Y-J. Kim, Y. Matsuzawa, S. Ozaki, K. C. Park, C. Kim, M. Endo, H. Yoshida, G. Masuda, T. Sato and M. S. Dresselhaus, *J. Electrochem. Soc*., 2005, **1524**, A710 – A715.

[120] D. R. MacFarlane, J. Sun, J. Golding, P. Meakin and M. Forsyth, *Electrochim. Acta*, 2000, **45**, 1271 – 1278.

[121] H. Matsumoto, M. Yanagida, K.Tanimoto, M. Nomura, Y. Kitagawa and Y. Miyazaki, *Chem. Lett.,* 2000, **29**, 922 - 932.

[122] H. Matsumoto, H. Kageyama and Y. Miyazaki, *Chem. Lett.,* 2001, **2**, 182 – 183.

[123] J. Sun, M. Forsyth and D. R. MacFarlane, *J. Phys. Chem. B*, 1998, **102**, 8858 – 8864.

[124] W. Lu, K. Henry, C. Turchi and J. Pellegrino, *J. Electrochem. Soc.,* 2008, **155,** A361 – A367.

[125] Merck KGaA, Darmstadt, Germany, www.merck-chemicals.com (2008).

[126] I. Fletcher, F. B. Sillars, N. E. Hudson and P. J. Hall, in press, *J. Chem. Eng. Data.,* 2010, **55**, 778 – 782

[127] J. M. Crosthwaite, M. J. Muldoon, J. K. Dixon, J. L. Anderson and J. F. Brennecke, *Pure and Appl. Chem*., 2009, **81**, 791 – 828

[128] K. R. Harris and L. A. Woolf, *J. Chem. Eng. Data*, 2005, **50**, 1777 – 1782.

[129] D.R. MacFarlane, P. Meakin, J. Sun, N. Amini and M. Forsyth, *J. Phys. Chem. B.,* 1999, **103**, 4164 – 4170.

[130] A. B. McEwen, H. L. Ngo, K. LeCompte and J. Goldman, *J. Electrochem. Soc.,* 1999, **146,** 1687 – 1695.

[131] H. Tokuda, K. Hayamizu, K. Ishii, A. B. H. Susan, M. Watanabe, *J. Phys. Chem. B* 2004, **108**, 16593–16600.

[132] H. Tokuda, K. Hayamizu, K. Ishii, A. B. H. Susan, M. Watanabe, *J. Phys. Chem. B* 2005, **109**, 6103-6110.

[133] H. Tokuda, K. Hayamizu, K. Ishii, A. B. H. Susan, M. Watanabe, *J. Phys. Chem. B,* 2006, **110**, 2833 – 2839.

[134] M. E. Kandil and K. N. Marsh, *J. Chem. Eng. Data*, 2007, **52**, 2382 – 2387.

[135] A. Noda, K. Hayamizu and M. Watanabe, *J. Phys. Chem.,* 2001, **105**, 4603 – 4610.

[136] H. Ohno and M. Yoshizawa, *Solid State Ionics*, 2002, **154-155**, 303 – 309.

[137] J. A. Widegren, E. M. Saurer, K. M. Marsh and J. W. Magee, J. Chem. *Thermodynamics*, 2005, **37**, 569 – 575

[138] G. Sun, K. Li, C. Sun, *J. Power Sources*, 2006, **162**, 1444 – 1450

[139] E. Raymundo-Pinero, K. Kierzek, J. Machnikowski, F. Béguin, Carbon, 2006, **44**, 2498 – 2507

[140] J. Chmiola, G. Yushin, Y. Gogotsi, C. Portet, P. Simon, P. L. Taberna, *Science* 2006, **313**, 1760 – 1763

[141] J. Chmiola, C. Largeot, P. L. Taberna, P. Simon, Y. Gogotsi, *Angew. Chem. Int. Ed.,* 2008, **47**, 3392 – 3395.

[142] A. Balducci, R. Dugas, P. L. Taberna, P. Simon, D. Plée, M. Mastragostino, S. Passerini, *J. Power Sources*, 2007, **165**, 922 – 927

[143] C. Largeot, C. Portet, J. Chmiola, P. L. Taberna, Y. Gogotsi, P. Simon, *J. American Chemical Society*, 2008, **130**, 2730 – 2731

[144] C. O. Ania, J. Pernak, F. Stefaniak, E. Raymundo-Pinero, F. Béguin, *Carbon*, 2006, **44**, 3126 – 3130

[145] J.A. Fernandez, S. Tennison, O. Kozynchenko, F. Rubiera, F. Stoeckli, T.A. Centeno, *Carbon*, 2009, **47**, 1598 – 1604

[146] J. Huang, B. Sumpter, V. Meunier, *Chem. Eur. J*., 2008, **14**, 6614 - 6626

[147] C. Kim, K. S. Yang, *App. Phys. Lett*., 2003, **83**, 1216 – 1218

[148] J. A. Fernandez, T. Morishita, M. Toyoda, M. Inagaki, F. Stoeckli, T. A. Centeno, *J. Power Sources*, 2007, **175**, 675 – 679

[149] A. Fuertes, F. Pico, and J. M. Rojo, *J. Power Sources*, 2004, **133**, 329 – 336

[150] P. L. Taberna, C. Portet, P. Simon, *Applied Physic A*, 2006, **82**, 639 – 646

[151] C. Portet, P. L. Taberna, P. Simon, C. Laberty-Robert, *Electrochim. Acta*, 2004, **49**, 905 – 912

[152] B.W. Ricketts, C. Ton-That, *J. Power Source*s, 2000, **89**, 64 – 69

[153] E. Lust, A. Jänes, M. Arulepp, *J. Electroanal. Chem.,* 2004, **562**, 33 – 42

[154] C-T. Hsieh, H. Teng, *Carbon*, 2002, **40**, 667 – 672

[155] B. Xu, F. Wu, S. Chen, C. Zhang, G. Cao, Y. Yang, *Electrochim. Acta*, 2007, **52**, 4595 – 4598

[156] S. Yoon, J. Lee, T. Hyeon, S.M. Oh, *J. Electrochem. Soc*., 2000, **147**, 2507 – 2512

[157] 'Introduction to Carbon Science', Harry Marsh, Butterworths 1989 ISBN 0-408-03837-3

[158] 'Active Carbon', R. C. Bansal, J. B. Donnet, F. Stoeckli, Marcel Dekker Inc New York 1988, ISBN 0-8247-7842-1

[159] Science of Fullerenes and Carbon Nanotubes, M. S. Dresselhaus, G. Dresselhaus, P. C. Eklund, Elsevier Science 1996

[160] M. Dubinin, E. Zaverina, *Russian Chemical Bulletin*, 1961, **10,** 182 – 185

[161] 'Powder Surface Area and Porosity', S Lowell, J. E. Shields, Chapman & Hall, Third Edition, 1991, ISBN 0-412-39690-4

[162] S. J. Gregg, K. S. W. Sing, Academic Press, Second Edition, 1967, ISBN 0-123009561

[163] IUPAC Recommendations, *Pure App. Chem.*, 1985, **57**, 603 – 619

[164] IUPAC Recommendations, *Pure App. Chem.*, 1994, **66**, 1739 – 1758

[165] IUPAC Recommendations, *Pure App. Chem.*, 1989, **61**, 1845 – 1852

[166] I. Langmuir, *J. Amer. Chem. Soc*., 1918, **40**, 1361 – 1368

[167] S. Brunauer, P. H. Emmett, E. Teller, *J. Amer. Chem. Soc.,* 1938, **60**, 309 – 319

[168] E. P. Barrett, L. G. Joyner, P. P. Halenda, *J. Amer. Chem. Soc.,* 1951, **73**, 373 – 380

[169] 'Adsorption Analysis: Equilibria and Kinetics', D. D. Duong, Imperial College Press, 1998, ISBN 1-86094-130-3

[170] 'Undergraduate Instrumental Analysis', J. W. Robinson, G. M. Frame, Marcel Dekker, Fifth Edition, 1995, ISBN 0-8247-9215-7

[171] www.anasys.co.uk/library/

[172] 'Fundamentals of Fourier Transform Infrared Spectroscopy', B. C. Smith, CRC Press LLC, 1996, ISBN 0-8493-2461-0

[173] 'Interpretation of Infrared Spectra, A Practical Approach', J. Coates, John Wiley & Sons, Encyclopaedia of Analytical Chemistry, 2000, 10815 – 10837

[174] 'Electrode Kinetics for Chemists, Chemical Engineers, and Materials Scientists', E. Gileadi, VCH Publishers, Inc. 1993, ISBN 1-56081-561-2

[175] R. de Levie, *Electrochim. Acta,* 1963, **8**, 751 – 780

[176] 'Electrochemical Impedance Spectroscopy' M. E. Orazem, B. Tribollet, The Electrochemical Society Series, John Wiley & Sons, 2008, ISBN 978-0-470-04140-6

[177] S. Buller, E. Karden, D. Kok, R. W. De Doncker, *IEEE Transactions on Industry App.,* 2002, **38**, 1622 – 1626

[178] R. Bonert, L. Zubieta, *IEEE Industry App. Society Annual Meeting Proceedings*, 1997, 1097 – 1100

[179] L. Zubieta, R. Bonert, *IEEE Transactions on Industry App*., 2000, **36**, 199 – 205

[180] M. Lipsztajn, R. A. Osteryoung, *Electrochim. Acta*, 1984, **29**, 1349 – 1352

[181] J. Xie, T. L. Riechel, *J. Electrochem. Soc*., 1998, **145**, 2660 – 2664

[182] L. Xiao, K. E. Johnson, *J. Electrochem. Soc*., 2003, **150**, E305 – E309

[183] G. A. Snook, A. S. Best, A. G. Pandolfo, A. F. Hollenkamp, *Electrochem. Comm*., 2006, **8**, 1405 – 1411

[184] U. Schroder, J. D. Wadhawan, R. G. Compton, F. Marken, P. A. Z. Suarez, C. S. Consorti, R. F. de Souza, J. Dupont, *New J. Chem*., 2000, 24, 1009 – 1015

[185] www.carbolite.com

[186] www.mt.com

[187] www.spexcsp.com/sampleprep

[188] Q. Xiao, X. Zhou, *Electrochim. Acta*, 2003, **48**, 575 – 580

[189] C. Lin, J. A. Ritter, *Carbon*, 1997, **35**, 1271 – 1278

[190] L. Zhang, H. Lui, M. Wang, W. Lui, Rare Metals, 2006, **25**, 51 – 57

[191] S. R. Tennison, *Appl. Catal. A. Gen*., 1998, **173**, 289 – 311

[192] H. Tamon, H. Ishizaka, T. Araki, and M. Okazaki, Carbon,1998, **36**, 1257 – 1262

[193] M. Mirzaeian, P. J. Hall, *J. Materials Science*, 2009, **44**, 2705 – 2713

[194] CRC Handbook of Chemistry and Physics

[195] J. Wang, X. Yang, D. Wu, R. Fu, M. S. Dresselhaus, G. Dresselhaus, *J. Power Sources,* 2008, **185**, 589 – 594

[196] D. R. MacFarlane, S. A. Forsyth, J. Golding, G. B. Deacon, *Green Chemistry*, 2002, **4**, 444 – 448

[197] M. Armand, W. Gorecki, R. Ardreani, *2nd Inter. Symp. Polym. Electrolytes*, Sienna, Italy, 1989

[198] J. J. Golding, D. R. MacFarlane, L. Spiccia, M. Forsyth, B. W. Skelton, A. H. White, *Chem. Commun*., 1998, **15**, 1593

[199] D. Aurbach, M. D. Levi, G. Salitra, N. Levy, E. Pollak, J. Muthu, *J. Electrochem. Soc.*, 2008, **155**, A745 – A753

[200] J. Nui, B. E. Conway, W. Pell, *J. Power Sources*, 2004, **135**, 332 – 343

[201] M. Yaniv, A. Soffer, *J. Electrochem. Soc*., 1976, **123**, 506 –

[202] W. Pell, B. E. Conway, W. Adams, J. Oliveira, *J. Power Sources*, 1999, **80**, 134 – 141

[203] B. E. Conway, W. Pell, T. Lui, *J. Power Sources*, 1997, **65**, 53 – 59

[204] J. Black, H. Andreas, *Electrochim. Acta*, 2009, **54**, 3568 – 3578

Appendix A

A1 Galvanostatic Charge-Discharge – Supplementary Graphs

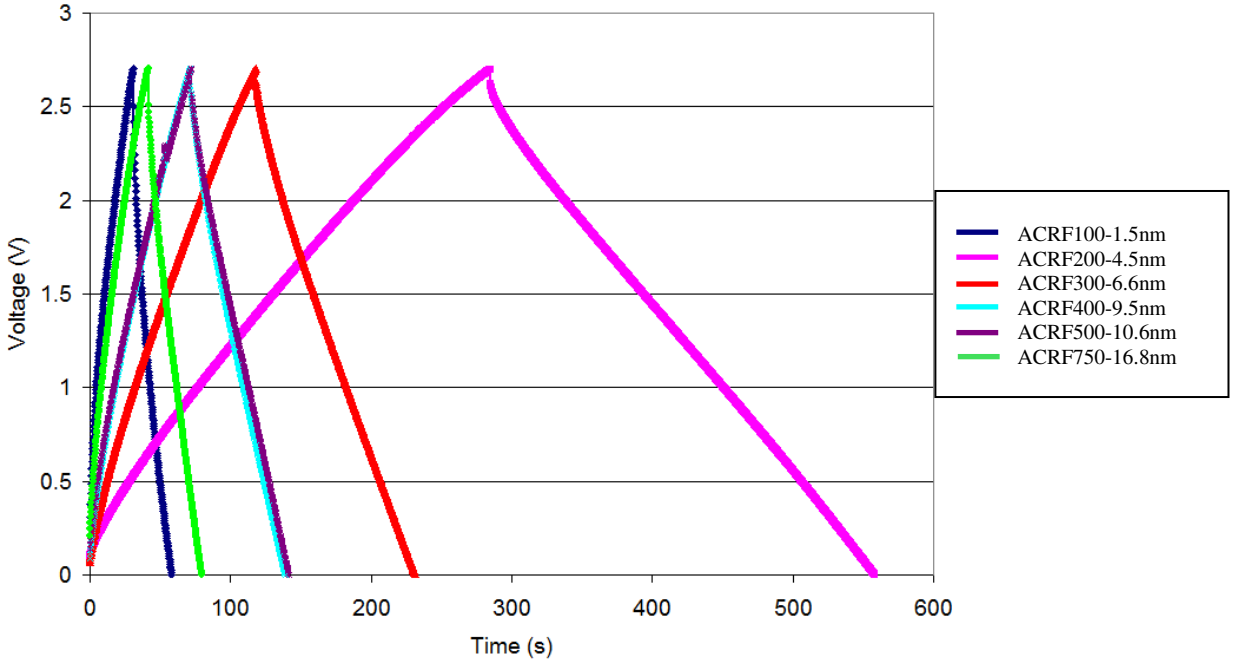

Figure A1.1 – Galvanostatic Charge – Discharge DMPImTFSI

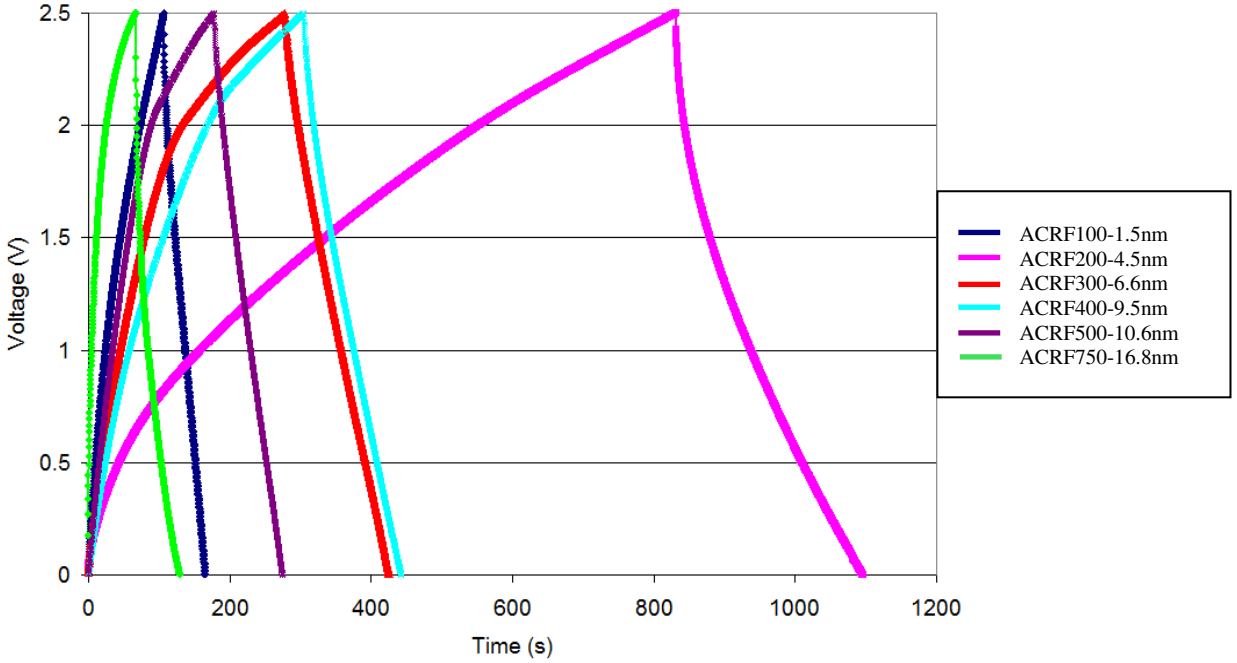

Figure A1.2 – Galvanostatic Charge – Discharge EMImCN

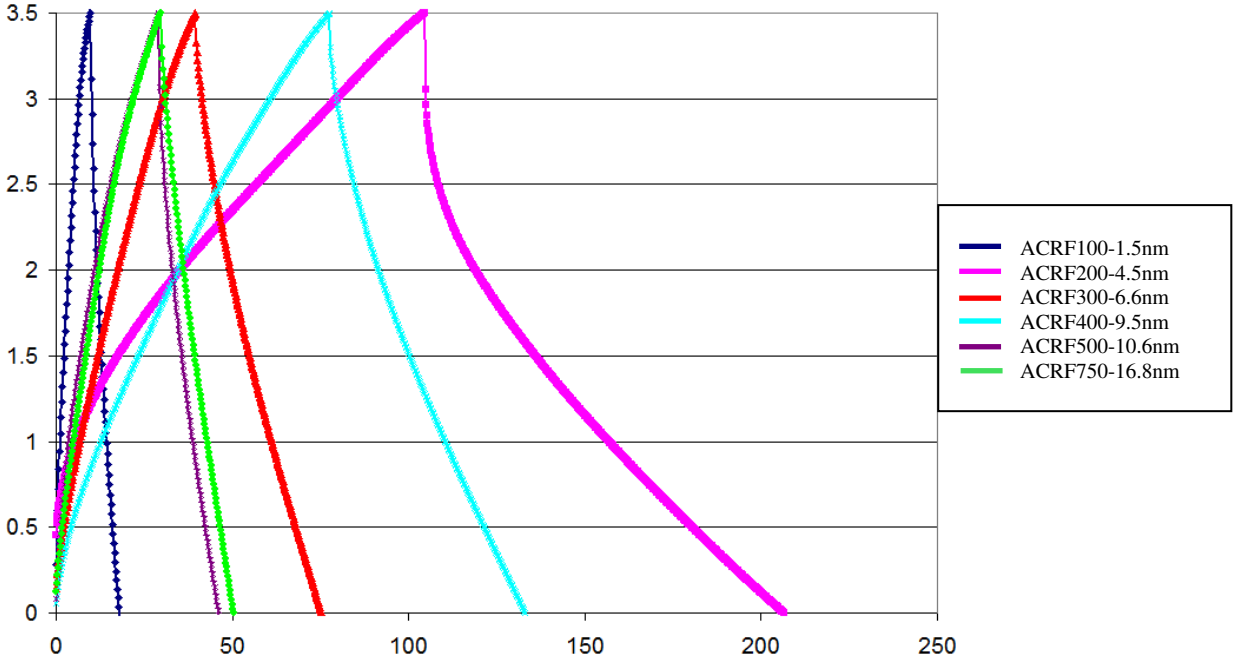

Figure A1.3 – Galvanostatic Charge – Discharge $BMPyTf_5Et_3PF_3$

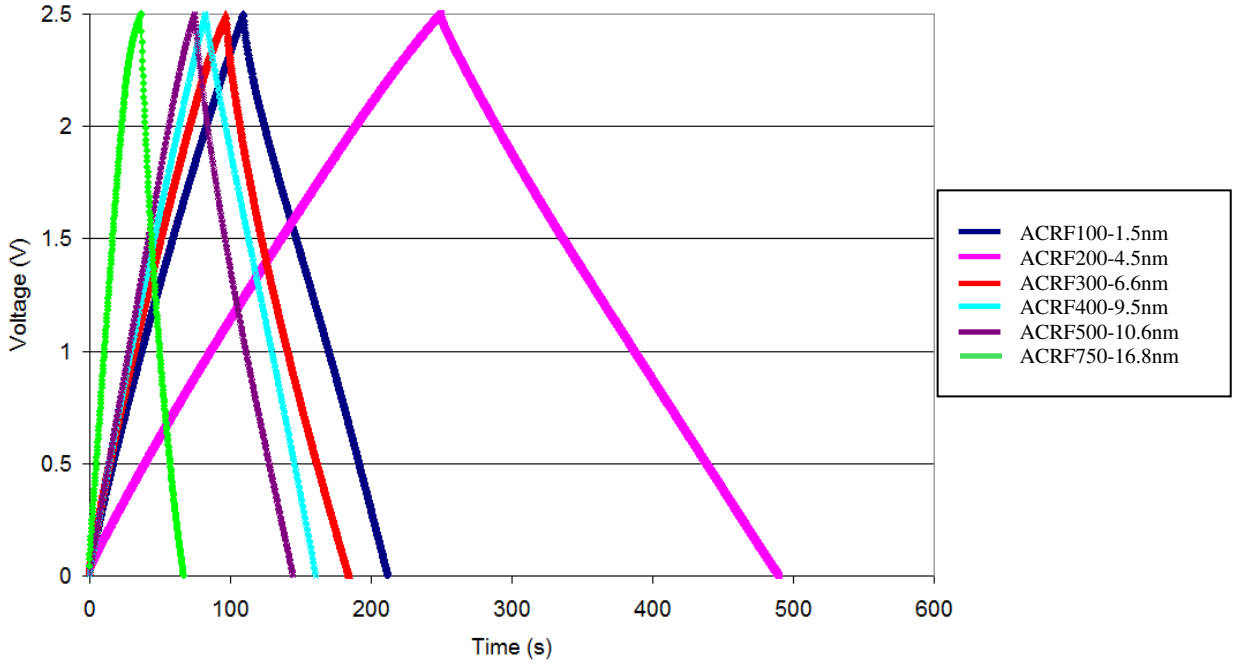

Figure A1.4 – Galvanostatic Charge – Discharge Et_4NBF_4 – PC 1M

A2 Electrochemical Impedance Spectroscopy – Supplementary Graphs

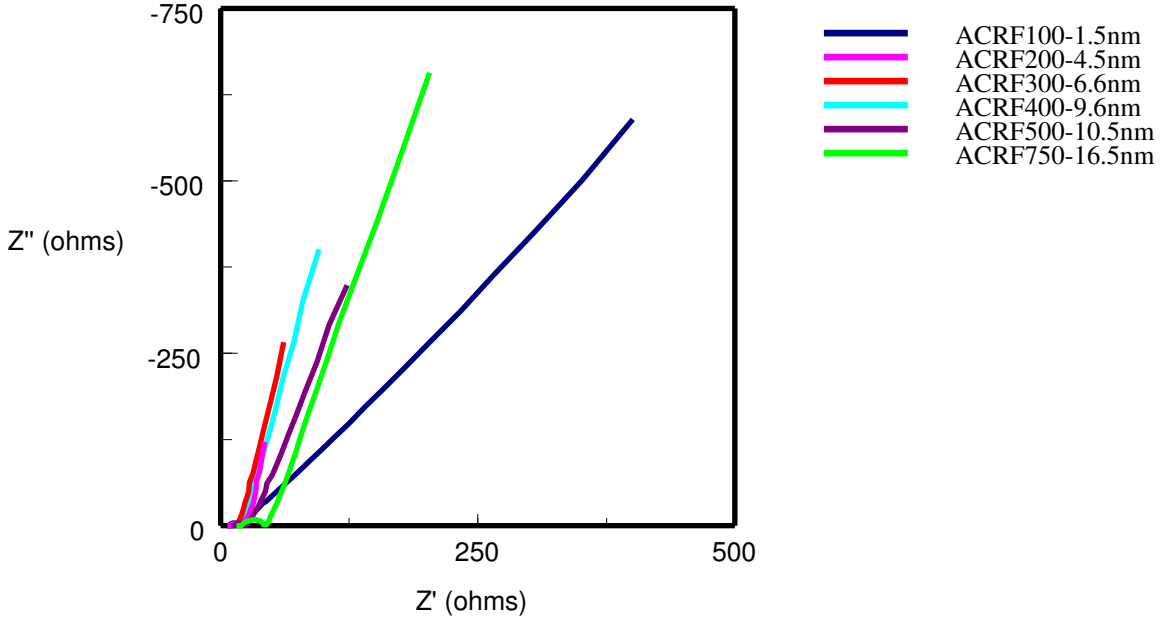

Figure A2.1 (a) – Nyquist Plot DMPImTFSI

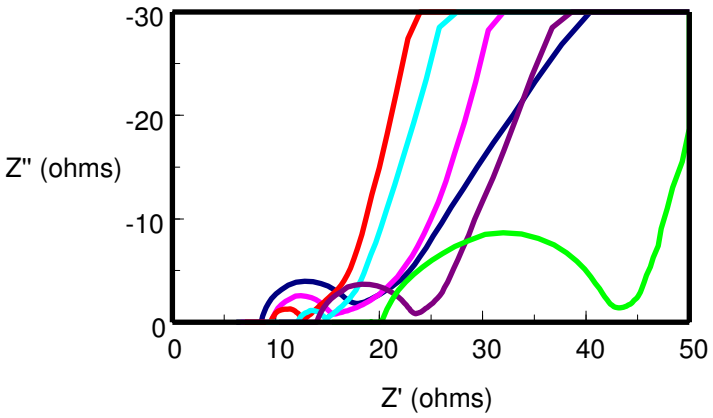

Figure A2.1 (b) – Expanded Nyquist Plot DMPImTFSI

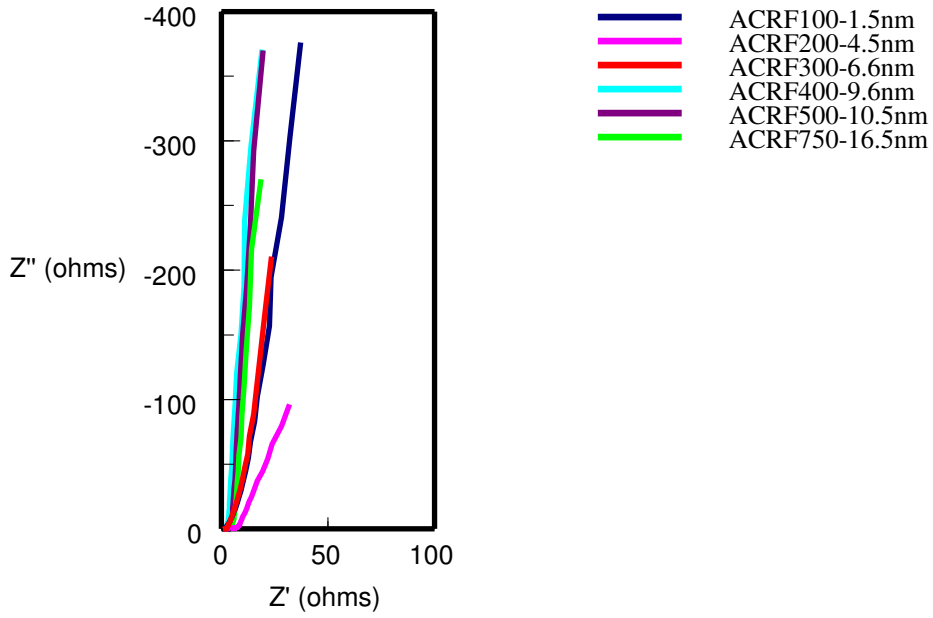

Figure A2.2 (a) – Nyquist Plot EMImCN

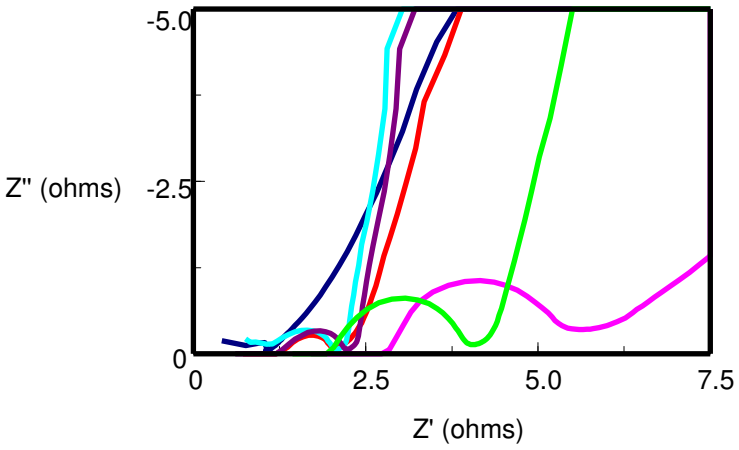

Figure A2.2 (b) – Expanded Nyquist Plot EMImCN

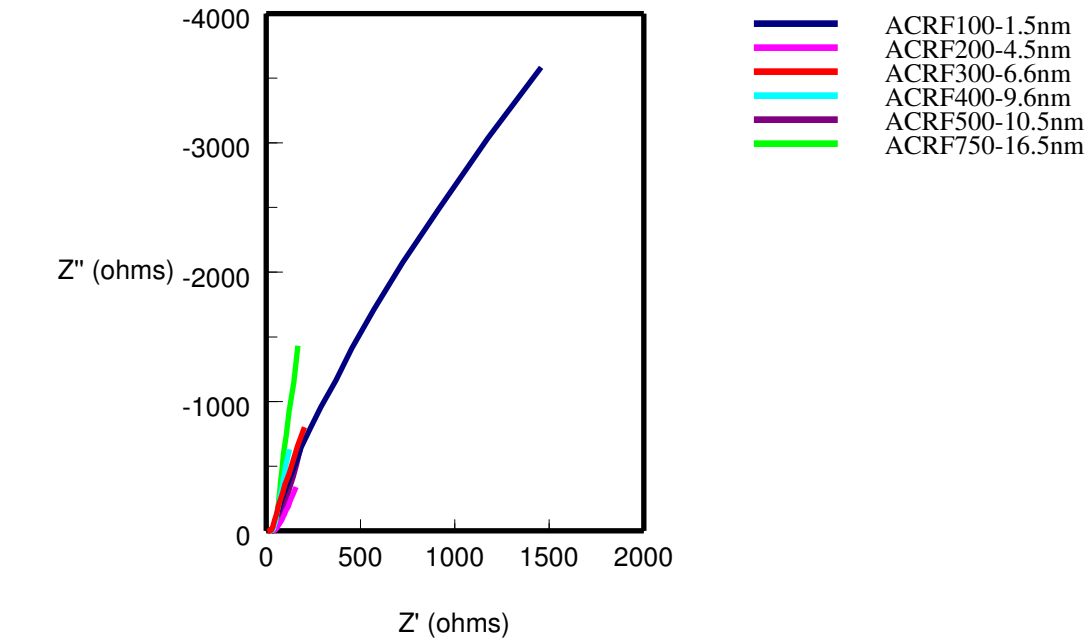

Figure A2.3 (a) – Nyquist Plot $BMPyTf_5Et_3PF_3$

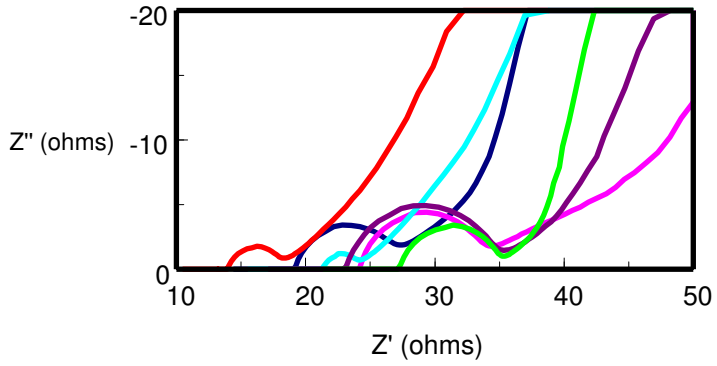

Figure A2.3 (b) – Expanded Nyquist Plot $BMPyTf_5Et_3PF_3$

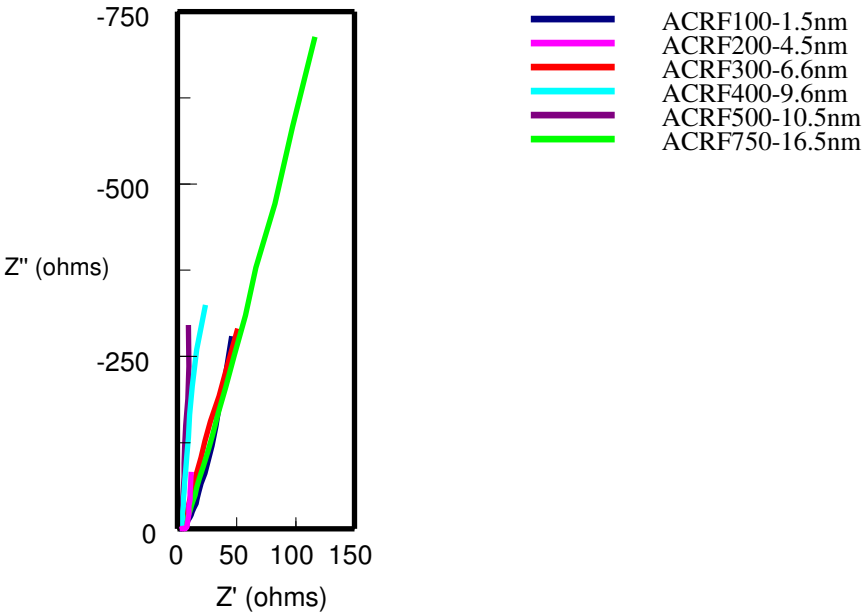

Figure A2.4 (a) – Nyquist Plot Et_4NBF_4 – PC 1M

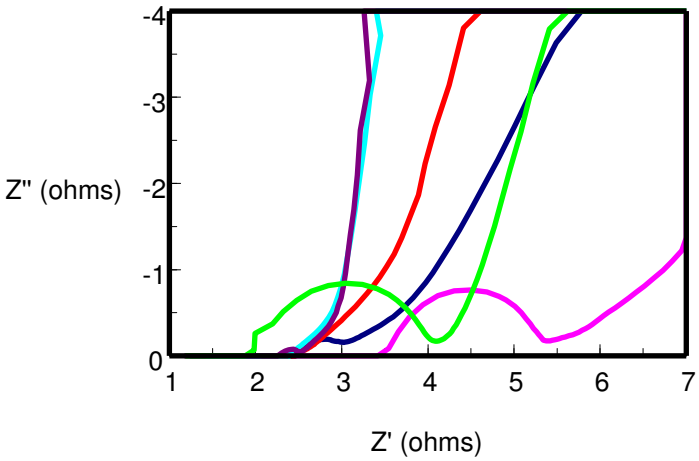

Figure A2.4 (b) – Expanded Nyquist Plot Et_4NBF_4 – PC 1M

A3 Cyclic Voltammetry – Supplementary Graphs

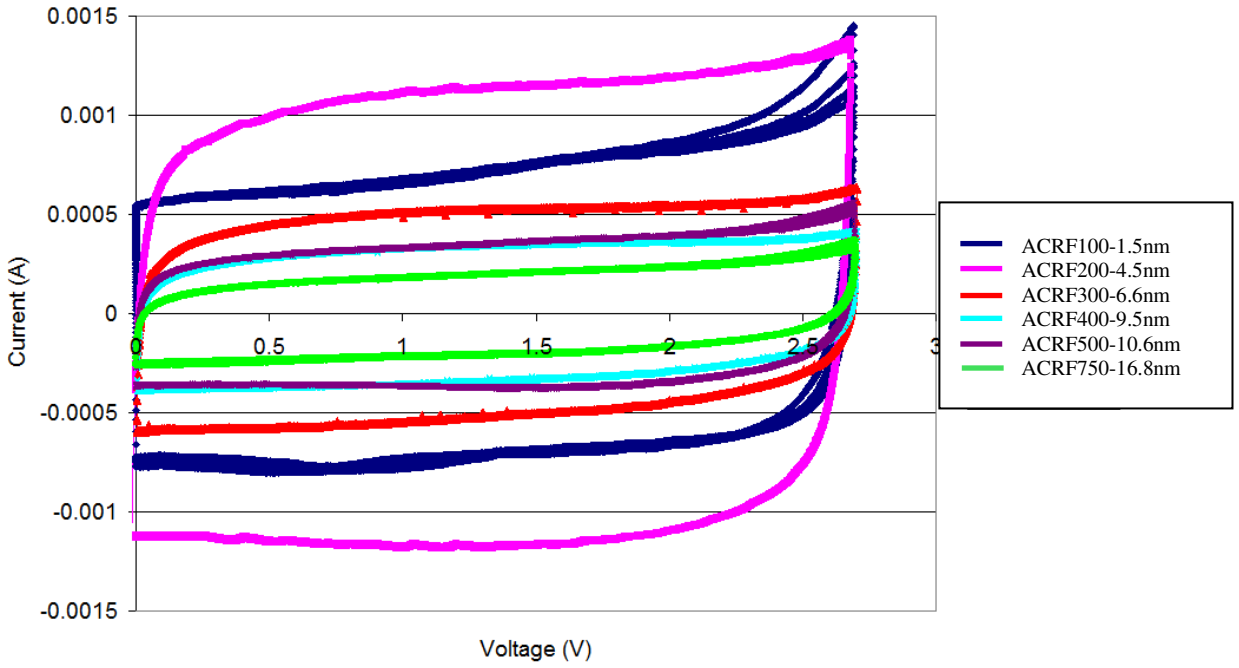

Figure A3.1 – Cyclic Voltammogram DMPImTFSI

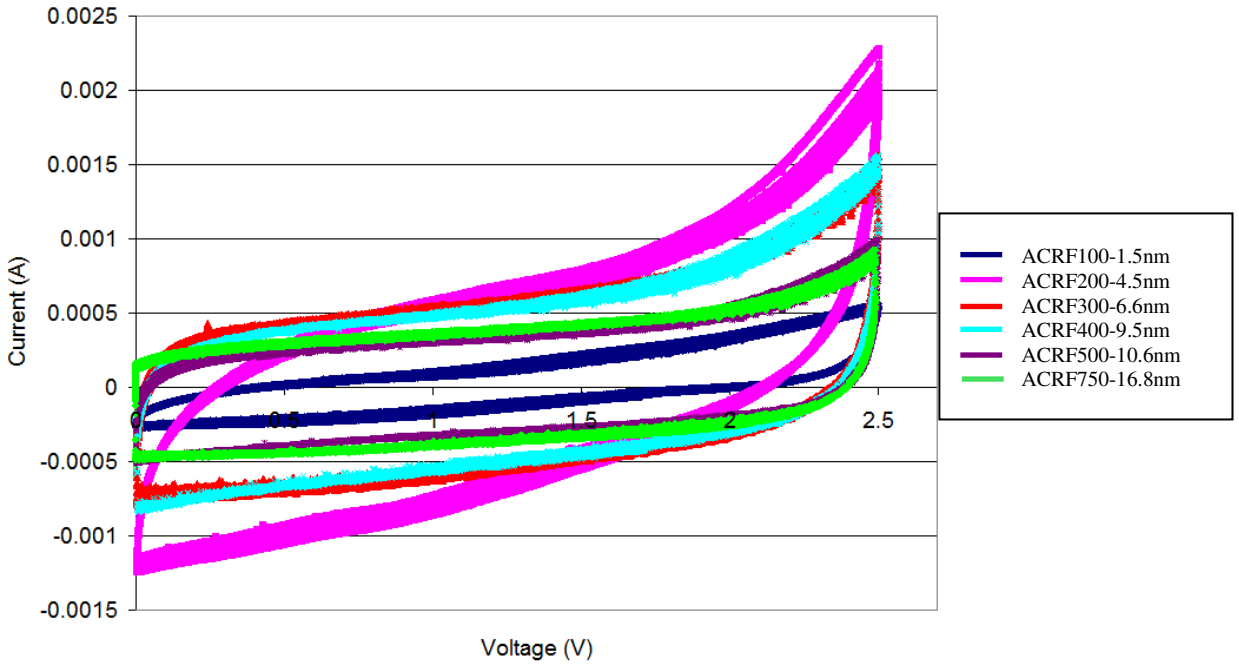

Figure A3.2 – Cyclic Voltammogram $EMImN(CN)_2$

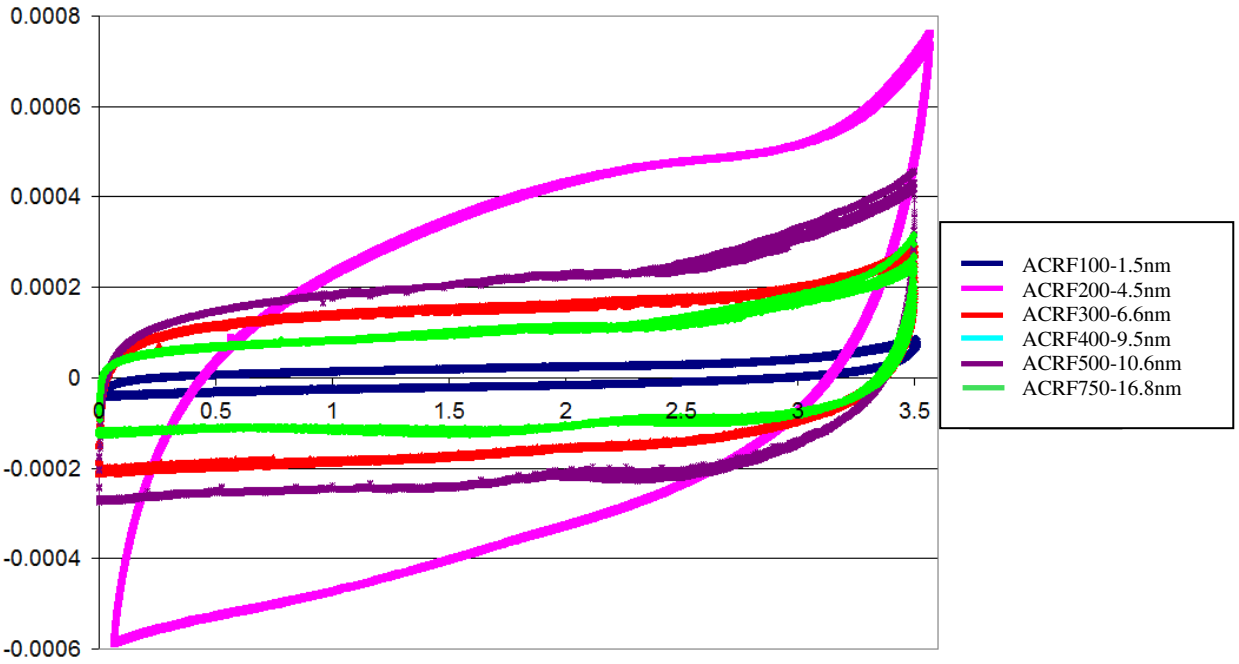

Figure A3.3 – Cyclic Voltammogram $BMPyTf_5Et_3PF_3$

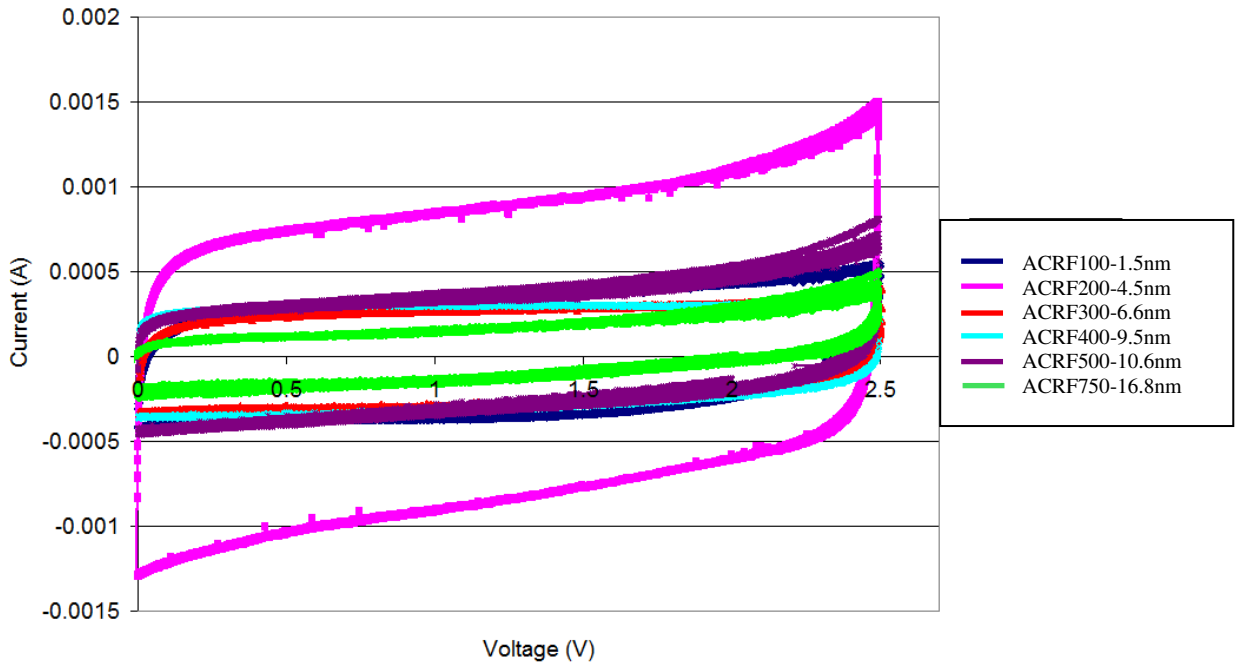

Figure A3.4 – Cyclic Voltammogram Et_4NBF_4 – PC 1M

A4 Self-discharge – Supplementary Graphs

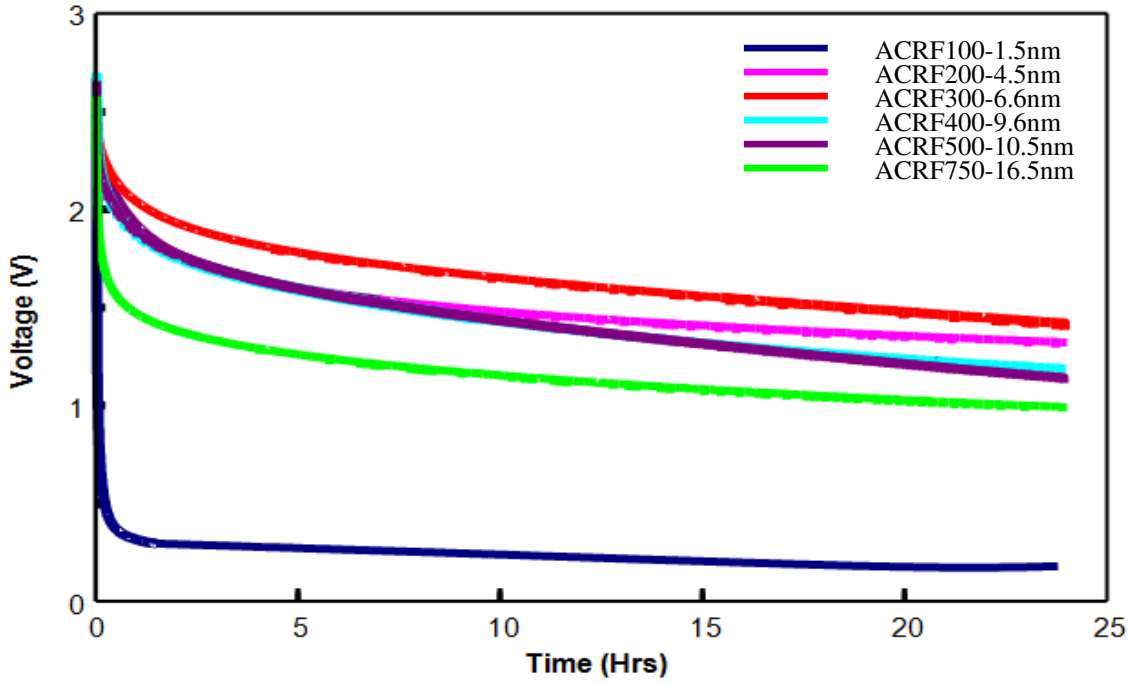

Figure A4.1 – Variance of Self-discharge with Pore Size for DMPImTFSI

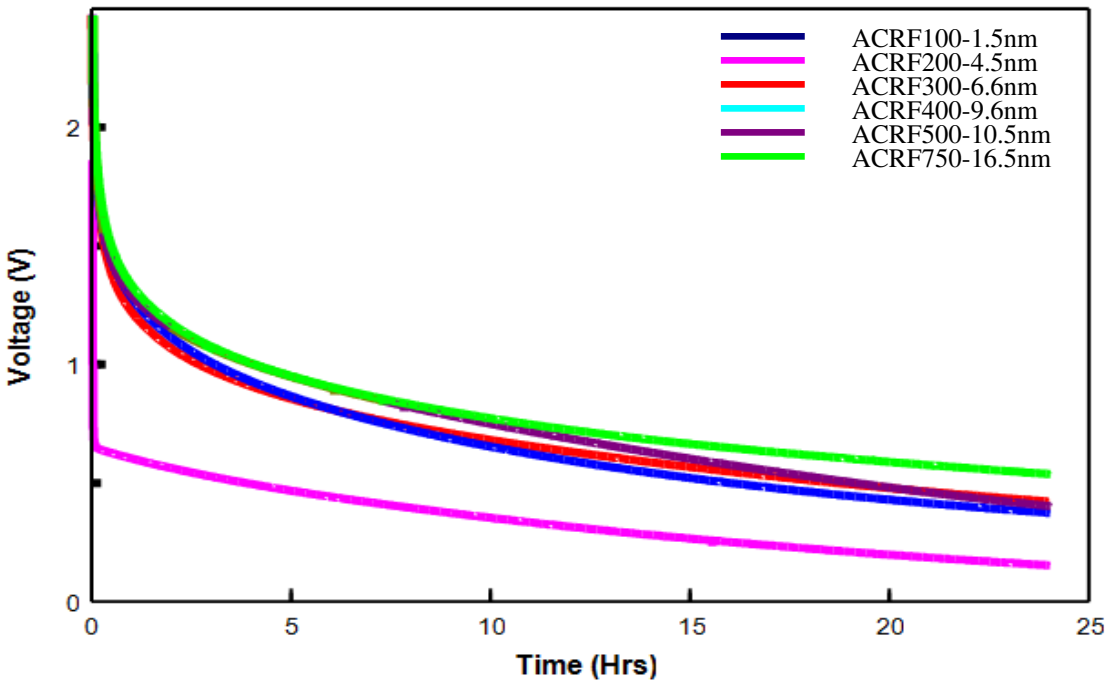

Figure A4.2 – Variance of Self-discharge with Pore Size for EMImN$(CN)_2$

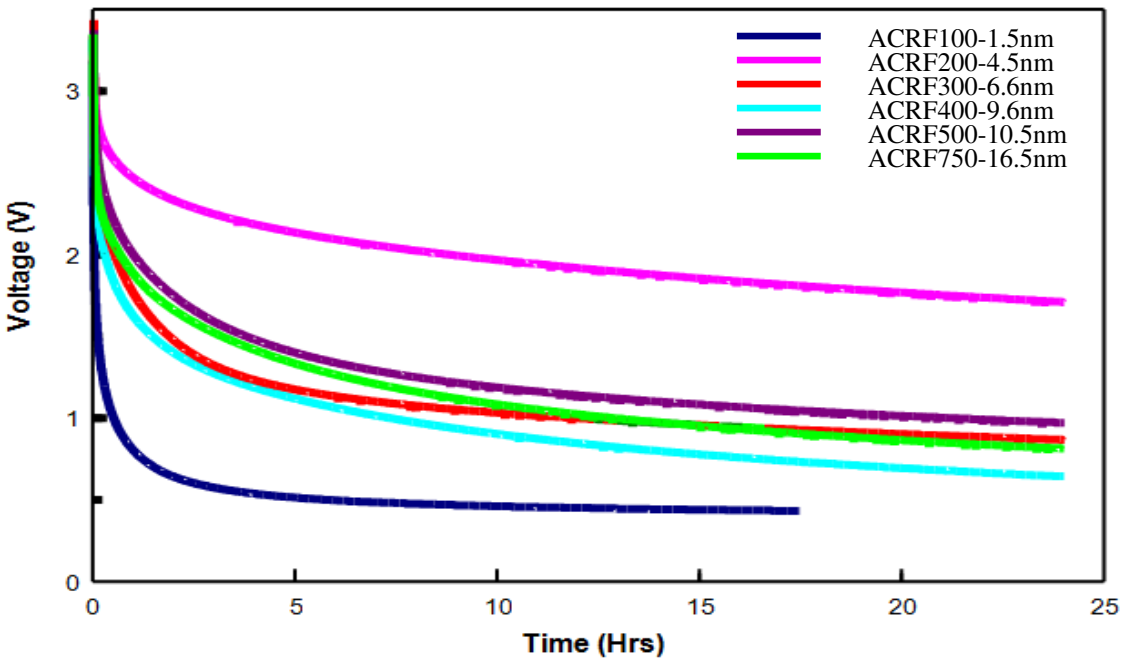

Figure A4.3 – Variance of Self-discharge with Pore Size for BMPyT(f_5Et)PF_3

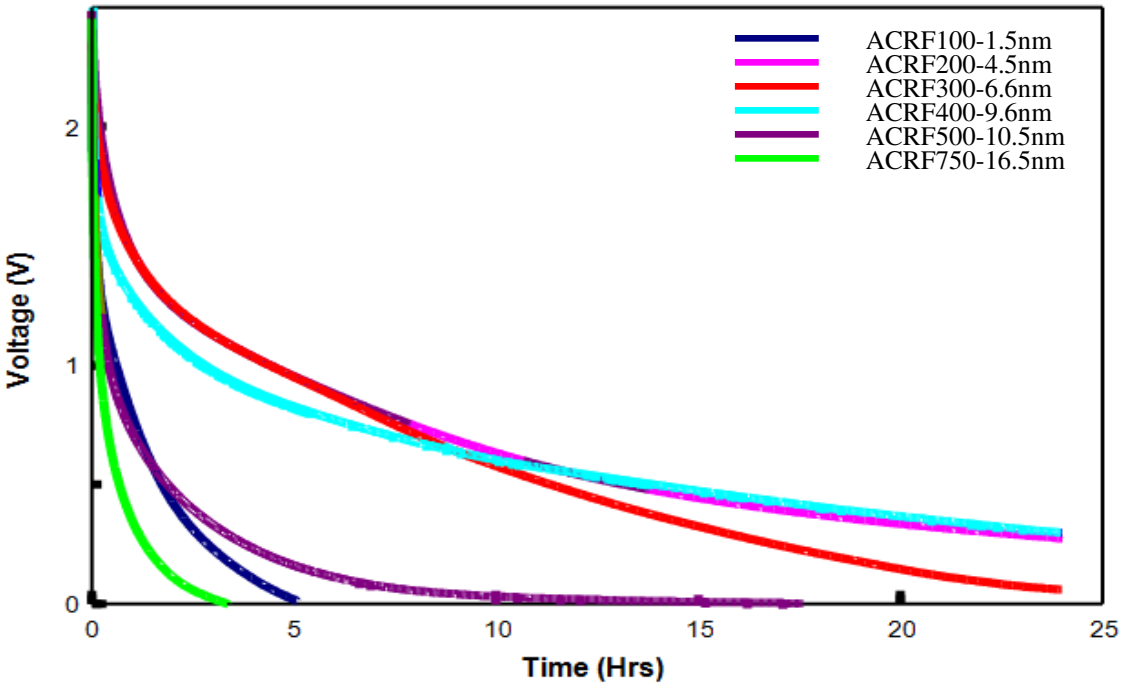

Figure A4.4 – Variance of Self-discharge with Pore Size for Et_4NBF_4 – PC 1M

A5 Ragone Plot – Supplementary Graph

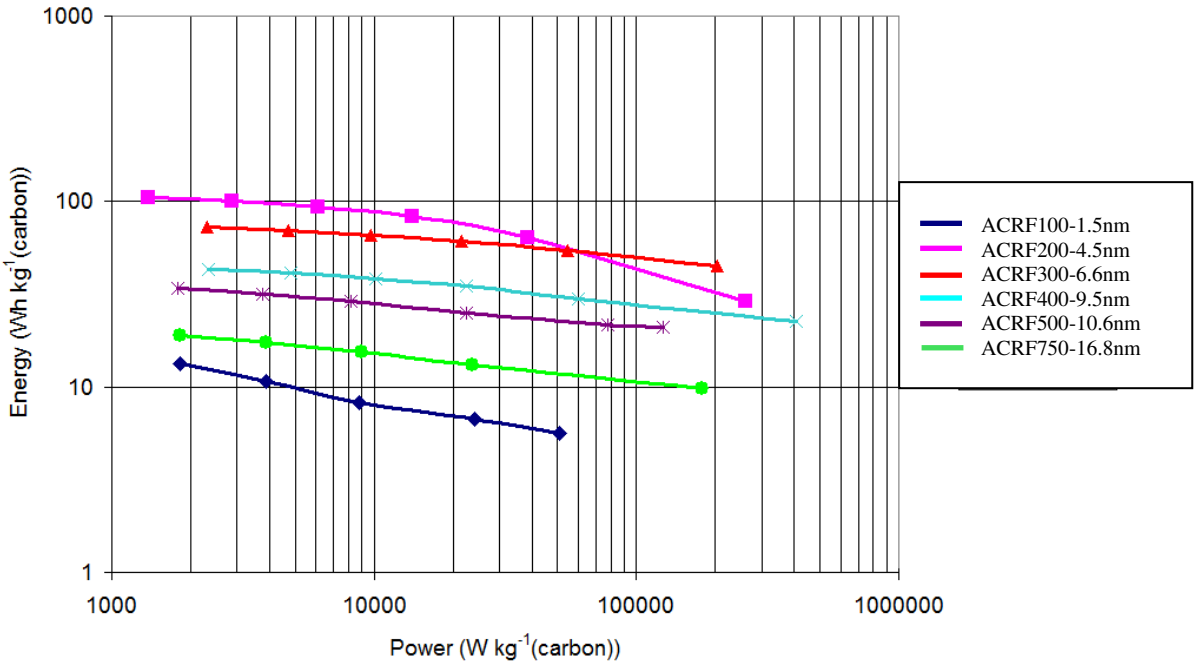

Figure A5.1 – Ragone Plot of Operating Energy and Power Density for DMPImTFSI

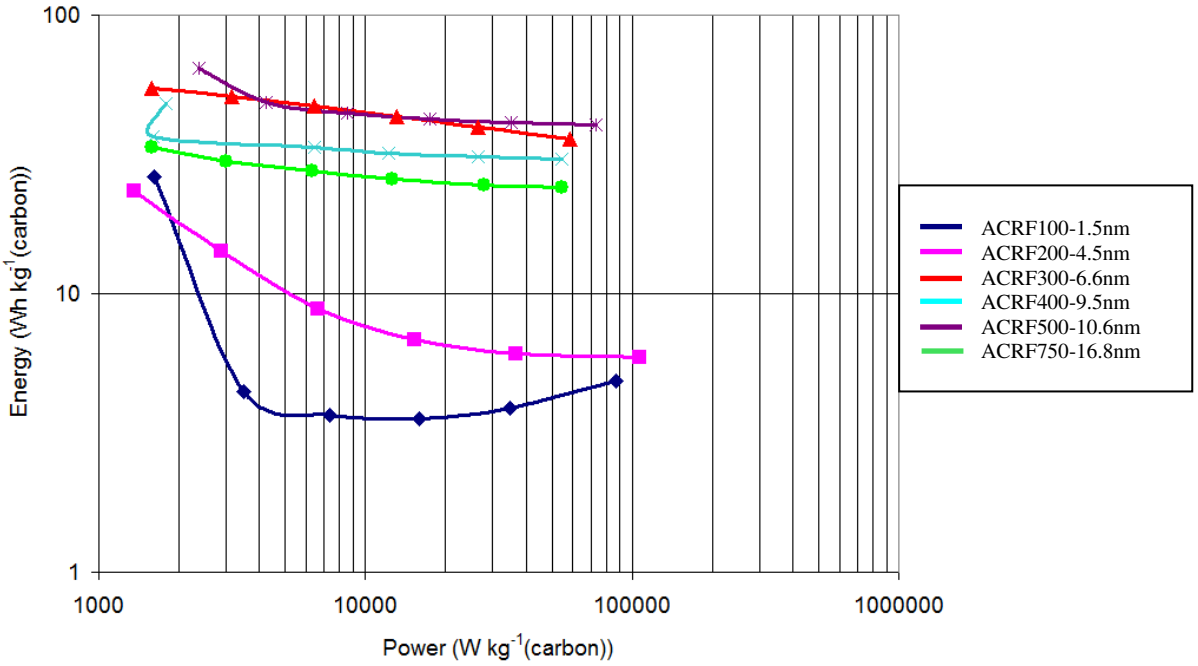

Figure A5.2 – Ragone Plot of Operating Energy and Power Density for $EMImN(CN)_2$

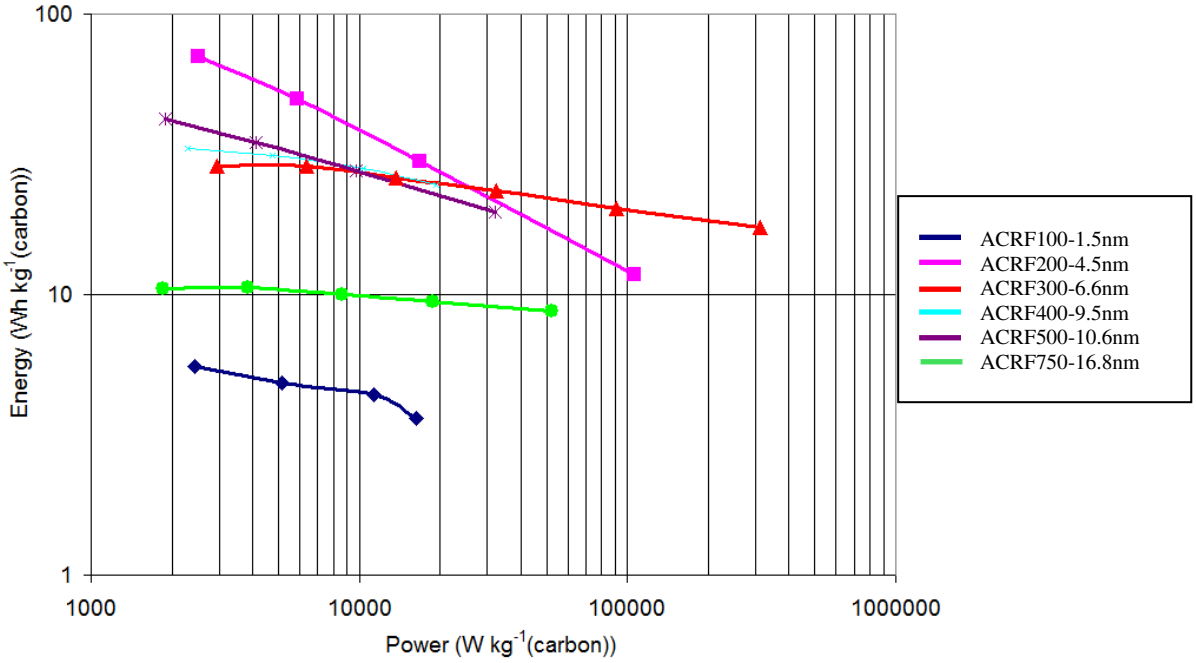

Figure A5.3 – Ragone Plot of Operating Energy and Power Density for $BMPyT(f_5Et)PF_3$

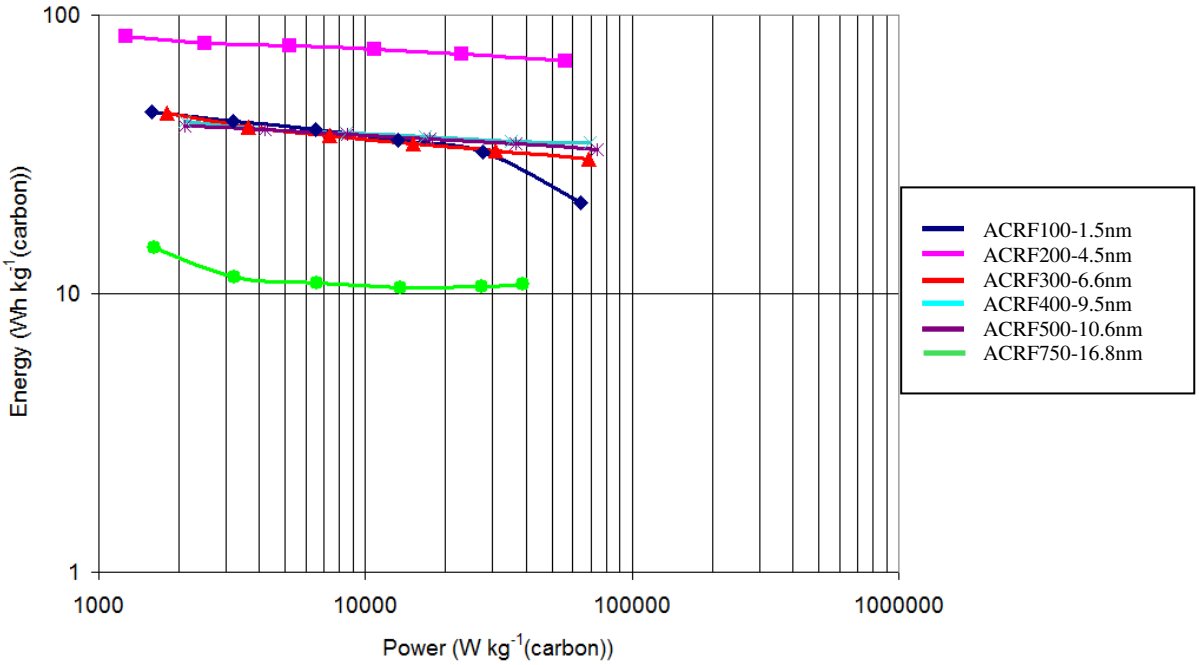

Figure A5.4 – Ragone Plot of Operating Energy and Power Density for Et_4NBF_4 – PC 1M

A6 Viscosity of RT Ionic Liquid Electrolytes

Table A6.1 – Viscosity data for Ionic Liquids at T = 17 to 92°C

(Data courtesy of Dr Isobel Fletcher of the University of Strathclyde)

Temperature **T/°C**	**$EMImN(CN)_2$** **η** **/Pa.s**	**DMPImTFSI** **η** **/Pa.s**	**$BMPyT(f_5Et)PF_3$** **η** **/Pa.s**	**$EMImBF_4$** **η** **/Pa.s**
17	0.024	0.131	0.355	0.046
22	0.021	0.106	0.272	0.041
27	0.019	0.085	0.209	0.032
32	0.018	0.069	0.163	0.031
37	0.017	0.058	0.129	0.027
42	0.016	0.049	0.105	0.024
47	0.015	0.042	0.087	0.022
52	0.015	0.037	0.072	0.021
57	0.014	0.033	0.062	0.019
62	0.014	0.029	0.053	0.018
67	0.013	0.027	0.047	0.018
72	0.013	0.024	0.041	0.016
77	0.012	0.023	0.037	0.015
82	0.012	0.021	0.034	0.015
87	0.012	0.020	0.030	0.015
92	0.012	0.019	0.028	0.013